

Creation and Manipulation of Topological Magnetic Textures in Chiral and Frustrated Magnets

Dissertation
zur Erlangung des Grades
„Doktor der Naturwissenschaften“
am Fachbereich Physik, Mathematik und Informatik
der Johannes Gutenberg-Universität Mainz
in Mainz
vorgelegt von

Ross John Knapman

geb. in Northallerton, Vereinigtes Königreich



JOHANNES GUTENBERG
UNIVERSITÄT MAINZ

Mainz, den 22. Februar 2024

Berichtersteller/-innen: Prof. Dr. Karin Everschor-Sitte
Prof. Dr. Jairo Sinova
J-Prof. Dr. Angela Wittmann
Apl. Prof. Dr. Pierre Capel

Tag der mündlichen Prüfung: 14. Mai 2024

Abstract

Magnetic skyrmions are vortex-like spin textures in ferromagnetic materials that have seen a surge in research interest in recent years. Their small size, energetic stability, and the low applied electric currents required for their manipulation have made them promising candidates in next-generation information storage and processing applications. Skyrmions are a subset of a broader class of topological magnetic textures which includes domain walls and more novel structures such as magnetic hopfions. Magnetic hopfions are three-dimensional, smoke ring-like topological magnetic structures which are experiencing a steady growth in research interest at the time of preparing this Thesis.

In this Thesis, we investigate the creation and dynamics of magnetic solitons, with a particular focus on magnetic skyrmions, subject to various external influences. The Thesis is divided into three parts.

In the first Part, we review relevant concepts, methods, and literature. Specifically, we introduce magnetic skyrmions and hopfions through topological considerations, as well as the mechanisms through which they are stabilised. We also discuss the micromagnetic model, which is the framework within which we perform both the analytical and numerical calculations.

In the second Part of this Thesis, we investigate the current-driven creation of skyrmions and vortex rings in chiral magnets. As electrons pass through a magnetic material, their spin aligns with the local magnetisation, which induces a torque that acts on the magnetisation. This torque is known as the spin-transfer torque and causes the magnetisation to vary over time. The interplay between spin-transfer torque and magnetic impurities can result in the creation of magnetic textures at the impurity. Following from earlier literature, we propose a method whereby skyrmions can be created in spin spiral states. Furthermore, we demonstrate a similar mechanism through which vortex rings can be created in bulk magnetic systems.

In the final Part of this Thesis, we study the dynamics of skyrmions in both chiral and frustrated magnets. In the former case, we show that subjecting skyrmions to an oscillating magnetic field at unit fractions of their eigenfrequencies can result in efficient excitation of the eigenmodes. This has applications in the frequency multiplication of magnons. In the latter case, we show that the application of an applied electric field can excite internal modes of the skyrmion, which we describe using the topology of magnetic hopfions.

Kurzzusammenfassung

Magnetische Skyrmionen sind wirbelartige Spintexturen in ferromagnetischen Materialien, die in den letzten Jahren ein starkes Forschungsinteresse erfahren haben. Ihre geringe Größe, energetische Stabilität sowie die für ihre Manipulation benötigten geringen angelegten elektrischen Ströme haben Skyrmionen zu vielversprechenden Kandidaten für künftige Anwendungen in der Informationsspeicherung und -verarbeitung gemacht. Skyrmionen sind eine Untergruppe einer breiteren Klasse topologischer magnetischer Texturen, zu denen Domänenwände und neuere Strukturen wie magnetische Hopfionen gehören. Magnetische Hopfionen sind dreidimensionale, rauchringförmige, topologische magnetische Texturen, die zum Zeitpunkt der Erstellung dieser Dissertation ein stetig wachsendes Forschungsinteresse erfahren.

Diese Dissertation untersucht die Erzeugung und Dynamik von magnetischen Solitonen, wobei ein Schwerpunkt auf magnetischen Skyrmionen liegt, die verschiedenen äußeren Einflüssen ausgesetzt sind. Die Dissertation gliedert sich in drei Teile.

Im ersten Teil der Dissertation wird ein Überblick über die Konzepte, Methoden und Literatur gegeben. Insbesondere stellen wir magnetische Skyrmionen und Hopfionen durch topologische Betrachtungen vor, sowie die Mechanismen, durch die sie stabilisiert werden. Wir besprechen auch das mikromagnetische Modell, in dessen Rahmen wir sowohl die analytischen als auch die numerischen Berechnungen durchführen.

Im zweiten Teil dieser Dissertation untersuchen wir die strominduzierte Erzeugung von Skyrmionen und Wirbelringen in chiralen Magneten. Wenn Elektronen ein magnetisches Material durchfließen, richtet sich ihr Spin an der lokalen Magnetisierung aus, was ein Drehmoment induziert, das auf die Magnetisierung wirkt. Dieses Drehmoment wird als Spin-Transfer-Drehmoment bezeichnet und bewirkt, dass sich die Magnetisierung mit der Zeit verändert. Das Zusammenspiel von Spin-Transfer-Drehmoment und magnetischen Inhomogenitäten kann dazu führen, dass an der Inhomogenität magnetische Texturen erzeugt werden. In Anlehnung an die Literatur schlagen wir eine Methode vor, mit der Skyrmionen in Spin-Spiral-Zuständen erzeugt werden können. Darüber hinaus demonstrieren wir einen ähnlichen Mechanismus, durch den Wirbelringe in dreidimensionalen magnetischen Systemen erzeugt werden können.

Im letzten Teil dieser Dissertation untersuchen wir die Dynamik von Skyrmionen in chiralen und frustrierten Magneten. Im ersten Fall zeigen wir, dass Skyrmionen, die einem oszillierendem Magnetfeld, dessen Frequenz ein Bruchteil der Eigenfrequenz ist, ausgesetzt sind, effizient zu einer Eigenmode angeregt werden können. Dies findet Anwendungen bei der Frequenzmultiplikation von Magnonen. Im zweiten Fall zeigen wir, dass das Anlegen eines oszillierendes Feldes Resonanzmoden von Skyrmionen anregen kann, die wir mit Hilfe der Topologie der magnetischen Hopfionen beschreiben.

Contents

I. Preliminaries	1
1. Introduction	3
2. Topological Magnetic Textures: From Domain Walls to Skyrmions	5
2.1. Homotopy Groups and Magnetic Textures	5
2.2. Prediction and Observation of Magnetic Skyrmions	9
2.3. Applications of Magnetic Skyrmions	11
3. Magnetic Hopfions	13
3.1. Topology of Magnetic Hopfions	13
3.2. Stabilisation of Magnetic Hopfions	16
3.3. Experimental Progress with Magnetic Hopfions	17
3.4. Applications of Magnetic Hopfions	18
4. Statics and Dynamics of Magnets	19
4.1. Magnetostatics	19
4.2. Landau-Lifshitz-Gilbert Equation	26
4.3. Collective Coordinate Modelling of Magnetic Textures	29
5. Stabilisation of Magnetic Skyrmions	31
5.1. Stabilisation of Skyrmions in Chiral Magnets	31
5.2. Skyrmions in a Cycloidal Background	32
5.3. Stability of the Cycloidal State	35
5.4. Frustrated Magnets	38
II. Current-Driven Creation of Topological Magnetic Textures	41
6. Magnetic Texture Creation in the Ferromagnetic State	43
6.1. Current-Driven Creation of Magnetic Domain Walls	43
6.2. Current-Driven Skyrmion-Antiskyrmion Pair Creation	44
7. Current-Driven Skyrmion Creation in the Cycloidal State	51
7.1. Stability of the Cycloidal State Under an Applied Current	51
7.2. Current-Driven Creation of Skyrmions in the Cycloidal State	53
7.3. Protocol for the Controlled Creation of Skyrmions in the Cycloidal State	55
8. Current-Driven Creation of Magnetic Textures in Bulk Systems	59
8.1. Current-Driven Dynamics of Magnetic Vortex Rings and Hopfions	59
8.2. Current-Driven Creation of Magnetic Vortex Rings	61

III. Skyrmion Dynamics	65
9. Current-Driven Motion of Magnetic Skyrmions	67
9.1. Fundamentals of Current-Driven Motion of Skyrmions	67
9.2. Current-Driven Motion of Skyrmions in the Cycloidal State	69
10. Internal Modes of Skyrmions in Chiral Magnets	73
10.1. Skyrmion-Magnon Interactions	73
10.2. Basic Principles of Frequency Multiplication	75
10.3. Numerical Study of Skyrmion Frequency Multiplication	77
10.4. Generalisation to Arbitrary Magnetic Structures	81
11. Electric Field-Driven Dynamics of Skyrmions in Frustrated Magnets	85
11.1. Dynamics of Skyrmions in Frustrated Magnets	85
11.2. Electric Field Amplitude-Frequency Phase Diagram	89
11.3. Finite-Temperature Simulations	96
11.4. Topological Interpretation as Spacetime Magnetic Hopfions	97
12. Summary	101
IV. Appendices	103
A. Numerical Calculation of Topological Indices	105
A.1. Numerical Calculation of the Skyrmion Number	105
A.2. Numerical Calculation of the Hopf Index	106
B. Derivation of Frustrated Energy Functional	109
C. Numerical Implementation of Effective Fields in MuMax3	115
C.1. Internal Structure of MuMax3	115
C.2. Implementation of Higher-Order Exchange	119
C.3. Implementation of an Applied Electric Field	126
D. Frustrated Magnet Ground State	131
E. Derivation of the Cycloidal State Critical Current	133
F. Integration of Frustrated Magnet Skyrmion Thiele Equations	137
Bibliography	147
Acknowledgements	163
V. Anhänge gemäß Prüfungsordnung	165
List of Publications	167
Curriculum Vitae	169

Part I.

Preliminaries

Chapter

1

Introduction

In the 19th century, inspired by the work of Helmholtz on *Wirbelbewegung*, or vortex motion, in fluids [1], Lord Kelvin proposed his vortex theory of atoms [2]. In this theory, he considered atoms as localised, knotted structures in the ‘aether’, a material that was previously hypothesised to permeate space to explain, for example, the propagation of light. The impossibility of continuously deforming one type of knot into another would explain the distinct elements, while resonances in these structures would explain the atomic spectra. Although this theory ultimately proved unsuccessful and was later abandoned with the discovery of the electron and the subsequent advent of quantum mechanics in the early 20th century, the idea of localised structures in continuous fields remains important to this day.

One example of a system that can be described as a continuous field is the magnetisation in a ferromagnetic material. Below the Curie temperature, the overall magnetisation of a lattice unit cell in a ferromagnet, which is the sum of the individual magnetic moments of the magnetically active atoms, tends to align with that of the neighbouring cell. Thus, zooming out from this microscopic picture with individual spins, one can consider the magnetisation \mathbf{M} as a vector field of constant magnitude M_s , that is a function of position \mathbf{r} . Although the concept of an aether in which knots correspond to chemical elements has long since been abandoned, the ideas of Kelvin still very much apply in magnetism, where continuous field theory can be applied.

Depending on the interactions at play in a particular magnetic system, various structures of the magnetisation field $\mathbf{M}(\mathbf{r})$ can be stabilised. Structures which have received significant research attention in recent decades are topological solitons, which cannot be created or destroyed by a continuous deformation of $\mathbf{M}(\mathbf{r})$ without being moved to the boundary. This gives the object robustness against perturbations. One example of such a structure is a domain wall separating regions of different uniform magnetisations. Another example of topological solitons arising in magnetic materials is a magnetic skyrmion, which is a localised region in the magnetisation field for which the magnetisation at the core points in the opposite direction to the background magnetisation. The uniform variation between the core and the background creates a vortex-like shape. A further example proposed in bulk magnetic systems is a magnetic hopfion. Magnetic hopfions are knotted structures somewhat akin to vortex rings in fluids.

In this Thesis, we investigate the behaviour of magnetic textures subject to various

Chapter 1. Introduction

external factors: applied current and dynamic electric and magnetic fields, within the micromagnetic model, with emphasis on magnetic skyrmions. The applied currents and fields induce a range of dynamical behaviours. Under this umbrella, the Thesis is divided into three parts.

Part I contains a discussion of the core concepts underlying the various investigations. In Chapter 2 we introduce topological magnetic structures, specifically skyrmions, followed by a discussion of magnetic hopfions and recent progress into the study of these objects in Chapter 3. In Chapter 4 we introduce the micromagnetic framework used throughout the Thesis to model magnetisation textures. The methods discussed are supported by the discussion of Chapter 5, in which we discuss the stabilisation of skyrmions in various magnetic systems.

Part II is concerned with the creation of magnetic textures through the application of electric current to magnetic systems containing impurities. In Chapter 6 we discuss the current-driven creation of domain walls and skyrmions in the ferromagnetic state, before discussing the creation of skyrmions in spin spiral states in Chapter 7. In Chapter 8 we consider analogous processes in bulk systems, resulting in the creation of magnetic vortex rings.

In Part III, we study the dynamics of skyrmions in a variety of contexts. In Chapter 9 after providing a general introduction to the motion of skyrmions when subjected to spin-transfer torque, we investigate this phenomenon for the case of skyrmions in a cycloidal background. In Chapter 10 we discuss the resonance modes of skyrmions in chiral magnets, and their application to frequency multiplication of magnons. We argue that the results of this investigation apply to general topological magnetic structures. In Chapter 11 we turn to the internal dynamics of skyrmions in frustrated magnets, investigating rotations of their in-plane magnetisation direction induced by an applied oscillating electric field. We end Chapter 11 with an interpretation of the resulting dynamics as hopfions in spacetime. A summary of the studies presented in this Thesis is given in Chapter 12. The Appendices contain background information pertinent to the results reported, such as derivations and code.

Chapter 2

Topological Magnetic Textures: From Domain Walls to Skyrmions

Topology is a branch of mathematics which deals with properties that do not change under continuous deformations. A commonly used example to illustrate this concept is the morphing of a coffee mug into a doughnut, illustrated in Fig 2.1. Because both a coffee mug and a doughnut each have one hole, a one-to-one mapping between each point on the mug and on the doughnut is possible. Removing the hole, on the other hand, would require a mapping from many points to one (‘pinching the hole shut’). As we will see in this Chapter, similar notions can be applied to the field configurations of the magnetisation field in magnetic materials, in which localised field configurations, known as topological solitons, exist that cannot be continuously deformed into states with different topologies.

2.1. Homotopy Groups and Magnetic Textures

One of the simplest topological objects in a ferromagnet is a one-dimensional domain wall: a boundary between two magnetic domains with different orientations of the normalised magnetisation $\mathbf{m}(\mathbf{r}) = \mathbf{M}(\mathbf{r})/M_s$ [3]. Let us consider a domain wall along the x -axis for which $\mathbf{m}(x \rightarrow -\infty) = -\hat{z}$ and $\mathbf{m}(x \rightarrow \infty) = \hat{z}$, where the magnetisation is restricted to rotate in the xz -plane. One example of a profile which satisfies these boundary conditions is

$$\mathbf{m} = \sin[\Theta(x)]\hat{x} + \cos[\Theta(x)]\hat{z}, \quad (2.1)$$



Figure 2.1.: Deformation of a mug into a doughnut. As each object has one hole, there is a one-to-one mapping between each point on the doughnut and the mug.

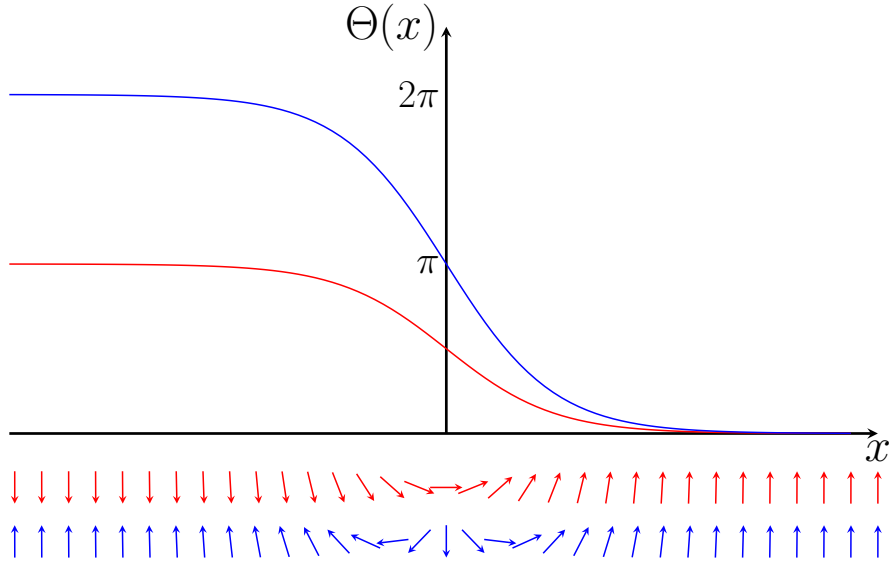


Figure 2.2.: Domain wall profile with a rotation of π , shown in red, and 2π , shown in blue.

where $\Theta(x) = \pi[1 - \tanh(x/\lambda)]/2$, with λ representing the domain wall width. This is plotted as a red curve in Fig. 2.2. The number of times that the spin rotates is given by

$$w = \frac{1}{2\pi} \int_{-\infty}^{\infty} dx \partial_x \Theta(x), \quad (2.2)$$

which, in this case, is

$$w = \frac{1}{2\pi} [\Theta(x \rightarrow \infty) - \Theta(x \rightarrow -\infty)] = \frac{1}{2}. \quad (2.3)$$

This number not being an integer reflects the fact that $\mathbf{m}(x \rightarrow -\infty) \neq \mathbf{m}(x \rightarrow \infty)$. Thus, the endpoints cannot be ‘glued together’, or identified. This can be remedied by requiring that the magnetisation performs a full 2π rotation (or, more generally, an integer number of 2π rotations), such as $\Theta(x) = \pi[1 - \tanh(x/\lambda)]$, shown as a blue curve in Fig. 2.2. In this case, $\mathbf{m}(x \rightarrow -\infty) = \mathbf{m}(x \rightarrow \infty) = \hat{z}$, and it is possible to identify the endpoints infinitely far away from the domain wall in both directions along the x -axis.

The idea of making infinity a single point to create a compact manifold is known as compactification and, in this case, the x -axis has been compactified to a (unit) circle S^1 . Explicitly, a mapping between these two spaces is given by the stereographic projection, which is illustrated in Fig. 2.3. One possible mapping of this compactification is given by, for a point (x, z) on S^1 and a point X along the x -axis,

$$X = \frac{x}{1 - z}. \quad (2.4)$$

As both x and $\mathbf{m}(x)$ take values on S^1 , the S^1 -winding number w_{S^1} is a topological invariant of the mapping from one unit circle to another. In general, homotopy groups $\pi_n(X)$ characterise mappings between an n -sphere and a topological space X [3]. This notion of the $S^1 \rightarrow S^1$ mapping being characterised by an integer is formalised in

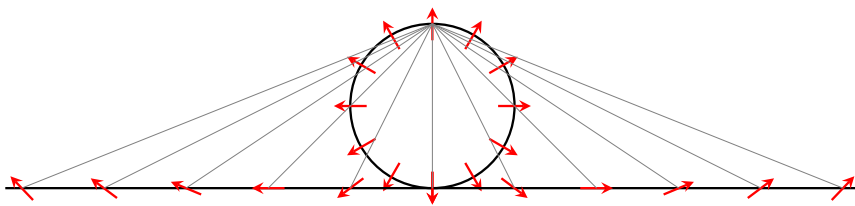


Figure 2.3.: Illustration of the one-dimensional stereographic projection from S^1 to \mathbb{R} . Note that in (2.4), (2.7), and (3.1), the plane goes through the equator of the n -sphere, rather than the sphere being tangent to the plane, which is another convention that is used here for illustrative purposes.

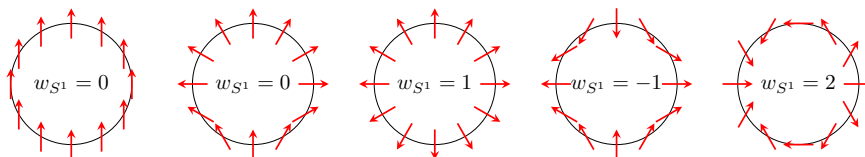


Figure 2.4.: Illustration of various S^1 winding numbers.

homotopy theory, with the expression

$$\pi_1(S^1) = \mathbb{Z}, \quad (2.5)$$

where the subscript 1 indicates that the base space is a 1-sphere, or unit circle. Examples of such a mapping with various winding numbers are illustrated in Fig. 2.4. Although the textures with a given winding number can be smoothly deformed into one another, a smooth deformation between mappings of different winding numbers is, for a continuous vector field, mathematically forbidden. This introduces the idea of topological protection: the example of a domain wall with $w_{S^1} = 1$ cannot be smoothly deformed into the topologically trivial state where $\mathbf{m}(x) = \hat{\mathbf{z}}$ everywhere, and thus the domain wall is said to be topologically protected.

It is important to note, however, that topology alone does not guarantee the stability of localised structures. To see this, we invoke the argument of Derrick and Hobart [4, 5]. Considering the energy of this one-dimensional system being given by, for the profile (2.1)¹,

$$U[\mathbf{m}(x)] = \int dx (\partial_x \mathbf{m})^2 = \int dx (\partial_x \Theta)^2 \propto \frac{1}{\lambda}, \quad (2.6)$$

the energy is minimised when the domain wall characteristic width λ becomes infinitely large, such that the object ceases to be local. To fix a finite length scale, terms must be added to the energy functional that have different scaling with length. For example, while $(\partial_x \Theta)^2$ scales as length⁻², a quartic term $(\partial_x^2 \Theta)^2$ would scale as length⁻⁴.

Moving up to two dimensions, we can consider folding a domain wall around in a circle, to create a vortex-like structure, such that $\mathbf{m}(\mathbf{r} = \mathbf{0}) = -\hat{\mathbf{z}}$ and $\mathbf{m}(|\mathbf{r}| \rightarrow \infty) = \hat{\mathbf{z}}$, as illustrated in Fig 2.5. This structure is known as a magnetic skyrmion. In addition to

¹Throughout this Thesis, we use the non-standard notation U for the energy. E is often used in the literature, but we do not use this to avoid confusion with the electric field in later chapters.

moving the base space up a dimension to \mathbb{R}^2 , we have also relaxed the restriction that $\mathbf{m}(\mathbf{r})$ takes values on a unit circle, instead taking values on a 2-sphere S^2 . Just as we considered identifying $\pm\infty$ of the x -axis, we now consider identifying all points $|\mathbf{r}| \rightarrow \infty$, such that the \mathbb{R}^2 plane of infinite extent in x and y is compactified onto a unit 2-sphere, as illustrated in Fig. 2.6. The stereographic projection in this case is analogous to (2.4). Namely, for points (x, y, z) on a 2-sphere and points (X, Y) in \mathbb{R}^2 ,

$$X = \frac{x}{1-z}, \quad Y = \frac{y}{1-z}. \quad (2.7)$$

The north pole of the 2-sphere is mapped to the points infinitely far away from $X = Y = 0$ in \mathbb{R}^2 . Thus, the magnetisation $\mathbf{m}(\mathbf{r})$ now represents a mapping $S^2 \rightarrow S^2$. As with $S^1 \rightarrow S^1$, the mapping $S^2 \rightarrow S^2$ can be described in homotopy theory by an integer: $\pi_2(S^2) = \mathbb{Z}$. This is also a winding number, counting the number of times that the magnetisation target space wraps the unit sphere base space. This topological invariant, known as the skyrmion number N_{sk} , is given by

$$N_{\text{sk}} = \frac{1}{4\pi} \int_{\mathbb{R}^2} d^2r \mathbf{m} \cdot (\partial_x \mathbf{m} \times \partial_y \mathbf{m}), \quad (2.8)$$

where the integral evaluates the solid angle subtended by the magnetisation texture over the unit sphere. A skyrmion texture is typically written as

$$\mathbf{m} = \begin{bmatrix} \cos \Phi \sin \Theta \\ \sin \Phi \sin \Theta \\ \cos \Theta \end{bmatrix}, \quad (2.9)$$

where Φ and Θ are the azimuthal and polar angles respectively. In analytical calculations, $\Theta(\rho)$ is typically a function that decreases monotonically from π at the centre of the texture to 0 as the radial coordinate $\rho \rightarrow \infty$. $\Phi(\psi)$ is a function that varies with the polar angle ψ from the x -axis in the xy -plane as

$$\Phi(\psi) = m\psi + \eta, \quad (2.10)$$

where $m = -N_{\text{sk}}$ is the vorticity and η is the helicity. Conventionally, textures with $m = 1$, or $N_{\text{sk}} = -1$, are known as skyrmions and those with $N_{\text{sk}} = 1$ are antiskyrmions². For skyrmions, $\eta = 0, \pi$ corresponds to a Néel-type skyrmion and $\eta = \pi/2, 3\pi/2$ corresponds to a Bloch-type skyrmion, shown in Figs. 2.6(a) and (b) respectively, as their radial profiles correspond to Néel and Bloch domain walls. For an antiskyrmion, varying η only rotates the texture about $\rho = 0$. Which type of skyrmion is stabilised depends on the microscopic interactions in the system, which is discussed further in Chapter 5. As with the one-dimensional case, magnetisation textures of different N_{sk} cannot be continuously deformed into one another. As shown in Fig. 2.6(c), a texture for which the integration in (2.8) yields a non-integer value cannot strictly be assigned a topological charge as there is no unique value of $\mathbf{m}(\mathbf{r})$ for $|\mathbf{r}| \rightarrow \infty$; instead, the magnetisation takes all values on the equator of S^2 infinitely far from the origin, depending on the polar angle.

²In (2.8), a skyrmion with vorticity $m = 1$ and polarity $p = -1$ (meaning that the magnetisation at the core points along $-\hat{z}$) has $N_{\text{sk}} = -1$. The expression for N_{sk} given in (2.8) often has an additional minus sign so that N_{sk} has the same sign as m

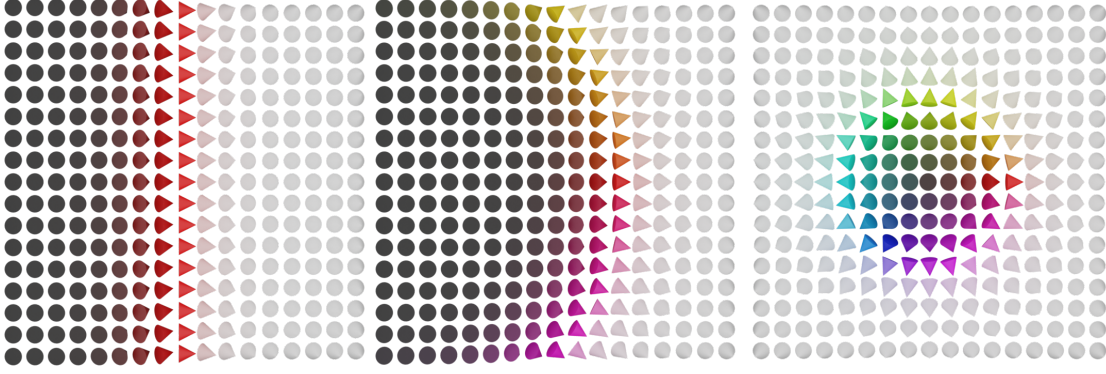


Figure 2.5.: Illustration of the closing of a domain wall on itself to construct a skyrmion.

2.2. Prediction and Observation of Magnetic Skyrmions

In this Thesis, we consider skyrmions as localised, topologically protected quasiparticles with the homotopy group $\pi_2(S^2)$ in quasi-two-dimensional ferromagnetic materials. However, the concept of the skyrmion was proposed by Skyrme in the mid-20th century as a model for nucleons [6–10], in the same vein as Kelvin’s model of atoms described in Chapter 1. In this context, skyrmions are topological solitons in a pion field in three spatial dimensions. As this model considers an $SU(2)$ field (which is topologically equivalent to S^3) in three spatial dimensions (which can be compactified to S^3), the homotopy group of the system considered by Skyrme is $\pi_3(S^3)$. Due to the difference in homotopy classification between the objects that Skyrme envisaged and those typically studied in magnetic materials, the latter are sometimes referred to as ‘baby skyrmions’. Since Skyrme’s pioneering theoretical work, skyrmions have appeared in various fields of physics, including in the study of Bose-Einstein condensates [11, 12], superconductors [13], liquid crystals [14, 15], as well as in magnetic materials.

Magnetic skyrmions (generally referred to as simply ‘skyrmions’ in the magnetism community) have seen a significant increase in research efforts in recent years. In a series of papers, Bogdanov theoretically investigated ‘magnetic vortices’, which would later be called magnetic skyrmions, in materials with the Dzyaloshinskii-Moriya interaction [16–21] discussed in Section 4.1. This texture turned out to be that of the unexplained ‘A-phase’ [22, 23] in the magnetic phase diagram of the chiral magnet MnSi, observed using magnetoresistance and small-angle neutron scattering (SANS). This phase diagram was observed for magnetic fields magnitudes at the order of 0.1 T applied perpendicular to the plane of the thin film sample at temperatures below, but close to, the Curie temperature. It will be discussed in more detail in Section 5.1. The experimental confirmation linking the A-phase to a skyrmion lattice came in 2009 when Mühlbauer et al. [24] accidentally measured the neutron diffraction pattern with the applied magnetic field perpendicular to, rather than parallel to, the neutron beam, resulting in a six-fold diffraction pattern: an experimental signature of a skyrmion lattice [25]. By a stroke of luck, the measurements happened to have been taken at the correct temperature and magnetic field amplitude for the skyrmion lattice to be the ground state of the system, and these measurements helped to kick-start the study of skyrmions, known as skyrmionics. Furthermore, in 2010, real-space observations of skyrmions in MnSi and $Fe_{1-x}Co_xSi$ were made using Lorentz transmission electron microscopy [26]. Throughout

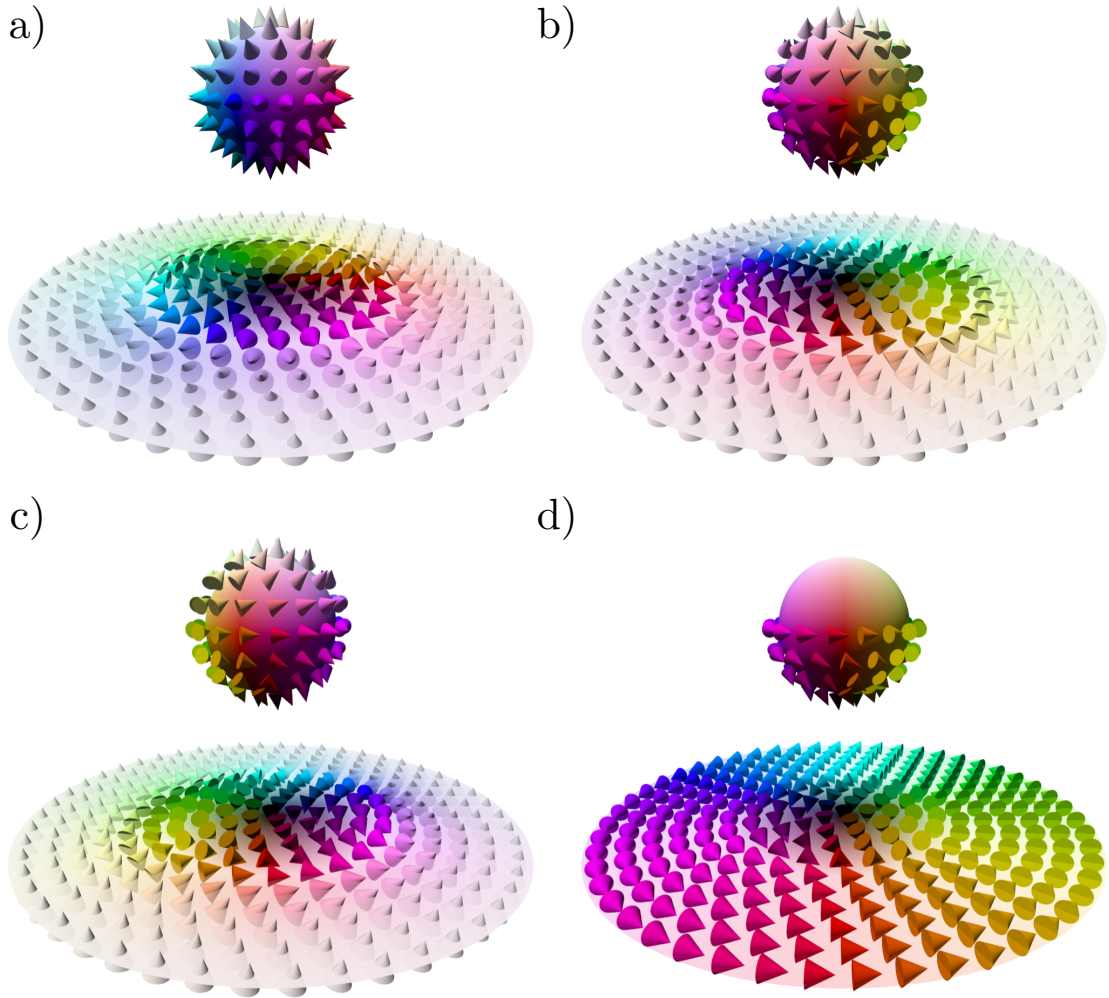


Figure 2.6.: Illustration of the stereographic projection of a vector field over S^2 onto \mathbb{R}^2 . (a) and (b) Construction by stereographic projection of a Néel- and Bloch-type skyrmion ($N_{\text{sk}} = -1$) respectively. (c) Construction of an antiskyrmion with $N_{\text{sk}} = 1$. (d) For a meron, only half of the sphere is covered, resulting in a non-integer skyrmion number (in this case, $N_{\text{sk}} = 1/2$), such that \mathbf{m} is not defined one-to-one as $|\mathbf{r}| \rightarrow \infty$.

the 2010s and continuing into the 2020s, there has been an intense research effort into skyrmions [27, 28].

2.3. Applications of Magnetic Skyrmions

Real-world applications of magnetisation textures such as domains, and potentially skyrmions, in ferromagnets, include data storage and processing. The concept of magnetic racetrack memory was proposed by Parkin, Hayashi and Thomas [29] in 2008 and consists of a thin magnetic material with successive magnetic domains of opposite polarisation, with the orientation (up or down) representing ‘1’ and ‘0’ binary digits (bits). Such tracks could be folded up to form a three-dimensional structure, providing high information densities. This concept has been extended to skyrmions [30–32], and is illustrated in Fig 2.7. Figure 2.7 shows read and write elements, as well as a track along which skyrmions can be moved by spin torques. Skyrmion racetrack memory offers several advantages over magnetic domain-based racetrack memory. Firstly, magnetic domain walls would necessarily extend to the edges of the system, which may have a roughness that results in reduced stability and effectiveness of the domain wall motion. Magnetic skyrmions, on the other hand, can propagate in the racetrack without touching the sides, allowing for more efficient transport. Secondly, the small size of skyrmions in comparison with magnetic domains could also allow for high densities of information to be stored. Their current-driven dynamics also offer advantages over magnetic domains. For a lattice of skyrmions, the threshold current density required to set them in motion is very low, of the order of 10^6 A m^{-2} [33], compared to that for domain walls, around 10^{10} A m^{-2} to 10^{12} A m^{-2} [29, 34]. Skyrmions also usually couple only weakly with pinning centres [35, 36]. The current-driven motion of magnetic skyrmions is discussed in more detail in Chapter 9. There are various methods by which magnetic skyrmions can be written, which are discussed in Chapter 6. The data represented by the presence or absence of skyrmions in the device could be read using magnetoresistive techniques such as giant magnetoresistance, tunnel magnetoresistance, or through the topological Hall effect [37]. The manipulation of skyrmions in logic gates has also been considered, with skyrmion logic gates demonstrated in numerical simulations [38, 39]. Furthermore, the implementation of transistors using magnetic skyrmions, where the operation is controlled by an externally applied electric field which locally modifies the uniaxial anisotropy, has been investigated [40, 41].

Outside of conventional computing, the use of skyrmions in unconventional computing has been the subject of intense theoretical and experimental investigation in recent years [42]. One potential application is in stochastic computing, where, instead of using precise bitwise operations to perform calculations, the problem is represented in terms of random bitstreams. The values are then encoded as the probability of observing a ‘0’ or ‘1’ in a random sequence of bits, which can result in a speedup of the calculation at the cost of precision [43]. Probabilistic computing using skyrmions has been investigated using magnetic skyrmions both theoretically and experimentally, where magnetic skyrmions are reshuffled to remove correlations between two bitstreams which cause inaccurate results [44, 45]. Additionally, applications in neuromorphic computing, where the computation is inspired by the function of the brain, have been investigated. In this paradigm, instead of using the von Neumann architecture in which the processing and memory units are physically separated (leading to the so-called ‘von

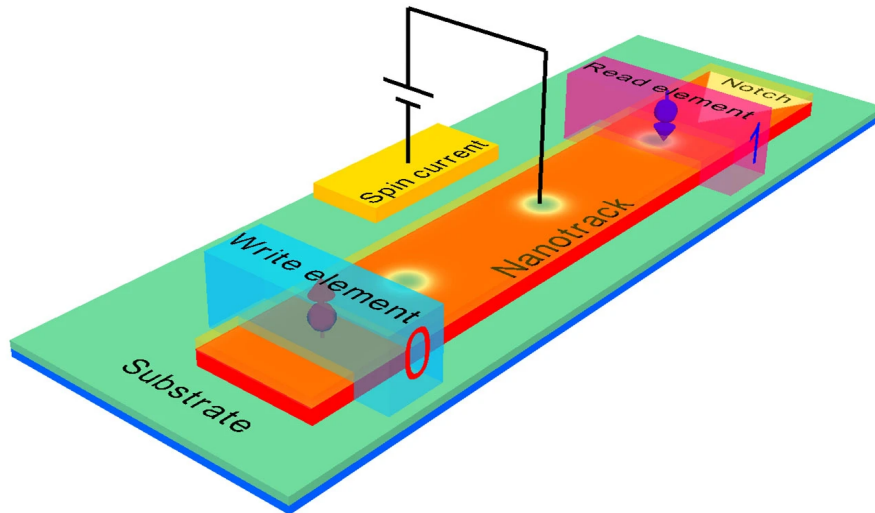


Figure 2.7.: Illustration of a skyrmion racetrack memory device. The skyrmions are created at the write element, driven along the nanotrack by a spin-polarised current, and read at the read element. Figure taken from Ref. [32].

Neumann bottleneck’ where the data transfer between the units is the limiting factor in speeding up calculations), data is processed in the same place that it is stored, allowing for low-power, highly parallel computing. It has been suggested theoretically [46, 47] and demonstrated experimentally [48] that skyrmions can emulate synapses. Another form of neuromorphic computing is reservoir computing [49], in which the input is fed into a fixed, highly nonlinear ‘reservoir’, which represents a higher dimensional computational space. In contrast to backpropagation-based neural network training algorithms, in reservoir computing, the training only occurs on the output weights. A complex magnetic texture consisting of many skyrmions has been proposed to act as a reservoir in this computational paradigm, where, for example, the skyrmions create an anisotropic electric resistance through the texture [50–54]. Aside from data information and processing applications, skyrmions have potential applications in nano-oscillators for microwave signal generation and detection [55–58], as discussed in Chapter 10.

Chapter 3

Magnetic Hopfions

In the previous Chapter, we discussed topological solitons in magnets, with domain walls in one dimension and skyrmions in two dimensions. As magnets can also exist as bulk systems, it is natural that we can conceive of three-dimensional topological solitons in magnetic materials. Various examples of these exist, such as chiral bobbars, which are skyrmion tubes (a skyrmion texture extruded along the direction perpendicular to the plane in which it lies) extending from the edge of the sample and terminating in a Bloch point (also referred to as a magnetic monopole or hedgehog) at which the magnetisation vanishes [59]. A related object is a toron, also known as a magnetic globule, monopole-antimonopole pair, or dipole string. This is similar to a chiral bobber, except that the ends of the skyrmion tube terminate in oppositely charged Bloch points [60–63]. A texture that has seen a sharp rise in interest over the years leading up to the preparation of this Thesis is the magnetic hopfion. This is a localised topological soliton whose topology is defined in a somewhat analogous manner to domain walls and skyrmions, but differently in the sense that the base and target spaces of the mapping $\mathbf{m}(\mathbf{r})$ have different dimensionalities. At a conceptual level, a hopfion can be considered as a texture for which the preimages of the mapping from three-dimensional space to the unit sphere on which the magnetisation exists, *i.e.* the closed loops in space at which the magnetisation $\mathbf{m}(\mathbf{r})$ points in a given direction, are linked. This is illustrated in Fig. 3.1, and discussed in the following Section. In this Chapter, we provide an introduction to these textures and an overview of recent progress in their study.

3.1. Topology of Magnetic Hopfions

For a normalised magnetisation vector field $\mathbf{m}(\mathbf{r})$ in a bulk magnet, the target space is still the unit sphere S^2 , but the base space is \mathbb{R}^3 . As before, we can map between three-dimensional space \mathbb{R}^3 and the 3-sphere S^3 existing in four-dimensional space through the stereographic projection analogous to (2.4) and (2.7). For points (x, y, z, w) on a 3-sphere $x^2 + y^2 + z^2 + w^2 = 1$ and (X, Y, Z) in \mathbb{R}^3 , we consider the compactification

$$X = \frac{x}{1-w}, \quad Y = \frac{y}{1-w}, \quad Z = \frac{z}{1-w}, \quad (3.1)$$

where the set of points infinitely far from the origin corresponds to the point $w = 1$, $x = y = z = 0$ in S^3 . Thus, $\mathbf{m}(\mathbf{r})$ represents the mapping $\mathbb{R}^3 \cup \{\infty\} \cong S^3 \rightarrow S^2$, and

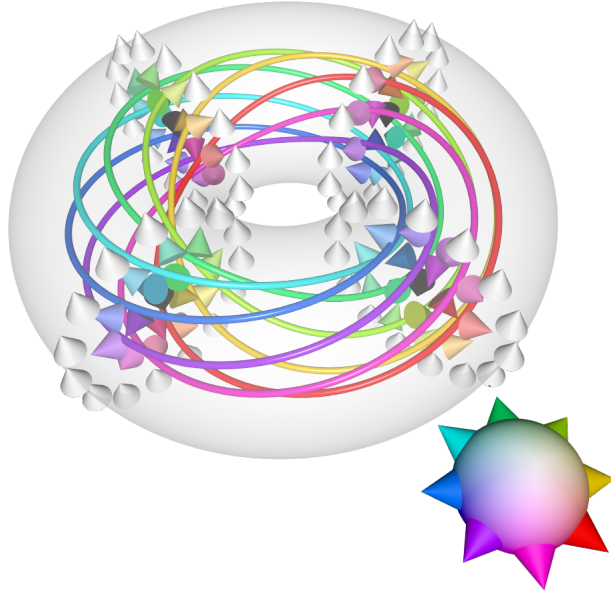


Figure 3.1.: Magnetic hopfion texture created from a tube of in-plane magnetic skyrmions, with various preimages around the S^2 -equator, $\Theta = \pi/2$, shown.

the relevant homotopy class is $\pi_3(S^2)$. This homotopy class is associated with an integer topological invariant, *i.e.* $\pi_3(S^2) = \mathbb{Z}$, which was discovered by Hopf [64] in 1931. Hopf lends his name to topological solitons of this homotopy class: hopfions. Unlike with the domain wall and skyrmion, the base space and target space do not have the same dimension in the Hopf map $S^3 \rightarrow S^2$, and the topological invariant does not have the interpretation of a winding number. Each point on S^2 of the map corresponds to a great circle S^1 of S^3 , such that the 3-sphere is an S^1 -bundle over the 2-sphere¹. The topological invariant then has the interpretation of a linking number, quantifying the number of times the preimages S^1 of the mapping link each other. In terms of the magnetisation vector field $\mathbf{m}(\mathbf{r})$, this can be seen by considering all of the points in the system which align in two distinct directions, forming closed loops (the preimages), and counting the number of times the closed loops link each other.

An example of hopfion magnetic texture is given by the Hopf map, $\mathbf{m}(\mathbf{r}) = \langle \chi | \boldsymbol{\sigma} | \chi \rangle$, where $\boldsymbol{\sigma} = (\sigma_x, \sigma_y, \sigma_z)$ is the Pauli vector and the spinor $|\chi\rangle = (x + iy, z + iw)$ [67]. x, y, z, w are coordinates on S^3 in terms of the \mathbb{R}^3 coordinates X, Y, Z , and can be calculated using the inverse of (3.1),

$$x = \frac{2X}{1 + R^2}, \quad y = \frac{2Y}{1 + R^2}, \quad z = \frac{2Z}{1 + R^2}, \quad w = \frac{R^2 - 1}{R^2 + 1}, \quad (3.2)$$

where $R^2 = X^2 + Y^2 + Z^2$. A selection of preimages of this mapping is shown in Fig. 3.2.

¹Put informally, a fibre bundle is a structure that looks locally like a product space but is not necessarily a product space globally. In this context, S^3 can be constructed by assigning a unit circle S^1 to each point on S^2 , so that S^3 locally looks like $S^2 \times S^1$, though this is not the case globally. A discussion of fibre bundles can be found in, for example, Ref. [65], and a discussion on the Hopf bundle specifically can be found in Ref. [66].

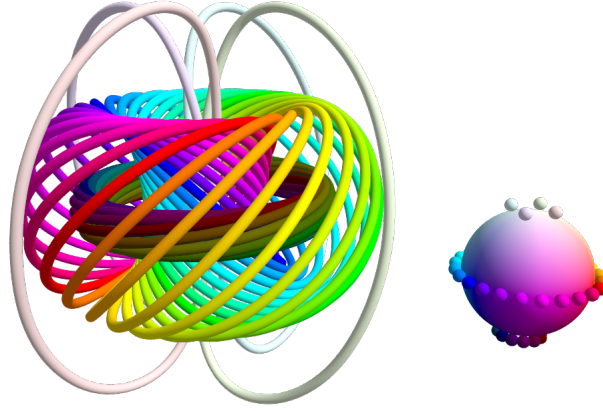


Figure 3.2.: Various preimages of the Hopf map generated by projecting the fibres S^1 of the inverse Hopf map $S^2 \rightarrow S^3$ into \mathbb{R}^3 . The fibres corresponding to a selection of points on the unit sphere are shown (matched by their colour).

The topology of a magnetic hopfion with unit topological charge can be considered as a magnetic skyrmion tube where the skyrmion helicity is rotated through 2π along the length of the tube, and the ends are joined together. If the helicity is instead rotated $n \in \mathbb{Z}$ times, the Hopf index of the texture is n . We note, however, that the boundary condition that $\mathbf{m}(\mathbf{r})$ tends to a constant value as $|\mathbf{r}| \rightarrow \infty$ must be satisfied, and thus, an alternative way to consider hopfions in bulk is to consider an in-plane skyrmion tube (where the helicity is not rotated). This satisfies both the linking of preimages and $\mathbf{m}(\mathbf{r})$ tending to a constant value in all directions away from the localised hopfion, as illustrated with selected preimages in Fig 3.1. For the case of two interlinked hopfion textures, as in Fig. 3.3(c), of index H_1 and H_2 respectively, the total Hopf index is $H = H_1 + H_2 + 2$, where the extra 2 accounts for the linking of the preimages in the respective hopfion textures with each other [68]. More complicated structures are also possible, and a cinquefoil knot with $H = 8$ is also shown in Fig. 3.3(d). In practice, structures with higher Hopf indices tend to cost more energy and be less stable [69–71].

In 1947, Whitehead [72] showed that the Hopf index can be expressed as the integral

$$H = -\frac{1}{(8\pi)^2} \int_{\mathbb{R}^3} d^3r \mathbf{F}(\mathbf{r}) \cdot \mathbf{A}(\mathbf{r}), \quad (3.3)$$

where $F_i(\mathbf{r}) = \varepsilon_{ijk} \mathbf{m} \cdot (\partial_j \mathbf{m} \times \partial_k \mathbf{m})$ is the emergent magnetic field and $\mathbf{A}(\mathbf{r})$ is the corresponding vector potential defined through $\mathbf{F} = \nabla \times \mathbf{A}$. Though this is a deep theorem and the fact that (3.3) represents the linking number of preimages is not immediately obvious, it provides a convenient way to determine whether or not a given magnetic texture is a hopfion without the need to plot and examine the preimages. We remark that it has the same mathematical and physical interpretation of magnetic

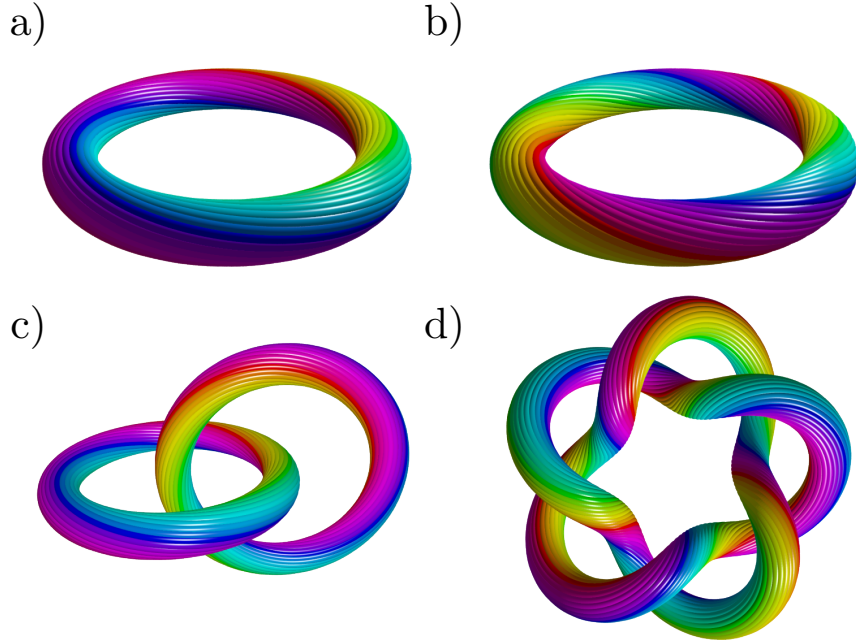


Figure 3.3.: Preimages of hopfion textures with various Hopf indices, with (a) a single twist ($H = 1$), (b) a double twist ($H = 2$), (c) interlinked $H = 1$ tubes which have $H = 4$ taken overall, and (d) a cinquefoil knot with $H = 8$.

helicity [73] for magnetic fields and hydrodynamical helicity [74] for fluid velocity fields, which measures the twist, linkage, and writhe of the fields². To evaluate (3.3), \mathbf{A} can be calculated through integrals such as $A_x(\mathbf{r}) = -\int_{-\infty}^y dy' F_z(\mathbf{r})$, which can be discretised to evaluate them numerically³. Python code to numerically integrate (3.3) to calculate the Hopf index is provided in Appendix A.

3.2. Stabilisation of Magnetic Hopfions

Hopfions in bulk ferromagnetic systems have received a surge of interest starting in the late 2010s and going into the 2020s, though the attention they receive still lags significantly behind that of magnetic skyrmions at the time of writing this Thesis. Field-theoretical consideration of the stabilisation of hopfions, however, has been a subject of study since the 1970s. Hopfions have also been studied in non-magnetic systems such as liquid crystals [75–77], colloidal dispersions [78], and ferroelectric nanoparticles [79]. Work by Faddeev in the 1970s considered an extension to Skyrme’s original theory, including spatial derivatives of various orders such that localised structures can be stabilised as per Derrick and Hobart’s scaling argument discussed in the previous Chapter [80, 81]. This is now known as the Skyrme-Faddeev model [82], in which the lower bound of the hopfion’s energy scales as $|H|^{3/4}$ [83, 84].

Finding magnetic systems in which magnetic hopfions can be stabilised is still an area of

²Helicity in this context is not to be confused with skyrmion helicity, which is the in-plane angle of a skyrmion texture’s spins with respect to the radial direction.

³Alternatively to calculating $\mathbf{A}(\mathbf{r})$ explicitly, (3.3) can be calculated in momentum space, as in Ref. [60].

active research. The stabilisation of hopfions in ferromagnetic systems was first studied theoretically by Bogolubsky [85] in the 1980s, in which an isotropic energy functional was considered. Such an energy functional might be realised in a bulk frustrated magnets with competing exchange interactions under an applied magnetic field, which will be discussed in more detail generally in Chapter 4, as well as Chapters 5 and 11 for the case of skyrmions in thin films. The energetics of magnetisation textures in such systems with Hopf indices of 1, as well as higher Hopf indices, has been studied by Sutcliffe [71]. It has also recently been derived from considerations of the underlying lattice, with a generalisation to the anisotropic case made, by Rybakov et al. [84]⁴. The energy barriers for the collapse of hopfions in this model to the ferromagnetic and toron states have recently been studied by Sallermann, Jónsson and Blügel [63] using the geodesic nudged elastic band [86] and dimer [87] methods, which are algorithms to numerically find saddle points in the energy landscape (and thus paths of minimum energy between two states) of a system.

A further method by which it has been proposed to stabilise magnetic hopfions is in chiral magnetic nanocylinders capped at both ends with thin films that have perpendicular magnetic anisotropy. This was suggested in three independent studies published in 2018 within a few months of each other [60, 88, 89]. Unlike the other methods, however, the boundaries play a pivotal role in the stabilisation of the hopfion. The dynamic stabilisation of hopfions has also been considered, which will be discussed in more detail in Chapter 8.

3.3. Experimental Progress with Magnetic Hopfions

Due to the difficulty in imaging bulk textures, experimental work on magnetic hopfions is significantly behind theoretical work, though progress is being made. A method for the reconstruction of preimages from X-ray nanotomography data was proposed by Donnelly et al. [90]. In their 2021 work, they determined the vortex rings they imaged to have a Hopf index of zero [91]. In the same year, the observation of hopfions in Ir/Co/Pt was reported by Kent et al. [92], though the lack of the reconstruction of the full three-dimensional vector field prevented the claim of hopfions from being made without ambiguity. Furthermore, the observation of ‘hopfion rings’: coupled states of hopfions and skyrmion strings, has been recently reported, with a protocol proposed to nucleate them [93].

Some theoretical works have suggested methods by which magnetic hopfions could be detected. The emergent magnetic field of a hopfion leads to a local topological Hall signature, which vanishes on a global level due to the vanishing spatially averaged emergent magnetic field. It has been proposed by Göbel et al. [94] to use the local topological Hall signature to detect magnetic hopfions. It was later shown by Pershoguba, Andreoli and Zang [95] that, despite the vanishing emergent magnetic field, there is a nonzero topological Hall signal. Further theoretical studies have modelled the propagation of spin waves through hopfion textures [96, 97], potentially providing a further method with which to detect them. The resonance modes of hopfions have also been investigated numerically [98–101], potentially providing a way to detect them using radio frequency

⁴Although Ref. [84] was published in 2022, it first appeared as a preprint on arXiv in 2019, and as such, various research works using its results appeared before its 2022 publication.

magnetic fields.

3.4. Applications of Magnetic Hopfions

While the field of skyrmionics is well-developed, with many envisaged applications of magnetic skyrmions as discussed in Section 2.3, the field of ‘hopfionics’ is far newer, and much of the research effort is thus focused on their more fundamental aspects than potential applications. Nonetheless, as with magnetic domains and skyrmions, hopfions have potential applications in data information and processing. Their current-driven motion has been investigated in recent years. Unlike magnetic skyrmions, which suffer from the so-called skyrmion Hall effect, in which a spin-polarised current induces current-driven motion with components both parallel and perpendicular to the direction of the applied current (an effect which is generally seen as undesirable), hopfions do not show such an effect [67, 102]. Because of this, it has been suggested, as with magnetic domains and skyrmions, to use magnetic hopfions in racetrack memory devices [94]. The excitation spectra of magnetic hopfions discussed in the previous Section could have applications in neuromorphic computing. Specifically, it has been proposed by Zhang et al. [96] to use magnon scattering by magnetic hopfions in neuromorphic devices, with the high nonlinearity of the hopfion magnetisation textures making them ideal candidates for reservoirs in reservoir computing.

Chapter

4

Statics and Dynamics of Magnets

Our understanding of ferromagnets has increased drastically over the past century. Around the turn of the 20th century, Weiss attempted to explain the spontaneous magnetisation of ferromagnetic materials through the existence of a very high ‘molecular field’ experienced by the magnetic moments within the material [103]. This theory was incomplete, however, as the ‘molecular field’ relied on the spins being aligned in the first place, creating a causality dilemma. The underlying physics was later unveiled by Heisenberg, who was able to explain the spontaneous alignment [104], which is discussed in the following Section.

The field of micromagnetics originated in the early 20th century. In the 1930s, Bloch calculated the shape and energy of domain walls considering the exchange interaction and uniaxial anisotropy [105]. Such techniques were expanded upon in the work of Landau and Lifshitz when they derived the equation of motion of the magnetic moments using the variational principle [106], the so-called Landau-Lifshitz equation, discussed in Section 4.2. In the late 1950s, instead of starting with domain walls and deriving their properties, Brown generalised the equation derived by Landau and Lifshitz to a general vector field, suggesting that magnetic domains form naturally upon time integration of the equation, without the prior assumption of their existence [107–109]. He also suggested that the Landau-Lifshitz equation could be numerically integrated using computers, though computational power was too limited at the time for this to be feasible. In the meantime, however, computational power has increased significantly, making the numerical modelling of ferromagnetic systems much more feasible, with simulations modelling systems with sizes on the order of microns being feasible on personal computers. The advent of the acceleration of calculations using graphics processing units (GPUs) [110, 111] has further aided numerical micromagnetic modelling. GPU acceleration allows the parallelisation of the time integration of the equations of motion of magnetisation vector fields, further making such numerical modelling techniques more attractive.

4.1. Magnetostatics

The micromagnetic model is referred to as a semiclassical model as, although the spins underlying the magnetisation are fundamentally quantum mechanical, the magnetisation

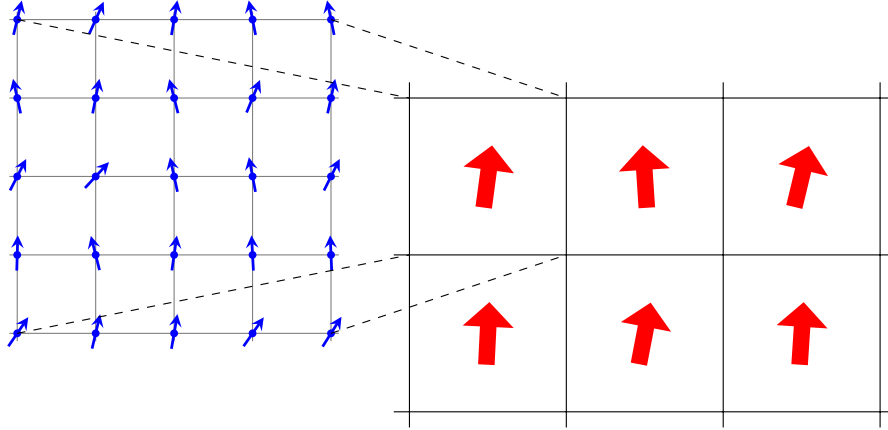


Figure 4.1.: Illustration of how microscopic spins on the underlying lattice are averaged out in micromagnetic modelling.

is modelled using a classical field theory. Its scale sits somewhere between a microscopic theory and a macroscopic theory. While individual spins are not resolved (as in, for example, atomistic simulations), domain structures are accounted for (in contrast to, for example, the macroscopic Maxwell equations where the domain structures are averaged out). The microscopic arrangement of the magnetically active ions is ignored, and the system is described by a continuous vector field $\mathbf{M}(\mathbf{r}, t) = M_s \mathbf{m}(\mathbf{r}, t)$, where $|\mathbf{m}| = 1$ and M_s is the spontaneous magnetisation. For temperatures θ far below the Curie temperature θ_c above which a material ceases to be ferromagnetic, the temperature dependence of the spontaneous magnetisation is approximately given by Bloch's law [112], $M_s(\theta) = M_s(0)[1 - (\theta/\theta_c)^{3/2}]$. In the zero-temperature regime, which is the case in most of the investigations of this Thesis, the spontaneous magnetisation is equal to the saturation magnetisation, which is the maximum magnetisation that can be achieved when increasing an externally applied magnetic field. The principle of averaging out the underlying spins to obtain the semiclassical magnetisation vector field discretised over a lattice, is illustrated in Fig. 4.1. Furthermore, it is assumed that the temperature is uniform such that M_s is uniform throughout the system, and well below the Curie temperature of the material.

With $\mathbf{m}(\mathbf{r})$ as an order parameter, an effective energy functional for the system can be written as a series expansion in the components m_i of \mathbf{m} , and its spatial derivatives ∂_α as [113–115]

$$U[\mathbf{m}(\mathbf{r})] = \int d^3r \left[-B_i m_i - K_{ij} m_i m_j - K_{ijkl} m_i m_j m_k m_l - D_{ij}^\alpha m_i \partial_\alpha m_j \right. \\ \left. + A_{ij}^{\alpha\beta} \partial_\alpha m_i \partial_\beta m_j + A_{ijkl}^{\alpha\beta} m_i m_j \partial_\alpha m_k \partial_\beta m_l + A_{ij}^{\alpha\beta\gamma\delta} \partial_\alpha \partial_\beta m_i \partial_\gamma \partial_\delta m_j - \dots \right]. \quad (4.1)$$

Typically, it is sufficient to consider only a few leading-order terms, as higher-order terms become negligible on larger length scales. The terms which are included in a given model depend on the properties of the specific system under study, such as the symmetries of the underlying lattice. For example, if the lattice is inversion-symmetric, all $D_{ij}^\alpha = 0$. The magnitudes of the tensor components are determined by the microscopic interactions and can be determined from experimental data or microscopic theories such as density

functional theory.

An alternative view of (4.1) is as the continuum limit of an atomistic model, in which interactions between spins on the underlying lattice are considered. Specifically, the term in (4.1) labelled by B is the Zeeman term, those with A are symmetric exchange terms, those with K are anisotropy terms, and that with D is the Dzyaloshinskii-Moriya interaction term. In the following, we explore the various terms seen in frequently studied magnetic systems.

Symmetric Exchange Interaction

The symmetric exchange interaction is a quantum mechanical effect resulting from the fact a state in which electron spins are aligned (spin triplet) has a different energy to one in which the spins are antialigned (spin singlet). It can be modelled using the Heisenberg model, the derivation of which is discussed in many textbooks on quantum mechanics and/or magnetism, such as Ref. [116] for an overview, or Ref. [117] for a more in-depth discussion. In this model, the interaction energy between two spins \mathbf{S}_i and \mathbf{S}_j at lattice sites i and j respectively is given by $J_{ij}\mathbf{S}_i \cdot \mathbf{S}_j$, where J_{ij} is known as the exchange constant¹. The Heisenberg model is written as

$$\hat{\mathcal{H}}_{\text{ex}} = - \sum_{i>j} J_{ij} \mathbf{S}_i \cdot \mathbf{S}_j, \quad (4.2)$$

where the sum is taken pairwise over all lattice site i, j , and $i > j$ prevents double-counting. If it is assumed that the lattice is isotropic such that J_{ij} remains constant for equivalent lattice sites throughout the structure, the continuum limit of this equation becomes, to quartic order in the spatial derivatives [118, 119],

$$U_{\text{ex}}[\mathbf{m}(\mathbf{r})] = \int d^3r \left[-\frac{I_1}{2} (\nabla \mathbf{m})^2 + \frac{I_2}{2} (\nabla^2 \mathbf{m})^2 \right]. \quad (4.3)$$

Here, $(\nabla \mathbf{m})^2 = (\partial_i m_j)(\partial_i m_j)$ and $(\nabla^2 \mathbf{m})^2 = (\partial_\alpha \partial_\alpha m_i)(\partial_\beta \partial_\beta m_i)$, with Einstein summation convention applied. A derivation of (4.3) is given in Appendix B. In many skyrmion-hosting systems, the higher-order term is not relevant due to a lack of frustration, as discussed in Section 5.4. In this case, the symmetric exchange energy functional takes the more conventional form

$$U_{\text{ex}}[\mathbf{m}(\mathbf{r})] = A \int d^3r (\nabla \mathbf{m})^2, \quad (4.4)$$

where $A = -I_1/2$.

In this Thesis, we will use the former notation with I_1 and I_2 when we deal with frustrated magnets with competing exchange interactions, and the latter with A when we deal with chiral magnets for which only the quadratic-order exchange term is relevant, in order to be as close to literature conventions as possible. The conditions for the higher-order exchange term to be relevant to the energetics of the system are discussed in Section 5.4. In (4.4), the theory is only well-defined if $A > 0$, which is the case for all studies in this Thesis where only the lowest-order exchange term is used. The exchange energy term

¹Heisenberg's original convention was to write this with an extra factor of 2, but in line with more modern literature, we do not do this.

then penalises gradients in the magnetisation vector field. In studies where we use the form (4.3), we take $I_1 > 0$ and $I_2 > 0$, such that the quadratic term favours gradients in $\mathbf{m}(\mathbf{r})$ and the quartic term favours $\mathbf{m}(\mathbf{r})$ being smooth.

The exact conversion between the atomistic exchange coupling constants J_{ij} and the micromagnetic exchange stiffness constant depends on the specific lattice structure under consideration (a triangular lattice in Appendix B). For a simple cubic lattice where only nearest-neighbour coupling with constant J is considered, $A = JS^2n/a$, where S is the spin magnitude, n is the number of atoms per unit cell, and a is the lattice constant.

Dzyaloshinskii-Moriya Interaction

The antisymmetric exchange interaction, more frequently referred to as the Dzyaloshinskii-Moriya interaction (DMI), arises in systems where the underlying lattice has noncentrosymmetric symmetry, such that it breaks inversion symmetry $\mathbf{r} \rightarrow -\mathbf{r}$ with respect to the midpoint between the two interacting spins. The effect was introduced by Dzyaloshinskii, who analysed it in terms of the symmetry of the crystal structure [120], and a microscopic explanation was offered by Moriya [121]. The coupling is given in this case by $\mathbf{D}_{ij} \cdot (\mathbf{S}_i \times \mathbf{S}_j)$, and the Heisenberg exchange Hamiltonian is

$$\hat{\mathcal{H}}_{\text{DMI}} = \sum_{i>j} \mathbf{D}_{ij} \cdot (\mathbf{S}_i \times \mathbf{S}_j), \quad (4.5)$$

which favours spins being perpendicular to each other in a plane perpendicular to \mathbf{D}_{ij} , the Dzyaloshinskii-Moriya (DM) vector. For spins at positions \mathbf{r}_i and \mathbf{r}_j coupled to a neighbour at site \mathbf{r}_n , the DM vector \mathbf{D}_{ij} is proportional to $(\mathbf{r}_i - \mathbf{r}_n) \times (\mathbf{r}_j - \mathbf{r}_n)$, illustrated in Fig. 4.2. The combined symmetric exchange and DMI terms can be written as

$$\hat{\mathcal{H}}_{\text{ex and DMI}} = - \sum_{i>j} \mathbf{S}_i \mathcal{J}_{ij} \mathbf{S}_j, \quad \mathcal{J}_{ij} = \begin{bmatrix} J_{ij} & D_{ij}^z & -D_{ij}^y \\ -D_{ij}^z & J_{ij} & D_{ij}^x \\ D_{ij}^y & -D_{ij}^x & J_{ij} \end{bmatrix}. \quad (4.6)$$

The antisymmetry of the off-diagonal terms makes clear the alternative name for this interaction: the antisymmetric exchange interaction. At a microscopic level, these interactions result from the hopping of electrons from the site i to n and then from n to j [117]. As it results from, and scales with, spin-orbit coupling, it is generally weak compared to symmetric exchange.

The continuum approximation of the DMI term in the energy functional can be derived in a manner analogous to that of the symmetric exchange interaction. The most general functional form of the DMI energy contribution is given by

$$U_{\text{DMI}}[\mathbf{m}(\mathbf{r})] = D_{ik}^j \int d^3r m_i \partial_j m_k, \quad (4.7)$$

where D_{ik}^j is a tensor of rank three that is determined by the symmetry of the crystal lattice [115, 122, 123]. Usually, in bulk, most of the components of D_{ik}^j vanish, leaving just a few terms in the energy functional. The case where surface terms are relevant is discussed in Ref. [124]. The bulk terms can be written as a combination of the Lifshitz

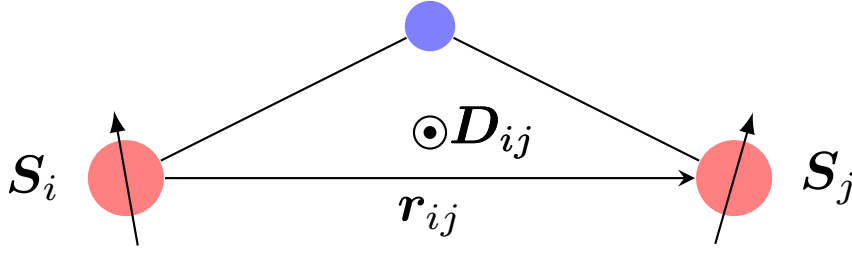


Figure 4.2.: Schematic of the arrangement of adjacent spins resulting in the Dzyaloshinskii-Moriya interaction (DMI). The two spin sites are coupled to a third, nonmagnetic site (such as an oxygen atom), resulting in a breaking of the inversion symmetry of the lattice. This symmetry breaking defines the orientation of the DMI vector \mathbf{D}_{ij} .

invariants

$$\mathcal{L}_{ik}^{(j)} = m_i \partial_j m_k - m_k \partial_j m_i. \quad (4.8)$$

For example, systems that stabilise Bloch-type skyrmions, such as MnSi and Cu_2OSeO_3 , have symmetry class tetrahedral T or octahedral O , for which the DMI energy functional is

$$U_{\text{DMI}}[\mathbf{m}(\mathbf{r})] = D \int d^3r (\mathcal{L}_{zy}^{(x)} + \mathcal{L}_{xz}^{(y)} + \mathcal{L}_{yx}^{(z)}) = D \int d^3r \mathbf{m} \cdot (\nabla \times \mathbf{m}), \quad (4.9)$$

where D is the DMI strength. Systems with n -fold cyclic symmetry and n mirror planes parallel to the rotation axis, C_{nv} , such as at Fe/Ir interfaces [125] and in polar magnets such as GaV_4S_8 [126], have DMI of the form

$$U_{\text{DMI}}[\mathbf{m}(\mathbf{r})] = D \int d^3r (\mathcal{L}_{xz}^{(x)} + \mathcal{L}_{yz}^{(y)}) = D \int d^3r (\mathbf{m} \cdot \nabla m_z - m_z \nabla \cdot \mathbf{m}). \quad (4.10)$$

As magnetic skyrmions stabilised by DMI of the form (4.10) often result from broken inversion symmetry at interfaces (despite the existence of bulk crystal systems with that symmetry class in which skyrmions can be stabilised, as discussed in Section 5.1), DMI of this form is often referred to as ‘interfacial DMI’, while that of the form (4.9) is often called ‘bulk DMI’. Systems with the dihedral symmetry D_{2d} such as the Heusler compound $\text{Mn}_{1.4}\text{Pt}_{1-x}\text{Pd}_x\text{Sn}$ [127] have DMI of the form

$$U_{\text{DMI}}[\mathbf{m}(\mathbf{r})] = D \int d^3r (\mathcal{L}_{yz}^{(x)} + \mathcal{L}_{xz}^{(y)}) = D \int d^3r \mathbf{m} \cdot \left(\frac{\partial \mathbf{m}}{\partial x} \times \hat{\mathbf{x}} - \frac{\partial \mathbf{m}}{\partial y} \times \hat{\mathbf{y}} \right). \quad (4.11)$$

Magnetocrystalline Anisotropy

Due to the lattice structure of the crystal, alignment of the magnetisation along certain directions may be favoured. Microscopically, this results from the interaction of the electrons carrying the magnetic moments with the crystal field via the Coulomb and exchange interactions. Due to spin-orbit coupling, this results in a change in orientation of the magnetic moment [117]. The microscopic details of this can be computed using density functional theory [128, 129], which is beyond the scope of this Thesis.

With uniaxial anisotropy, there is one ‘easy axis’ along which it is energetically favourable for the magnetisation to align. Other types of anisotropy, such as cubic anisotropy, exist,

though we consider only uniaxial anisotropy in this Thesis as this is the form found in the hexagonal and tetragonal crystals that typically host skyrmions. Uniaxial anisotropy can be modelled phenomenologically through the energy functional

$$U_{\text{anis}}[\mathbf{m}(\mathbf{r})] = K \int d^3r [1 - (\mathbf{m} \cdot \hat{\mathbf{u}})^2], \quad (4.12)$$

where $K > 0$ is the uniaxial anisotropy strength and $\hat{\mathbf{u}}$ is the direction of the easy axis. We note that this anisotropy discussed here is not to be confused with shape anisotropy, which results from the demagnetising field, discussed below. The existence of an easy axis plays an important role in the coercivity of the magnet or the external field that must be applied to change the magnetisation of the system. Magnetically hard materials, such as the CoPtCr alloys used in hard disk drives, gain their high coercivities due to high uniaxial anisotropy strengths².

Zeeman Interaction

When an external magnetic field \mathbf{B}_{ext} is applied to a magnetic system, the magnetisation tends to align with it due to Zeeman coupling. The corresponding contribution to the energy functional is (where \mathbf{B}_{ext} is measured in Teslas in SI units and M_s is measured in A m^{-1})

$$U_Z[\mathbf{m}(\mathbf{r})] = -M_s \int d^3r \mathbf{B}_{\text{ext}} \cdot \mathbf{m}. \quad (4.13)$$

Magnetostatic (Dipole-Dipole) Interaction

Gauss's law for magnetism states that magnetic flux density \mathbf{B} is divergenceless, *i.e.* $\nabla \cdot \mathbf{B} = 0$. As the magnetic flux density $\mathbf{B} = \mu_0(\mathbf{H} + \mathbf{M})$, where \mathbf{H} is the magnetic field and \mathbf{M} is the magnetisation, we have that

$$\nabla \cdot \mathbf{H} = -\nabla \cdot \mathbf{M}. \quad (4.14)$$

\mathbf{H} can be split up into externally applied field $\mathbf{H}_{\text{ext}} = \mathbf{B}_{\text{ext}}/\mu_0$ and a demagnetising field $\mathbf{H}_{\text{demag}}$, *i.e.* $\mathbf{H} = \mathbf{H}_{\text{ext}} + \mathbf{H}_{\text{demag}}$, where the demagnetising field allows the condition $\nabla \cdot \mathbf{B}_{\text{ext}} = 0$ to be fulfilled. The demagnetising field can be considered to result from fictitious 'magnetic monopoles' at the edges of the material (coulombian picture) or from a fictitious current flowing at the material's surface (amperian picture). At the microscopic level, the field is the sum of the dipolar fields from the individual dipole moments within the system, and thus this energy term is often referred to as the dipole-dipole interaction. The energy contribution due to this field is

$$U_d[\mathbf{m}(\mathbf{r})] = -\frac{\mu_0}{2} \int d^3r \mathbf{H}_{\text{demag}} \cdot \mathbf{m}, \quad (4.15)$$

where the prefactor of 1/2 accounts for the double-counting of the individual dipoles. In-depth discussions of the form of $\mathbf{H}_{\text{demag}}$ can be found in various literature sources such as Ref. [132]. This is a long-range interaction depending on the size and shape of

²One might expect that the coercivity, or the external field required to demagnetise a material, would be of the order of the anisotropy field. In reality, it is around an order of magnitude less, a phenomenon known as Brown's paradox [130, 131].

the system. It favours the magnetisation being orientated parallel to the boundary of a sample to reduce the energy of the stray field, and plays a key role along with symmetric exchange, in the formation of magnetic domains.

To optimise the calculation of the demagnetising field, various techniques exist beyond a computationally expensive element-wise summation. For example, fast Fourier transforms with the convolution theorem can be used to determine $\mathbf{H}_{\text{demag}}$ [133]. In analytical calculations, simplifying assumptions can often be made to account the demagnetising field term. In this Thesis, we make use of the approximation of the demagnetising field as a correction to the perpendicular magnetic anisotropy energy (PMA) in a thin film, in which the magnetisation is orientated perpendicular to the plane of the film. In this case, the demagnetising energy term can be approximated by subtracting $\mu_0 M_s^2/2$ from the PMA strength, which is exact in the limit of a ferromagnetic thin film of infinite extent [134].

Magnetoelectric Interaction

In a magnetoelectric material, there is coupling between the electric field and the magnetisation, and between the magnetic field and the electric polarisation, known as the magnetoelectric effect. The magnetoelectric effect was predicted theoretically by Dzyaloshinskii [135] and soon afterwards experimentally observed by Astrov [136] in Cr_2O_3 . This can result in the material possessing ferromagnetic order (including antiferromagnetic, ferrimagnetic, and helimagnetic orders) and ferroelectric order simultaneously. Materials with multiple ferroic order parameters, especially those with simultaneous ferromagnetic and ferroelectric order, are known as multiferroics.

Various microscopic mechanisms involving spin ordering can lead to ferroelectricity, which is discussed in the reviews Refs. [137, 138]. In this Thesis, we only consider the so-called inverse Dzyaloshinskii-Moriya interaction. A microscopic explanation for this was given by Katsura, Nagaosa and Balatsky [139], whereby a spontaneous spin current flows between two atomic sites with mutually canted spins coupled via the exchange interaction. The polarisation is given by

$$\mathbf{P} = \eta \mathbf{e}_{ij} \times (\mathbf{S}_i \times \mathbf{S}_j), \quad (4.16)$$

where \mathbf{e}_{ij} is the unit vector connecting the spins and η is a coupling constant determined by the spin-orbit and superexchange interactions. While the DMI results in canted spins due to noncentrosymmetric bonds, in this effect, canted spins (resulting from, for example, competing exchange interactions) can result in inversion symmetry breaking to induce an electric polarisation, hence the name ‘inverse DMI’ [140]. In the continuum limit, the induced polarisation has the form [141–143]

$$\mathbf{P} = P_E a [(\nabla \cdot \mathbf{m})\mathbf{m} - (\mathbf{m} \cdot \nabla)\mathbf{m}], \quad (4.17)$$

where a is the lattice constant and P_E is the polarisation density. The resulting micromagnetic energy is given by

$$U = - \int d^3r \mathbf{P} \cdot \mathbf{E}_{\text{ext}}, \quad (4.18)$$

where \mathbf{E}_{ext} is the externally applied electric field. We note that the $\mathbf{P} \cdot \mathbf{E}_{\text{ext}}$ term is of

the form of an effective DMI which is experimentally tunable through the manipulation of an external electric field, such that $\mathbf{E}_{\text{ext}} \cdot \mathbf{P} = D_{ik}^j(E)m_i\partial_j m_k$, with nonvanishing tensor elements $D_{ij}^k = -D_{ji}^k = E_i\delta_{jk}$.

4.2. Landau-Lifshitz-Gilbert Equation

In the previous Section we have discussed magnetisation in the static regime. In this Section we address its dynamical behaviour. The equation of motion of the magnetisation vectors used in this Thesis is the Landau-Lifshitz-Gilbert (LLG) equation, which includes a phenomenological damping constant α introduced by Gilbert in his 1956 doctoral thesis [144, 145]. The equation reads³

$$\frac{\partial \mathbf{m}}{\partial t} = -\gamma \mathbf{m} \times \mathbf{B}_{\text{eff}} + \alpha \mathbf{m} \times \frac{\partial \mathbf{m}}{\partial t}, \quad (4.19)$$

where γ is the electron gyromagnetic ratio $\gamma = ge/2m_e$, where $g \approx 2$ is the Landé factor and e and m_e are the electron charge and mass respectively. \mathbf{B}_{eff} is the effective field (in Teslas), given by⁴,

$$\mathbf{B}_{\text{eff}} = -\frac{1}{M_s} \frac{\delta U[\mathbf{m}(\mathbf{r})]}{\delta \mathbf{m}(\mathbf{r})}, \quad (4.20)$$

where $U[\mathbf{m}(\mathbf{r})]$ is the energy functional describing the system which takes various forms in this Thesis, depending on the system being modelled. The first term on the right-hand side of (4.19) corresponds to a precession about the axis of the effective field, while the second term corresponds to the damping term, which accounts for energy dissipation through, for example, eddy currents and phonon excitations. These two terms, along with the overall evolution of the magnetisation, are illustrated in Fig. 4.3. The Gilbert damping factor α is of the order of magnitude 10^{-4} to 10^{-1} [146–148]. The Landau-Lifshitz equation, *i.e.* (4.19) with α set to zero, can be derived from the variational principle, which is performed in, for example, Refs. [149, 150]. For the case of finite damping, a Rayleigh dissipation functional can be used to derive (4.19) including the Gilbert damping term [144, 145]. This equation is valid when the magnetisation can be considered as a continuous vector field of constant amplitude, *i.e.* far below the material's Curie temperature θ_c and where typical length scales are sufficiently bigger than the lattice constant.

Some of the work in this Thesis requires the modelling of the magnetisation texture under the application of electrical currents. Due to Hund's rule coupling between the conduction electrons and local moments, the conduction electrons tend to align their spin with the localised magnetic moments. The timescale of the magnetisation dynamics is much lower than that of conduction electrons⁵, with the timescales of the changes in the conduction electrons' spin orientations being sufficiently fast compared to the

³For the numerical implementation of the LLG equation, it is typically written in a form where the time derivative $\partial_t \mathbf{m}$ is only on the left-hand side. This can be achieved by substituting the right-hand side of the equation into the $\alpha \mathbf{m} \times \partial_t \mathbf{m}$ term and applying vector identities.

⁴Often \mathbf{H}_{eff} is used, measured in A m^{-1} , in which case the prefactor to the first term on the right-hand side $\gamma_0 = \mu_0 \gamma$ is used instead.

⁵Taking our study in Section 5.3 for example, the characteristic timescale for the magnetisation dynamics from Table 5.1 is $\sim 10^{-11} \text{ ms}^{-1}$, while electrons typically spend 10^{-16} s to 10^{-15} s at each spin site [151].

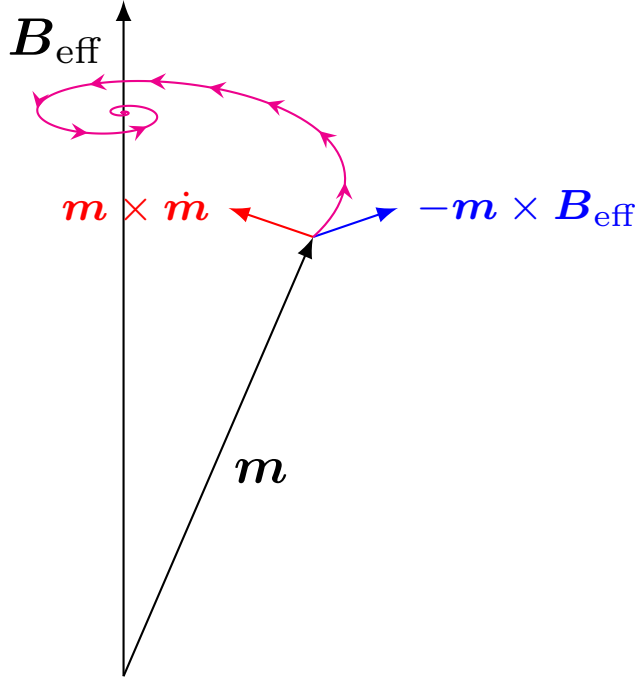


Figure 4.3.: Schematic of the Landau-Lifshitz-Gilbert equation (4.19), with the precession term shown in blue, the damping term shown in red, and the overall motion shown in magenta.

speed of the electrons that the electrons' spins following the magnetisation texture quasiadiabatically [151–153]. This is illustrated in Fig. 4.4. We note in passing that the torques experienced by the conduction electrons can be interpreted as having been produced by ‘emergent’ magnetic and electric fields that are created by the magnetisation texture [150, 154, 155]. As electrons experience a torque during their alignment to a magnetic moment, the magnetisation experiences an opposite torque, resulting in a net change in the magnetisation resulting from the spin current, known as spin-transfer torque (STT). In 2004, Zhang and Li showed how (4.19) could be modified to account for this effect [156], with the resulting equation reading

$$\frac{\partial \mathbf{m}}{\partial t} = -\gamma \mathbf{m} \times \mathbf{B}_{\text{eff}} + \alpha \mathbf{m} \times \frac{\partial \mathbf{m}}{\partial t} - \mathbf{m} \times (\mathbf{m} \times [b\mathbf{j} \cdot \nabla] \mathbf{m}) - \beta \mathbf{m} \times [b\mathbf{j} \cdot \nabla] \mathbf{m}, \quad (4.21)$$

where β is the degree of non-adiabaticity parametrising how imperfectly the electron's spin adiabatically follows the magnetisation and b is a quantity which we define by

$$b = \frac{P\mu_B}{eM_s(1 + \beta^2)}. \quad (4.22)$$

Here, P is the polarisation of the spin-polarised current and μ_B is the Bohr magneton. We note that the Zhang-Li STT only acts where there is a spatial variation of the magnetisation, such that the gradient is nonzero. Before the work by Zhang and Li, the effect of spin-transfer torque was considered with the spin-polarised current being polarised by a layer of fixed magnetisation, with the spin polarisation being constant [157]. This was only applicable to systems with uniform magnetisation in the direction of the current, for example, when a current flows into a thin film along its

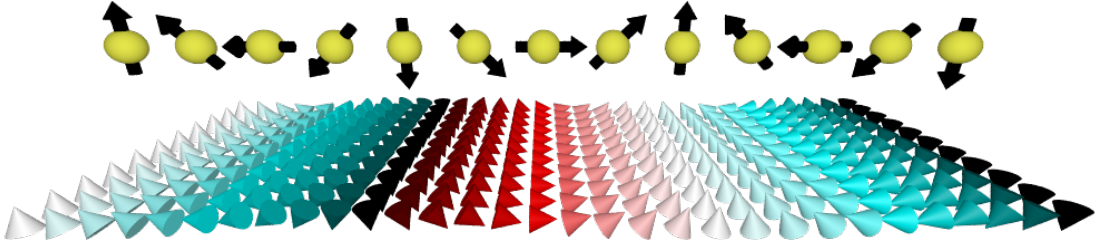


Figure 4.4.: Illustration of electron spins aligning with the magnetisation texture adiabatically. The magnetic moments experience a torque opposite to that experienced by the electrons (spin-transfer torque).

normal. This is commonly referred to as the Slonczewski spin-transfer torque. The form of the torque used here better describes, for example, a current applied in the plane of a thin film. Furthermore, for systems where a ferromagnetic material is coupled to a heavy metal, spin-orbit coupling can cause an in-plane current in the heavy metal layer to generate a transverse spin current. This transfers angular momentum to the magnetic moments in the magnetic layer [158]. These so-called spin-orbit torques are, however, beyond the scope of this Thesis.

The LLG equation as given in (4.19) and (4.21) is a zero-temperature model. The problem of thermal fluctuations in ferromagnets was first studied by Brown [159] in 1963, in which he derived a Fokker-Planck equation for the evolution of the probability density of orientations of a statistical ensemble of ferromagnetic nanoparticles. The modification of the LLG equation to account for thermal fluctuations was first investigated by Lyberatos, Berkov and Chantrell [160] in 1993, giving the so-called stochastic LLG, or sLLG, equation. The exact implementation of the stochasticity in solving the sLLG equation can vary. Typically, including in the software used for the simulations in this Thesis, a randomly fluctuating field is added to \mathbf{B}_{eff} of the form [161]

$$\mathbf{B}_{\text{therm}} = \boldsymbol{\eta} \sqrt{\frac{2\alpha k_{\text{B}} \theta}{M_{\text{s}} \gamma V \Delta t}}, \quad (4.23)$$

where $\boldsymbol{\eta}$ is a random vector drawn from a standard normal distribution at every integration time step, k_{B} is the Boltzmann constant, θ is the temperature, V is the volume of a discretisation cell, and Δt is the time step. This model of thermal fluctuations is valid for the temperature being uniform across the system, as the material parameters, most notably the spontaneous magnetisation M_{s} , vary with temperature. Furthermore, the temperature should be much lower than the Curie temperature, as for higher temperatures, fluctuations in the magnitude of the magnetisation become important [162–164]. A model accounting for such fluctuations is given by the Landau-Lifshitz-Bloch equation, derived by Garanin [165] in 1997, which provides an interpolation between the low-temperature behaviour described by the sLLG equation and that

4.3. Collective Coordinate Modelling of Magnetic Textures

close to the Curie temperature described by Ginzburg-Landau theory. This is, however, beyond the requirements of the investigations in this Thesis.

For the LLG equation to be numerically integrated over a system, it must be discretised. Typically, one of two schemes is chosen for this: the finite-difference method (FDM) and the finite-element method (FEM) [166]. In the former, the system is divided into a regular grid, typically using cuboidal cells, with each cell corresponding to a magnetisation vector. The derivatives can be discretised directly in this case. In the latter, the system is divided into a tetrahedral mesh and the integration is performed by the transformation of the problem into a variational problem. This method is better suited to the modelling of systems with curved geometries such as nanospheres, though in this Thesis, our investigations are restricted to cuboidal geometries. In this Thesis, all of the micromagnetic simulations are carried out using MuMax3 [167], which uses the FDM. The size of the discretisation cells must be chosen such that it is less than the characteristic length scale of the system. For example, for a system in which the only interactions being considered are symmetric exchange with stiffness A and uniaxial anisotropy with strength K , this length would be the magnetocrystalline exchange length⁶ given by $\sqrt{A/K}$. For finite-difference computations, micromagnetic solvers typically use explicit Runge-Kutte methods [111, 167]. Many solvers, such as the Dormand-Prince method [168] used by default in MuMax3, adapt the time step to keep the error per step approximately constant. The numerical implementation of the effective fields is discussed in Appendix C.

4.3. Collective Coordinate Modelling of Magnetic Textures

As the magnetisation vector field has an infinite number of degrees of freedom, numerically integrating the LLG equation in micromagnetic modelling can require a large amount of time and computational resources. When only the behaviour of low-energy excitations, such as a skyrmion's translational motion, is sought, it is possible to reduce the problem to the consideration of the system's soft modes. A typical example of this is a skyrmion driven by spin-transfer torque. If it is assumed that the skyrmion does not deform during the current-driven motion (the 'rigid skyrmion ansatz'), such that $\mathbf{m}(\mathbf{r}, t) = \mathbf{m}[\mathbf{r} - \mathbf{R}(t)]$, where \mathbf{R} is the position vector of the skyrmion's centre, one can reduce the time integration of the dynamics to the numerical integration of the evolution of only two degrees of freedom, the skyrmion's x - and y -positions, enabling the dynamics of interest to be extracted with significantly reduced computational effort. This is used in Chapter 9 to calculate the equation of motion of a skyrmion in the cycloidal background with an applied spin-polarised current. We note that this method also applies to non-skyrmionic magnetic solitons such as domain walls.

The collective coordinate equation of motion is often referred to as the Thiele equation, as this approach was used by Thiele in the prediction of the dynamics of magnetic domains [169]. The Thiele equation of motion for generalised collective coordinates $\boldsymbol{\xi}(t) = \{\xi_1(t), \xi_2(t), \dots\}$, where $\mathbf{m}(\mathbf{r}, t) = \mathbf{m}[\mathbf{r}, \boldsymbol{\xi}(t)]$, can be derived by taking the cross product of the LLG equation (4.19) with \mathbf{m} and writing $\partial_t \mathbf{m} = (\partial_{\xi_j} \mathbf{m}) \dot{\xi}_j$, taking the

⁶For magnetically soft materials where dipole-dipole interactions dominate over magnetocrystalline anisotropy, the relevant length scale is instead the magnetostatic exchange length $\sqrt{2A/\mu_0 M_s^2}$. For chiral magnets with DMI, it is typically the spin spiral wavelength.

dot product with $\partial_{\xi_i} \mathbf{m}$, and integrating over space (making use of the assumption that $|\mathbf{m}|$ is fixed, such that $\partial_t \mathbf{m} \cdot \mathbf{m} = 0$). The result is [170, 171]

$$G_{ij} \dot{\xi}_j + F_i - \alpha \Gamma_{ij} \dot{\xi}_j = 0, \quad (4.24)$$

where F_i is the generalised force, $G_{ij} = -G_{ji}$ is the gyrotropic tensor, and $\Gamma_{ij} = \Gamma_{ji}$ is the dissipative tensor⁷,

$$F_i = \int d^3r \frac{\delta U}{\delta \mathbf{m}} \cdot \frac{\partial \mathbf{m}}{\partial \xi_i} = -\frac{\partial U}{\partial \xi_i}, \quad (4.25a)$$

$$G_{ij} = J \int d^3r \mathbf{m} \cdot \left(\frac{\partial \mathbf{m}}{\partial \xi_i} \times \frac{\partial \mathbf{m}}{\partial \xi_j} \right), \quad (4.25b)$$

$$\Gamma_{ij} = J \int d^3r \frac{\partial \mathbf{m}}{\partial \xi_i} \cdot \frac{\partial \mathbf{m}}{\partial \xi_j}, \quad (4.25c)$$

where $J = M_s/\gamma$ is the angular momentum density. In addition to modelling the current-driven dynamics of skyrmions in the cycloidal state, we use collective coordinate modelling in Chapter 11 to obtain equations of motion of internal dynamics of skyrmions in frustrated magnets.

⁷In some conventions, (4.25c) includes the damping parameter α as a prefactor, but we omit this and write α explicitly at points in this Thesis where the dissipative tensor appears in order to make relationships that include the damping constant more transparent.

Chapter **5**

Stabilisation of Magnetic Skyrmions

The stabilisation of localised topological solitons in a magnetic material occurs through competition between various interactions, which defines a length scale over which the structures, such as skyrmions, can form. Various mechanisms that induce twisting in the magnetisation texture can lead to the formation of skyrmions. In this Thesis, we consider two such mechanisms, namely competition between symmetric exchange and DMI, as well as magnetic frustration. We note, however, that other mechanisms beyond the scope of this Thesis stabilise skyrmions, such as dipole-dipole interactions [172] and four-spin exchange interactions [125].

5.1. Stabilisation of Skyrmions in Chiral Magnets

By far the most well-studied mechanism by which magnetic skyrmions are stabilised at the time of writing this Thesis is through the Dzyaloshinskii-Moriya interaction, favouring the perpendicular alignment of neighbouring spins, which was discussed in Section 4.1. As this interaction exists in materials with the symmetric exchange interaction that favours parallel alignment, the result of the competition between the two interactions is a gradual canting of spins, with the length scale over which the magnetisation changes being determined by the interactions' relative strengths. As the DMI is a chiral interaction, it produces chiral magnetic textures, such as skyrmions and spin spirals. Skyrmions stabilised through this mechanism tend to have sizes on the order of 10 nm to 100 nm [24, 26, 173, 174].

As discussed in Section 4.1, different forms of DMI stabilise different types of skyrmions. While the principle of broken inversion symmetry leading to a canted spin ordering applies generally, the exact mechanism through which the inversion symmetry is broken varies between materials. Magnetic skyrmions were first observed in B20 compounds, which consist of transition metals and group 14 elements with a composition ratio of 1:1. These have the space group $P2_13$. These compounds have the crystallographic class T and hence have DMI of the form (4.9), stabilising Bloch-type skyrmions and helices, discussed below. Another material that stabilises Bloch-type skyrmions is the insulator Cu_2OSeO_3 , due to its space group also being $P2_13$, despite having a different atomic arrangement to the B20 compounds. This material's multiferroicity allows for the manipulation of skyrmion lattices by the application of external electric fields [175–177].

Other noncentrosymmetric skyrmion-hosting materials are those with D_{2d} symmetry, such as the inverse tetragonal Heusler compound $\text{Mn}_{1.4}\text{Pt}_{0.9}\text{Pd}_{0.1}\text{Sn}$ [127]. In such materials, the DMI of the form (4.11) changes sign along perpendicular crystal axes, allowing the stabilisation of antiskyrmions with alternating Bloch-type and Néel-type radial profiles around the structure, as shown in Fig. 2.6. Néel-type skyrmions, on the other hand, can be stabilised by DMI of the form (4.10), where the point group is C_{nv} . Examples of crystals with this point group symmetry are polar magnets such as GaV_4S_8 [126] and GaV_4Se_8 [178], where Jahn-Teller distortion drives a phase transition which causes the lattice to become stretched along one axis, resulting in an electric polarisation. In this case, the space group is R3m. Néel-type skyrmions can also be realised at heterostructure interfaces between heavy metals and magnets such as Fe/Ir [125] and Co/Pt [179] interfaces, where the mismatch of crystal lattices naturally results in inversion symmetry breaking. Due to the scaling of spin-orbit coupling with Z^4 , where Z is the atomic number, the heavy metal with a high Z can have large spin-orbit coupling, resulting in a high DMI. A detailed discussion of the materials hosting magnetic skyrmions can be found in Ref. [123].

Figure 5.1 shows schematic magnetic phase diagrams of temperature θ against applied magnetic field B for materials that host Bloch-type and Néel-type skyrmions. The phase diagrams for various magnetic materials exhibit a similar overall structure [24, 126, 178, 180–182]. For materials that host Bloch-type skyrmions, shown in Fig 5.1(a), the ground state below the Curie temperature θ_c is the helical state, illustrated in Fig 5.2(a). As the field is increased further, the modulations are overcome, and the system becomes conical, then field-polarised. In a small pocket of the phase diagram, just below θ_c , a skyrmion lattice (SkX), illustrated in Fig. 5.2(b), is stabilised due to thermal fluctuations. Analytically, this can be derived by incorporating Gaussian thermal fluctuations about the mean-field solution in the Ginzburg-Landau energy functional [24]. For materials in which Néel-type skyrmions are stabilised, a schematic phase diagram of which is shown in Fig 5.1(b), the cycloidal state occurs for lower fields, rather than the helical state. This is sketched in Fig. 5.1(a).

In this Thesis, we often consider skyrmions in a field-polarised background. The skyrmions are then not ground states of the system, but rather metastable states with an energy barrier preventing their annihilation. It has also been suggested that the topology of magnetic skyrmion textures endows them with resilience to perturbations [183, 184], though the role of topology, as opposed to thermodynamic considerations in their stability, is disputed due to the fact that they emerge fundamentally from a discrete lattice of magnetic moments [185–187].

5.2. Skyrmions in a Cycloidal Background

As discussed in the previous Section, the ground state of chiral magnets for weak or absent applied magnetic fields is not the spin-polarised state, but rather the spin spiral state, *i.e.* the helical or cycloidal state, depending on the form of the DMI present. The helical state was first proposed by Yoshimori [188] in 1959 to explain neutron diffraction data from MnO_2 . This was explained in 1980 by Bak and Jensen [114] in terms of the competition between symmetric exchange and DMI and was first observed in real space in 2006 by Uchida et al. [189].

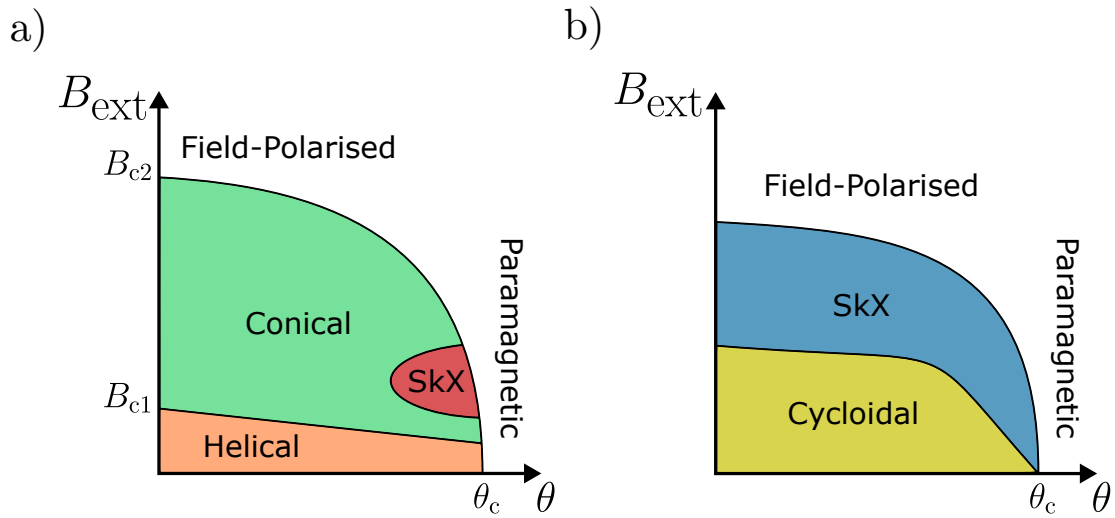


Figure 5.1.: (a) Generic phase diagram for a helimagnet such as MnSi. At a lower critical field (B_{c1} at zero temperature), the system undergoes a phase transition from the helical to the conical state, then to the field-polarised state at an upper critical field (B_{c2} at zero temperature). The skyrmion lattice is the ground state for a small pocket of the phase diagram. (b) Generic phase diagram for a magnet in which a cycloidal ground state is exhibited, such as the polar magnet GaV₄S₈. Note that the exact shapes and sizes of the regions can vary significantly between materials.

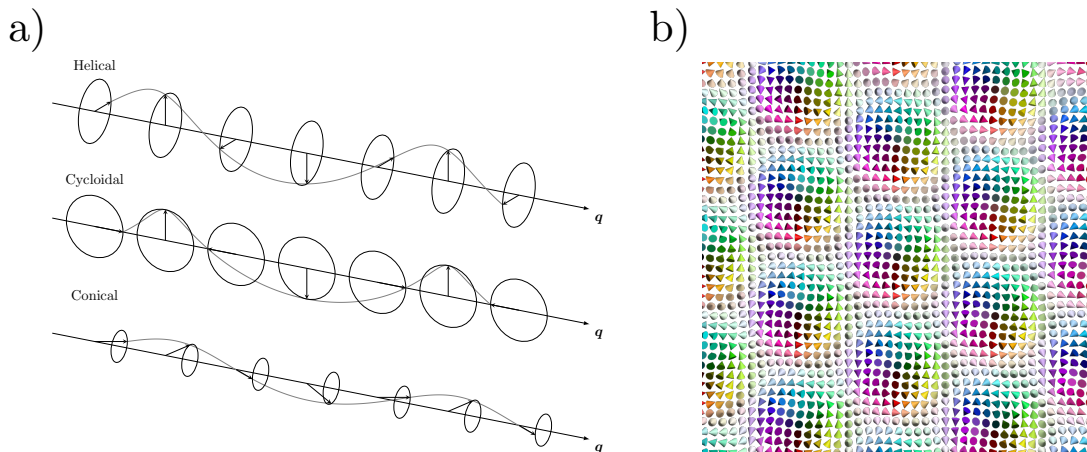


Figure 5.2.: (a) Schematic of helical and cycloidal spin textures. In the helical state, the magnetisation lies in the plane perpendicular to the wavevector q , while for the cycloidal state, the magnetisation is in a plane in which q lies. (b) Schematic of a hexagonal lattice of Bloch-type skyrmions.

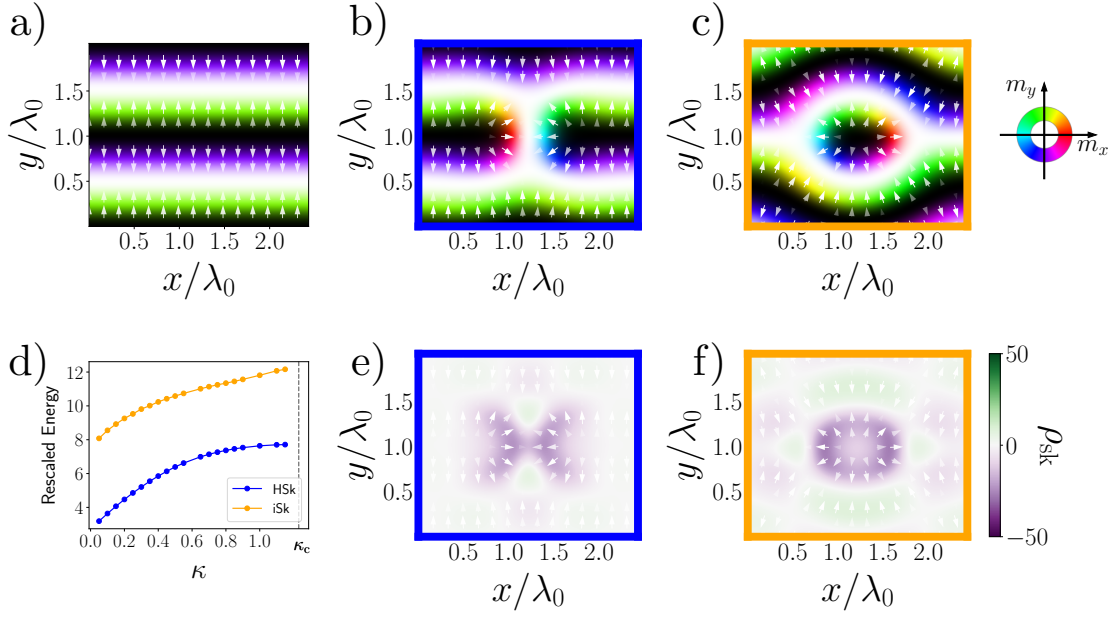


Figure 5.3.: (a)-(c) Various stable magnetic states in cycloidal magnets: the cycloidal ground state, the H-shaped skyrmion (Hsk), and the interstitial skyrmion (iSk) respectively, for $\kappa = 0$. (d) The rescaled energy as a function of κ for the HSk (blue) and iSk (orange). (e)-(f) Spatial distribution of skyrmion number density of the HSk and iSk respectively. Figure taken from our publication Ref. [191].

The first theoretical study of skyrmions in a helical background was carried out by Ezawa [190] in 2011. We can consider two different types of skyrmions: interstitial (iSk) and H-shaped (Hsk) skyrmions. For interstitial skyrmions, a typical circular (usually of the Bloch or Néel type) skyrmion is embedded between the stripes of the spin spiral, with a magnetisation texture as shown in Fig. 5.3(c), and skyrmion number density as shown in Fig. 5.3(f). On the contrary, H-shaped skyrmions can be considered as ‘broken stripes’ in the spin spiral, where the two tips, individually called merons with $N_{\text{sk}} = 0.5$, form a bound pair. The magnetisation and skyrmion number density of these objects are shown in Figs. 5.3(b) and (e) respectively. A helical state without skyrmions is shown in Fig. 5.3(a) for reference.

The stability and current-driven dynamics of skyrmions in the spin spiral state have been studied theoretically and experimentally. Unlike for skyrmions in the ‘typical’ case of the spin-polarised state, the competition between the symmetric exchange interaction and DMI is sufficient for the skyrmions to be metastable, without the need for a strong magnetic field or uniaxial anisotropy perpendicular to the plane of the skyrmion. Furthermore, skyrmions of opposite topological charge can be stabilised in the same system. This is in contrast to skyrmions in a ferromagnetic background, where the form of DMI can only stabilise either a skyrmion or antiskyrmion, but not both. While the motion of skyrmions along the ‘tracks’ of the spin spiral background is a zero mode, the energy required to move a skyrmion between tracks is very high [192]. The behaviour of interactions between skyrmions in a spin spiral background also deviates from that in a ferromagnetic background in that there are strong attractions between the skyrmions

which can lead to clustering [192–195], instead of repulsion between them.

5.3. Stability of the Cycloidal State

In this Section, we consider the static cycloidal state in the absence of skyrmions, which is important for our later investigations into the behaviour of skyrmions in a cycloidal background. We model a thin film in the xy -plane with easy axis $\hat{\mathbf{y}}$ using the energy functional

$$U[\mathbf{m}(\mathbf{r})] = d \int d^2r [A(\nabla\mathbf{m})^2 + D\mathbf{m} \cdot (\hat{\mathbf{y}} \times \partial_x\mathbf{m} - \hat{\mathbf{x}} \times \partial_y\mathbf{m}) - K(\mathbf{m} \cdot \hat{\mathbf{y}})^2], \quad (5.1)$$

where $\mathbf{m}(\mathbf{r})$ is the normalized magnetisation vector at position \mathbf{r} , A is the exchange stiffness, D is the Dzyaloshinskii-Moriya interaction strength, and K is the uniaxial anisotropy strength, which favours (anti)parallel alignment to the y -axis. d is the thickness of the thin film, assumed to be sufficiently thin that the magnetisation texture is approximately uniform along the z -direction. For simplicity, we neglect dipole-dipole interactions, which is a reasonable approximation as the texture has no net magnetisation, so including it would likely only slightly alter the profile.

To reduce the number of parameters in our study, we rescale quantities according to Table 5.1. This gives us the rescaled energy functional with a single effective anisotropy parameter $\kappa = 2AK/D^2$

$$\tilde{U}[\mathbf{m}(\tilde{\mathbf{r}})] = \int d^2\tilde{r} \left[\frac{1}{2} (\partial_{\tilde{x}}\mathbf{m} - \hat{\mathbf{y}} \times \mathbf{m})^2 + \frac{1}{2} (\partial_{\tilde{y}}\mathbf{m} + \hat{\mathbf{x}} \times \mathbf{m})^2 + \frac{1}{2} m_x^2 + \left(\frac{1}{2} - \kappa \right) m_y^2 \right], \quad (5.2)$$

where the first two terms contribute to the chiral spin spiral structure while the others act as effective anisotropy terms. This energy functional has been written in completed square form. For the rest of this Chapter, we drop the tildes.

By requiring that the energy density of a domain wall is negative, as in Ref. [196], a critical anisotropy strength at which the wavelength of the spin spiral diverges, $\kappa_c = \pi^2/8 \approx 1.23$ can be derived. Above this value, a two-domain solution with $\mathbf{m} = \pm\hat{\mathbf{y}}$ is favoured. For $\kappa < \kappa_c$, the ground state of (5.2) is a spin spiral with \mathbf{m} rotating in the yz -plane, given by

$$\mathbf{m}(\mathbf{r}) = \cos[\Theta(\mathbf{r} - \mathbf{r}_0)]\hat{\mathbf{q}} + \sin[\Theta(\mathbf{r} - \mathbf{r}_0)]\hat{\mathbf{z}}, \quad (5.3)$$

where Θ is the angle between \mathbf{m} and $\hat{\mathbf{q}}$. We note that the wavevector \mathbf{q} is parallel to the easy axis $\hat{\mathbf{y}}$. Due to translational invariance in y , we can choose $\mathbf{r}_0 = \mathbf{0}$ without loss of generality. At $\kappa = 0$, the profile is

$$\Theta(\mathbf{r}) \equiv \Theta_c^0(\mathbf{r}) = \hat{\mathbf{q}} \cdot \mathbf{r} = y, \quad (5.4)$$

corresponding to a cycloidal state with dimensionless wavelength $\lambda_0 = 2\pi$. Varying the energy functional (5.2) for the profile (5.3) yields the Euler-Lagrange equation

$$\partial_y^2\Theta = \kappa \sin(2\Theta). \quad (5.5)$$

Characteristic	Definition	SI Unit
Length	$2A/D$	m
Time	$2AM_s/\gamma D^2$	s
Energy	$2Ad$	J
Effective Uniaxial Anisotropy Strength	$2AK/D^2$	Dimensionless

Table 5.1.: Summary of natural units used in our studies of skyrmions in the cycloidal state for the rescaling of various quantities to dimensionless units.

This is a sine-Gordon equation mathematically equivalent to the exact equation of motion of a simple pendulum. Multiplying both sides by $\partial_y \Theta$ and integrating over y allows the profile to be written as

$$\Theta(\mathbf{r}) \equiv \Theta_c(y) = \text{am} \left(\sqrt{2\kappa c} y, \frac{1}{c} \right) + \frac{\pi}{2}, \quad (5.6)$$

where the Jacobi amplitude $\text{am}(u, m)$ is defined through, if $\varphi = \text{am}(u, m)$,

$$u = \int_0^\varphi \frac{dt}{\sqrt{1 - m \sin^2 t}}. \quad (5.7)$$

The solution (5.6) is defined for $0 < \kappa < \kappa_c$, such that the profile (5.4) has been deformed by the presence of the uniaxial anisotropy. The constant c is given explicitly by

$$c = (\partial_y \Theta)^2 / (2\kappa) + \sin^2 \Theta, \quad (5.8)$$

and is bound by $1 < c < 1 + 1/(2\kappa)$ due to the DMI-induced open boundary condition $\partial_y \Theta_c = 1$ [196]¹. c is proportional to the energy of the system, which can be seen by writing (5.2) as

$$\begin{aligned} U &= L_x \kappa \int dy \left[\frac{1}{2\kappa} (\partial_y \Theta)^2 - \cos^2 \Theta + \partial_y \Theta \right] \\ &= L_x \kappa \left[\int dy \left(\frac{1}{2\kappa} (\partial_y \Theta)^2 + \sin^2 \Theta \right) + \Theta_{\text{top}} - \Theta_{\text{bottom}} \right] \\ &= L_x \kappa (L_y c + \Theta_{\text{top}} - \Theta_{\text{bottom}}), \end{aligned} \quad (5.9)$$

where Θ_{top} and Θ_{bottom} are the values of Θ at the top and bottom boundaries of the sample. The fact that the energy is invariant with respect to translations in y in the static case can be seen by projecting the LLG equation (4.19) onto $\mathbf{m} \times \partial_y \mathbf{m}$,

$$(\mathbf{m} \times \partial_y \mathbf{m}) \cdot \left(\mathbf{m} \times \frac{\delta U}{\delta \mathbf{m}} \right) = \partial_y \mathbf{m} \cdot \frac{\delta U}{\delta \mathbf{m}} = \frac{\partial U}{\partial y} = 0, \quad (5.10)$$

implying that c is constant in y .

As the periodicity of $\text{am}(u, m)$ is $4K(m)$, where $K(m)$ is the complete elliptic integral of the first kind

$$K(m) = \int_0^{\pi/2} \frac{dt}{\sqrt{1 - m \sin^2(t)}}, \quad (5.11)$$

¹The condition is that, at the edges, $\partial_y \Theta = D/(2A) = 1$ in our rescaled units.

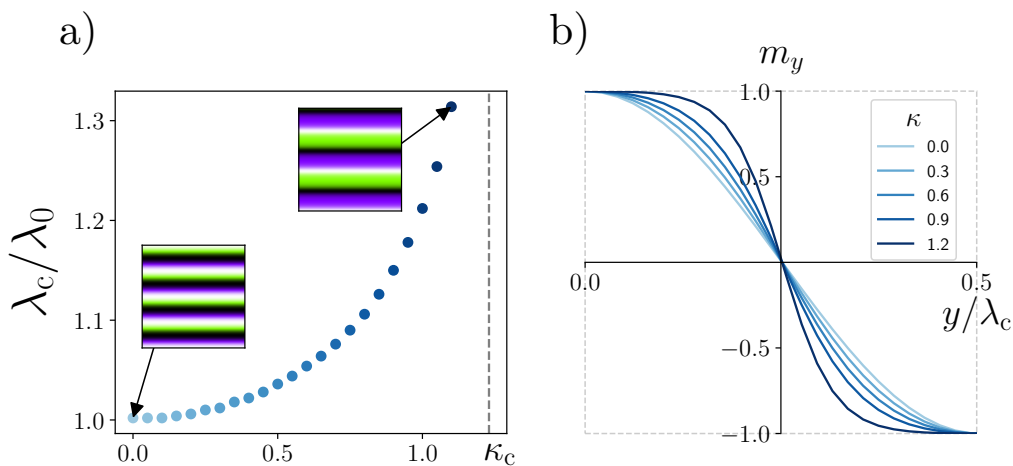


Figure 5.4.: (a) Cycloidal wavelength as a function of the effective anisotropy. The insets show the magnetisation, which diverges to a two-domain state as $\kappa \rightarrow \kappa_c$. (b) Magnetisation y -component as a function of y over a single wavelength for various values of κ . Figure adapted from our publication Ref. [191].

the distorted helix has wavelength $\lambda_c = 4K(1/c)/\sqrt{2\kappa c}$. The nonlinearity of (5.6) represents an obstacle to obtaining an approximate analytical expression for c as a function of κ that minimises the energy density. The interesting limits of the profile are at $\kappa = 0$ and $\kappa = \kappa_c$. Due to (5.8) with the boundary condition $\partial_y \Theta = 1$, in the limit $\kappa \rightarrow 0$, $c \rightarrow \infty$, and $\sqrt{2\kappa c} \rightarrow 1$. Hence, the profile (5.6) recovers the profile (5.4). Additionally, $K(0) = \pi/2$, recovering the wavelength $\lambda_c = 2\pi$. In the limit $\kappa \rightarrow \kappa_c$, c tends to its lower bound of 1, and the cycloidal wavelength diverges as $K(m \rightarrow 1)$ diverges. By plugging $c = 1$ into (5.6), we obtain

$$\Theta = \arctan[\sinh(\sqrt{2\kappa}y)] + \frac{\pi}{2}, \quad (5.12)$$

corresponding to a single domain wall between two regions of opposite in-plane magnetisation along $\pm \hat{y}$.

In addition to these analytical calculations, we determined the dependence of the cycloidal wavelength λ_c on anisotropy strength κ using micromagnetic simulations, the results of which are shown in Fig. 5.4(a). For each value of κ , we varied the y -extent of the system to obtain the value which minimised the total energy, corresponding to the relaxed wavelength. To finely vary the vertical extent of the system, we varied the size Δ_y of the simulation cells along the y -axis. We first initialised the system as a spin spiral state with wavelength $\lambda_0 = 2\pi J/D$ and set $\Delta_y = 5\lambda_0/N_y$, such that five wavelengths fit vertically in the system. We then looped through a range of values of the y -discretisation $\Delta_y = f\lambda_0/N_y$, varying f , and loaded the relaxed spin spiral into the system. For each value of κ , we found the value of f that minimises the energy, allowing us to determine the wavelength.

For $\kappa = 0$, the profile is sinusoidal, while as $\kappa \rightarrow \kappa_c$, the ground state tends towards a ferromagnetic domain with the magnetisation aligned along $\pm \hat{y}$. This distortion to the profile for various values of κ over a single period is shown in Fig. 5.4(b). Unlike

the ferromagnetic state, the structure of the spin spiral state is strongly influenced by the confinement of the system for samples where the number of wavelengths is relatively low, as is the case in this study.

Fig. 5.3(d) shows the energies of both HSKs and iSKs as a function of κ (with the energy of the cycloidal background subtracted), and demonstrates that HSKs have lower energy than iSKs, due to the fact that they distort the cycloidal background less. This agrees with the results from Ref. [192]. For each simulation relaxing the skyrmion, the y -discretisation Δ_y is set such that 5 cycloidal wavelengths fit into the system vertically, where the wavelength is determined using the results of Fig. 5.4(a). Numerical artefacts in the data in Fig. 5.3(d) were omitted, resulting in the gaps.

5.4. Frustrated Magnets

In Section 4.1, we discussed interactions of competing order with an energy functional of the form (4.3). In the above discussion on chiral magnets, only the quadratic term was relevant, meaning that the exchange energy took shorter form (4.4). In this Section, we consider centrosymmetric compounds (such that DMI is absent), in which the higher-order exchange term is relevant, and the competition between symmetric exchange terms of differing orders plays a pivotal role in the stabilisation of skyrmions.

Various theoretical studies have considered the stabilisation of magnetic skyrmions by geometrical frustration, with competition between short-ranged exchange interactions [119, 197, 198]. This is illustrated in Fig 5.5(a): if there is antiferromagnetic coupling between spins on a triangular lattice (or another lattice that induces geometrical frustration such as a kagome lattice), there is no way for the spins to arrange themselves to achieve antiferromagnetic alignment between the neighbours [199]. Another way through which magnetic frustration occurs is via RKKY interaction in itinerant ferromagnets, whereby coupling between spins is mediated through the conduction electrons, resulting in an interaction with a longer range than with geometrical frustration. In this case, next-nearest neighbours can interact with one another and compete with nearest-neighbour exchange interactions, which is illustrated for a square lattice in Fig 5.5(b). Skyrmions stabilised by this interaction have been studied in gadolinium compounds such as Gd_2PdSi_3 [200], $\text{Gd}_3\text{Ru}_3\text{Al}_{12}$ [201], and GdRu_2Si_2 [202].

For isolated skyrmions to be stabilised in a ferromagnetic background for a system that can be described by the energy functional (4.3), an externally applied magnetic field must be applied. The energy functional then becomes that studied in Ref. [119],

$$U[\mathbf{m}(\mathbf{r})] = \int d^3r \left[-\frac{I_1}{2}(\nabla\mathbf{m})^2 + \frac{I_2}{2}(\nabla^2\mathbf{m})^2 - M_s\mathbf{B}_{\text{ext}} \cdot \mathbf{m} \right]. \quad (5.13)$$

To reduce the number of free parameters of the theory, it is convenient to rescale the units to work with dimensionless quantities. We define dimensionless length \tilde{r} in terms of the dimensionful length r through $r = \sqrt{I_2/I_1}\tilde{r}$, dimensionless applied magnetic field $\tilde{\mathbf{B}}_{\text{ext}}$ through $\mathbf{B}_{\text{ext}} = (I_1^2/M_s I_2)\tilde{\mathbf{B}}_{\text{ext}}$, and dimensionless energy \tilde{U} through $U = \sqrt{I_1 I_2}\tilde{U}$. We then obtain the rescaled energy functional

$$\tilde{U}[\mathbf{m}(\tilde{\mathbf{r}})] = \int d^3\tilde{r} \left[-\frac{1}{2}(\tilde{\nabla}\mathbf{m})^2 + \frac{1}{2}(\tilde{\nabla}^2\mathbf{m})^2 - \tilde{\mathbf{B}}_{\text{ext}} \cdot \mathbf{m} \right]. \quad (5.14)$$

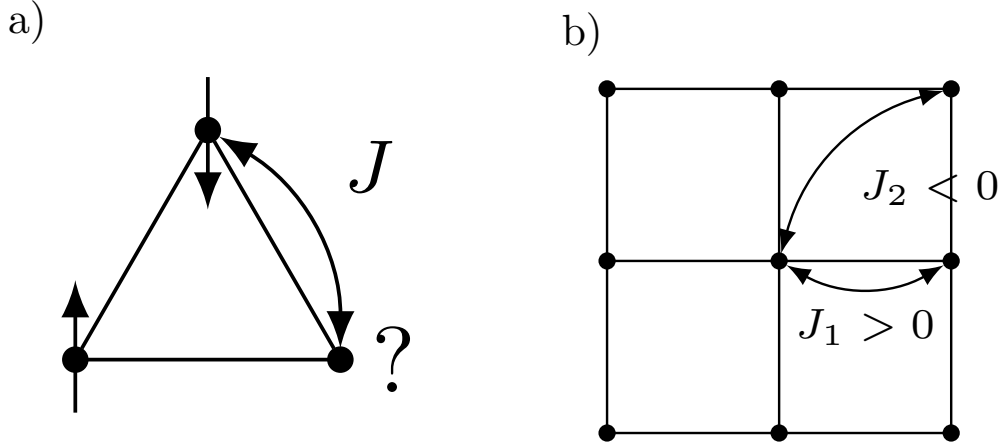


Figure 5.5.: Illustration of competing exchange interactions on a lattice. (a) For two antiferromagnetically aligned spins, it is not possible to satisfy the antiferromagnetic alignment between nearest neighbours. (b) A system with ferromagnetically coupled nearest neighbours and antiferromagnetically coupled next-nearest neighbours has competing exchange interactions.

In our investigations of frustrated magnets, we work exclusively in this rescaled system and drop the tildes for convenience. The ground state of the energy functional (5.14) with the externally applied magnetic field along the z -axis, $\mathbf{B}_{\text{ext}} = B_{\text{ext}}\hat{z}$, is the conical state

$$\mathbf{m}(\mathbf{r}) = \begin{bmatrix} \sqrt{1 - m_0^2} \cos(qz) \\ \sqrt{1 - m_0^2} \sin(qz) \\ m_0 \end{bmatrix}, \quad (5.15)$$

where q is the conical wavenumber, Θ is the cone angle, and $m_0 = \cos \Theta$, if $B_{\text{ext}} < 1/4$. Minimising the energy density with respect to q gives $q = 1/\sqrt{2}$, and minimising it with respect to Θ gives $m_0 = B_{\text{ext}}/(k^2 - k^4) = 4B_{\text{ext}}$. At $B_{\text{ext}} = 1/4$, the system makes a second-order phase transition to the collinear state. That the conical state is the ground state for $B_{\text{ext}} < 1/4$ and the collinear state is the ground state otherwise is shown in Appendix D.

Unlike for skyrmions stabilised in chiral magnets, where a specific value of the skyrmion's helicity is favoured depending on the type of DMI, this is not the case for skyrmions stabilised through (5.14). Here, the helicity is a zero, or Goldstone, mode. In reality, the demagnetising field slightly favours Bloch-type skyrmions, but this is weak compared to the other interactions at play in the system [203]. We make use of the ease of tuning the skyrmion's helicity in Chapter 11. The typical spin spiral wavelengths associated with frustrated magnets are typically of the order of 1 nm to 10 nm, which is small compared to those of chiral magnets².

²These numerical values can be obtained by, for example, plugging in the values of the exchange integrals from Paddison et al. [204] into (B.17) and obtaining the cyclidal wavelength $\lambda = \sqrt{8\pi^2 I_2/I_1}$.

Part II.

**Current-Driven Creation of
Topological Magnetic Textures**

Chapter

6

Magnetic Texture Creation in the Ferromagnetic State

The potential applications of topological magnetic textures, such as in data storage and processing, have been discussed in previous chapters. Important for the implementation of these magnetic textures in future technologies is the ability to create them, *e.g.* when data is written. For the case of domain walls, such as in the original proposal of racetrack memory Ref. [29], one method to create them on-demand has been studied in ferromagnetic nanowires by Sitte et al. [205]. Here, the interaction between a spin-polarised current and a magnetic defect leads to the periodic creation of domain walls, the frequency of which can be tuned by varying the current strength. Unlike commercial technologies which require the application of external magnetic fields [206], the system under consideration provides an all-electrical means to create the domains. A similar mechanism has been proposed for magnetic skyrmions by Everschor-Sitte et al. [207], where the interaction between spin-transfer torques and a magnetic impurity leads to the periodic creation of skyrmion-antiskyrmion pairs. In this Chapter, we first review the former case of magnetic domain wall creation, before investigating the latter case further for the creation of magnetic skyrmions by an all-electrical means.

6.1. Current-Driven Creation of Magnetic Domain Walls

The work of Sitte et al. [205] considers a nanowire which is sufficiently thin that spatial variations in the magnetisation perpendicular to the wire's axis can be neglected. At one end of the wire ($x = 0$), the magnetisation is pinned to point along $+\hat{z}$, and a uniaxial anisotropy term in the energy functional enforces that boundary condition that the magnetisation points along \hat{x} as $x \rightarrow \infty$. In the absence of an applied current, the static magnetisation texture rotates in the xz -plane to satisfy these boundary conditions. For an applied current with current density j below a critical current density j_c , the static magnetisation textures have a nonzero y -component. Above j_c , the texture is no longer static and there is a periodic creation, or 'shedding', of domain walls. These three cases are illustrated in Fig. 6.1.

In the study, a minimal energy functional containing only symmetric exchange and

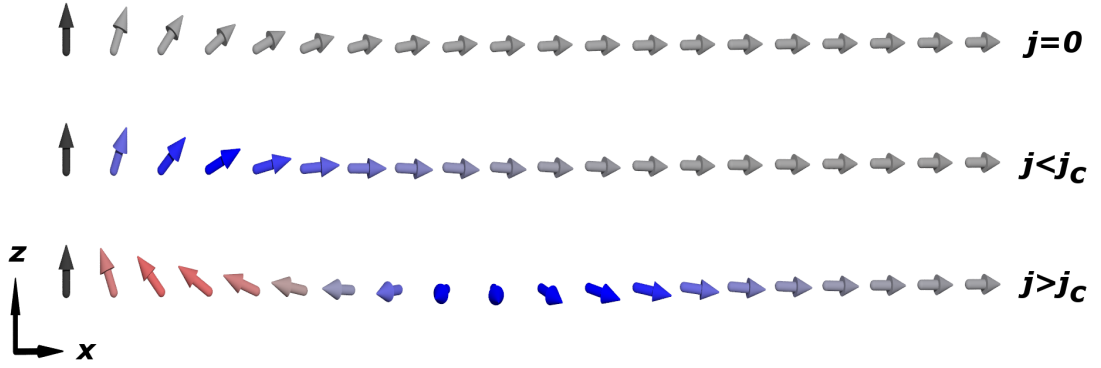


Figure 6.1.: The setup considered in Ref. [205]. For zero applied current, the magnetisation rotates in the xz -plane to satisfy the boundary conditions. For a finite applied current density j below a critical current density j_c , the static texture has a finite y -component. For $j > j_c$, domain walls are created periodically. Figure taken from Ref. [205].

uniaxial anisotropy contributions is used, which reads

$$U[\mathbf{m}(\mathbf{r})] = \int_0^\infty dx [A(\partial_x \mathbf{m})^2 + K\Pi(m_x)], \quad (6.1)$$

where $\Pi(m_x)$ is a monotonic function modelling the uniaxial anisotropy with the boundary conditions $\Pi(0) = 1$, $\Pi'(0) = 0$, and $\Pi(1) = 0$. As usual, A is the exchange stiffness constant and K is the uniaxial anisotropy strength. The dynamics of the system are modelled using the LLG equation including the spin-transfer torque terms (4.21). By considering solutions for the static case where $\partial_t \mathbf{m} = \mathbf{0}$, a critical current j_c is derived, above which domain walls of alternating sense are periodically created at the impurity.

The frequency of the domain wall creation is additionally calculated analytically in Ref. [205] by mapping the problem onto that of a particle oscillating in a potential well, the exact shape of which is determined by the system parameters, which corresponds physically to the oscillation of the x -component of the magnetisation. It is found that the shedding frequency $f \propto \sqrt{j - j_c}$ which, when the extrapolation of the value of the applied current for $f \rightarrow 0$ is made, yields good agreement with their calculation of j_c . These analytical insights were confirmed using micromagnetic simulations. Subsequent work by Rodrigues, Sommer and Everschor-Sitte [208] examined a similar setup with a chiral magnet, with the addition of DMI to the energy functional, which reduced the threshold current strength required for domain wall creation.

6.2. Current-Driven Skyrmion-Antiskyrmion Pair Creation

The creation of skyrmions has been the subject of various investigations since the first experimental observations of magnetic skyrmions in the late 2000s and early 2010s. In many cases, the creation of skyrmions is rather random, as opposed to being a controlled, on-demand process. One of the earlier and more well-known investigations in this topic was carried out by Romming et al. [209], who showed experimentally that skyrmions can be created and deleted using spin-polarised currents from a scanning tunnelling

6.2. Current-Driven Skyrmion-Antiskyrmion Pair Creation

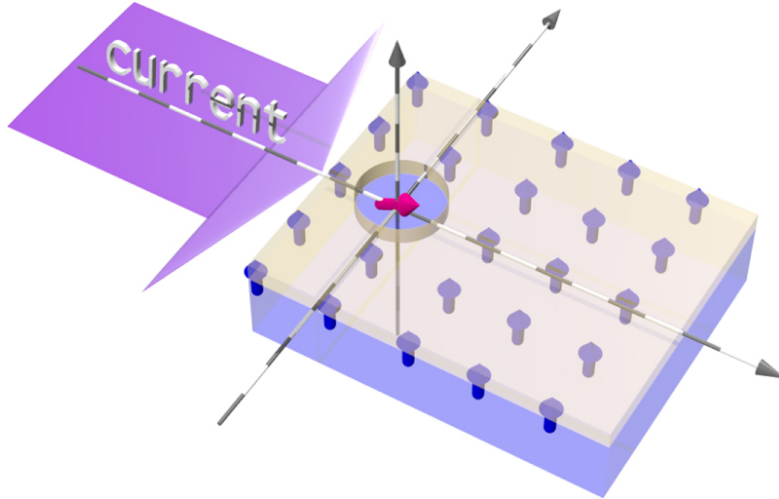


Figure 6.2.: Schematic of the system considered in this Section, as well as in Ref. [207]. A steady spin-polarised current is applied to a thin film with perpendicular magnetic anisotropy, within which a circular impurity with modified uniaxial anisotropy exists. Figure taken from Ref. [207].

microscope. At a low temperature, the current allows for the energy barrier for the creation of skyrmions to be overcome. The nucleation of skyrmions in nanodisks through the perpendicular application of a spin-polarised current has also been investigated numerically [210]. It has also been shown experimentally that skyrmions can be nucleated in thin films through focussed ion beam irradiation, which creates defects from which skyrmions can be nucleated [211, 212]. The geometry of the system can also be exploited to induce the creation of skyrmions, such as in the cases of the current-driven creation of skyrmions using an antinotch geometry [213], and the creation of skyrmions from a constriction in the thin film with the application of a spin-polarised current [214–216]. Other potential mechanisms for the creation of skyrmions include the application of surface acoustic waves [217], local heating using a laser pulse [218], and the application of spin-polarised currents to existing antiskyrmions in the system [219].

Here, we will focus on the creation of skyrmion-antiskyrmion pairs in the ferromagnetic state through the application of a spin-polarised current, which has been demonstrated in various works. Specifically, the creation of skyrmion-antiskyrmion pairs due to the interaction of a spin-polarised current with small fluctuations in the ferromagnetic background was studied by Stier et al. [220]. Furthermore, an experimental study by Brock et al. [221] demonstrated the creation of skyrmions breaking off from defect sites. In this Chapter, however, we predominantly draw inspiration from Everschor-Sitte et al. [207], in which the application of a spin-polarised current to a circular impurity in a thin film with PMA is considered. The impurity is modelled in micromagnetic simulations as a circular region of modified uniaxial anisotropy strength, with an additional in-plane component, illustrated in Fig. 6.2. Above a critical current j_c , the interplay of the spin-transfer torque and the gradients induced by the impurity¹ result in the creation of skyrmion-antiskyrmion pairs. The skyrmion and antiskyrmion move in opposite directions perpendicular to the axis of the applied current due to their opposite

¹Recall that the Zhang-Li spin-transfer torque terms in (4.21) only act on gradients of magnetisation m .

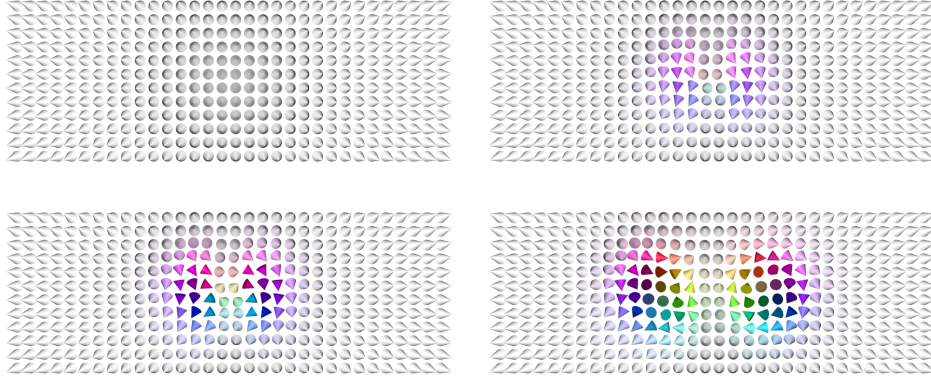


Figure 6.3.: Schematic of a continuous deformation of a collinear state into a skyrmion-antiskyrmion pair. Throughout the deformation, the overall topological charge remains zero due to the opposite skyrmion numbers of the skyrmion and antiskyrmion.

topological giving inducing motion in opposite directions in the skyrmion Hall effect, discussed in more detail in Chapter 9. To conserve topological charge, a skyrmion-antiskyrmion pair, where the skyrmion and antiskyrmion have opposite N_{sk} , is produced. The creation of a skyrmion-antiskyrmion pair through a continuous deformation of a magnetisation vector field $\mathbf{m}(\mathbf{r})$ that is initially collinear is illustrated in Fig. 6.3. A snapshot of a micromagnetic simulation of this skyrmion-antiskyrmion pair creation is shown in Fig. 6.4.

In this Section, we obtain the frequency dependence of the skyrmion-antiskyrmion pair creation frequency f on the applied current density j . We consider a minimal model with symmetric exchange of strength A , PMA with strength K , and an impurity with a uniform strength of \bar{K} , modelled by the energy functional

$$U[\mathbf{m}(\mathbf{r})] = \int d^3r [A(\nabla\mathbf{m})^2 + K(1 - m_x^2) + \bar{K}\Pi(\mathbf{r})], \quad (6.2)$$

where $\Pi(\mathbf{r})$ models the circular impurity, equal to 1 within a circle of radius R_i and 0 outside of it. Defining a dimensionless length \tilde{r} through $r = \sqrt{A/\bar{K}}\tilde{r}$, the energy functional can be written as

$$\begin{aligned} U[\mathbf{m}(\tilde{\mathbf{r}})] &= \int d^3\tilde{r} \left(\frac{A}{\bar{K}}\right)^{\frac{3}{2}} \left[\left(\frac{K}{A}\right) A(\tilde{\nabla}\mathbf{m})^2 + K(1 - m_z^2) + \bar{K}\Pi(\tilde{\mathbf{r}}) \right] \\ &= \int d^3\tilde{r} \left[\frac{A^{\frac{3}{2}}}{K^{\frac{1}{2}}} (\tilde{\nabla}\mathbf{m})^2 + \frac{A^{\frac{3}{2}}}{K^{\frac{1}{2}}} (1 - m_z^2) + \frac{A^{\frac{3}{2}}\bar{K}}{K^{\frac{3}{2}}}\Pi(\tilde{\mathbf{r}}) \right]. \end{aligned} \quad (6.3)$$

Multiplying through by $\sqrt{K/A^3}$ and defining dimensionless energy \tilde{U} through $U = \sqrt{A^3/\bar{K}}\tilde{U}$, we obtain the dimensionless energy functional

$$\tilde{U}[\mathbf{m}(\tilde{\mathbf{r}})] = \int d^3\tilde{r} [(\tilde{\nabla}\mathbf{m})^2 + (1 - m_z^2) + \kappa\Pi(\tilde{\mathbf{r}})], \quad (6.4)$$

with only a single free parameter $\kappa = \bar{K}/K$. Furthermore, we define dimension-

6.2. Current-Driven Skyrmion-Antiskyrmion Pair Creation

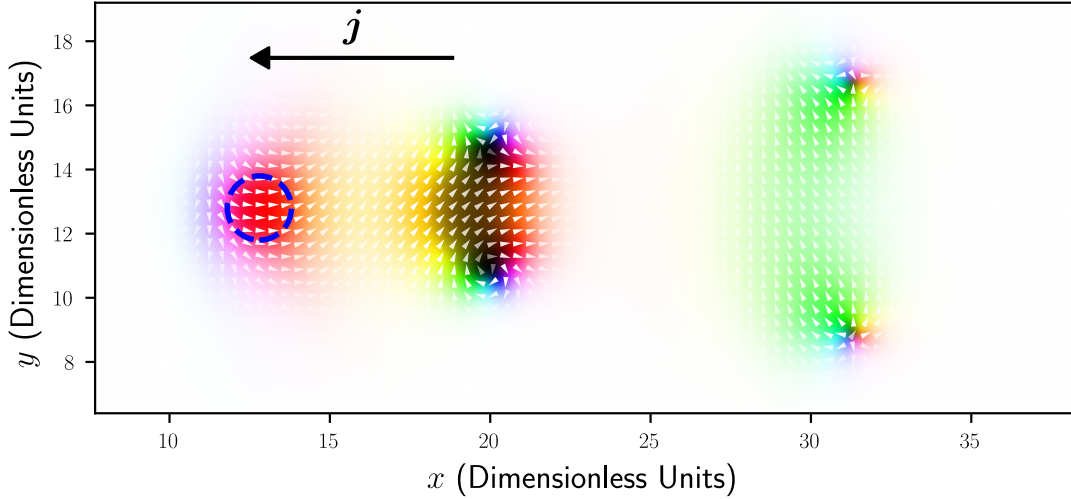


Figure 6.4.: Micromagnetic simulation of the pairwise creation of skyrmion-antiskyrmion pairs due to the interplay of spin-polarised current and the gradients in magnetisation induced by a circular impurity. The impurity is in the region shown by the dashed blue circle.

less time \tilde{t} through $t = (M_s/\gamma K)\tilde{t}$, and dimensionless current density \tilde{j} through $j = (e\gamma\sqrt{AK}/P\mu_B)\tilde{j}$. We make use of this rescaling procedure in various studies throughout this Thesis, but we only show it explicitly here. The effect of a demagnetising field in a thin film in which the magnetisation is aligned perpendicular to the plane of the film can be approximated by subtracting $\mu_0 M_s^2/2$ from the PMA strength [134], but this only represents a rescaling in the conversion between SI and dimensionless units in our case. In our micromagnetic simulations, we fix $R_i = 1$, $\kappa = 10$, and $\alpha = 0.15$. We relax the system and ramp up the current over a time t_r in a sinusoidal manner such that, during the ramping, it is given by $j_r(t) = j \sin(\pi t/2t_r)$, to avoid sharp deformations to the relaxed system. We choose $t_r = 30$, and subsequently run the system for a (rescaled) time of 100. We discretise our system into cells of size $\Delta = 0.2$, and use $N_x = 256$ cells along x , $N_y = 128$ cells along y , and a single cell along z . The current is applied along $-x$, which results in skyrmion-antiskyrmion pairs being shed from the impurity along $+x$. To determine the skyrmion-antiskyrmion pair creation frequency, we calculate the skyrmion number in a subsection of the simulation box over the time of the simulation (excluding the initial ramping), and apply a fast Fourier transform of this. The frequency with the highest amplitude is the determined creation frequency. This procedure is illustrated in Fig. 6.5. In Fig. 6.5(b), the numerically calculated skyrmion number does not reach the ideal value of -1 due to the discretisation.

Having carried out this procedure, we show the skyrmion-antiskyrmion pair creation frequency as a function of the applied current in Fig. 6.6(a). Contrary to the analytical results of Ref. [207], which treats the pinning centre as a point defect and finds that $f \propto \sqrt{j - j_c}$, we find that $f \propto j$. Fitting a straight line to this and projecting to $f = 0$, we find that $j_c \approx 2.0$, a result which was confirmed using various values of α . The discrepancy between the scaling of the current found here numerically and analytically in Ref. [207] could be explained by the fact that, in their work, they assume that the impurity can be modelled as point pinning site; the spatial extent of the region of

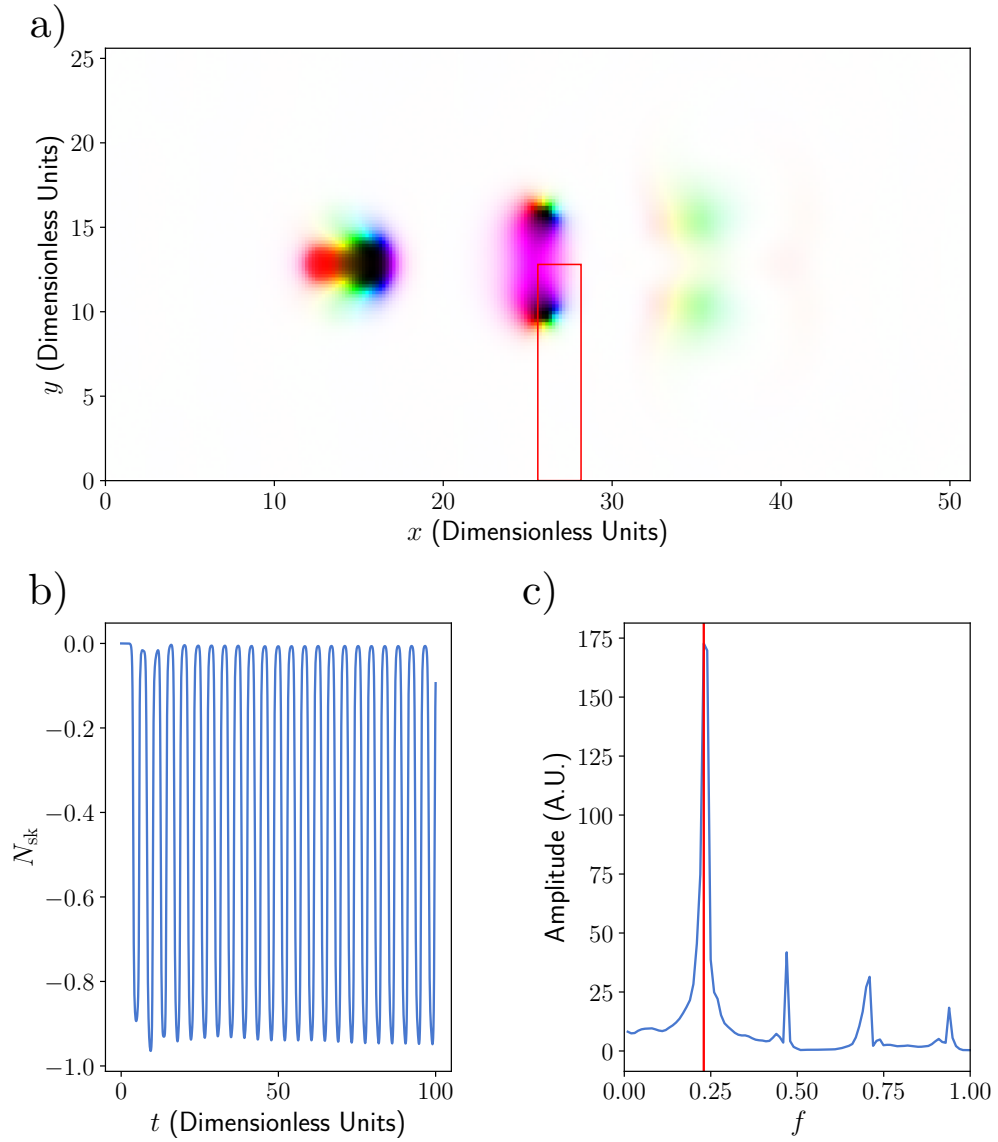


Figure 6.5.: Illustration of the method used to obtain the creation frequency. (a) Magnetisation texture, from which the skyrmion number in the region marked by a red box is calculated as a function of time. (b) Calculated skyrmion number as a function of time. (c) Fourier transform of skyrmion number over time, from which the skyrmion-antiskyrmion pair creation frequency is extracted by finding the position of the peak marked by a vertical red line.

6.2. Current-Driven Skyrmion-Antiskyrmion Pair Creation

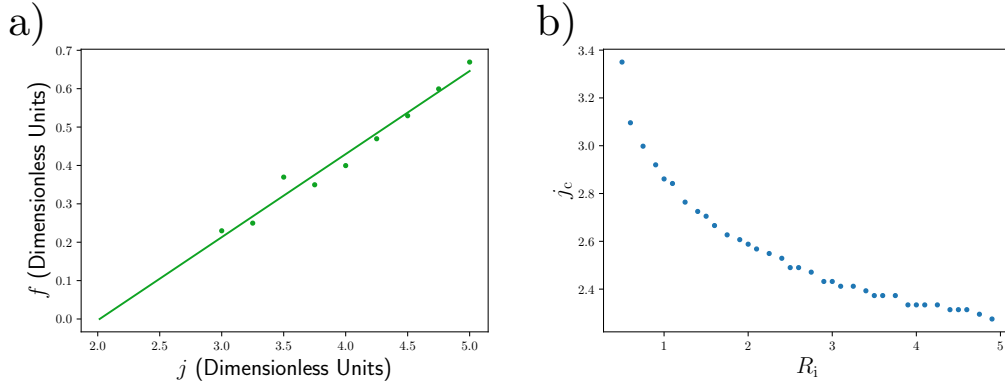


Figure 6.6.: (a) Skyrmion-antiskyrmion pair creation frequency obtained as a function of applied current for a circular impurity of radius $R_i = 1$ in a ferromagnetic thin film. (b) Critical current for skyrmion-antiskyrmion pair creation as a function of impurity radius.

modified anisotropy is not considered.

To investigate the effect of the spatial extent of the impurity, we ran simulations to obtain the critical current as a function of the impurity radius R_i . For this, we performed an interval search for a range of impurity radii to calculate the critical current for each. The results of this are shown in Fig. 6.6(b), which shows that the critical current drops as a function of the impurity radius. This makes sense physically, as the area over which the interplay between the spin-polarised current and the gradients occurs to induce skyrmion-antiskyrmion pair creation increases. We note, however, that the critical currents obtained using an interval search do not match those extrapolated to in Fig. 6.6(a), suggesting a breakdown in the linear relationship as the current decreases. The current-driven creation of magnetic skyrmions in a cycloidal background, instead of a ferromagnetic background, is the subject of the next Chapter.

Chapter 7

Current-Driven Skyrmion Creation in the Cycloidal State

In the previous Chapter, we explored the current-driven creation of skyrmion-antiskyrmion pairs in a ferromagnetic background. As discussed in Chapter 5, magnetic skyrmions can also be stabilised in a cycloidal background, in which they are confined to the natural channels created by the cycloidal texture. In this Chapter, we propose a protocol for the creation of magnetic skyrmion-antiskyrmion pairs from impurities in the cycloidal state through the application of a spin-polarised current.

7.1. Stability of the Cycloidal State Under an Applied Current

To understand the current regimes in which the cycloidal state is stable, we can use the LLG equation with the Zhang-Li spin-transfer torque term (4.21). Working in the rescaled given units in Table 5.1, this becomes

$$\frac{\partial \mathbf{m}}{\partial t} = -\mathbf{m} \times \mathbf{B}_{\text{eff}} - (\mathbf{v}_s \cdot \nabla) \mathbf{m} + \alpha \mathbf{m} \times \frac{\partial \mathbf{m}}{\partial t} + \beta \mathbf{m} \times (\mathbf{v}_s \cdot \nabla) \mathbf{m}, \quad (7.1)$$

where \mathbf{v}_s is the (dimensionless) effective spin velocity, which is the electric current density up to a prefactor, and hence the terms are used interchangeably in the following discussion. Its dimensionful form is $\mathbf{v}_s = -\mathbf{j}P\mu_B/e\gamma D(1 + \beta^2)$, where P is the polarisation, μ_B is the Bohr magneton, and $e > 0$ is the absolute value of the electron charge.

The behaviour of the spin spiral state is split into various regimes, depending on the applied current density v_s . In the presence of impurities which pin the background and an applied current below a pinning current density v_{pin} , the texture remains static. The pinning current density is zero for a pure cycloidal state in the absence of impurities. Above a critical current density v_C , the system undergoes a Walker breakdown, which results in the destabilisation of the long-range order [222]. For $v_{\text{pin}} < v_s < v_C$, the texture evolves in a controllable manner. The different regimes are illustrated in Fig. 7.1, which shows example magnetisation textures for the different current regimes. The exact values depend on factors such as the geometry and concentration of impurities in the system. In sufficiently homogeneous systems with straight stripes, an example of the

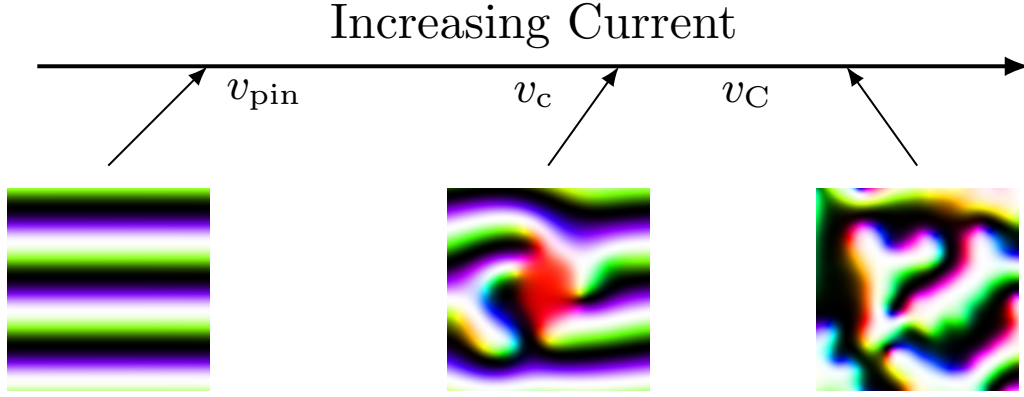


Figure 7.1.: Regimes of the behaviour of the cycloidal state as current is increased. Below an effective spin velocity v_{pin} , the cycloidal magnetisation texture remains static. Above a lower critical current v_c , fluctuations occur on the order of the cycloidal wavelength λ_c . Above a higher critical current v_C , the long-range order of the cycloidal state breaks down.

controlled behaviour for $v_{\text{pin}} < v_s < v_C$ is the steady translation of rigid skyrmions. In the presence of an inhomogeneity, an example is the creation of skyrmion-antiskyrmion pairs as the spin-polarised current interacts with the gradients in magnetisation induced by the impurity.

For a defect-free cycloidal state at zero temperature with wavevector direction $\hat{\mathbf{q}} = \hat{\mathbf{y}}$ such that $m_x = 0$ everywhere, $v_{\text{pin}} = 0$ and the magnetisation gradients couple to the y -component of a driving current only. This results in a translation of the helix along the y -direction. Because of this, in our micromagnetic simulations of skyrmions in the cycloidal state, we freeze the top and bottom boundaries of the system. The regime for which $v_{\text{pin}} < v_s < v_C$ is split into two further regimes separated by v_c : for $v_{\text{pin}} < v_s < v_c$, fluctuations in the magnetisation texture are induced on a length scale much smaller than the cycloidal wavelength λ_c . For $v_c < v_s < v_C$, fluctuations have a length scale on the order of magnitude of the cycloidal wavelength λ_c , which is the regime interesting for the controlled creation of skyrmions. Thus, v_c represents an approximate critical current required for the creation of skyrmions in the cycloidal state.

We now estimate the critical current v_c for the current-driven creation of skyrmion-antiskyrmion pairs for an anisotropy strength $\kappa \lesssim \kappa_c$. κ_c is the anisotropy strength at which the cycloidal wavelength diverges to give a single domain wall, discussed in Section 5.3. For this, we assume that the cycloidal state for such a high anisotropy strength can be reasonably approximated by a series of domain walls. We parametrise the magnetisation as

$$\mathbf{m}(\mathbf{r}) = \sin \Theta(\mathbf{r}) \hat{\mathbf{z}} + \cos \Theta(\mathbf{r}) [\cos \Phi(\mathbf{r}) \hat{\mathbf{x}} + \sin \Phi(\mathbf{r}) \hat{\mathbf{y}}], \quad (7.2)$$

7.2. Current-Driven Creation of Skyrmions in the Cycloidal State

with the profile

$$\Theta(\mathbf{r}) = \arctan \left[\sinh \left(\sqrt{2\kappa} [y - y_0(x)] \right) \right] + \frac{\pi}{2}, \quad (7.3a)$$

$$\Phi(\mathbf{r}) = \frac{\pi}{2} + \varphi(x). \quad (7.3b)$$

Here, $y_0(x)$ and $\varphi(x)$ describe small fluctuations along the tracks due to local perturbations close to a domain wall, $y - y_0(x) \ll \lambda_c$. We then assume that energy deviations resulting from a small translation $y_0(x)$ of the domain wall result in energy perturbations quadratic in $y_0(x)$,

$$\begin{aligned} U[\mathbf{m}(\mathbf{r})] &\approx U[y_0(x), \varphi(x)] + \int dx 2y_0^2/\lambda_c^2 \\ &= \int dx \left[\frac{1}{\sqrt{2\kappa}} (\partial_x \varphi)^2 + \sqrt{2\kappa} (\partial_x y_0)^2 - \frac{\pi}{2} \varphi \partial_x y_0 \right. \\ &\quad \left. + \left(\frac{\pi}{2} + \sqrt{2\kappa} \right) \varphi^2 + \frac{2y_0^2}{\lambda_c^2} \right], \end{aligned} \quad (7.4)$$

where the last two terms correspond to confining potentials which fix the helicity and position of the domain wall along the y -axis respectively. For current flowing in the x -direction and with $\beta = 0$, the energy (7.1) for profile (7.3), the LLG equation (7.1) leads to the linearised equations of motion of the fluctuations

$$\partial_t \varphi = \left(v_x + \frac{\pi}{2} \right) \partial_x \varphi - \sqrt{2\kappa} \partial_x^2 y_0 + \frac{2}{\lambda_c^2} y_0 - \sqrt{2\kappa} \alpha \partial_t y_0, \quad (7.5a)$$

$$\partial_t y_0 = \left(v_x + \frac{\pi}{2} \right) \partial_x y_0 + \frac{1}{\sqrt{2\kappa}} \partial_x^2 \varphi - \left(\frac{\pi}{2} + \sqrt{2\kappa} \right) \varphi + \frac{1}{\sqrt{2\kappa}} \alpha \partial_t \varphi. \quad (7.5b)$$

For a small damping parameter α , this gives, for $\kappa \lesssim \kappa_c$, that perturbations in the system damp out for currents below a critical value of

$$v_c^{\kappa \lesssim \kappa_c} \approx \sqrt{2\kappa + \frac{\pi}{2} \sqrt{2\kappa}} - \frac{\pi}{2}, \quad (7.6)$$

which is $v_c \approx 0.65$ in limit of $\kappa \rightarrow \kappa_c = \pi^2/8$. This is derived in Appendix E. Although the dynamics of the magnetisation texture around a magnetic impurity in the presence of spin-polarised current are generally much more complex than can be captured in this simplified analytical calculation, it gives a rough estimate of the current strength that must be applied to create skyrmion-antiskyrmion pairs in the cycloidal state.

7.2. Current-Driven Creation of Skyrmions in the Cycloidal State

We now turn to micromagnetic simulations to study the current-driven creation of skyrmions in the cycloidal state. For this, we add to the energy functional (5.2) an additional uniaxial anisotropy term corresponding to a circular impurity of radius R_i

centred at (x_i, y_i) , with anisotropy strength κ_i and easy axis $\hat{\mathbf{n}}$. Explicitly, this is

$$U_i[\mathbf{m}(\mathbf{r})] = - \int d^2r \kappa_i (\hat{\mathbf{n}} \cdot \mathbf{m})^2 H [R_i^2 - (x - x_i)^2 - (y - y_i)^2], \quad (7.7)$$

where $H(x)$ is the Heaviside step function with $H(x) = 1$ for $x \geq 0$ and $H(x) = 0$ for $x < 0$. As shown in Figs. 7.2(a) and (d), the inhomogeneity induces a local deformation of the helix. This leads to an instability for a drive above v_c . Figure 7.2 also shows the critical current densities calculated using micromagnetic simulations for various ratios of the impurity anisotropy strength κ_i to the global anisotropy strength κ , and impurity radii R_i , determined using an interval search, analogous that used in Section 6.2. The results are shown for impurities with easy axes along $\hat{\mathbf{x}}$ and $\hat{\mathbf{z}}$, and currents along $+\hat{\mathbf{x}}$ and $-\hat{\mathbf{x}}$. In these simulations, we take $\kappa \approx 0.31$, $\alpha = 0.05$, and $\beta = 0$. Generally, the critical current decreases as a function of the impurity's anisotropy strength κ_i due to the initial perturbation being stronger for higher κ_i . A higher anisotropy size plays a greater role than its strength in determining the critical current, producing a larger initial perturbation that couples more strongly to spin-transfer torque. We note that the values for $\hat{\mathbf{n}} = \hat{\mathbf{z}}$ in Figs. 7.2(e) and (f) are identical for currents along the positive and negative $\hat{\mathbf{x}}$ directions due to the mirror symmetry along $\hat{\mathbf{x}}$ for an easy axis along $\hat{\mathbf{z}}$. In general, these values of v_s are within an order of magnitude of the $v_c^{\kappa_i \lesssim \kappa_c} \approx 0.65$ predicted analytically in (7.6). However, assigning a precise numerical value to the critical current from the micromagnetic simulations is not trivial, as the domain wall becomes increasingly distorted with increasing currents at this order of magnitude. As such, there is no definite transition value of the current beyond which increasing the currents leads to a breakdown of the domain wall.

The (dimensionful) energetic parameters used in our micromagnetic simulations are summarised in Table 7.1. In all simulations, periodic boundary conditions are applied along the x - and y -axes. The system is discretised into cells of 1 nm along the x - and z -axes, while along the y -axis, the discretisation is chosen such that an integer number of cycloidal wavelengths fit into the system. The cycloidal background is pinned by freezing the spins at the edges of the system along the y -direction, *i.e.* at the top and bottom. Furthermore, for the simulations in which skyrmions are shed, absorbing boundary conditions are used at the horizontal ends of the system along the x -axis. The value of DMI strength is $2D_c$, where $D_c = 4\sqrt{AK}/\pi$ is the critical DMI strength above which the cycloidal state is stabilised [196].

The impurity is placed at $x = L_x/4$ for a current along the $+x$ -direction and at $x = 3L_x/4$ for a current along the $-x$ -direction. The criterion we use for shedding is that the z -component of the magnetisation at the centre of the system $(L_x/2, L_y/2)$, which is aligned along $-\hat{\mathbf{z}}$ initially, becomes positive (if there is no shedding, the simulation finishes after 20 ns of steady current). Throughout this work, where there are impurities in the system, the impurities are placed such that their position within the helix minimises energy. Where the impurity's easy axis is $\hat{\mathbf{z}}$, it is placed where the magnetisation is out-of-plane, at $y = L_y/2$, and when it is $\hat{\mathbf{x}}$, the impurity is placed where the magnetisation is in-plane, $y = L_y/2 - \lambda_c/4$. In each simulation, the current is ramped up to the maximum value sinusoidally over 20 ns.

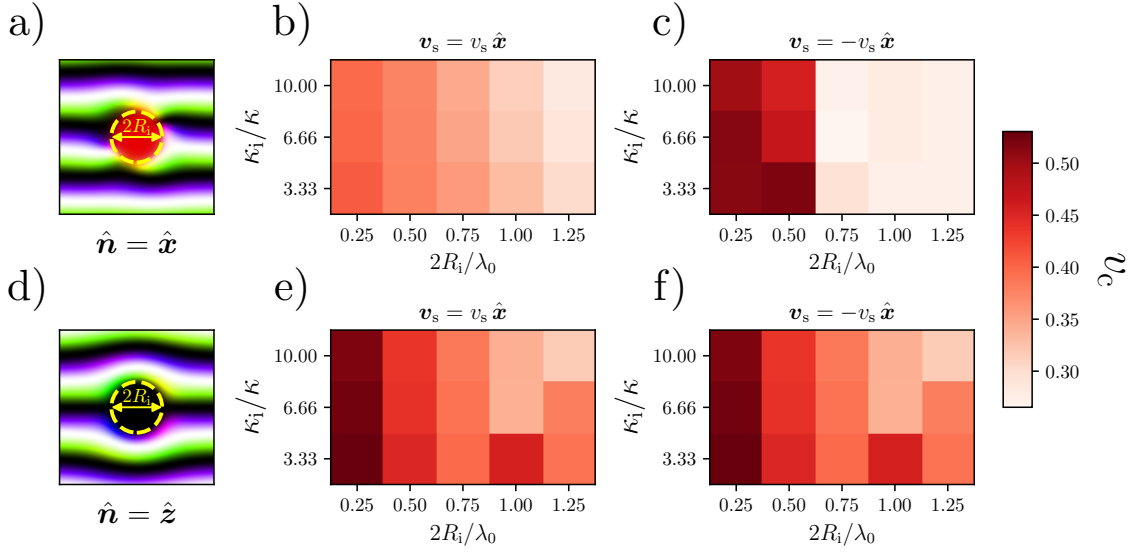


Figure 7.2.: (a), (d) Magnetisation texture around the impurity, depicted as a dashed yellow circle, for an easy axis within the impurity along the x - and z -axes respectively. (b), (c), (e), (f) The critical current density for the creation of skyrmions as a function of impurity radius and relative anisotropy strength κ_i/κ . For all panels, $\kappa \approx 0.31$, $\alpha = 0.05$, and $\beta = 0$. For the textures in (a) and (d), $2R_i = \lambda_0$ and $\kappa_i/\kappa = 10$. (e) and (f) are identical due to the mirror symmetry along the x -axis for an impurity easy axis along \hat{z} . Figure taken from our publication Ref. [191].

7.3. Protocol for the Controlled Creation of Skyrmions in the Cycloidal State

In the following, we bring together the controlled creation and current-driven motion of magnetic skyrmions to propose a protocol by which skyrmions can be created in the cycloidal state. We use $\hat{\mathbf{n}} = \hat{\mathbf{x}}$, $\kappa_i = 10\kappa$, $2R_i/\lambda_0 = 1.0$, and a current in the x -direction¹ which, referring to Fig. 7.2(c), has a relatively low critical current strength v_c . The method from Ref. [207] in which a constant current was used to periodically create skyrmion-antiskyrmion pairs. In contrast, we propose a protocol in which the currents in the x - and y -directions are periodically switched on and off, which can be repeated

¹Recall that the sign of \mathbf{v}_s is opposite to that of the current.

Quantity	Symbol	Value	Unit
Exchange Stiffness	A	10^{-11}	J m^{-1}
Uniaxial Anisotropy Strength	K	10^5	J m^{-3}
DMI Strength	D	2.55×10^{-3}	J m^{-2}
Saturation Magnetisation	M_s	10^6	A m^{-1}
Electric Current Polarisation	P	1	Dimensionless

Table 7.1.: Parameters common to all simulations in this investigation. Simulation-specific parameters are discussed in the text.

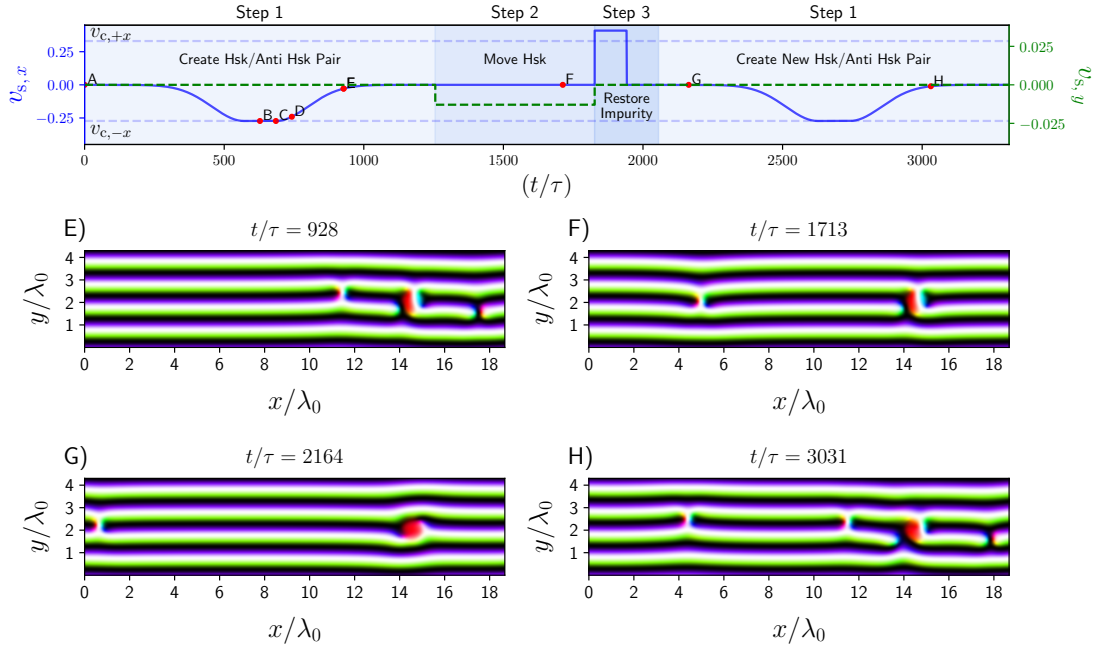


Figure 7.3.: Overview of the all-electrical protocol to create H-shaped skyrmions by the application of a spin-polarised current to an impurity in the cycloidal state. The details of the HSK/anti-HSK creation (A)-(E) are shown in Fig. 7.4. (E)-(H) show each step: the initial skyrmion-antiskyrmion pair creation, the current-driven motion of the skyrmion away from the impurity, the impurity after removing the domain wall inside of it using a current pulse, and the subsequent creation of a skyrmion-antiskyrmion pair. Figure taken from our publication Ref. [191].

an arbitrary number of times to create an arbitrary number of skyrmion-antiskyrmion pairs. The full protocol, shown in Fig. 7.3, is divided into three steps:

Step 1 The current along the x -direction is ramped up to just above the critical current v_c . It is increased sinusoidally to a constant current to ensure that the change is not too abrupt. The current is maintained at a constant value for sufficiently long such that the skyrmion-antiskyrmion pair is created before it is decreased in a similar sinusoidal manner. Note that this creates a domain wall inside the impurity which hinders further shedding, which can be seen in Figs. 7.3(E) and (F).

Step 2 A constant current is applied in the y -direction, which drives the skyrmion away from the impurity. The skyrmion and antiskyrmion move in opposite directions.

Step 3 A short, sharp current pulse is applied along the $-x$ -direction, which resets the impurity by causing the meron and antimeron on either side of the impurity to collide and annihilate.

The protocol then goes back to Step 1 to produce a subsequent skyrmion-antiskyrmion pair. In principle, it is possible to produce an arbitrary number of skyrmions by repeating this process indefinitely. It may also be possible to use the skyrmions and antiskyrmions as binary digits (bits) with, for example, a skyrmion representing a ‘1’ and an antiskyrmion representing a ‘0’, analogous to as proposed in Ref. [223]. The

7.3. Protocol for the Controlled Creation of Skyrmions in the Cycloidal State

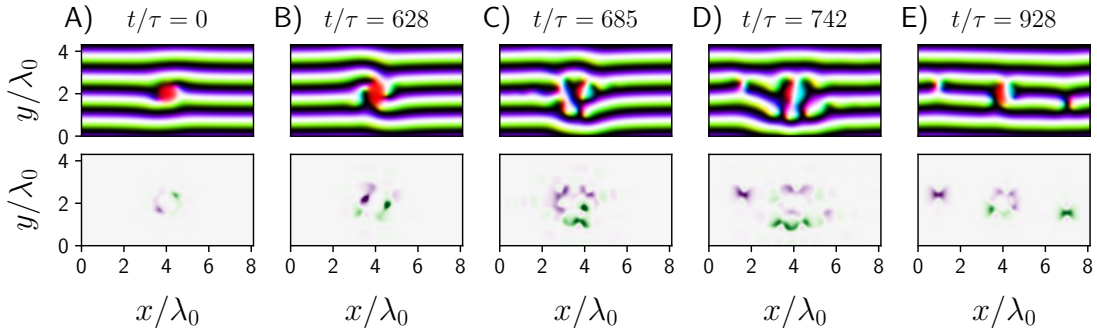


Figure 7.4.: Creation of a skyrmion-antiskyrmion pair in the cycloidal state through the application of a spin-polarised current to an inhomogeneity. The top row shows the magnetisation configuration, while the bottom row shows the corresponding skyrmion number density. Figure taken from our publication Ref. [191].

ability to create skyrmions confined in the natural lanes of the cycloidal background makes this protocol promising for their application in the data storage and processing applications discussed in Chapter 2.

Chapter **8**

Current-Driven Creation of Magnetic Textures in Bulk Systems

The discussions of Chapters 6 and 7 have been concerned with quasi-two-dimensional thin films. Specifically, we have considered the creation of the skyrmion-antiskyrmion pairs at impurities. In bulk systems, different magnetic structures exist, one of which is the smoke ring-like magnetic vortex ring. Vortex rings can be both topologically trivial, with a Hopf index of zero, and nontrivial, with a nonzero Hopf index. In this Chapter, we first review the literature surrounding magnetic vortex rings. We then consider their current-driven creation through a similar mechanism to that of the skyrmion-antiskyrmion pair creation discussed in previous chapters.

8.1. Current-Driven Dynamics of Magnetic Vortex Rings and Hopfions

Vortex rings are widely known in the context of fluid dynamics, where they are localised, toroidal regions of a turbulent fluid in which the fluid circulates about the closed axis line [224]. Smoke rings are a well-known example of this. Analogous structures exist in ferromagnetic materials, where the magnetisation field forms a ring shape that rotates around the vortex axis line. This is illustrated in Fig. 8.1, which shows a magnetic vortex ring illustrated by lines of constant magnetisation direction propagating along its symmetry axis.

The dynamic stabilisation of vortex ring textures in ferromagnetic materials has been studied theoretically in various works. In the 1970s, Dzyloshinskiĭ and Ivanov [225] found that topologically nontrivial vortex rings could be stabilised in systems with symmetric exchange and uniaxial anisotropy by the precession of the magnetisation about the symmetry axis. This problem has been examined in more detail by Borisov and Rybakov [226] using finite-element micromagnetic modelling. However, it was pointed out by Papanicolaou [227] that, for magnetic vortex rings with a nonzero Hopf index, their dynamic stabilisation necessitates a simultaneous translation along the symmetry axis, illustrated in Fig. 8.1. This is analogous to the dynamic stabilisation of propagating smoke rings, which retain their structure as they propagate through air, until energy losses due to friction cause them to collapse.

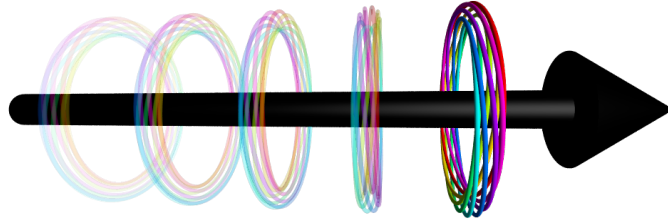


Figure 8.1.: Illustration of a propagating magnetic vortex ring, represented by its preimages (lines of constant magnetisation direction). In this case, the vortex ring has a Hopf index of 1.

Papanicolaou’s study Ref. [227] laid a heuristic foundation for research into magnetic vortex rings, and a numerical study of the propagation of magnetic vortex rings was carried out in 1999 by Cooper [228] for both topologically trivial (zero Hopf index) and nontrivial (nonzero Hopf index) vortex rings. It was confirmed that, within the framework of the LLG equation, magnetic vortex rings of various Hopf indices could be stabilised through their propagation at a constant speed along the symmetry axis of the system, with a concurrent precession of the magnetisation about the symmetry axis. The stability and robustness in the presence of perturbations of these propagating vortex rings was investigated by Sutcliffe [229] in 2007. Sutcliffe found that the presence of uniaxial anisotropy in the system resulted in a pinching instability of the vortex rings. In the absence of an easy axis, however, the vortex rings were still stable under the breaking of the axial symmetry of the initial field configuration.

Various research works from the late 2010s into the early 2020s investigating the propagation of magnetic vortex rings have accompanied the rise in interest in magnetic hopfions. The current-driven dynamics of hopfions under the application of both spin-transfer and spin-orbit torques were studied by Wang, Qaiumzadeh and Brataas [102] in 2019. Unlike with magnetic skyrmions, where there is a component of motion perpendicular to an applied spin current (the skyrmion Hall effect, explored in more detail in Section 9.1), the direction of motion of hopfions is in the direction of the applied current, due to a vanishing gyrovector. As such, magnetic hopfions do not suffer from an analogy of the skyrmion Hall effect, and propagate either parallel or perpendicular to the applied current, depending on whether the hopfion is of Bloch- or Néel-type (referring to the type of skyrmion in a plane through the hopfion), and whether spin-transfer or spin-orbit torque is applied. In Ref. [102], the hopfions are stabilised geometrically by confinement in a thin film (of sufficient thickness for the hopfion to exist) analogous to the situation in Refs. [60, 88, 89] discussed in Sec. 3.2, and as such, motion along the axis perpendicular to the film is suppressed.

A further 2020 work by Liu et al. [67] considered a hopfion stabilised by competing exchange interactions, analogous to in Refs. [71, 84], without confinement to a thin film. They found using both collecting coordinate modelling and micromagnetic simulations that, in the presence of spin-transfer torque from a spin current applied perpendicular to the hopfion’s symmetry axis, in addition to a translational motion of the hopfion,

a rotation of the hopfion's symmetry axis was induced. When the current was instead applied along the symmetry axis, in addition to a translation along the direction of the current, a rotation of the structure about the symmetry axis was induced, as well as a dilation of the structure.

8.2. Current-Driven Creation of Magnetic Vortex Rings

In this Chapter, we show that magnetic vortex rings can be created through the interaction of spin-transfer torques at magnetic impurities in a manner analogous to the creation of skyrmion-antiskyrmion pairs in thin films. We show results for both spherical and toroidal impurities, but the process is similar in each case. To model such processes, we consider a minimal model with the lowest-order symmetric exchange interaction, uniaxial anisotropy along the current direction x , and a region of modified anisotropy to represent an impurity. For this, we use the energy functional

$$U[\mathbf{m}(\mathbf{r})] = \int d^3r [A(\nabla\mathbf{m})^2 + K(1 - m_x^2) + \bar{K}\Pi(\mathbf{r})], \quad (8.1)$$

identical to (6.2), with the exception that x is now the easy axis. The functional form of $\Pi(\mathbf{r})$ is naturally also different, being equal to 1 within three-dimensional impurity (discussed below) and 0 elsewhere. As in Chapter 6, this can be rescaled to

$$\tilde{U}[\mathbf{m}(\tilde{\mathbf{r}})] = \int d^3\tilde{r} [(\tilde{\nabla}\mathbf{m})^2 + (1 - m_x^2) + \kappa\Pi(\tilde{\mathbf{r}})], \quad (8.2)$$

where the dimensionless length, energy, time, and current density are as in Chapter 6, and $\kappa = \bar{K}/K$. As in previous investigations, we ramp the current up sinusoidally to a constant value, and we set $\beta = 0$.

We first consider a toroidal impurity, for which the results are shown in Fig. 8.2. This impurity is located at $x = 0$, such that only half of it is embedded in the sample. We choose this over an embedded ring-shaped impurity for two reasons. Firstly, it is more experimentally feasible to consider impurities at the edge of the sample as opposed to in bulk. Secondly, we found empirically that the vortex ring creation was more controlled (for example, with the vortex rings holding their shape for longer) than where the impurity was not at the boundary. In the top-left of Fig. 8.2, isosurfaces of constant z -component $m_z = 0.7$ and $m_z = -0.7$ (which enclose preimages $m_z = 1$ and $m_z = -1$) are shown in red and blue respectively. It is evident that the preimages do not link, such that the vortex rings have Hopf index $H = 0$, which we confirmed by numerical integration of the Whitehead formula (3.3) using the code in Appendix A. Also shown in a horizontal slice in the xy -plane, showing that the cross-section through the vortex ring consists of two in-plane skyrmion-antiskyrmion pairs. To make this clear, a subset of a slice through the vortex ring is shown, with the colour maps showing the out-of-plane component m_z of the magnetisation and the skyrmion number density ρ_{sk} . These vortex rings propagate some distance, but their size eventually decreases and they collapse due to energy dissipation.

We now turn to the case of a spherical impurity, which is shown in Fig. 8.3. This is analogous to that with a toroidal impurity, with the difference that a slice through the vortex rings reveals only a single skyrmion-antiskyrmion pair, rather than two. This can

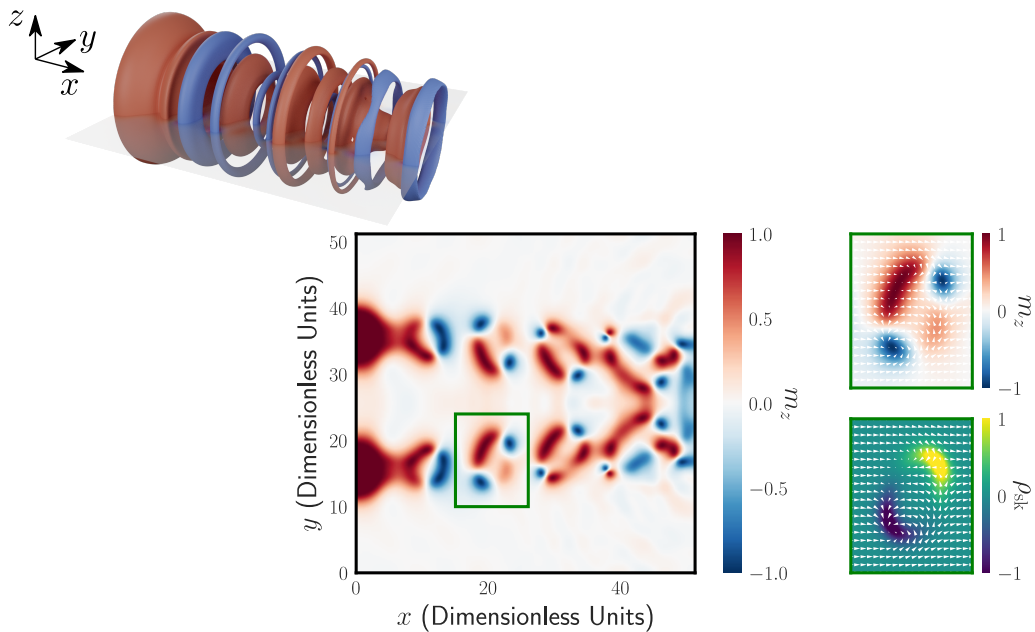


Figure 8.2.: Micromagnetic simulation of the periodic creation of magnetic vortex rings through the application of spin-transfer torque in the presence of a ring-shaped impurity at the boundary of a ferromagnet. On the top-left, the isosurfaces $m_z = 0.7$ and $m_z = -0.7$ are shown in red and blue respectively. In the centre, the out-of-plane component of magnetisation is shown. On the right, the magnetisation texture of a cross-section through the vortex ring is shown with both the z -component of the magnetisation and the skyrmion number density ρ_{sk} (in arbitrary units).

be understood by analogy with the skyrmion-antiskyrmion pair creation in a thin film discussed in Chapter 6, where a slice through the centre of the system reveals only a single impurity, rather than two separate impurities as with a slice through a ring-shaped impurity. In this case, we also see unlinked preimages, *i.e.* vortex rings with $H = 0$.

In addition to the results presented in this Chapter, we speculate that the creation of vortex rings with nonzero Hopf indices through the interaction between spin currents and impurities might be possible under the correct circumstances. For example, this may be possible with the introduction of an interaction that induces twisting, encouraging the interlinking of preimages. We note, however, that this would likely involve a more convoluted experimental setup than that investigated here, and that further simulations with the inclusion of DMI did not yield hopfions. Furthermore, we note that any hopfions produced may not necessarily need to be stable in bulk, just as DMI that stabilises skyrmions does not need to be present for the skyrmion-antiskyrmion pair creation discussed in Chapter 6.

Another method by which magnetic hopfions may be created could be from existing bulk magnetic structures with $H = 0$ through the variation of an external parameter, such as the magnetic field. This was investigated in Ref. [60], where varying the applied magnetic field can transform a monopole-antimonopole pair into a hopfion. Aside from this, experimental evidence has suggested that topologically trivial vortex rings are stable

8.2. Current-Driven Creation of Magnetic Vortex Rings

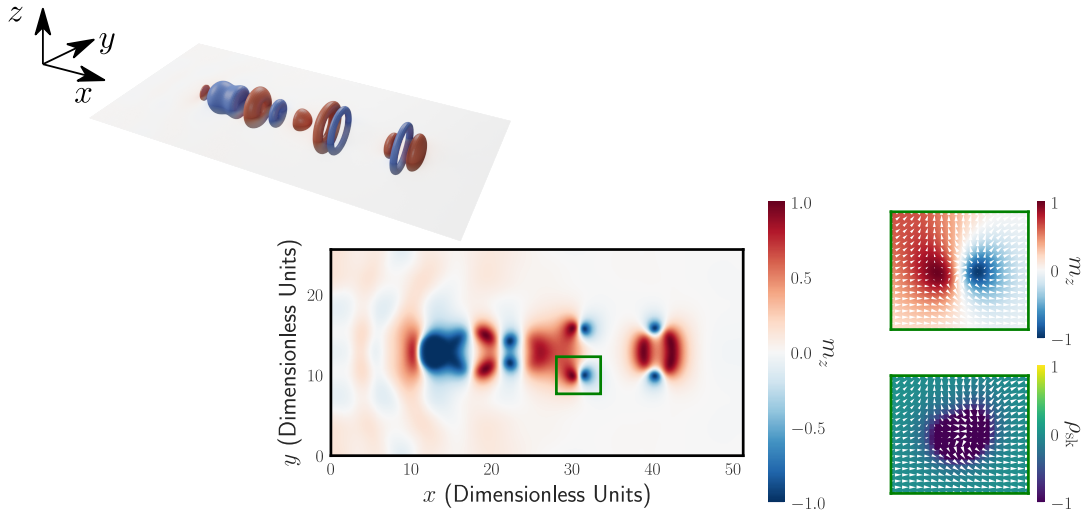


Figure 8.3.: Vortex ring creation from a spherical impurity, analogous to Fig. 8.2.

in their own right [91], and may themselves have applications similar to those proposed for skyrmions and hopfions, such as in neuromorphic computing.

Part III.

Skyrmion Dynamics

Chapter 9

Current-Driven Motion of Magnetic Skyrmions

The current-driven motion of magnetic skyrmions in the presence of spin-transfer torques is well-understood¹, and has been the subject of much theoretical and experimental investigation. It was first observed experimentally by Jonietz et al. [33] in 2010, who observed the current-induced rotation of a skyrmion lattice. They found that the currents required to depin the skyrmions were around five orders of magnitude lower than those required to set domain walls in motion. Translational motion of skyrmions was later observed by Yu et al. [233] using LTEM. In this Chapter we discuss the fundamentals of current-driven skyrmion motion, before considering the specific case of skyrmions in a cycloidal background.

9.1. Fundamentals of Current-Driven Motion of Skyrmions

As discussed in Chapter 4, the current-driven dynamics of arbitrary² magnetic textures can be modelled by integrating (4.21). When studying the current-driven dynamics of skyrmions, typically only the translational soft modes are of interest, and it is thus often preferable to use collective coordinate modelling, as discussed in Section 4.3. This has the advantage that the computational resources required to solve for the current-driven motion are greatly reduced, as well as that the approximate analytical equations of motion, and hence the motion's underlying mechanisms, are more easily understood than the LLG equation, which involves an infinite number of degrees of freedom.

To obtain the equation of motion of the collective coordinates, in this case the x - and y -position of the skyrmion, we assume that the skyrmions have a rigid structure such that the time-dependent magnetisation dynamics can be written as $\mathbf{m}(\mathbf{r}, t) = \mathbf{m}(\mathbf{r} - \dot{\mathbf{R}}t)$, where $\mathbf{R} = (x, y)$ is the position of the centre of the skyrmion given by

$$\mathbf{R} = \frac{1}{N_{\text{sk}}} \int d^2r \rho_{\text{sk}}(\mathbf{r}) \mathbf{r}, \quad (9.1)$$

¹The dynamics induced by spin-orbit torques is also well-understood [215, 216, 230–232], but is beyond the scope of this Thesis.

²Arbitrary as far as the assumptions made in the micromagnetic model still apply, *e.g.* the characteristic length scales being at least several lattice constants.

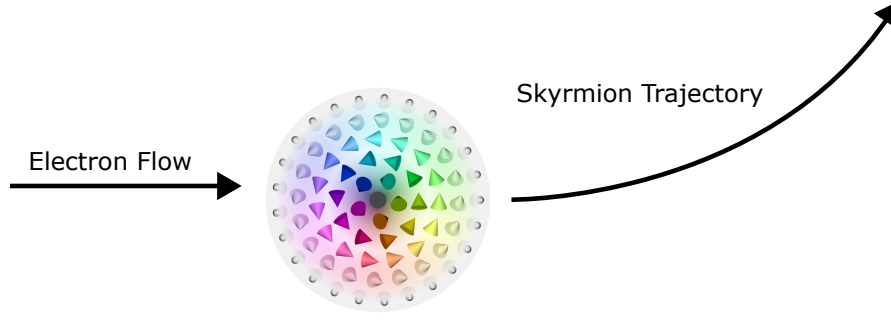


Figure 9.1.: Illustration of the skyrmion Hall effect. Due to the skyrmion’s nonvanishing gyrovector, the skyrmion experiences a force perpendicular to the flow of the spin-polarised electrons in addition to the parallel component. This results in the skyrmion following a curved trajectory.

where $\rho_{\text{sk}} = \mathbf{m} \cdot (\partial_x \mathbf{m} \times \partial_y \mathbf{m})/4\pi$. In this discussion, we work in the dimensionless unit system introduced in Chapter 5. Projecting the LLG equation (7.1) along $\mathbf{m} \times \partial_x \mathbf{m}$ and $\mathbf{m} \times \partial_y \mathbf{m}$ gives the Thiele equation of motion

$$\mathcal{G} \times (\mathbf{v}_s - \dot{\mathbf{R}}) + \Gamma(\beta \mathbf{v}_s - \alpha \dot{\mathbf{R}}) + \mathbf{F} = \mathbf{0}, \quad (9.2)$$

where $\mathcal{G} = 4\pi N_{\text{sk}} \hat{\mathbf{z}}$ is the gyrovector, analogous to (4.25b), Γ is the dissipative tensor³ given by (4.25c), which, in the dimensionless units introduced in Chapter 7, becomes $\Gamma_{ij} = \int d^2r \partial_x \mathbf{m} \cdot \partial_y \mathbf{m}$, and $\mathbf{F} = -\partial_x U[\mathbf{m}(\mathbf{r})] \hat{\mathbf{x}} - \partial_y U[\mathbf{m}(\mathbf{r})] \hat{\mathbf{y}}$ is the force resulting from spatial variations in the energy functional. For low current densities, the current-induced forces are cancelled out by the pinning forces, while at higher currents, the skyrmion undergoes translational motion. The first term in (9.2) represents a Magnus force term, which results in a component of the skyrmion’s velocity perpendicular to the applied current, illustrated in Fig. 9.1. This is somewhat analogous to the Magnus force experienced by a football that is spinning as it flies through the air [155], and can be understood as a counter-force to the force on the conduction electrons resulting due to the emergent magnetic fields mentioned in Section 4.2. The second term, involving the dissipative tensor, captures the force pushing the skyrmion in the direction of the spin current.

The Magnus force is responsible for the skyrmion Hall effect, which is generally viewed as detrimental. This is because it complicates the current-driven motion of skyrmions in device applications, such as in skyrmion racetrack memory. The existence of a nonzero angle between the current direction and the direction of motion of the skyrmion is known as the skyrmion Hall effect. Various methods have been proposed to overcome it, including coupling skyrmions of opposite polarity in bilayers [234], engineering the potential at the edges of the racetrack [235–238], using in-plane- [216] and antiskyrmions [239], using hybrid bulk and interfacial DMI [240], and using curved tracks with field gradients [241]. In some contexts, the skyrmion Hall effect is viewed as advantageous, where it is exploited in combination with the device geometry to produce a ratchet motion [242]. A further method could be to exploit the natural confinement of skyrmions

³In the context of Thiele modelling of the translational modes of skyrmions, Γ is often written as \mathcal{D} , but we keep our notation consistent with that in Section 4.3.

to the lanes of a spin spiral background, which is the subject of the rest of this Chapter. In this context, it has been proposed that skyrmions in different lanes could be used to encode bits by, for example, a skyrmion in one lane representing a ‘1’ and in another lane, a ‘0’ [223]. Much of the content of the following Section was published in our paper Ref. [191]. The current-driven creation of skyrmions in the helimagnet FeGe has since been experimentally demonstrated [243], and the current-driven motion of iSkS has been discussed in a recent preprint [244]. In the next Section, we study the current-driven dynamics of skyrmions in the cycloidal background.

9.2. Current-Driven Motion of Skyrmions in the Cycloidal State

In the derivation of (9.2), no assumptions were made about the specific structure of the skyrmions or the background except for the rigidity of the skyrmions, meaning that the equation can also be applied to the case of interstitial and H-shaped skyrmions in a cycloidal background. Assuming now that \mathbf{F} acts to constrain the skyrmion to move along the direction of the cycloidal stripes, *i.e.* the x -direction, (9.2) becomes

$$\dot{\mathbf{R}} = \left(\frac{4\pi(\mathbf{v}_s \cdot \hat{\mathbf{y}})}{\alpha\Gamma_{xx}} + \frac{\beta}{\alpha}\mathbf{v}_s \cdot \frac{\Gamma_{xx}\hat{\mathbf{x}} + \Gamma_{xy}\hat{\mathbf{y}}}{\Gamma_{xx}} \right) \hat{\mathbf{x}}. \quad (9.3)$$

For small v_s , the skyrmions do not significantly deform from their rigid shape. Hence, the components of Γ remain approximately constant and the skyrmion speed is linearly proportional to v_s . For $\beta = 0$, only the y -component of \mathbf{v}_s contributes to the skyrmion’s motion. This linearity for small v_s can be seen in Fig. 9.2(a), which shows the HSk and iSk speed as a function of current density. Shown are the skyrmion speeds calculated from both micromagnetics and (9.3), where, in the latter case, the dissipative tensor components Γ_{ij} have been calculated using micromagnetics, shown in Fig. 9.2(c). The deformation of both the iSk and HSk for high currents close to their destabilisation are shown as insets in Fig. 9.2(a). The results for the HSk are shown for a wider range of currents as the iSk is less stable. The iSk collides with the striped background, becoming annihilated, for higher current densities. Shown in Fig. 9.2(b) is the skyrmions’ speed as a function of $1/\alpha$, showing that a higher value of α increases the skyrmion’s speed. The results are approximately linear for low v_s , as predicted by (9.3). For higher drives, the relation between skyrmion speed and applied current strength becomes nonlinear due to the deformation of the skyrmions. Figure 9.3 shows the magnetisation texture from a micromagnetic simulation of the current-driven motion of both iSkS HSkS and iSkS in micromagnetic simulations.

To obtain the skyrmions’ speeds in Figs. 9.2(a) and (c), we calculated the skyrmion’s position using (9.1) numerically, with the skyrmion number density ρ_{sk} calculated in a similar manner as with N_{sk} , discussed in Appendix A. We differentiated this numerically to obtain the skyrmion velocity for a range of different currents. In Figs. 9.2(a) and (c), we set $\alpha = 0.1$. We also ran the simulations with $\alpha = 0.01$ but found that the skyrmions were too unstable in this case. The calculation is performed in the steady-state regime when the skyrmion moves at a constant speed after an initial sinusoidal ramping of the current from zero. In Fig. 9.2(b), α is varied, and current density is kept at $v_s = 2.1 \times 10^{-3}$ for all values of α . The tensor elements shown in Fig. 9.2(c) were calculated numerically

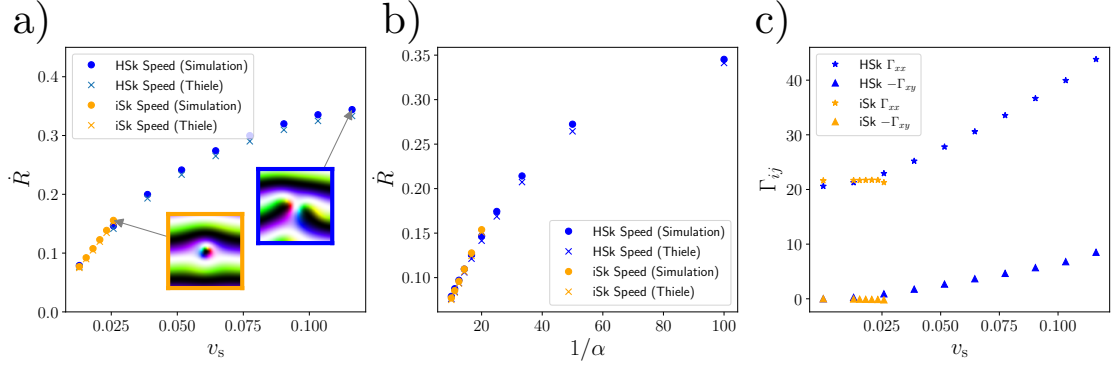


Figure 9.2.: Analysis of skyrmion motion in the cyclodial phase induced by spin-transfer torques. (a) Speed of the H-shaped and interstitial skyrmions as a function of the applied current from both micromagnetic simulations and (9.3), where the dissipative tensor elements Γ_{ij} are calculated from micromagnetics. The insets show both types of skyrmions close to the limits of the current above which they are no longer stable. (b) Speed as a function of inverse damping. In both cases, the relation is linear for small driving currents and becomes sublinear for larger drives. (c) Components of the dissipative tensor as a function of the applied current strength. For this plot, $\kappa \approx 0.31$ and $\beta = 0$. In (a) and (c), $\alpha = 0.1$, and in (b), $v_s \approx 2.1 \times 10^{-3}$. Figure adapted from our publication Ref. [191].

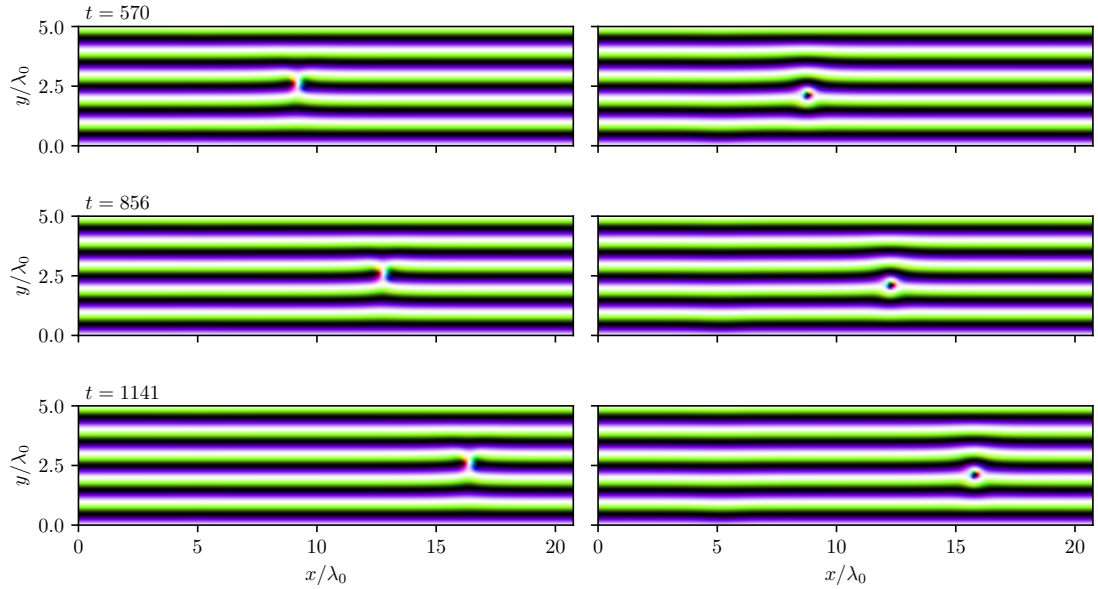


Figure 9.3.: Snapshots of a micromagnetic simulation of the current-driven motion of H-shaped (left) and interstitial (right) skyrmions in a cyclodial background. The current is applied along the y -axis, and the skyrmions move from left to right. Here, $\kappa \approx 0.31$, $\alpha = 0.1$, $\beta = 0$, and $v_s \approx 2.1 \times 10^{-3}$.

9.2. Current-Driven Motion of Skyrmions in the Cycloidal State

from the micromagnetic simulations using a discretised version of (4.25c).

Confinement of skyrmions by the cycloidal background both mitigates the skyrmion Hall effect and results in higher skyrmion speeds for a given applied current [192]. This, combined with our protocol to create skyrmions in the cycloidal state from Chapter 7, is promising for potential applications of skyrmions in data storage and processing. As a final remark, although these results are reported for the case of a cycloidal background with interfacial DMI, the qualitative results are also applicable to a helical⁴ background with bulk DMI, in materials such as FeGe.

⁴In our publication Ref. [191], we used ‘helical’ and ‘cycloidal’ interchangeably. In this Thesis, however, we differentiate between the helical and cycloidal as shown in Fig. 5.2.

Chapter

10

Internal Modes of Skyrmions in Chiral Magnets

In many studies, such as those in Chapter 9, magnetic skyrmions are considered to be rigid textures so that their dynamics can be reduced to their translational motion within the material. However, in numerous studies, interest has been shown in the internal dynamics of skyrmions [245–247]. In this Chapter, we will numerically show that skyrmion eigenmodes can be excited by externally applied magnetic fields oscillating at unit fractions of the eigenfrequencies of a skyrmion. Furthermore, we show that the general theory applies to general topological solitons in magnetism, without the assumption of a specific microscopic structure.

10.1. Skyrmion-Magnon Interactions

Spin waves are collective, low-energy excitations in the ferromagnetic ordering, which are quantised as magnons. Spin excitations have been an area of focus of research interest in the emerging field of magnonics [246, 248], with interest growing in potential applications of spin waves in information transmission, storage, and processing. This can be applied to, for example, logic devices [249, 250] or neuromorphic computing [96, 251]. An advantage of the use of spin waves in computing applications is the lack of an electric current, and therefore energy losses through Joule heating [252]. Furthermore, magnons have tunable frequencies that cover a broad range of values, from the GHz to THz range, with wavelengths from micron to sub-nanometre scales [253], allowing for coupling between microwave electronics and photonics systems. Their ease of manipulation by applied magnetic fields within magnetic nanostructures that allow for re-programming on sub-nanosecond timescales also makes them attractive [254]. Furthermore, the long propagation distances observed with magnons (on the order of centimetres), in comparison with those of spin diffusion, (less than a micron) also make them promising candidates for use in information transfer [249].

For a ferromagnet with symmetric exchange and uniaxial anisotropy, the magnon dispersion relation is $\omega = 2\gamma(K + Aq^2)/M_s$, where q is the magnon wavenumber and the other parameters are as used elsewhere in this Thesis. This can be derived from the LLG equation (4.19) by assuming fluctuations of the form $\sim \exp[i(\mathbf{q} \cdot \mathbf{r} - \omega t)]$ [255]. The anisotropy therefore creates a gap above which a continuum of magnon states exists.

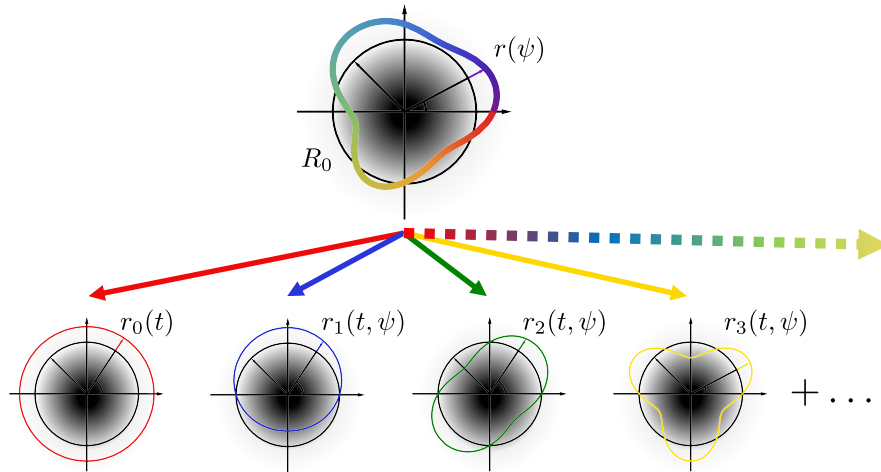


Figure 10.1.: Sketch of the decomposition of a skyrmion's smooth deformation into discrete eigenmodes. Black represents the magnetisation texture going into the page, and white out of it. R_0 is the skyrmion's equilibrium radius, and r_n characterises the various bound modes, where n is an integer characterising the quantised angular momentum. Figure adapted from our publication Ref. [258].

Below the magnon gap, resonance modes of skyrmions are classified by an integer n , representing a quantised angular momentum. The behaviour of these eigenmodes depends on the value of n . $n = 0$ corresponds to a skyrmion's breathing modes, where its centre remains fixed and its radius oscillates. Due to the rotational symmetry of this mode, it couples to an out-of-plane field. $n = \pm 1$ corresponds to gyration modes, where the skyrmion's core rotates. The resonance modes generally become more complex with higher $|n|$, where the sign of n determines whether the rotation is clockwise or anticlockwise. For example, elliptical ($n = \pm 2$) and triangular ($n = \pm 3$) modes form, which break rotational symmetry, and thus couple to in-plane fields [256, 257]. As shown in Fig. 10.1, a general skyrmion excitation can be Fourier-decomposed into individual excitation modes.

The internal dynamics of skyrmions have potential applications in radio frequency devices, such as in spin-torque nano-oscillators (STNOs) [259]. In STNOs, a spin-polarised current applied to a ferromagnetic material results in a self-sustained oscillation, giving a periodic microwave signal. These have been proposed with uniform magnetisation [260], as well as with magnetic vortex textures [261]. More recently, the application of skyrmions in these devices for microwave generation and detection, in place of vortices, has been investigated [55–58]. Skyrmions have the advantage over vortices in that they are localised objects, so more than one can be used per STNO, as well as a lower current density required to induce the oscillations.

Skyrmion resonance modes have been studied using a variety of experimental and theoretical techniques, though the number of experimental studies on this topic remains much lower than the number of theoretical studies at the time of writing this Thesis. This is due to several challenges, such as high damping and inhomogeneities in experimental systems [247]. Resonances of skyrmion lattices were first studied numerically by Mochizuki [256] in 2012, where a breathing mode and two rotational modes (clockwise

and anticlockwise) were identified. This was followed by an experimental study by Onose et al. [257], in which the breathing and rotation modes of a skyrmion crystal in Cu_2OSeO_3 were investigated using the microwave response of the system. Other experimental studies have included employing microwave transmittance spectroscopy [262] and an all-electrical broadband spectroscopy technique [263].

Various theoretical methods have been applied in the study of skyrmion eigenmodes. In many such studies, the LLG equation (4.19) is linearised about a stable equilibrium configuration, recasting it in the frequency domain as an eigenvalue problem [264–268]¹. Some studies investigate the internal dynamics of skyrmions by assuming their structure to be approximated by a closed, thin domain wall string [268, 270–272]. The method that we use in this Chapter to investigate eigenmodes of magnetic skyrmions is the simulation of skyrmion textures to which time-dependent magnetic fields are applied [256, 267, 273, 274], the resulting dynamics of which are analysed. This can be done via the ringdown method [275], in which a cardinal sine pulse is applied to the system. If the drive is an external magnetic field $\mathbf{B}_{\text{ext}}(t)$, this takes the form $\mathbf{B}_{\text{ext}}(t) = \mathbf{B}_{\text{max}} \text{sinc}(2\pi f_c t)$, which is applied for a time t_{app} . As the Fourier transform of the cardinal sine function is the rectangular function, the pulse excites all eigenmodes with a frequency up to the cutoff frequency f_c approximately equally, each with an amplitude of $B^f = |\mathbf{B}_{\text{max}}|/2f_c t_{\text{app}}$, thus allowing the determination of the eigenfrequencies within this frequency range using a single simulation. The spatially resolved power spectrum P_{sr} can be calculated through

$$P_{\text{sr}}(f) = \frac{1}{N} \sum_{j=x,y,z} \sum_{k=1}^N \left| \sum_{l=1}^n \Delta m_j(\mathbf{r}_k, t_l) e^{-2\pi i f t_l} \right|^2, \quad (10.1)$$

where N is the number of cells in the micromagnetic simulation and n is the number of times the magnetisation texture is sampled. This is a Fourier analysis on the time-dependent part of the magnetisation vector field, $\Delta \mathbf{m}(\mathbf{r}_k, t_l) = \mathbf{m}(\mathbf{r}_k, t_l) - \mathbf{m}_0(\mathbf{r}_k)$, where $\mathbf{m}_0(\mathbf{r}_k)$ is the static texture in the absence of $\mathbf{B}_{\text{ext}}(t)$. An example of this is shown in Fig. 10.4(b), where the power spectrum obtained using this method is plotted as a function of frequency.

10.2. Basic Principles of Frequency Multiplication

In frequency multiplication, a periodic signal of frequency ω interacts with a nonlinear system, resulting in the outgoing signal having a component with a frequency that is an integer multiple of ω . A typical example of this is in nonlinear optics, where an electromagnetic wave interacts with a material which has a nonlinear response, producing radiation with double (or, more generally, an integer multiple of) the incident frequency [276]. To elucidate this, we can consider a system whose response $y(t)$ to a signal $x(t)$ has a linear response, with an additional, small quadratic response, $y = ax - bx^2$, where $b < a$. Such a response is illustrated in the graph of y as a function of x in Fig. 10.2, where the linear part is shown in green. If $x(t) = x_0 \cos(\omega t)$ is a

¹This method is implemented in some micromagnetic codes, such as the finite-element package **FinMag** [269].

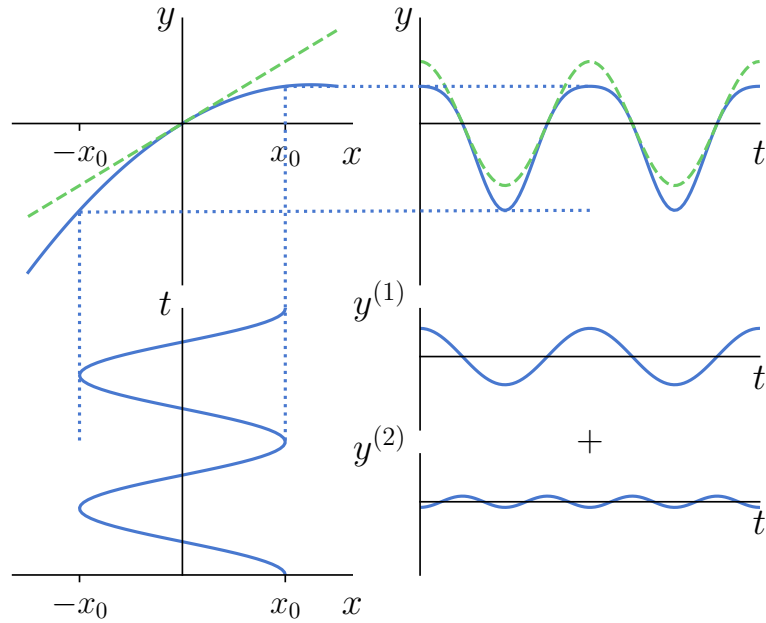


Figure 10.2.: Sketch of the frequency doubling of a signal by a nonlinear system with a quadratic response. If a signal with frequency ω is fed into the system, the nonlinearity results in an output signal composed of a linear combination of a signal with the input frequency and a frequency-doubled signal.

sinusoidal signal, the response has the form

$$\begin{aligned} y &= ax_0 \cos(\omega t) - bx_0^2 \cos^2(\omega t) \\ &= ax_0 \cos(\omega t) - \frac{bx_0^2}{2} [1 + \cos(2\omega t)]. \end{aligned} \quad (10.2)$$

This yields an output, shown in the top-right of Fig. 10.2, to an input shown in the bottom-left, that deviates from the linear sinusoidal response shown in green. As illustrated in the bottom-right of the figure, this can be decomposed into a first-order term $y^{(1)}(t) = ax_0 \cos(\omega t)$ and a second-order, frequency-doubled term $y^{(2)}(t) = -bx_0^2 \cos(2\omega t)/2$ (and a constant term $y^{(0)} = -bx_0^2/2$). We note that this quadratic case is a simple illustrative example and that nonlinear systems are typically much more complicated, with many higher order modes, resulting in responses with frequencies of higher integer multiples of the input frequency. Frequency multiplication has a wide range of applications, including in communications systems [277, 278] and medical imaging [279].

In this Chapter, we consider the frequency multiplication of magnons using skyrmions. The magnon spectrum is modified in the presence of a skyrmion, which represents a confining potential, supporting localised modes below the anisotropy gap [265]. Magnons can be created through parametric pumping, which is the periodic variation of a parameter of a system to inject energy. An everyday example of parametric pumping is a child on a playground swing where the child sustains the oscillations by periodically folding and extending their legs. This varies the moment of inertia of the system, leading to a self-sustained oscillation. In a magnetic system, parallel parametric pumping

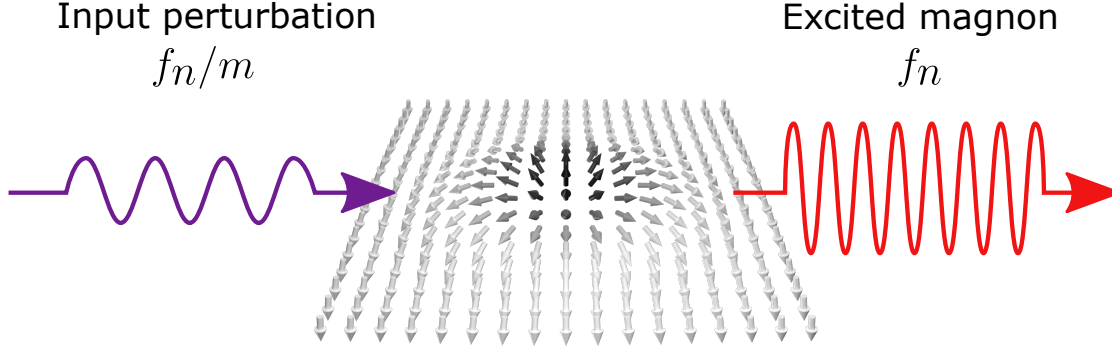


Figure 10.3.: Illustration of frequency multiplication using a magnetic skyrmion texture. Eigenmodes with eigenfrequency f_n can be excited with an input signal at a unit fraction of the eigenfrequency f_n/m , where m is an integer, resulting in an output signal at the eigenfrequency, thus multiplying the frequency of the input signal. Figure adapted from our publication Ref. [258].

(parallel referring to the applied field being parallel to the ferromagnetic background) using an applied oscillating magnetic field is a common method of producing spin wave excitations [280, 281]. We consider parallel parametric pumping of magnetic skyrmion textures to create skyrmion-magnon bound states from which magnons are produced with integer multiples of the applied magnetic field frequency. Magnons impinging upon a skyrmion can excite the skyrmion's eigenmodes, leading to skyrmion-magnon bound states [266, 282]. From this, due to the nonlinearity created by the skyrmion, it is possible to excite magnon-skyrmion bound states with frequencies that are integer multiples of the frequency of an applied oscillating magnetic field, such that the skyrmion acts as a frequency multiplier, as illustrated in Fig. 10.3. The results of this study are published in Ref. [258].

10.3. Numerical Study of Skyrmion Frequency Multiplication

To model magnetic skyrmions as frequency multipliers, we consider a chiral magnetic thin film with perpendicular magnetic anisotropy (PMA), such that the energy functional is

$$U[\mathbf{m}(\mathbf{r})] = \int d^3r [A(\nabla\mathbf{m})^2 - D\mathbf{m} \cdot [(\hat{\mathbf{z}} \times \nabla) \times \mathbf{m}] + K(1 - m_z^2)], \quad (10.3)$$

where A is the exchange interaction strength, D is the Dzyaloshinskii-Moriya interaction strength, and K is the uniaxial anisotropy strength. The film's normal is along the z -direction. We restrict the DMI strength $D < D_c = 4\sqrt{AK}/\pi$, such that the ferromagnetic state is the ground state [196]. We consider an additional Zeeman term

$$U_Z = -M_s \int d^3r \mathbf{B}_{\text{ext}}(t) \cdot \mathbf{m}, \quad (10.4)$$

where $\mathbf{B}_{\text{ext}}(t)$ is the time-varying applied magnetic field². In our investigation, we use $A = 1.6 \times 10^{-11} \text{ J m}^{-1}$, $K = 5.1 \times 10^5 \text{ J m}^{-3}$, and $M_s = 1.1 \times 10^6 \text{ A m}^{-1}$, which correspond to Pt/Co/AlO_x samples [196, 268]. Unless otherwise stated, the Gilbert damping parameter $\alpha = 10^{-3}$. Dipole-dipole interactions are approximated by a modification to the PMA strength $K = K_u - \mu_0 M_s^2 / 2$ [134] where K_u is the uniaxial anisotropy strength of the material.

For the skyrmions in this system stabilised by PMA in the absence of an externally applied magnetic field, most modes exist only below the magnon gap for D close to D_c [268, 271]. We thus perform ringdown simulations on the skyrmion for a range of values of D , shown in Fig. 10.4. Figure 10.4(a) shows the frequency of the various excitation modes with quantised angular momenta $0 \leq n \leq 3$ as a function of the DMI strength. An example frequency spectrum from which the mode frequencies were extracted is shown for $D = 0.86D_c$ in Fig. 10.4(b). We note that an out-of-plane external magnetic field only excites the radially symmetric breathing mode, while an in-plane field can excite all modes with an eigenvalue below the cutoff frequency, and thus an in-plane field is used. This takes the form $\mathbf{B}_{\text{ext}}(t) = B_{\text{max}} \text{sinc}(2\pi ft) \hat{\mathbf{x}}$, where $B_{\text{max}} = 0.05 \text{ T}$. As we experienced some difficulty in exciting all of the modes with a single frequency f , a train of pulses was used, with frequencies 25 GHz, 50 GHz, 100 GHz, 200 GHz, and 500 GHz, with each pulse applied for a time window of 2 ns and its peak at the centre of each window. Following the application of the pulse train, the texture was allowed to evolve for 20 ns to allow oscillations not corresponding to the eigenmodes to dampen out, which decay much more quickly than eigenmodes, to dampen out, before sampling the texture for a further 10 ns at 0.01 ns intervals. The power spectra, an example of which is shown in Fig. 10.4(b), were obtained from the magnetic texture using (10.1), and the eigenfrequencies were extracted from this using the `find_peaks` function of SciPy [283].

We now turn our attention to excitations induced using pure sinusoidal pulses, $\mathbf{B}_{\text{ext}}(t) = B_{\text{max}} \sin(2\pi ft) \hat{\mathbf{x}}$. Shown in the black curve of Fig. 10.5 is the frequency response of a skyrmion to a sinusoidal pulse at half the breathing mode ($n = 0$) eigenfrequency: $f = f_0/2 = 3.6 \text{ GHz}$, and the frequency response to a pulse with a frequency slightly off this frequency, $f = 3.3 \text{ GHz}$, is shown in the grey curve. In contrast to the case of applying a cardinal sine pulse where all eigenmodes are excited approximately equally, a sine pulse predominantly excites the mode at the frequency of the pulse, as well as integer multiples thereof (harmonics). The excitation of modes at frequencies that are integer multiples of that of the applied pulse is due to the nonlinearity of the potential created by the skyrmion. For $f = f_0/2$, the frequency-doubled harmonic coincides with the breathing mode eigenfrequency, resulting in a resonance at frequency f_0 (the vertical red line). The amplitude of the harmonic is greater than the response at the applied frequency itself, which we explore in the following.

We now focus on the breathing ($n = 0$) and elliptical ($n = 2$) modes. These have eigenfrequencies f_0 and f_2 respectively. Shown in Fig. 10.6 are the time-averaged displacements of the skyrmion radii $r_{0,2}(t)$ from their equilibrium radii R_0 , $r_{0,2} = \langle r_{0,2}(t) - R_0 \rangle_t$, as a function of the frequency of the sine pulse f . As the modes are not symmetric in general

²In our publication Ref. [258], the frequencies reported in discussions of numerical results are out by a factor of 2π . For example, where a frequency ω_0 is applied, the field in the `MuMax3` script is $\sim \cos(2\pi\omega_0 t)$ instead of $\cos(\omega_0 t)$. In this Thesis, we use f to denote frequencies in both the text and the figures, *e.g.* if a field of frequency f is applied, it has the time dependence $\sim \cos(2\pi ft)$.

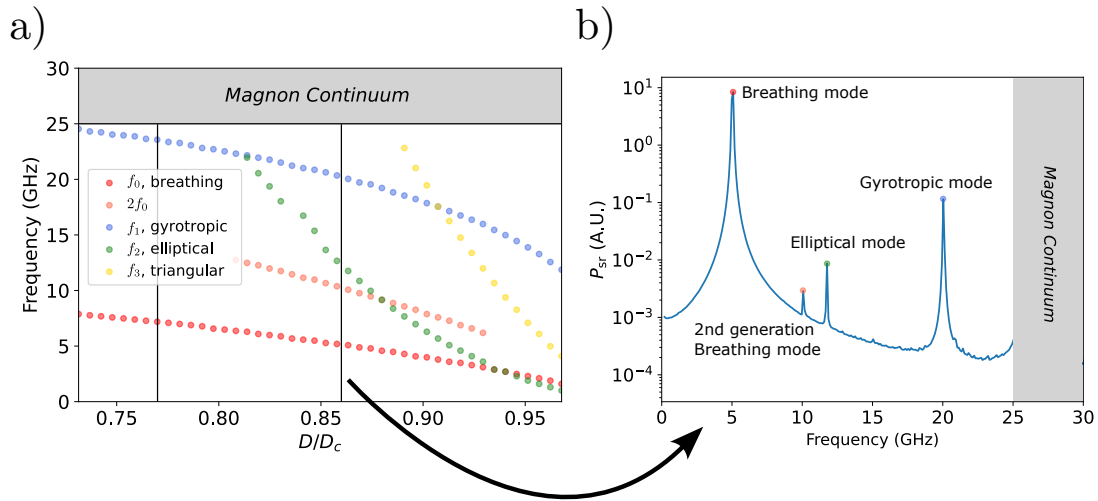


Figure 10.4.: Frequency analysis of the eigenmodes of a Néel skyrmion. (a) Frequencies of the various eigenmodes with quantised angular momenta $0 \leq n \leq 3$ as a function of the DMI strength. (b) Detailed analysis of the power spectrum for a fixed DMI strength of $D/D_c = 0.86$ obtained using (10.1). Figure adapted from our publication Ref. [258].

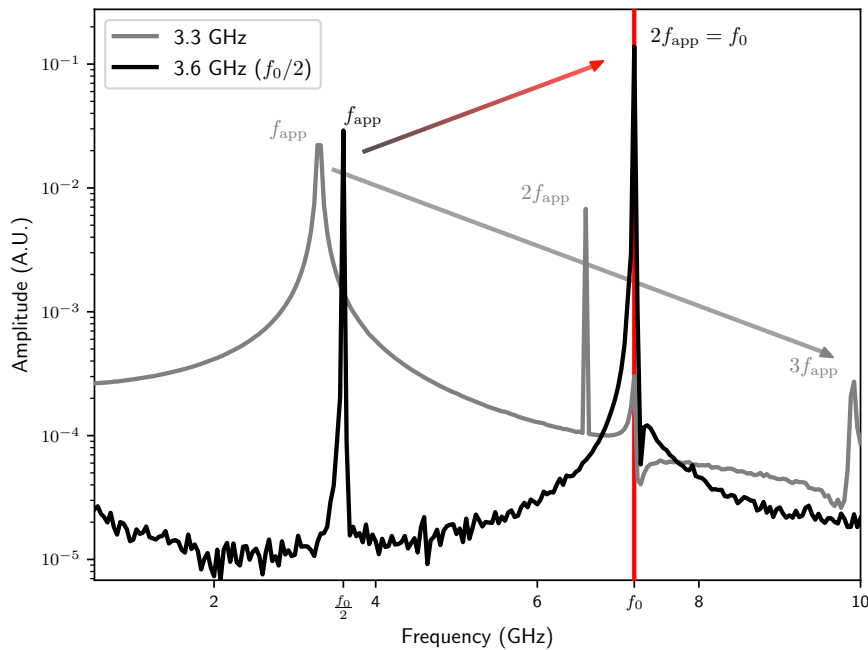


Figure 10.5.: Example of the general principles of the excitation of a magnetic texture by frequency multiplication. The excitation of a skyrmion texture by oscillating magnetic fields with an amplitude of 5 mT is shown for an applied frequency f_{app} at half the breathing mode frequency f_0 (in black) and at slightly less than half of f_0 in grey. For the case that $f_{app} = f_0/2$, there is a resonance and the corresponding multiple has a higher amplitude. Figure adapted from our publication Ref. [258].

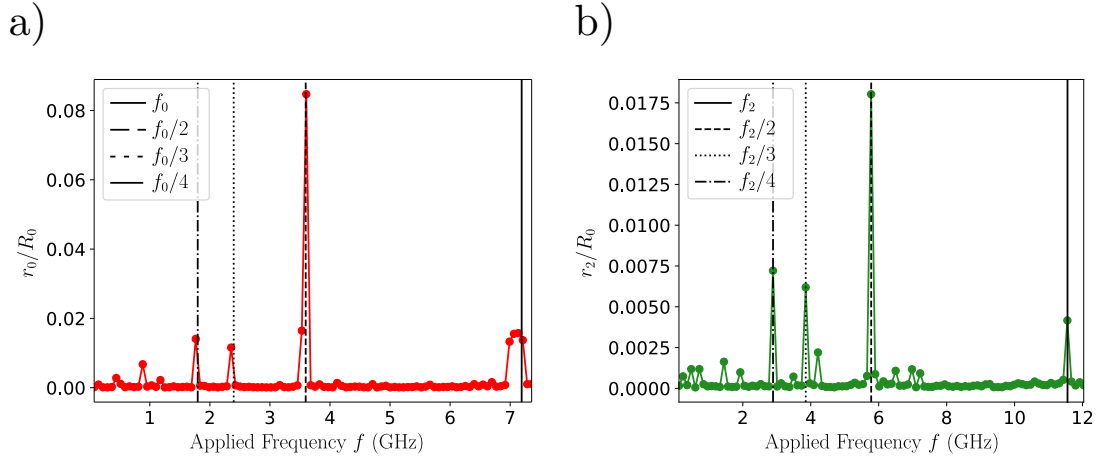


Figure 10.6.: Amplitude of the (a) breathing and (b) elliptical modes (with frequencies f_0 and f_2 respectively) as a function of the frequency of the in-plane applied field with amplitude 50 mT. We use a Gilbert damping constant of $\alpha = 10^{-3}$. Fractions of the eigenfrequencies can still strongly excite the corresponding eigenmodes. Figure adapted from our publication Ref. [258].

(the exception being the $n = 0$ breathing mode), the average is taken after the Fourier transform is calculated. The skyrmion radii are calculated using the `find_contours` function of `scikit-image` [284] to calculate contours of constant $m_z = 0.5$. The skyrmion's centroid is extracted by calculating the median of the contour and the radii are calculated by taking the distance from points on the contour to the centroid. As before, $B_{\max} = 50$ mT. The DMI strength is chosen for each simulation for the values of the D in Fig. 10.4 for which the magnon amplitudes were the highest, which were $0.77D_c$ for the breathing mode and $0.86D_c$ for the elliptical mode. An interesting result is that resonance is not only observed when the applied frequency is equal to the eigenfrequency f_0 and f_2 of the breathing and elliptical mode respectively but also at unit fractions $f = f_{0,2}/n$, $n \in \mathbb{Z}$, of the eigenfrequencies. We also observed this behaviour for the $n = 3$ triangular mode.

As the Gilbert damping is viscous, such that the rate of energy dissipation is proportional to $\partial_t \mathbf{m}$, perturbations of higher frequency are more strongly damped than those of lower frequency. This suggests that the frequency multiplication uncovered in this work can provide a method to excite skyrmion eigenmodes more efficiently than by simply applying the perturbing field at the eigenfrequency. A further advantage is that lower frequencies are more experimentally accessible. To gain a better understanding of the conditions for which the excitation of the eigenmodes using a perturbing field at unit fractions of the eigenfrequency is more efficient than at the eigenfrequency itself, we plot the breathing mode magnon amplitude as a function of the amplitude of a sinusoidal out-of-plane magnetic field pulse in Fig. 10.7. Shown in red are the amplitudes of the breathing modes, while the points in black correspond to oscillations at the forcing frequency. Shown on the right-hand side are the power spectra for $B_{\max} = 0.01$ T. Also shown are lines with slopes of 2 and 3 for applied frequencies at $f_0/2$ and $f_0/3$ respectively, demonstrating that the amplitude of the breathing mode grows with a power of 2 for $f = f_0/2$ and 3 for $f = f_0/3$, a phenomenon that will be explored in more detail

in Section 10.4. The amplitude of magnons at the forcing frequency grows linearly with B_{\max} . An important feature to note is that, above certain values of B_{\max} , the breathing eigenmode is more strongly excited by applied fields at unit fractions of the eigenfrequency than the forced perturbation \tilde{m} . As B_{\max} increases further, the linearity breaks down, as higher-order magnon scattering occurs. Also shown in Fig. 10.7 is the dependence of the magnon amplitudes of the eigenmodes and those at the forcing frequency for applied frequencies of $f_0/2$ and $f_0/3$ as a function of the damping parameter α . This shows that the forced perturbation amplitude is independent of damping, while r_0 decreases with damping. Thus, the presence of Gilbert damping causes a transfer of energy from the forced perturbation to the resonance mode, resulting in a decrease in the resonance mode. Therefore, higher damping reduces the efficiency of frequency multiplication.

10.4. Generalisation to Arbitrary Magnetic Structures

The principles explored in the previous Section for the specific case of magnetic skyrmions are generalisable to other topological magnetic textures such as magnetic vortices. Considering a field in a nonlinear system $\phi(\mathbf{r}, t)$ with small perturbations $\tilde{\phi}$ such that $\tilde{\phi} \ll \phi$, we can Taylor-expand about the ground state $\phi_0(\mathbf{r})$,

$$\frac{\partial \tilde{\phi}}{\partial t} = \mathcal{L}_1(\phi_0)\tilde{\phi} + \mathcal{L}_2(\phi_0)\tilde{\phi}^2 + \dots + \mathcal{L}_p(\phi_0)\tilde{\phi}^p + \dots, \quad (10.5)$$

where the \mathcal{L}_k are the Taylor expansion coefficients. $\mathcal{L}_1\tilde{\phi}$ is a linear approximation for the generally nonlinear system, which determines the eigenstates with eigenfrequencies ω_n , while the terms $\mathcal{L}_k\tilde{\phi}^k$ represent interactions between perturbations. To see how the terms $k > 1$ lead to frequency multiplication, we can consider a perturbation with a fraction of an eigenfrequency $\tilde{\phi}(t) \approx \phi_{\omega_n/2} \cos(\omega_n t/2)$. The quadratic term is then $\tilde{\phi}(t)^2 \approx \phi_{\omega_n/2}^2 [1 + \cos(\omega_n t)]/2$, *i.e.* a frequency-doubled term with an amplitude reduced by a factor of 2. This principle can be generalised to higher order terms, such that perturbations applied with unit fractions of eigenfrequencies ω_n excite the corresponding eigenmodes, where the amplitude of the eigenmode grows with the m th power of the driving amplitude with frequency ω_n/m . We also note that (10.5) is independent of the amplitude of the perturbation.

We generalise the results of the previous section to an arbitrary magnetic texture $\mathbf{m}(\mathbf{r}, t) = \mathbf{m}_0(\mathbf{r}) + \delta\mathbf{m}(\mathbf{r}, t)$, where $|\delta\mathbf{m}| \ll 1$ and $\delta\mathbf{m} \perp \mathbf{m}_0$, where \mathbf{m}_0 is the relaxed texture and $\delta\mathbf{m}$ is a perturbation behaving as an underdamped travelling wave

$$\delta\mathbf{m} = \phi_1(\rho, \psi, t)[\mathbf{m}_0 \times \hat{\mathbf{n}}] + \phi_2(\rho, \psi, t)[(\mathbf{m}_0 \times \hat{\mathbf{n}}) \times \mathbf{m}_0], \quad (10.6)$$

where ρ and ψ are the radial and angular polar coordinates, and $\hat{\mathbf{n}}$ is the direction of the field-polarised background. We consider a Fourier expansion of the perturbation in terms of eigenmodes n of the topological object of the form

$$\phi_i(r, \psi, t) = \sum_n \phi_{in}(r)\phi_n(r, n\psi - \omega_n t). \quad (10.7)$$

In this general framework, a perturbation can excite any mode with nonvanishing $\phi_{in}(r)$

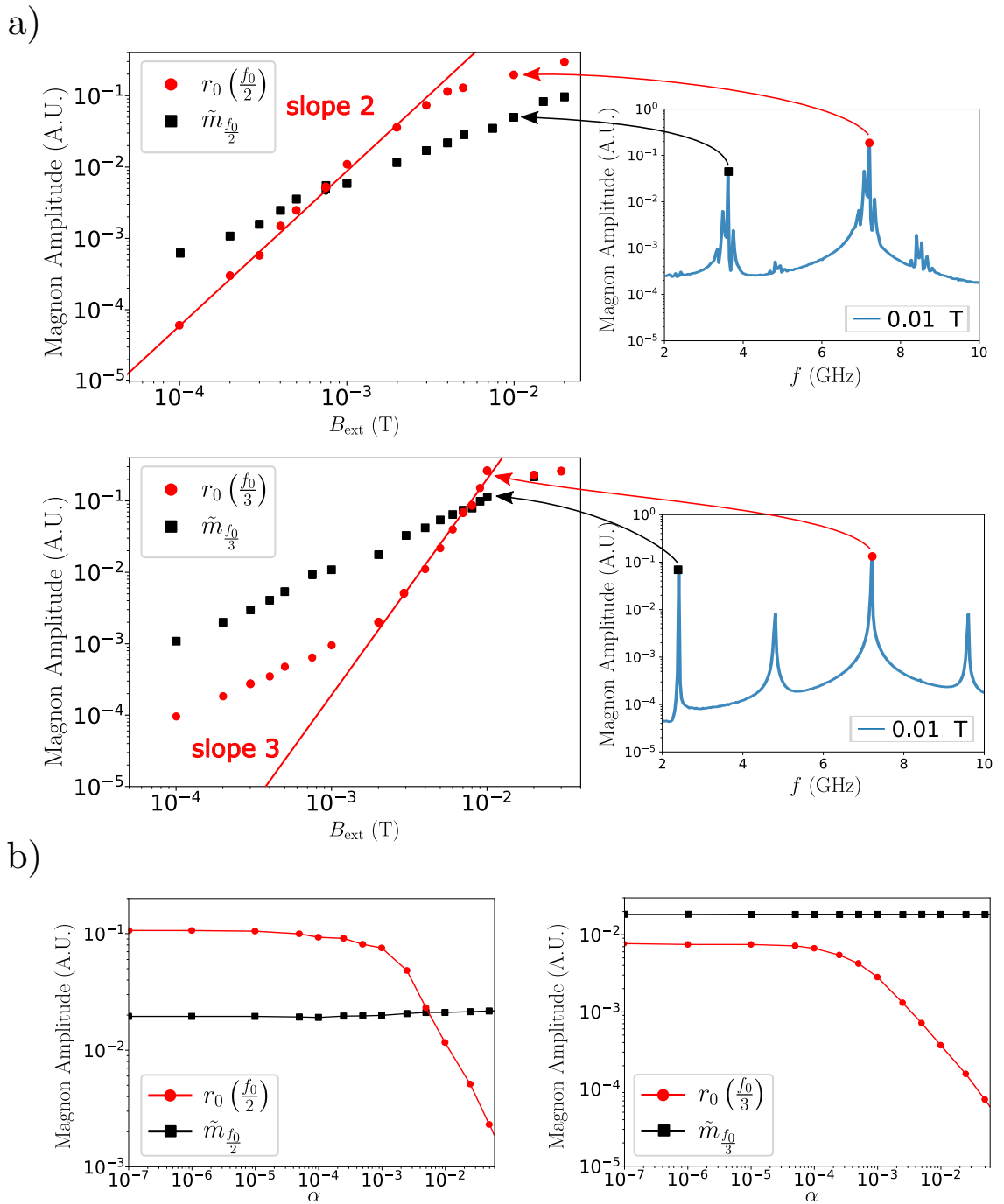


Figure 10.7.: Amplitudes of both the breathing mode r_0 and the forced perturbation \tilde{m} as a function of (a) amplitude of the applied magnetic field with $\alpha = 10^{-3}$ and (b) damping parameter for an AC magnetic field with amplitude 3 mT, excited with an out-of-plane oscillating magnetic field. In (a), straight lines with a slope of 2 and 3 indicate growth with a power of 2 and 3 for the second and third harmonic generation. Above a certain amplitude of the applied field, the eigenmode is more excited than the mode with the same frequency as the perturbation. Figure adapted from our publication Ref. [258].

10.4. Generalisation to Arbitrary Magnetic Structures

via frequency multiplication, where the principle that higher driving forces increase the amplitudes ϕ_{in} also applies generally.

In summary, we have demonstrated that, using the nonlinear properties of topological solitons in magnetic materials, it is possible to efficiently excite eigenmodes by applying oscillating magnetic fields with frequencies of unit fractions of the mode eigenfrequencies. We have demonstrated this numerically using the example of magnetic skyrmions, but our theoretical analysis in the limit of small perturbations without the assumption of a specific microscopic structure reveals that this can be applied to more general structures. This has potential applications in magnonics where the existence of such magnetic structures could be used for *in materia* frequency multiplication, as well as in other areas such as unconventional computing [285].

Chapter

11

Electric Field-Driven Dynamics of Skyrmions in Frustrated Magnets

Much of the research focus into magnetic skyrmions has been on the case where they are stabilised by competing symmetric exchange and Dzyaloshinskii-Moriya interactions, discussed in Section 5.1. As discussed in Section 5.4, however, skyrmions can also be stabilised by competing symmetric exchange interactions of different orders, in so-called frustrated magnets. In contrast to chiral magnets, in frustrated magnets, no specific helicity of the skyrmion is energetically favoured, such that it is a zero, or Goldstone, mode¹. This means that the helicity can be more easily rotated than in chiral magnets, a phenomenon which has been investigated in various theoretical studies. For example, it has been found that applying a perpendicular current to a skyrmion in a thin film of a frustrated magnetic material leads to a rotation of the skyrmion's helicity [119, 203]. In this Chapter, we consider the case of a static applied magnetic field perpendicular to the thin film (which serves to stabilise the ferromagnetic background) and an oscillating applied electric field. Furthermore, we propose a topological interpretation in (2 + 1)D spacetime in terms of the Hopf index, creating a 'spacetime magnetic hopfion'. The results of this Chapter are reported in Ref. [286].

11.1. Dynamics of Skyrmions in Frustrated Magnets

In this Chapter, we model skyrmions in a frustrated magnet with the energy functional (5.13), with the additional application of an externally applied electric field. As discussed in Section 4.1, an externally applied electric field can couple with the polarisation that is induced as a result of non-collinear magnetic textures (such as skyrmions) in frustrated magnets. We can model an external electric field \mathbf{E}_{ext} applied to a frustrated magnet with the energy functional

$$U[\mathbf{m}(\mathbf{r})] = \int d^3r \left[-\frac{I_1}{2}(\nabla\mathbf{m})^2 + \frac{I_2}{2}(\nabla^2\mathbf{m})^2 - M_s\mathbf{B}_{\text{ext}} \cdot \mathbf{m} - \mathbf{E}_{\text{ext}} \cdot \mathbf{P} \right]. \quad (11.1)$$

¹We assume that the dipole-dipole interactions (which weakly favour Bloch-type skyrmions) lead to a renormalisation of the other parameters and that the difference between the renormalisation and the true magnetostatics is small.

Characteristic	Definition	SI Unit
Length	$\sqrt{I_2/I_1}$	m
Time	$M_s I_2 / \gamma I_1^2$	s
Energy	$\sqrt{I_1 I_2}$	J
External Magnetic Field	$I_1^2 / M_s I_2$	T
External Electric Field	$(\gamma / M_s^2) \sqrt{I_1^7 / I_2^3}$	V m ⁻¹
Electric Polarisation	$(M_s^2 / \gamma) \sqrt{I_2 / I_1^3}$	C m ⁻²

Table 11.1.: Summary of natural units used in our study of the dynamics of skyrmions in frustrated magnets.

To reduce the number of free parameters of the theory, it is convenient to rescale our units by the quantities in Table 11.1 to work with dimensionless quantities. The energy functional in terms of the rescaled quantities is

$$\tilde{U}[\mathbf{m}(\tilde{\mathbf{r}})] = \int d^3\tilde{\mathbf{r}} \left[-\frac{1}{2}(\tilde{\nabla}\mathbf{m})^2 + \frac{1}{2}(\tilde{\nabla}^2\mathbf{m})^2 - \tilde{\mathbf{B}}_{\text{ext}} \cdot \mathbf{m} - \tilde{\mathbf{E}}_{\text{ext}} \cdot \tilde{\mathbf{P}} \right], \quad (11.2)$$

which has just the two dimensionless free parameters $\tilde{\mathbf{B}}_{\text{ext}}$ and $\tilde{\mathbf{E}}_{\text{ext}}$. For the remainder of this Chapter, we work in dimensionless units and drop the tildes for convenience. As discussed in Section 4.1, the electric field-polarisation coupling term is of the form of a DMI that is tunable by manipulating the applied electric field. In this Chapter, we consider a skyrmion in a frustrated magnet subject to a sinusoidal electric field² with a period T applied perpendicular to the thin film, given by $\mathbf{E}_{\text{ext}} = E_0 \cos(\omega t) \hat{\mathbf{z}}$, where $\omega = 2\pi/T$ and E_0 is its amplitude.

For the investigation of the behaviour of skyrmions in a frustrated magnet in a broad parameter space, the numerical solution of the LLG equation (4.19) in the micromagnetic model becomes impractical. We therefore make use of collective coordinate modelling, discussed in Section 4.3. Using this, we reduce our problem from an infinite number of degrees of freedom to just two degrees of freedom: the skyrmion's radius R , *i.e.* the radial distance between the skyrmion's centre where $m_z = -1$ and the contour on which $m_z = 0$, and its helicity η . As such, we assume that the skyrmion can be approximated as being perfectly circular and that its magnetisation $\mathbf{m} = (\cos \Phi \sin \Theta, \sin \Phi \sin \Theta, \cos \Theta)$ can be described by the ansatz [287, 288]

$$\Theta = 2 \arctan \left(\frac{\sinh[R(t)/w]}{\sinh(\rho/w)} \right), \quad (11.3a)$$

$$\Phi = \psi + \eta(t), \quad (11.3b)$$

where $\rho = \sqrt{x^2 + y^2}$ and $\psi = \arctan(y/x)$ are the radial and angular polar coordinates respectively, with the skyrmion's $m_z = -1$ at $x = y = 0$. w is the domain wall width, which we take to be 1.4 throughout this work. To determine this value, we relaxed a skyrmion in MuMax3 and fitted the resulting profile of m_z to (11.3a). We also confirmed that the width which minimised the energy for a given radius did not vary significantly for the variations of radii seen in our work.

²Although Maxwell's equations state that a time-varying electric field induces a magnetic field, this induced field is so small in comparison with the other energy terms at play that it need not be considered.

11.1. Dynamics of Skyrmions in Frustrated Magnets

The equation of the collective coordinates R and η become, when substituted into (4.24),

$$\begin{bmatrix} \dot{R} \\ \dot{\eta} \end{bmatrix} = \frac{1}{G_{R\eta}^2 + \alpha^2 \Gamma_{RR} \Gamma_{\eta\eta}} \begin{bmatrix} \alpha \Gamma_{\eta\eta} F_R + G_{R\eta} F_\eta \\ -G_{R\eta} F_R + \alpha \Gamma_{RR} F_\eta \end{bmatrix}, \quad (11.4)$$

where, in our ansatz (11.3), the gyrotropic and dissipative tensors are

$$G_{R\eta} = 2\pi d \int_0^\infty d\rho \sin \Theta \frac{\partial \Theta}{\partial R}, \quad (11.5a)$$

$$\Gamma_{RR} = 2\pi d \int_0^\infty d\rho \left(\frac{\partial \Theta}{\partial R} \right)^2, \quad (11.5b)$$

$$\Gamma_{\eta\eta} = 2\pi d \int_0^\infty d\rho \sin^2 \Theta. \quad (11.5c)$$

Here, d is the thickness of the thin film (the profile is assumed to be uniform along the axis normal to the film) and the factor of 2π results from the integration over the polar coordinate ψ . The generalised forces are

$$\begin{aligned} F_R = 2\pi d E_0 \cos(\omega t) \cos \eta \int_0^\infty \left[\cos(2\Theta) \frac{\partial \Theta}{\partial R} + \rho \frac{\partial^2 \Theta}{\partial R \partial \rho} \right] d\rho \\ - \frac{\partial U_{\text{ex}}}{\partial R} - 2\pi d B_{\text{ext}} \int_0^\infty \rho \sin \Theta \frac{\partial \Theta}{\partial R} d\rho, \end{aligned} \quad (11.6a)$$

$$F_\eta = -2\pi d E_0 \cos(\omega t) \sin \eta \int_0^\infty \left[\cos \Theta \sin \Theta + \rho \frac{\partial \Theta}{\partial \rho} \right] d\rho, \quad (11.6b)$$

where $U_{\text{ex}} = 2\pi d \int d\rho \left[-\frac{1}{2}(\nabla \mathbf{m})^2 + \frac{1}{2}(\nabla^2 \mathbf{m})^2 \right]$ is the exchange interaction part of (11.2).

The energy landscape (11.2) with zero applied electric field is shown as a function of the collective coordinates R and η , transformed to polar coordinates for ease of interpretation, in Fig. 11.1(a). Here, the Zeeman energy of the background is subtracted, and the resulting energy is represented by ΔU . The U(1) symmetry in η reflects the fact that it is a zero mode. The unphysical ‘horn’ in the energy landscape for small R results from the quartic term within the skyrmion profile approximation (11.3a) for fixed w . The assumption of a fixed w is no longer valid for $R \rightarrow 0$. The divergence in energy for large values of R results from the increase in Zeeman energy. This gives a radius R^* that minimises the total energy at the ‘trough’ in the energy landscape. The effect of the applied electric field is to tilt the energy landscape, breaking the U(1) symmetry of the helicity, illustrated in Fig. 11.1(b). When the electric field is along the $+z$ -direction, the Zeeman energy term proportional to $\cos \eta$ is minimised for $\eta = \pi$, and $\eta = 0$ minimises the energy when the electric field is along the $-z$ -direction. As the field oscillates, the energy landscape rocks back and forth about the $R \cos \eta = 0$ line, injecting energy into the system. At certain values of the amplitude E_0 and angular frequency ω of the electric field, after an initial transient, the skyrmion’s helicity rotates at an angular frequency equal to that of the applied electric field, an example of synchronisation [289]. Snapshots of a micromagnetic simulation illustrating this over a single period of oscillation are shown in Fig. 11.2(a). The corresponding evolution of the energy landscape and the collective coordinates (which agree closely with the micromagnetics) is shown in Fig. 11.2(b). We note that from the Thiele equations (11.4), it is not possible with our model to induce a helicity rotation in the absence of an electric

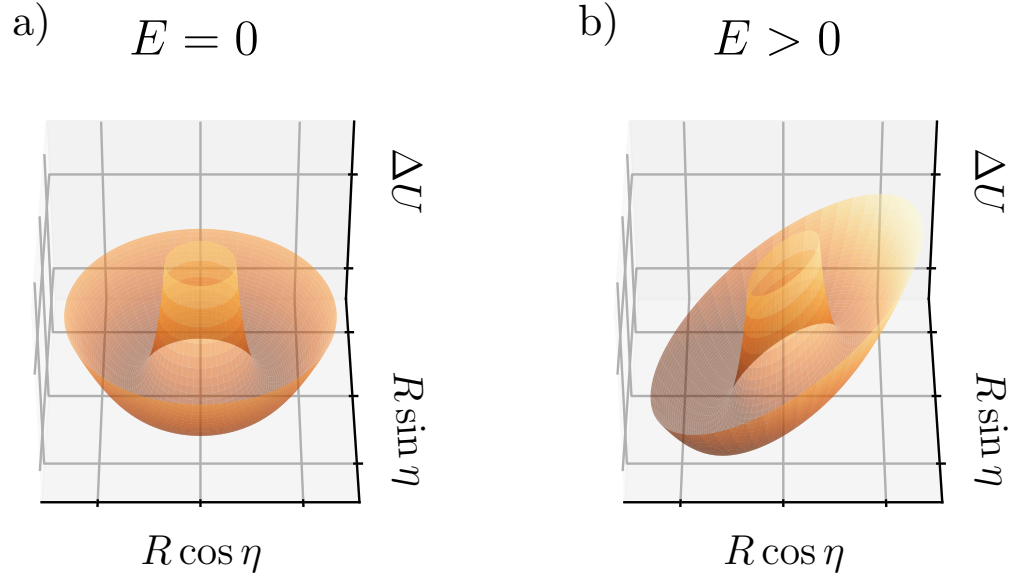


Figure 11.1.: The energy landscape (11.2) in the (a) absence and (b) presence of an electric field along the $+z$ -direction, as a function of the collective coordinate skyrmion radius R and helicity η . The electric field breaks the $U(1)$ symmetry of the energy functional with respect to helicity η .

field. For the helicity rotation to be sustained, sufficient energy must be injected such that it compensates energy losses due to damping and the system has sufficient energy to pass over the saddle point in the energy landscape. An analogous discussion of this in the context of the $U(1)$ symmetry breaking induced by DMI instead of an applied electric field can be found in Ref. [272]. An oscillating magnetic field, for example, results in a back-and-forth oscillation of the skyrmion's helicity, with no overall evolution in one direction. However, we remark that we were able to observe helicity rotations with an oscillating magnetic field in the presence of a static, $U(1)$ symmetry-breaking applied electric field, and speculate that it would also be possible in the presence of DMI instead of an electric field.

An interesting limit of (11.4) is the absence of damping and electric field, the phase portrait of which is shown in Fig. 11.3. In this limit, $\dot{R} = 0$, *i.e.* the skyrmion's radius remains constant. This is because energy is neither absorbed nor dissipated, and energy only depends on the skyrmion's radius in the absence of an applied electric field within our collective coordinate model and not its helicity. The helicity η , however, can still change, and its equation of motion becomes

$$\dot{\eta} = B_{\text{ext}} + \frac{\partial_R U_4 - \partial_R U_2}{G_{R\eta}}, \quad (11.7)$$

where $U_2 = \pi d \int d\rho \rho (\nabla \mathbf{m})^2$ and $U_4 = \pi d \int d\rho \rho (\nabla^2 \mathbf{m})^2$ are the quadratic and quartic order exchange energies respectively. This implies that, for the minimal-energy case that $B_{\text{ext}} = G_{R\eta}^{-1}(\partial_R U_2 - \partial_R U_4)$ (*i.e.* when $F_R = 0$), the helicity does not rotate. $\dot{\eta}$ varies linearly with B_{ext} , rotating clockwise for low B_{ext} and anticlockwise for higher B_{ext} , for a given skyrmion radius. We confirmed this linear relationship using micromagnetic

11.2. Electric Field Amplitude-Frequency Phase Diagram

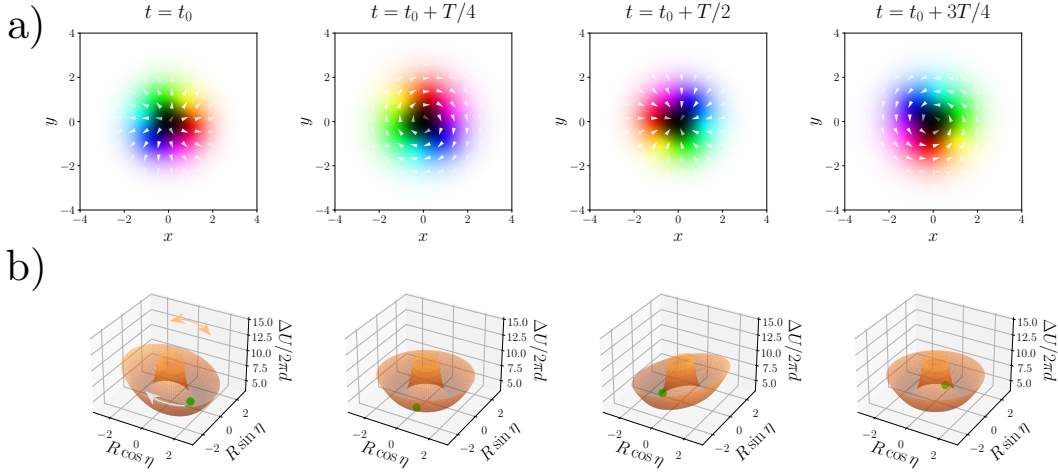


Figure 11.2.: Rotation of a skyrmion's helicity over one period of the applied oscillating electric field. (a) Micromagnetic simulation of the magnetisation texture over one period of helicity rotation. (b) Energy landscape during the evolution, with the Zeeman background subtracted. The green dot shows the time evolution of the collective coordinates. The direction of the helicity rotation is shown by the grey arrow and is determined by the amplitude and frequency of the applied electric field. Here, the parameters used are $E_0 = 0.20$, $\omega = 1.18$, and t_0 is deep in the steady state, with $\eta(t_0) = 0 \pmod{2\pi}$. Figure taken from our publication Ref. [286].

simulations. Alternatively, instead of varying B_{ext} , we can consider fixing it and instead varying the skyrmion's radius R . Then, in Fig. 11.3, we see that the rotation sense changes when crossing the radius of minimum energy R^* . This can also be seen by expanding (11.4) in the limit of small damping α ,

$$\dot{R} = c_1\alpha + E_0 \cos(\omega t) (c_2 + c_3\alpha) + \mathcal{O}(\alpha^2), \quad (11.8a)$$

$$\dot{\eta} = \dot{\eta}_0(R) + E_0 \cos(\omega t) (c_4 + c_5\alpha) + \mathcal{O}(\alpha^2), \quad (11.8b)$$

where c_1, \dots, c_5 are generally functions of the collective coordinates. $\dot{\eta}_0$ is the limit of the helicity's rotation speed in the limit of $E_0 = \alpha = 0$. From these equations, it can be seen that, in this limit, $\dot{R} = 0$, while $\dot{\eta} = \dot{\eta}_0(R)$ is constant, and swaps sign as at $R = R^*$, the value at which it is zero. The dynamics in the presence of an electric field for different values of its amplitude and frequency are explored in the following Section.

11.2. Electric Field Amplitude-Frequency Phase Diagram

In the rescaled model introduced in the previous Section, the free parameters are the externally applied electric field \mathbf{E}_{ext} , specifically its amplitude E_0 and angular frequency ω , the externally applied magnetic field \mathbf{B}_{ext} , and the Gilbert damping parameter α . As previously discussed, we require an externally applied magnetic field with a z -component

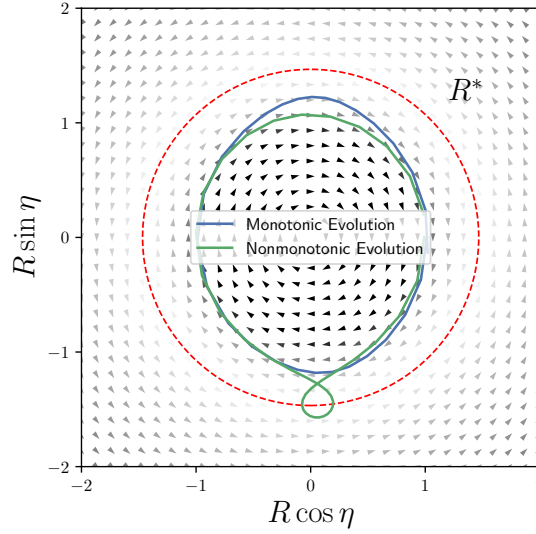


Figure 11.3.: Plot of the vector field (11.4) in the absence of damping and electric field, transformed to polar coordinates. The skyrmion radius R^* for which energy is minimised with zero applied electric field is shown as a red dashed circle, as well as plots of the collective coordinate evolution, both for the case of monotonic evolution where R remains lower than R^* , and where R evolves above R^* during the evolution, causing a temporary reversal in the direction of the helicity evolution.

of magnitude greater than $1/4$ to stabilise the ferromagnetic background. The skyrmion in the frustrated system exhibits interesting dynamics, the qualitative behaviour of which depends on the amplitude and frequency of the applied oscillating electric field. We choose to fix the magnetic field $\mathbf{B}_{\text{ext}} = \hat{z}$. We set the damping parameter $\alpha = 0.01$. To investigate the different regimes of the behaviour of the skyrmion, we integrate (11.4) for $0 \leq E_0 \leq 1.5$ with step size 0.05, and $0 \leq \omega \leq 4$, with step size 0.02. For values of $E_0 \gtrsim 1.5$, we found, using micromagnetics, that the background became destabilised, with the formation of spin spiral textures. The resulting phase diagram from the time integration of (11.4) with varying values of E_0 and ω are shown in Fig. 11.4. The time integration of the collective coordinates for each point is performed up to a dimensionless time of 1000, with an adaptive time step, using the Radau IIA integrator supplied by SciPy [283]. The SageMath code used for the numerical integration of the equations of motion of the collective coordinates (11.4) is given in Appendix F. To avoid computing the integrals $G_{R\eta}$, Γ_{RR} , $\Gamma_{\eta\eta}$, F_R , and F_η , we fit functions of the integrals in the range $0 \leq R \leq 10$. We verified that the error due to this fitting was negligible, in particular, as long as $R \lesssim 50$. To obtain the number of helicity rotations per electric field cycle, we summed up the change in helicity during the evolution and averaged them over all periods for $500 \leq t \leq 1000$, where we start at 500 to avoid the initial transient. The initial conditions are the values of R and η that minimise the total energy at $t = 0$. However, we confirmed that, for different starting conditions, the general long-term behaviour was the same. In order to numerically categorise the points, we classified an anticlockwise (clockwise) rotation as the average helicity rotation being greater than $0.9 \cdot 2\pi$ (less than $0.9 \cdot 2\pi$). In general, however, the points were much closer to 2π than this.

11.2. Electric Field Amplitude-Frequency Phase Diagram

We use **MuMax3** to validate our collective coordinate findings with self-written extensions for the higher-order exchange and electric field-polarisation coupling terms in the energy functional. These **MuMax3** extensions are discussed in Appendix C. We do not include the demagnetising field in the simulations as we consider a minimal model, and its effects are also not considered in the collective coordinate modelling. We did, however, run simulations with the inclusion of the demagnetising field, and found that the same qualitative behaviour was observed for values of M_s that would be found in typical materials. The system considered is a thin film with cubic discretisation cells of edge length $\Delta = 0.3\sqrt{I_2/I_1}$. $N = 128$ cells are used in the x - and y -directions, with a single cell along z . We set the damping $\alpha = 1$ over an area bordering the edges extending 5 simulation cells into the sample on each edge to suppress the reflection of the spin waves that are emitted during the skyrmion's evolution. The explicit parameters chosen are $\alpha = 0.01$ as with the collective coordinate modelling (with exception of the aforementioned boundaries), $I_1 = 10^{-12} \text{ J m}^{-1}$, $I_2 = 10^{-29} \text{ J m}$, and $M_s = 10^6 \text{ A m}^{-1}$. For these values, the applied dimensionless magnetic field of 1 would correspond to 100 mT, and a dimensionless length of 10 would correspond to 31.6 nm. We note, however, that this particular choice of I_1 , I_2 , and M_s only represents order-of-magnitude values for such systems, and that while the various scales such as length and time will change if the micromagnetic parameters are varied, the physics will remain the same regardless of what is chosen.

We noted in Section 5.4 that the length scales associated with magnetisation textures in frustrated magnets are around an order of magnitude lower than those in typical chiral magnetic systems. Although we work in dimensionless units for generality rather than considering parameters from a specific material, we acknowledge that this could be a limitation when applying the results of the phase diagram Fig. 11.4(a) to experimental systems. Nevertheless, the micromagnetic functional captures the qualitative details of the system such as the helicity being a Goldstone mode, and the length scales are still an order of magnitude above the typical lattice constant, so we assume that our results still lay a solid foundation on which experimental studies could be based.

To compare the results from the micromagnetic modelling with those from collective coordinate modelling, we calculate the skyrmion's radius for each time step of the simulation by extracting the contour on which $m_z = 0$ using the `scikit-image` library [284]. The centroid of the skyrmion is calculated using the median of the contour's x - and y -positions, and the radii are calculated by calculating the mean of the displacements from the centre. The skyrmion's helicity during the evolution is calculated by extracting the average helicity of the points on the $m_z = 0$ contour.

The results of the integration of the Thiele equations (11.4) for various values of electric field amplitude E_0 and frequency ω are summarised in Fig. 11.4(a). Shown in green are the points where the skyrmion's helicity rotates anticlockwise with the angular frequency synchronised with the driving frequency ω of the electric field. Dark green signifies points where the helicity's rotation is monotonic, while light green signifies points where the rotation is not monotonic. The same applies to the points shown in purple and pink, with monotonic and nonmonotonic clockwise instead of anticlockwise rotation. In white are points for which no such rotations are achieved. The Kittel frequency of the system $\omega_{\text{res}} = 1$ in the absence of dipolar interactions is marked as a dashed vertical line. The insets in Fig. 11.4(a) show the preimage of the associated spacetime hopfions, which will be discussed in Section 11.4.

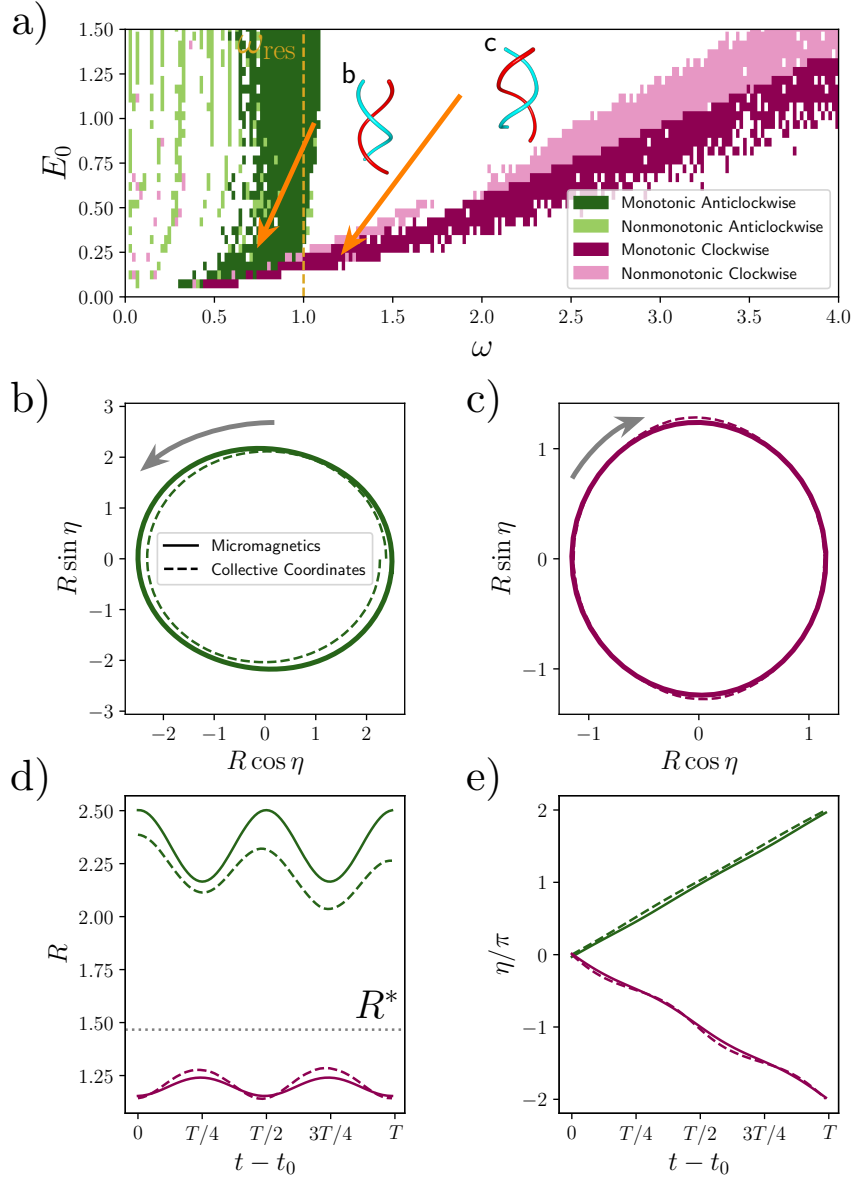


Figure 11.4.: (a) Phase diagram constructed by analysing the long-term solutions of the Thiele equations (11.4) with $\alpha = 0.01$, for different values of the amplitude E_0 and frequency ω of the oscillating electric field. The regions with nonzero spacetime Hopf index are shown in pink and green, corresponding to a clockwise ($H = +1$) and anticlockwise ($H = -1$) rotation of the helicity respectively. (b), (c) Example trajectories of the collective coordinate evolution for monotonic anticlockwise and clockwise helicity evolution, with parameters $E_0 = 0.25$, $\omega = 0.72$ and $E_0 = 0.20$, $\omega = 1.18$ respectively. The trajectories are elliptical due to the breathing of the radius, shown in (d). When the radius is smaller than R^* , the helicity increases (rotates anticlockwise), and vice versa. Figure taken from our publication Ref. [286].

11.2. Electric Field Amplitude-Frequency Phase Diagram

The most striking feature of the phase diagram is that it displays two ‘lobes’: one in which the helicity rotation is exclusively clockwise and another where it is predominantly anticlockwise. In the rightmost pink and purple lobe, we see that the skyrmion’s helicity rotates clockwise. Most of the points in this region are at a frequency far from ω_{res} , giving a favourable energy injection to dissipation ratio for a steady helicity rotation. The collective coordinate results are also in good agreement with the micromagnetics results in this region, as exemplified in Figs. 11.4(b) and (c), making this region promising for experimental investigation. One interesting feature of this is the appearance of a straight line separating the regions for which there is a monotonic and nonmonotonic rotation of the helicity. If the evolution is such that R becomes greater than R^* , the helicity starts to reverse direction, as can be seen in Fig. 11.3. This can be seen in Fig. 11.5(b), where the maximum radius obtained during the collective coordinate is approximately R^* , which corresponds to the white, straight line. This straight line can also be understood through energy considerations. The helicity rotation is induced by energy injection from an AC electric field, which competes with energy dissipation from the Gilbert damping. In Fig. 11.5(c), the time-averaged energy $\langle U \rangle$ with the energy of the skyrmion in the absence of \mathbf{E}_{ext} , $U^* \approx 4.05$, is shown. The time-periodic steady state where the helicity rotates happens where $\langle U \rangle \approx U^*$, where the energy injection and dissipation, on average, cancel out. For the white region of Fig. 11.4 below this lobe, the amplitude of the electric field is too small to induce a helicity rotation, and the helicity evolution simply rocks back and forth about its equilibrium value. For values of E_0 above this lobe, the dynamics become very complex, and synchronisation of the helicity with the electric field does not occur. The trajectories of the selected points shown in Figs. 11.4(b) and (c) have an elliptical shape, which reflects the coupled dynamics of the collective coordinates, *i.e.* that the helicity rotations are accompanied by breathing of the skyrmion.

In the leftmost lobe, concentrated around the resonance frequency, the helicity rotation is predominantly anticlockwise. The anticlockwise rotation can be phenomenologically understood by the fact that, for such proximity to resonance, the steady-state radius remains higher than R^* , resulting in an anticlockwise rotation. It should be noted that, for some of these points, particularly those with values of ω very close to ω_{res} , such assignment of a topological index is not strictly true. This is because the radius is often continuously increasing for the collective coordinate calculations around these points, meaning that points at time intervals T apart cannot be identified. In the micromagnetic simulations, instead of the radius diverging, the skyrmion profile approximation (11.3) breaks down and the skyrmion loses its structural integrity. We note that, had we chosen another magnitude of \mathbf{B}_{ext} , the phase diagram would look very similar, with the resonance shifted horizontally. We confirmed this by recalculating the phase diagram with $\mathbf{B}_{\text{ext}} = 2\hat{z}$, shown in Fig. 11.1(d). Within the dark green region of the leftmost lobe, but further away from ω_{res} , the dynamics are more well-behaved, and the collective coordinate and micromagnetic models agree well, as shown in Fig. 11.4(b), where the evolution over a single period for $E_0 = 0.25$ and $\omega = 0.72$ is shown.

At frequencies lower than those of the bulk of the left-hand lobe exist more isolated points with interesting dynamics. An example of such dynamics is shown in Fig. 11.6(a), with a looping around the helicity values $\eta = 0, \pi$. These dynamics can be understood in terms of the energy landscape shown in Fig. 11.6(c), which shows the energy landscape during the evolution where $E > 0$ and $E < 0$, and the future evolution of the trajectory.

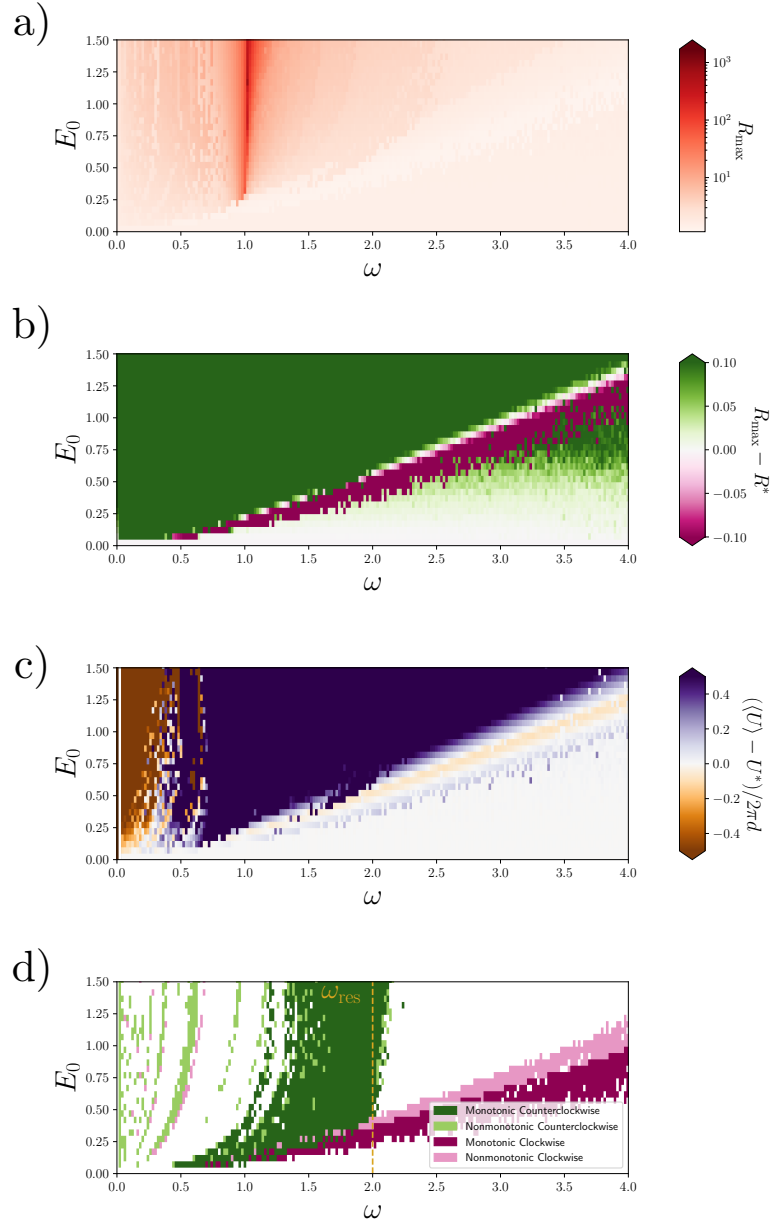


Figure 11.5.: Various phase diagrams further illustrating the dynamics of the skyrmion in a frustrated magnet subject to an oscillating electric field. (a) Maximum radius during the evolution in the long-term dynamics. The divergence at the Kittel frequency can be seen. (b) Difference between the maximum radius achieved during the evolution and the equilibrium skyrmion radius R^* in the absence of an applied electric field. The plotted range of $R_{\max} - R^*$ is restricted to $[-0.1, 0.1]$. (c) Time average of the energy of a driven skyrmion $\langle U \rangle$ over one period of the oscillating electric field is shown. Where $\langle U \rangle = U^*$, the energy of the skyrmion for zero electric field, the energy injected by the driving AC electric field is on averaged balanced by the Gilbert damping dissipation. (d) Phase diagram as in Fig. 11.4 with double the applied background magnetic field. Figure adapted from our publication Ref. [286].

11.2. Electric Field Amplitude-Frequency Phase Diagram

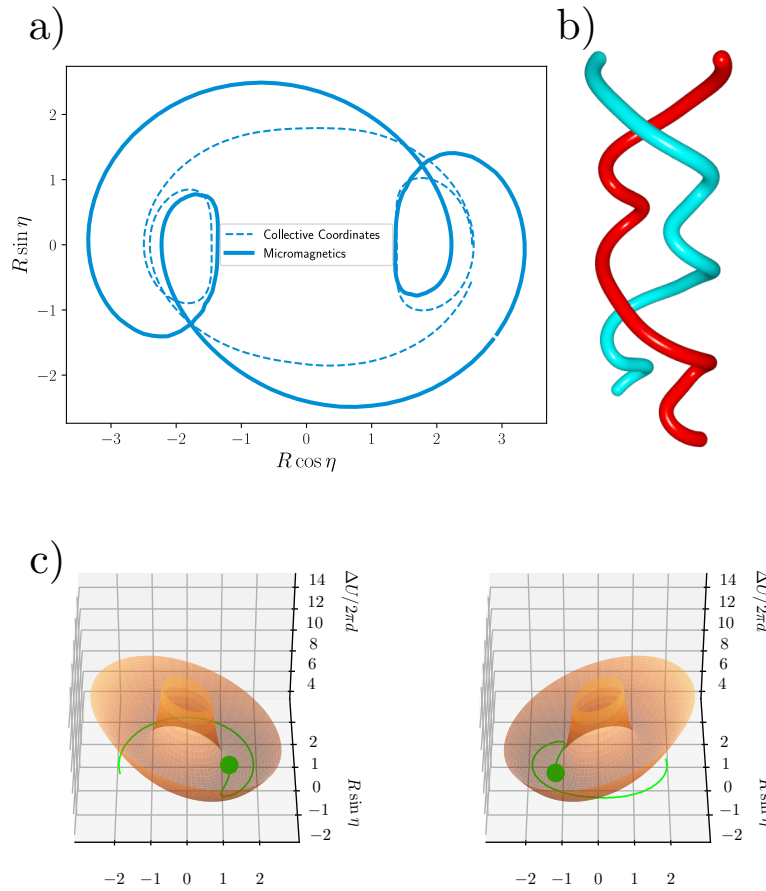


Figure 11.6.: More complicated evolution of the collective coordinates at a low frequency ω of the applied AC electric field. (a) Trajectory for $E_0 = 1.00$, $\omega = 0.30$ calculated using both collective coordinate and micromagnetic modelling. (b) Preimages of $m_x = 1$ and $m_x = -1$, with the vertical axis being time, over one period of the electric field, from the collective coordinate calculations. (c) Dynamics can be interpreted as the collective coordinate trajectory (green dot and line) orbiting the energy minimum basins.

The collective coordinates orbit the minimum energy basins during the evolution, giving rise to the shape of the trajectory. Also seen in this region are isolated points in which helicity rotates clockwise, in contrast to the rest of the ‘lobe’, where the rotation is anticlockwise. This is also seen in micromagnetic simulations, however, not at the same points. In this region, the behaviour is very sensitive to small perturbations, resulting in the evolution sometimes crossing the $R = R^*$ line ‘by chance’, and other times not. We emphasise that, because such dynamics are also observed in some micromagnetic simulations, these isolated points reflect the high sensitivity to small changes in this region of the phase diagram.

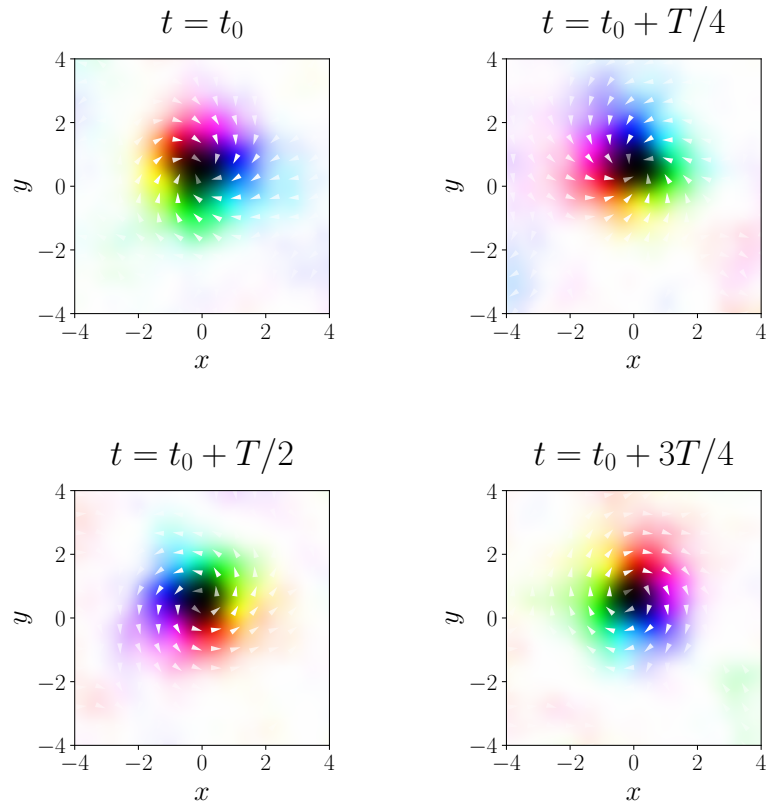


Figure 11.7.: Time evolution of a skyrmion texture during one period of oscillation of the externally applied magnetic field at a finite temperature $\theta = 20$ K.

11.3. Finite-Temperature Simulations

To ensure that the dynamics of the skyrmion in a frustrated magnet that we have uncovered are robust at finite temperatures, we ran simulations for temperatures $\theta \neq 0$ K. The inclusion of finite temperatures in micromagnetic simulations has been discussed in Section 4.2, which we make use of here. The time evolution of the skyrmion texture over one period of the applied oscillating electric field for $\theta = 20$ K is shown in Fig. 11.7 for an electric field amplitude of $E_0 = 0.20$ and angular frequency of $\omega = 1.18$. Although noise is visible, the skyrmion's helicity still rotates. The collective coordinates extracted from these simulations are shown for a range of temperatures in Fig. 11.8, where the skyrmion's breathing and helicity rotation can still be seen up to $\theta = 20$ K. Some of the noise at higher temperatures, especially for the helicity, comes from limitations of the code used to extract the collective coordinates, rather than being an artefact of the simulations. Despite being unable to observe helicity rotations in the collective coordinates extracted for higher temperatures, we still observed a helicity rotation for temperatures as high as 100 K in the simulations.

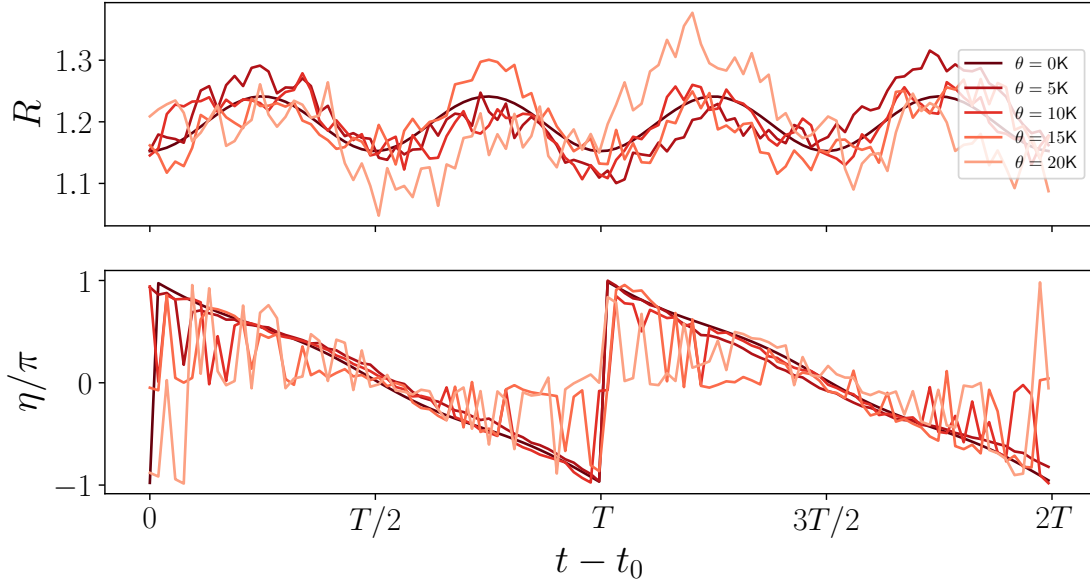


Figure 11.8.: Evolution of the collective coordinates R and η over two periods of oscillation of the applied electric field of amplitude $E_0 = 0.20$ and angular frequency $\omega = 1.18$ for various temperatures. Apart from added noise, the overall behaviour of breathing and a helicity rotation is still observed.

11.4. Topological Interpretation as Spacetime Magnetic Hopfions

Magnetic hopfions, as introduced in Chapter 3, are defined in terms of the mapping $S^3 \rightarrow S^2$. In much of the literature on magnetic hopfions, however, they are discussed as skyrmion tubes for which the skyrmion's helicity, or in-plane spin angle, is twisted through 2π along its length, such that the ends match [71, 290]. More generally, for a skyrmion texture with a skyrmion number N_{sk} , the Hopf index is given by $H = PN_{\text{sk}}$, where P is the number of twists. If we consider the twisting along the z -direction (before identification of the ends), the Hopf index, given by the Whitehead formula (3.3), becomes

$$\begin{aligned} H &= \frac{N_{\text{sk}}}{4\pi} \int_{-\infty}^{\infty} dz \int_0^{\infty} d\rho \sin \Theta (\partial_z \Theta \partial_\rho \eta - \partial_z \eta \partial_\rho \Theta) \\ &= N_{\text{sk}} P, \end{aligned} \quad (11.9)$$

It should be noted that the base space is no longer S^3 (by stereographic projection onto \mathbb{R}^3), but rather $S^2 \times S^1$, where $S^2 \cong \mathbb{R}^2 \cup \{\infty\}$ due to the stereographic projection $S^2 \rightarrow \mathbb{R}^2 \cup \{\infty\}$, as in Fig. 2.6, and S^1 is from the identification of the endpoints. As such, H is no longer a homotopy invariant of the system, but rather N_{sk} and P modulo $2N_{\text{sk}}$ are separately homotopy invariants [291, 292]³. Despite this difference in

³That P modulo $2N_{\text{sk}}$ is a homotopy invariant of the system can be seen by analogy with Dirac's belt trick [293]. Consider the preimages of a skyrmion tube with $N_{\text{sk}} = 1$ without the rotation, such that they do not twist around each other. Now consider twisting one end through 4π . By stretching the resulting twisted preimages such that they pass over one of the fixed ends of the tube, the tangling can be undone. Various animations of Dirac's belt trick exist online that illustrate this principle.

topology, objects for which (3.3) yields a finite integer when the integration is performed over $S^2 \times S^1$ have previously been studied in the Skyrme-Faddeev model [290, 292] and Bose-Einstein condensates [294], and we continue to refer to them as hopfions.

In previous sections, we have shown that a monotonic rotation of a skyrmion's helicity in a frustrated magnetic material can be induced by the application of an oscillating electric field. Here, we effectively have the situation of the previous discussion of skyrmion along z with the helicity changing by 2π over the tube, with the vertical spatial dimension having been replaced with time extending over the period T . The compactification of the \mathbb{R} time axis to S^1 is realised through the energy functional of the system being time-periodic, in such a way that it induces a rotation of the skyrmion's helicity of 2π over a period T , allowing for identification of the endpoints. The topological invariant to characterise magnetic hopfions in spacetime, which is invariant under the gauge transformation $\mathbf{A} \rightarrow \mathbf{A} + \nabla\chi$, where χ is an arbitrary scalar field, is then

$$H = -\frac{1}{(8\pi)^2} \int_0^T dt \int_{\mathbb{R}^2} d^2r \mathbf{F}(\mathbf{r}) \cdot \mathbf{A}(\mathbf{r}). \quad (11.10)$$

An illustration of the preimages associated with the skyrmion's helicity rotation is shown in Fig. 11.9(a), where the inset shows the identification of the preimages at $t = 0$ and $t = T$.

That the spacetime Hopf index is invariant under a gauge transformation is shown as follows. We consider a gauge transformation $\mathbf{A}' = \mathbf{A} + \nabla\chi$, where χ is an arbitrary scalar field. Equation (11.10) becomes

$$H' = H - \frac{1}{(8\pi)^2} \int_0^T dt \int_{\mathbb{R}^2} d^2r \mathbf{F}(\mathbf{r}) \cdot \nabla\chi(\mathbf{r}). \quad (11.11)$$

Using the identity $\mathbf{F} \cdot \nabla\chi = \nabla \cdot (\chi\mathbf{F}) - \chi\nabla \cdot \mathbf{F}$, the integral can be written as

$$\int_0^T dt \int_{\mathbb{R}^2} d^2r \nabla \cdot (\chi\mathbf{F}) - \int_0^T dt \int_{\mathbb{R}^2} d^2r \chi \nabla \cdot \mathbf{F}. \quad (11.12)$$

The of these integrals is a boundary term, which vanishes due to the periodic boundary conditions of t . In the second integral, $\nabla \cdot \mathbf{F}$ vanishes as, in cylindrical polar coordinates, $\mathbf{F} = 2 \sin \Phi (\nabla\Theta \times \nabla\Phi)$, and thus⁴

$$\begin{aligned} \nabla \cdot \mathbf{F} &= 2\nabla(\sin \Theta) \cdot (\nabla\Theta \times \nabla\Phi) \\ &= 2 \cos \Theta \nabla\Theta \cdot (\nabla\Theta \times \nabla\Phi) \\ &= 0. \end{aligned} \quad (11.13)$$

Hence, $H' = H$, and the spacetime Hopf index is gauge-invariant. This proof was based on the discussion in Ref. [295].

With this topological interpretation of the dynamics of skyrmions in frustrated magnets, we can assign a topological index to the various regimes of behaviour shown in Fig 11.4(a). In the left-hand lobe, in which the skyrmion's helicity rotates predominantly anticlockwise, we see that the spacetime Hopf index H is predominantly -1 . In the other lobe in which the helicity evolution is clockwise, $H = 1$. Shown in the insets are the

⁴We have used the identity $\nabla \cdot (fg) = \nabla f \cdot g + f \nabla \cdot g$ for a scalar field f and vector field g .

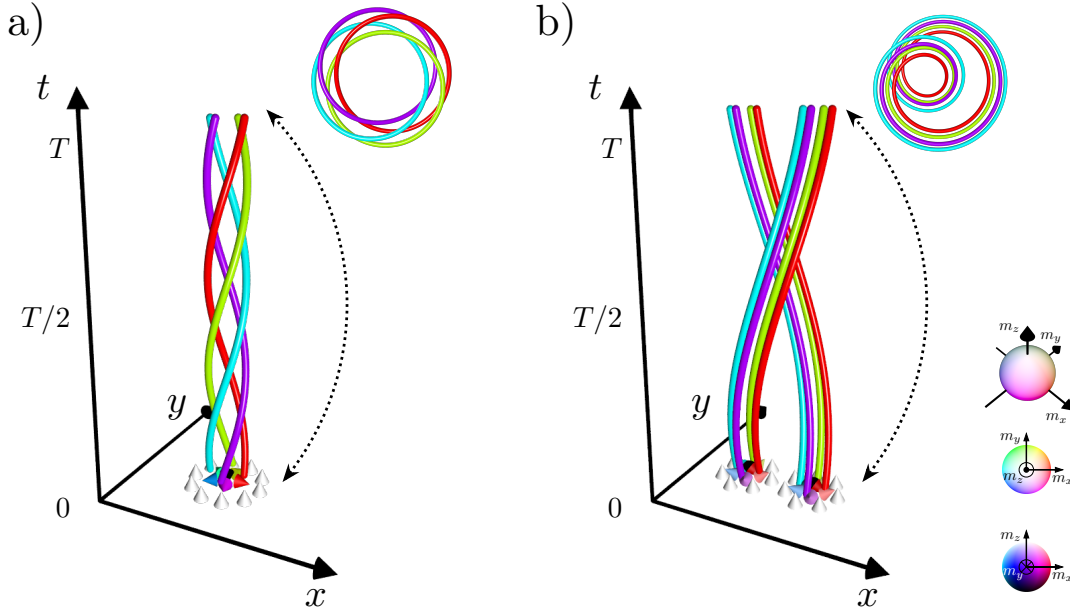


Figure 11.9.: Illustration of the creation of spacetime magnetic hopfions by (a) the rotation of a single skyrmion's helicity through 2π and (b) the braiding of two skyrmions around each other. The preimages, shown as coloured curves, are shown for four selected magnetisation directions. After the identification of the preimages at time intervals T , a spacetime magnetic hopfion with Hopf index $H = +1$ is formed, as shown in the insets. Figure taken from our publication Ref. [286].

preimages of $m_x = +1$ and $m_x = -1$ in red and cyan respectively. We also note that the more exotic dynamics shown in Fig. 11.6 also have this topological interpretation; the preimages in Fig. 11.6(b) have the same overall linking when the ends are identified.

Helicity rotation could potentially be observed in skyrmion-hosting systems with tunable or weak DMI for dynamically stabilised skyrmions where the helicity can be tuned [272, 296]. To observe spacetime magnetic hopfions constructed through the rotation of a magnetic skyrmion's helicity, one must measure the skyrmion's helicity. The helicity could be obtained from Lorentz transmission electron microscopy (LTEM) [297] and circularly polarised resonance elastic X-ray scattering [298]. The helicity can be made to rotate through various mechanisms, such as through the application of spin-polarised currents [119, 203, 299, 300], oscillating magnetic [198] and electric fields [286, 301, 302].

An alternative route for the realisation of spacetime magnetic hopfions is through the braiding of several skyrmions, illustrated in Fig. 11.9(b). The manipulation of skyrmions' positions has been an area of significant research interest, with various methods such as using electric currents (as discussed in Chapter 9), tilted magnetic fields [303], magnetic field gradients [241], temperature gradients [304], and circularly polarised laser illumination [305] having been proposed. Skyrmion braiding has also been proposed as a potential topological computing platform [306]. For the braiding of two skyrmions, the

period is defined by the time required to swap their positions. If the swap is anticlockwise, the spacetime Hopf index $H = 1$. If it is clockwise, $H = -1$. This construction could be generalised to an arbitrary number of skyrmions, arranged, for example, into skyrmion crystals, skyrmion bags, or engineered arrangements in nanopatterned substrates. In this case of the braiding of multiple magnetic skyrmions, spacetime magnetic hopfions with higher spacetime Hopf indices would result. The manipulation of skyrmion positions could be achieved using experimentally reported means in the metallic chiral magnet FeGe [233, 307], the insulating chiral magnet Cu_2OSeO_3 [177, 241, 308], the van der Waals ferromagnet Fe_3GeTe_2 [309], and magnetic multilayers [310, 311]. In order to measure the positions of the skyrmions, scanning transmission X-ray microscopy (STXM) could be used [311, 312], as well as magneto-optical Kerr effect (MOKE) microscopy [310, 313], and magnetic force microscopy (MFM) [314, 315].

In summary, we have uncovered different regimes skyrmion dynamics in frustrated magnets subject to an applied oscillating electric field using collective coordinate modelling, which we have validated using micromagnetic modelling. Furthermore, we have offered an interpretation of these structures in spacetime by proposing the spacetime magnetic hopfion.

Chapter

12

Summary

In this Thesis, we have used analytical and numerical modelling within the micromagnetic framework to model skyrmions in a variety of systems: in the ferromagnetic and spin spiral states of chiral magnets, as well as in frustrated magnets. Furthermore, we have discussed bulk magnetic textures: magnetic vortex rings and magnetic hopfions.

In Part II of this Thesis, inspired by results of previous works investigating the creation of skyrmion-antiskyrmion pairs through the interaction of spin-transfer torques with gradients induced by magnetic impurities considered in Chapter 6, we have proposed a protocol for the creation of skyrmion-antiskyrmion pairs in the cycloidal state of a magnet. This is presented at the end of Chapter 7. Here, the natural confinement of the skyrmions to lanes offers numerous advantages in device applications over systems where skyrmions are in a ferromagnetic background. The confinement mitigates the skyrmion Hall effect discussed in Chapter 9 and allows for higher translational motion speeds. Moreover, the skyrmions can be stabilised without the application of a perpendicular magnetic field. We have furthermore investigated the current-driven creation of magnetic vortex rings in bulk ferromagnetic systems and found that different impurity shapes lead to different internal structures of the vortex rings that are created.

In Part III, in addition to discussing the current-driven translational motion of magnetic skyrmions in regimes in which they behave as rigid, particle-like objects, we have modelled their internal dynamics in both chiral and frustrated magnets. For the case of chiral magnets, which was the subject of Chapter 10, we showed that applying external magnetic fields with frequencies corresponding to unit fractions of the skyrmions' eigenfrequencies excited the corresponding eigenmodes. For higher applied field amplitudes, we found the excitation of the eigenmodes with fractional frequencies of the eigenfrequencies to be more efficient than the applied field frequency matching the eigenfrequency. This has applications for frequency multiplication of magnons in magnonic devices, and we showed that the principle is generalisable to other magnetic textures. In Chapter 11, using collective coordinate modelling and micromagnetic simulations, we demonstrated that applying an oscillating electric field to a skyrmion in a frustrated magnet can excite the helicity internal mode. We uncovered various regimes of this behaviour, depending on the amplitude and frequency of the electric field. We additionally interpreted these dynamics in terms of a spacetime Hopf index.

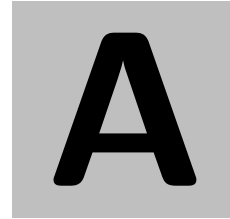
In summary, we have investigated methods to create magnetic skyrmions. Furthermore,

Chapter 12. Summary

we have explored their dynamics in various regimes, with potential device applications in magnonics, conventional computing, and unconventional computing. We envisage that the theoretical results presented will inspire experimental studies that pave the way towards the realisation of skyrmions in these applications.

Part IV.
Appendices

Appendix



Numerical Calculation of Topological Indices

In the analysis of some of the micromagnetic simulations in this Thesis, it is necessary to numerically calculate topological indices of magnetisation textures. In this Appendix, we present Python code to calculate the skyrmion number N_{sk} , given by (2.8), and the Hopf index H , given by (3.3). In both cases, we use the `findiff` module [316] to calculate the derivatives.

A.1. Numerical Calculation of the Skyrmion Number

In the analysis of data from certain simulations, such as those in which we calculate the skyrmion-antiskyrmion pair creation frequency in Chapter 6, it is necessary to numerically calculate the skyrmion number N_{sk} . The code used to calculate N_{sk} is shown in Listing A.1. Where the skyrmion number density $\rho_{\text{sk}}(\mathbf{r})$ is required, the skyrmion density array is output, instead of the final sum.

```
1 import numpy as np
2 import findiff
3
4 def skyrmionNumber(m, dx, dy, acc=4):
5     """Calculate the skyrmion number density of a magnetic texture
6     contained in an array of shape (Nx, Ny, 1, 3)
7
8     Args:
9     m (ndarray): Array of shape (Nx, Ny, 1, 3).
10    dx (float64): The simulation cell size in the x-dimension.
11    dy (float64): The simulation cell size in the y-dimension.
12    acc (int, optional): Order of the accuracy for which the
13    derivatives should be calculated.
14
15    Returns:
16    Two-dimensional array of skyrmion number densities over the xy-
17    plane.
18
19    """
20    # args: axis, discretisation, derivative order, accuracy
21    d_dx = findiff.FinDiff(0, dx, 1, acc=acc)
```

Appendix A. Numerical Calculation of Topological Indices

```
20 d_dy = findiff.FinDiff(1, dy, 1, acc=acc)
21
22 mdx = d_dx(m) / dx
23 mdy = d_dy(m) / dy
24
25 # Elementwise dot product
26 skDensityArray = np.einsum("ijk,ijk->ij", m, np.cross(mdx, mdy))
27
28 return np.sum(skDensityArray) / (4*np.pi)
```

Listing A.1: Code to numerically evaluate the skyrmion number of a magnetisation texture in a two-dimensional plane.

A.2. Numerical Calculation of the Hopf Index

In Chapter 8, we evaluate the Hopf index of the vortex rings shed from the impurity. The Hopf index can be calculated using a discretised form of the Whitehead formula (3.3), the implementation of which is provided below.

```
1 import numpy as np
2 import findiff
3
4 def HopfIdx(m, dx, dy, dz, acc=8):
5     """Calculate the Hopf index of a magnetisation vector field of shape (
6         Nx, Ny, Nz, 3).
7
8     Args:
9         m (ndarray): Magnetisation array of the shape (Nx, Ny, Nz, 3).
10        dx (float64): The simulation cell size in the x-dimension.
11        dy (float64): The simulation cell size in the y-dimension.
12        dz (float64): The simulation cell size in the z-dimension.
13        acc (int, optional): Order of the accuracy for which the
14        derivatives should be calculated.
15
16    Returns:
17        The calculated Hopf index of the texture.
18
19    """
20    # args: axis, discretisation, derivative order, accuracy
21    d_dx = findiff.FinDiff(0, dx, 1, acc=acc)
22    d_dy = findiff.FinDiff(1, dy, 1, acc=acc)
23    d_dz = findiff.FinDiff(2, dz, 1, acc=acc)
24
25    mdx = d_dx(m)
26    mdy = d_dy(m)
27    mdz = d_dz(m)
28
29    # Emergent magnetic field
30    Fx = 2 * np.einsum("ijkl,ijkl->ijk", m, np.cross(mdy, mdz))
31    Fy = 2 * np.einsum("ijkl,ijkl->ijk", m, np.cross(mdz, mdx))
32    Fz = 2 * np.einsum("ijkl,ijkl->ijk", m, np.cross(mdx, mdy))
33
34    F = np.zeros((Fx.shape[0], Fx.shape[1], Fx.shape[2], 3))
35    F[:, :, :, 0] = Fx
36    F[:, :, :, 1] = Fy
37    F[:, :, :, 2] = Fz
```

A.2. Numerical Calculation of the Hopf Index

```
37
38 # Vector potential
39 A = np.zeros((Fz.shape[0], Fz.shape[1], Fz.shape[2], 3))
40 A[:, :, :, 0] = -np.cumsum(Fz, axis=1)
41 A[:, :, :, 2] = np.cumsum(Fx, axis=1)
42
43 # Elementwise dot product
44 dotProduct = np.einsum("ijkl,ijkl->ijk", F, A)
45
46 return -np.sum(dotProduct) / (8 * np.pi)**2
```

Listing A.2: Code to numerically evaluate the Hopf index of a magnetisation texture.

Appendix

B

Derivation of Frustrated Energy Functional

The symmetric exchange interaction was discussed in Section 4.1. It was noted that the model in the continuum limit (4.3) can be derived from the Heisenberg Hamiltonian (4.2), which is the subject of this Appendix. In this derivation, we consider a triangular lattice with nearest, next-nearest, next-next-nearest and next-next-next-nearest exchange interactions with coupling constants J_1 , J_2 , J_3 , and J_4 respectively. The primitive lattice vectors are $(a, 0)$ and $(a/2, \sqrt{3}/2)$. This lattice is illustrated in Fig. B.1, where we only show the first two couplings to prevent the diagram being too cluttered.

The energy corresponding to this system is

$$U = -\frac{S^2}{2} \sum_j \sum_n J_{jn} \mathbf{m}_j \cdot \mathbf{m}_n, \quad (\text{B.1})$$

where each \mathbf{m}_i is a unit vector, S is the spin magnitude, the first sum is over all lattice sites j , and the second sum is over the neighbours of each lattice site n . The prefactor of $1/2$ prevents the double-counting of spins. We take the Fourier transform $\mathbf{m}_j = \sum_{\mathbf{q}} \mathbf{m}_{\mathbf{q}} e^{i\mathbf{r}_j \cdot \mathbf{q}}$. Explicitly performing the sum over the neighbours gives

$$U = -\frac{S^2}{2} \sum_j \sum_{\mathbf{q}} \sum_{\mathbf{q}'} J_{\mathbf{q}\mathbf{q}'} \mathbf{m}_{\mathbf{q}} \cdot \mathbf{m}_{\mathbf{q}'} e^{i\mathbf{r}_j \cdot (\mathbf{q} + \mathbf{q}')}, \quad (\text{B.2})$$

where we have defined

$$J_{\mathbf{q}\mathbf{q}'} \equiv J_1 J_{\mathbf{q}\mathbf{q}',\text{N}} + J_2 J_{\mathbf{q}\mathbf{q}',\text{NN}} + J_3 J_{\mathbf{q}\mathbf{q}',\text{NNN}} + J_4 J_{\mathbf{q}\mathbf{q}',\text{NNNN}}, \quad (\text{B.3})$$

Appendix B. Derivation of Frustrated Energy Functional

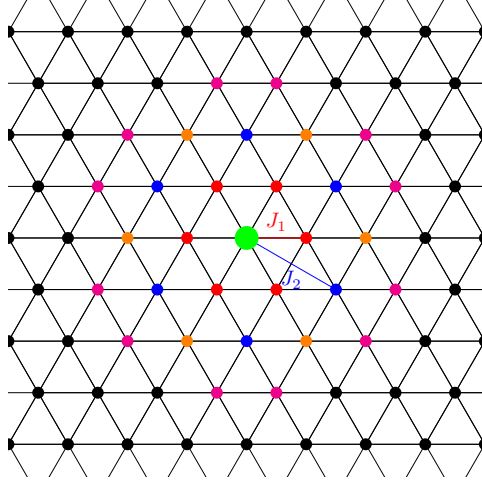


Figure B.1.: Schematic of frustrated exchange interactions in a triangular lattice. The nearest, next-nearest, next-next-nearest, and next-next-next-nearest neighbours from the spin at the site of the green dot are shown in red, blue, orange, and magenta respectively. We only explicitly show the exchange interactions for the nearest (J_1) and next-nearest (J_2) neighbours to avoid the diagram becoming too cluttered.

with¹

$$J_{\mathbf{q}',\text{N}} = 2 \left[\cos(aq'_x) + \cos\left(\frac{aq'_x}{2} + \frac{\sqrt{3}}{2}aq'_y\right) + \cos\left(\frac{aq'_x}{2} - \frac{\sqrt{3}}{2}aq'_y\right) \right], \quad (\text{B.4a})$$

$$J_{\mathbf{q}',\text{NN}} = 2 \left[\cos\left(\frac{3}{2}aq'_x + \frac{\sqrt{3}}{2}aq'_y\right) + \cos\left(\frac{3}{2}aq'_x - \frac{\sqrt{3}}{2}aq'_y\right) + \cos(\sqrt{3}aq'_y) \right], \quad (\text{B.4b})$$

$$J_{\mathbf{q}',\text{NNN}} = 2 \left[\cos(2aq'_x) + \cos(aq'_x + \sqrt{3}aq'_y) + \cos(aq'_x - \sqrt{3}aq'_y) \right], \quad (\text{B.4c})$$

$$\begin{aligned} J_{\mathbf{q}',\text{NNNN}} = 2 & \left[\cos\left(\frac{5}{2}aq'_x + \frac{\sqrt{3}}{2}aq'_y\right) + \cos(2aq'_x + \sqrt{3}aq'_y) \right. \\ & + \cos\left(\frac{aq'_x}{2} + \frac{3\sqrt{3}}{2}aq'_y\right) + \cos\left(\frac{5}{2}aq'_x - \frac{\sqrt{3}}{2}aq'_y\right) \\ & \left. + \cos(2aq'_x - \sqrt{3}aq'_y) + \cos\left(\frac{aq'_x}{2} - \frac{3\sqrt{3}}{2}aq'_y\right) \right]. \end{aligned} \quad (\text{B.4d})$$

Using $\sum_j e^{i\mathbf{r}_j \cdot (\mathbf{q} + \mathbf{q}')} = N\delta_{\mathbf{q}', -\mathbf{q}}$, where N is the number of lattice sites, we obtain

$$U = -\frac{NS^2}{2} \sum_{\mathbf{q}} J_{\mathbf{q}} \mathbf{m}_{\mathbf{q}} \cdot \mathbf{m}_{-\mathbf{q}}. \quad (\text{B.5})$$

We now take the continuum limit, where the reciprocal lattice vectors are sufficiently close together that the sum can be replaced by an integral as $\sum_{\mathbf{q}} \rightarrow \frac{L_x L_y}{(2\pi)^2} \int d^2q$, where

¹This comes from writing the exponentials out for each neighbour and using $2 \cos x \equiv e^{ix} + e^{-ix}$.

L_x and L_y are the horizontal and vertical extent of the lattice respectively. The energy then reads

$$U = -\frac{NS^2 L_x L_y}{2} \frac{1}{(2\pi)^2} \int d^2q J(\mathbf{q}) \mathbf{m}(\mathbf{q}) \cdot \mathbf{m}(-\mathbf{q}). \quad (\text{B.6})$$

We assume sufficiently smooth magnetisation textures such that terms of $\mathcal{O}(q^6)$ are negligible. Taylor expanding the cosines in $J(\mathbf{q})$ and setting $q_x = q \cos \phi$ and $q_y = q \sin \phi$ gives²

$$J(\mathbf{q}) = 6(J_1 + J_2 + J_3 + 2J_4) - \frac{3}{2}a^2 q^2 (J_1 + 3J_2 + 4J_3 + 14J_4) + \frac{3}{32}a^4 q^4 (J_1 + 9J_2 + 16J_3 + 98J_4) + \mathcal{O}(q^6). \quad (\text{B.7})$$

The energy then becomes

$$U = -\frac{NS^2 L_x L_y}{2(2\pi)^2} \left[6(J_1 + J_2 + J_3 + 2J_4) \int d^2q \mathbf{m}(\mathbf{q}) \cdot \mathbf{m}(-\mathbf{q}) - \frac{3}{2}a^2 (J_1 + 3J_2 + 4J_3 + 14J_4) \int d^2q q^2 \mathbf{m}(\mathbf{q}) \cdot \mathbf{m}(-\mathbf{q}) + \frac{3}{32}a^4 (J_1 + 9J_2 + 16J_3 + 98J_4) \int d^2q q^4 \mathbf{m}(\mathbf{q}) \cdot \mathbf{m}(-\mathbf{q}) \right]. \quad (\text{B.8})$$

We now turn to the evaluation of the integrals over q -space. The continuum form of $\mathbf{m}_j = \sum_{\mathbf{q}} \mathbf{m}_{\mathbf{q}} e^{i\mathbf{r}_j \cdot \mathbf{q}}$ is

$$\mathbf{m}(\mathbf{r}) = \frac{L_x L_y}{(2\pi)^2} \int d^2q \mathbf{m}(\mathbf{q}) e^{i\mathbf{r} \cdot \mathbf{q}}, \quad (\text{B.9})$$

for which the inverse transform is³

$$\mathbf{m}(\mathbf{q}) = \frac{1}{L_x L_y} \int d^2r \mathbf{m}(\mathbf{r}) e^{-i\mathbf{r} \cdot \mathbf{q}}. \quad (\text{B.10})$$

To evaluate the first integral in (B.8), we use the relation

$$\frac{1}{(2\pi)^2} \int d^2q e^{i\mathbf{q} \cdot (\mathbf{r}' - \mathbf{r})} = \delta(\mathbf{r}' - \mathbf{r}). \quad (\text{B.11})$$

²Including higher powers of q would yield terms that include ϕ , *i.e.* spatial anisotropy terms.

³This can be seen by multiplying (B.9) by $e^{-i\mathbf{r} \cdot \mathbf{q}'}$ and integrating over r , using the identity $(2\pi)^2 \delta(\mathbf{q}' - \mathbf{q}) = \int d^2r e^{i\mathbf{r} \cdot (\mathbf{q}' - \mathbf{q})}$.

Appendix B. Derivation of Frustrated Energy Functional

Thus, the first integral in (B.8) is

$$\begin{aligned}
\int d^2q \mathbf{m}(\mathbf{q}) \cdot \mathbf{m}(-\mathbf{q}) &= \frac{1}{(L_x L_y)^2} \int d^2q \int d^2r \int d^2r' \mathbf{m}(\mathbf{r}) \cdot \mathbf{m}(\mathbf{r}') e^{i\mathbf{q} \cdot (\mathbf{r}' - \mathbf{r})} \\
&= \frac{(2\pi)^2}{(L_x L_y)^2} \int d^2r \int d^2r' \mathbf{m}(\mathbf{r}) \cdot \mathbf{m}(\mathbf{r}') \delta(\mathbf{r}' - \mathbf{r}) \\
&= \frac{(2\pi)^2}{(L_x L_y)^2} \int d^2r \mathbf{m}(\mathbf{r}) \cdot \mathbf{m}(\mathbf{r}) \\
&= \frac{(2\pi)^2}{(L_x L_y)^2} \int d^2r, \tag{B.12}
\end{aligned}$$

where we have used that $\mathbf{m}(\mathbf{r}) \cdot \mathbf{m}(\mathbf{r}) = 1$.

To evaluate the second integral in (B.8), we can take the Laplacian of (B.11) to obtain the relation $\int d^2q q^2 e^{i\mathbf{q} \cdot (\mathbf{r}' - \mathbf{r})} = -(2\pi)^2 \nabla_{\mathbf{r}}^2 \delta(\mathbf{r}' - \mathbf{r})$, and we can apply the two-dimensional analogue of $f(x) \delta^{(n)}(x) = (-1)^n f^{(n)}(x) \delta(x)$ to obtain

$$\begin{aligned}
\int d^2q q^2 \mathbf{m}(\mathbf{q}) \cdot \mathbf{m}(-\mathbf{q}) &= \frac{1}{(L_x L_y)^2} \int d^2q \int d^2r \int d^2r' q^2 \mathbf{m}(\mathbf{r}) \cdot \mathbf{m}(\mathbf{r}') e^{i\mathbf{q} \cdot (\mathbf{r}' - \mathbf{r})} \\
&= -\frac{(2\pi)^2}{(L_x L_y)^2} \int d^2r \int d^2r' \mathbf{m}(\mathbf{r}) \cdot \mathbf{m}(\mathbf{r}') \delta(\mathbf{r}' - \mathbf{r}) \\
&= -\frac{(2\pi)^2}{(L_x L_y)^2} \int d^2r \mathbf{m}(\mathbf{r}) \cdot \nabla^2 \mathbf{m}(\mathbf{r}). \tag{B.13}
\end{aligned}$$

An analogous procedure yields, for the third integral in (B.8),

$$\int d^2q q^4 \mathbf{m}(\mathbf{q}) \cdot \mathbf{m}(-\mathbf{q}) = \frac{(2\pi)^2}{(L_x L_y)^2} \int d^2r \mathbf{m}(\mathbf{r}) \cdot \nabla^4 \mathbf{m}(\mathbf{r}). \tag{B.14}$$

Overall, the energy is then

$$\begin{aligned}
U &= -\frac{NS^2 L_x L_y}{2(2\pi)^2} \left[6(J_1 + J_2 + J_3 + 2J_4) \frac{(2\pi)^2}{(L_x L_y)^2} \int d^2r \right. \\
&\quad + \frac{3}{2} a^2 (J_1 3J_2 + 4J_3 + 14J_4) \frac{(2\pi)^2}{(L_x L_y)^2} \int d^2r \mathbf{m}(\mathbf{r}) \cdot \nabla^2 \mathbf{m}(\mathbf{r}) \\
&\quad \left. + \frac{3}{32} a^4 (J_1 + 9J_2 + 16J_3 + 98J_4) \frac{(2\pi)^2}{(L_x L_y)^2} \int d^2r \mathbf{m}(\mathbf{r}) \cdot \nabla^4 \mathbf{m}(\mathbf{r}) \right]. \tag{B.15}
\end{aligned}$$

The total number of spins is $N = 2nL_x L_y / (\sqrt{3}a^2)$, where n is the number of spins per unit cell. As we typically consider thin but three-dimensional systems, we further integrate over the direction perpendicular to the plane of the lattice. In this calculation, we assume that interactions between the lattice layers a distance c apart are small compared to the intra-layer interactions, and thus neglect them. Dropping the constant

first term, the energy can be written as

$$U = \int d^3r \left[-\frac{3nS^2}{2\sqrt{3}c}(J_1 + 3J_2 + 4J_3 + 14J_4)\mathbf{m}(\mathbf{r}) \cdot \nabla^2\mathbf{m}(\mathbf{r}) - \frac{3nS^2a^2}{32\sqrt{3}c}(J_1 + 9J_2 + 16J_3 + 98J_4)\mathbf{m}(\mathbf{r}) \cdot \nabla^4\mathbf{m}(\mathbf{r}) \right], \quad (\text{B.16})$$

where the extra factor of c^{-1} comes from transforming the sum over the lattice layers to an integral. We now define the exchange stiffness constants

$$I_1 \equiv -\frac{3nS^2}{\sqrt{3}c}(J_1 + 3J_2 + 4J_3 + 14J_4), \quad (\text{B.17a})$$

$$I_2 \equiv -\frac{3nS^2a^2}{16\sqrt{3}c}(J_1 + 9J_2 + 16J_3 + 98J_4), \quad (\text{B.17b})$$

such that the energy is written as

$$U = \int d^3r \left[\frac{I_1}{2}\mathbf{m}(\mathbf{r}) \cdot \nabla^2\mathbf{m}(\mathbf{r}) + \frac{I_2}{2}\mathbf{m}(\mathbf{r}) \cdot \nabla^4\mathbf{m}(\mathbf{r}) \right]. \quad (\text{B.18})$$

We note that $m_i\partial_\alpha m_i = 0$ as $|\mathbf{m}| = 1$ is constant, and hence the direction of infinitesimal changes in \mathbf{m} must be perpendicular to it. Then, $\partial_\alpha(m_i\partial_\alpha m_i) = 0 = \partial_\alpha m_i\partial_\alpha m_i + m_i\partial_\alpha\partial_\alpha m_i$, and thus $m_i\partial_\alpha\partial_\alpha m_i = -\partial_\alpha m_i\partial_\alpha m_i$, or $\mathbf{m} \cdot \nabla^2\mathbf{m} = -(\nabla\mathbf{m})^2$.

To re-write the other term, we use Green's vector identity

$$\nabla^2(\mathbf{a} \cdot \mathbf{b}) = \mathbf{a} \cdot \nabla^2\mathbf{b} - \mathbf{b} \cdot \nabla^2\mathbf{a} + 2\nabla \cdot [(\mathbf{b} \cdot \nabla)\mathbf{a} + \mathbf{b} \times (\nabla \times \mathbf{a})]. \quad (\text{B.19})$$

If we take $\mathbf{a} = \mathbf{m}$ and $\mathbf{b} = \nabla^2\mathbf{m}$, and noting that $\nabla^2(\mathbf{a} \cdot \mathbf{b}) = \nabla \cdot [\nabla(\mathbf{a} \cdot \mathbf{b})]$, we obtain

$$\nabla \cdot [\nabla(\mathbf{m} \cdot \nabla^2\mathbf{m})] = \mathbf{m} \cdot \nabla^4\mathbf{m} - \nabla^2\mathbf{m} \cdot \nabla^2\mathbf{m} + 2\nabla \cdot [(\nabla^2\mathbf{m} \cdot \nabla)\mathbf{m} + \nabla^2\mathbf{m} \times (\nabla \times \mathbf{m})]. \quad (\text{B.20})$$

When this expression is integrated over space, the terms that are divergences become boundary terms which are zero by Stoke's theorem and assuming that, infinitely far away, the texture is uniform such that the derivatives vanish. Thus, (B.18) can be re-written as

$$U = \int d^3r \left[-\frac{I_1}{2}(\nabla\mathbf{m})^2 + \frac{I_2}{2}(\nabla^2\mathbf{m})^2 \right], \quad (\text{B.21})$$

which completes the derivation of (4.3) from atomistic considerations of a triangular lattice. The procedure could be repeated for other lattice structures such as a square lattice with competing nearest and next-nearest neighbour interactions.

The expression for the saturation magnetisation M_s in terms of atomistic parameters for the triangular lattice reads

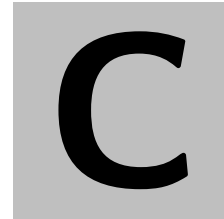
$$M_s = \frac{\mu}{V} = \frac{S\mu_B}{\sqrt{3}a^2c/2}, \quad (\text{B.22})$$

where μ is the magnetic moment and V is the volume of the system. As investigations into frustrated magnets in literature typically report the atomistic parameters, (B.17) and (B.22) are useful in performing micromagnetic simulations based on parameters

Appendix B. Derivation of Frustrated Energy Functional

for real materials. For example, using the values from Paddison et al. [204]: $S = 7/2$, $a = 0.406$ nm, $c = 0.409$ nm, $J_1 = 0.31$ K, $J_2 = 0.19$ K, $J_3 = 0.27$ K, $J_4 = -0.21$ K, as well as $n = 1$, we obtain the numerical values $I_1 = 3.51 \times 10^{-13}$ J m⁻¹, $I_2 = 5.25 \times 10^{-32}$ J m, $M_s = 5.56 \times 10^5$ A m⁻¹. This gives a characteristic length scale of our magnetic system of $\sqrt{I_2/I_1} = 0.39$ nm, or a spin spiral wavelength of $\lambda = \sqrt{8\pi^2 I_2/I_1} = 1.72$ nm.

Appendix



Numerical Implementation of Effective Fields in MuMax3

For the investigation of the behaviour of skyrmions in frustrated magnets subjected to an applied electric field of Chapter 11, it was necessary to write extensions to the micromagnetic solver `MuMax3` to include the higher-order exchange term and the interaction of the induced polarisation with the applied electric field in (11.1). In this Appendix, we discuss the implementation of these effective fields.

C.1. Internal Structure of MuMax3

As `MuMax3` is a package for numerically integrating the LLG equation, each energy contribution is programmed using its effective field, rather than the energy term itself¹. `MuMax3` is written in Go, with performance-critical parts (such as the calculation of effective fields) written in `CUDA`, a programming language for the parallelisation of calculations on Nvidia GPUs. Functions parallelised on the GPU using `CUDA` are known as `CUDA` kernels.

The two subdirectories of the `MuMax3` root directory that are important for adding additional energy terms are the `engine` and `cuda` directories. In this Section, we explain the functions that are called during each LLG time integration step to calculate the effective field, which is used by `MuMax3` to evolve the magnetisation.

Firstly, at each time integration step, the function `engine.SetEffectiveField()` of `engine/effectivefield.go` is called. This function is responsible for adding the effective fields from the various energy terms to the total effective field and calls functions to individually add each term. The function is shown in the following Listing C.1.

```
1 func SetEffectiveField(dst *data.Slice) {
2     SetDemagField(dst) // set to B_demag...
3     AddExchangeField(dst) // ...then add other terms
4     AddAnisotropyField(dst)
5     AddMagnetoelasticField(dst)
6     B_ext.AddTo(dst)
```

¹When the energy contribution from each interaction is required, rather than explicitly calculating the energy term, `MuMax3` takes the scalar product of the contribution's effective field with the magnetisation.

```

7     if !relaxing {
8         B_therm.AddTo(dst)
9     }
10    AddCustomField(dst)
11 }

```

Listing C.1: Code from `engine/effectivefield.go` which sets the effective field at each LLG integration time step

Taking the exchange interaction as an example, the relevant function to add this effective field term, called from `engine.SetEffectiveField()`, is `engine.AddExchangeField()`. This calls functions to calculate the exchange contribution to the total effective field, and is shown in the following Listing C.2.

```

1 func AddExchangeField(dst *data.Slice) {
2     inter := !Dind.isZero()
3     bulk := !Dbulk.isZero()
4     ms := Msat.MSlice()
5     defer ms.Recycle()
6     switch {
7     case !inter && !bulk:
8         cuda.AddExchange(dst, M.Buffer(), lex2.Gpu(), ms, regions.Gpu(),
9 M.Mesh())
10    case inter && !bulk:
11        Refer("mulkers2017")
12        cuda.AddDMI(dst, M.Buffer(), lex2.Gpu(), din2.Gpu(), ms, regions.
13 Gpu(), M.Mesh(), OpenBC) // dmi+exchange
14    case bulk && !inter:
15        cuda.AddDMIBulk(dst, M.Buffer(), lex2.Gpu(), dbulk2.Gpu(), ms,
16 regions.Gpu(), M.Mesh(), OpenBC) // dmi+exchange
17    case inter && bulk:
18        util.Fatal("Cannot have interfacial-induced DMI and bulk DMI at
19 the same time")
20    }
21 }

```

Listing C.2: Code from `engine/exchange.go` to call functions that calculate the contribution to the effective field from the symmetric exchange energy term.

In MuMax3, the exchange contribution to the effective field also includes the DMI effective field if this is present in the system being modelled, so the function called to calculate the effective field changes accordingly depending on whether or not DMI is present, and the type of DMI. This was implemented in the code above using a switch statement. As an example, we consider the case in which no DMI is present, such that `cuda.AddExchange()`, defined in `cuda/exchange.go`, is called. The function `cuda.AddExchange()` is shown below.

```

1 func AddExchange(B, m *data.Slice, Aex_red SymmLUT, Msat MSlice, regions
2 *Bytes, mesh *data.Mesh) {
3     c := mesh.CellSize()
4     wx := float32(2 / (c[X] * c[X]))
5     wy := float32(2 / (c[Y] * c[Y]))
6     wz := float32(2 / (c[Z] * c[Z]))
7     N := mesh.Size()
8     pbc := mesh.PBC_code()
9     cfg := make3DConf(N)
10    k_addexchange_async(B.DevPtr(X), B.DevPtr(Y), B.DevPtr(Z),
11 m.DevPtr(X), m.DevPtr(Y), m.DevPtr(Z),

```

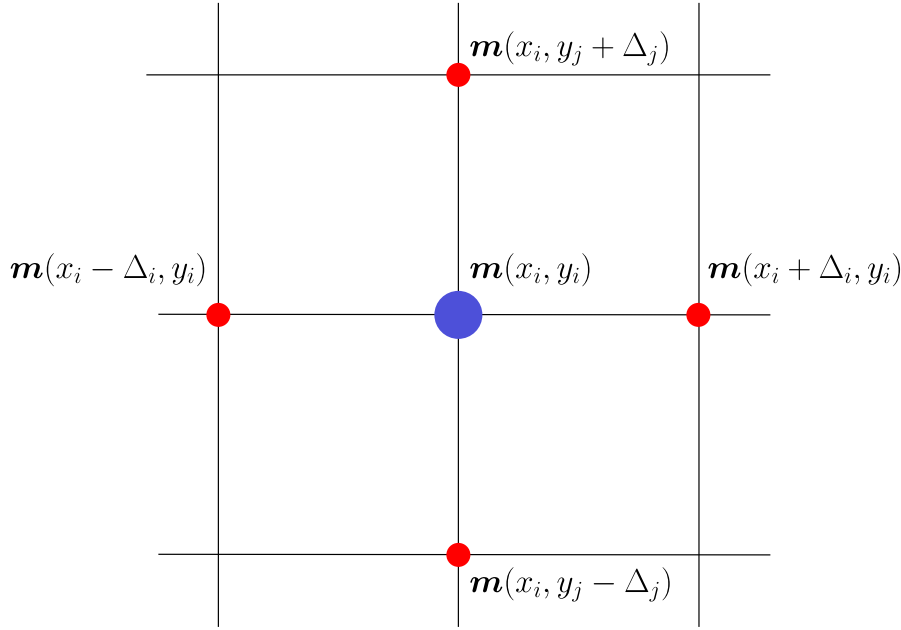


Figure C.1.: Stencil to approximate the derivatives of the magnetisation $\mathbf{m}(\mathbf{r})$ using nearest-neighbours.

```

11 Msat.DevPtr(0), Msat.Mul(0),
12 unsafe.Pointer(Aex_red), regions.Ptr,
13 wx, wy, wz, N[X], N[Y], N[Z], pbc, cfg)
14 }

```

Listing C.3: Code from `cuda/engine.go` which interfaces with the CUDA kernel to calculate the exchange effective field.

This function calls the `cuda.k_addexchange_async()` function, which is a CUDA wrapper to interface with the CUDA kernel. The file containing `cuda.k_addexchange_async()` is automatically generated when the CUDA kernels are compiled, and we do not show it here. Finally, the CUDA code to calculate the effective field is given in `cuda/exchange.cu`. This implements a discretised version of the effective field due to the symmetric exchange interaction

$$\mathbf{B}_{\text{eff}} = \frac{2A}{M_s} \sum_i \partial_i^2 \mathbf{m}, \quad (\text{C.1})$$

where the sum runs over $i \in \{x, y, z\}$. In MuMax3, this is discretised as

$$\mathbf{B}_{\text{eff}} = \frac{2A}{M_s} \sum_i \frac{\mathbf{m}(\mathbf{r}_i + \Delta_i) - 2\mathbf{m}(\mathbf{r}_i) + \mathbf{m}(\mathbf{r}_i - \Delta_i)}{\Delta_i}, \quad (\text{C.2})$$

which is illustrated in Fig. C.1. The CUDA kernel implementing this is shown in the following listing.

```

1 #include <stdint.h>
2 #include "exchange.h"
3 #include "float3.h"
4 #include "stencil.h"
5 #include "amul.h"
6

```

Appendix C. Numerical Implementation of Effective Fields in MuMax3

```

7 // See exchange.go for more details.
8 extern "C" __global__ void
9 addexchange(float* __restrict__ Bx, float* __restrict__ By, float*
  __restrict__ Bz,
10             float* __restrict__ mx, float* __restrict__ my, float*
  __restrict__ mz,
11             float* __restrict__ Ms_, float Ms_mul,
12             float* __restrict__ aLUT2d, uint8_t* __restrict__ regions,
13             float wx, float wy, float wz, int Nx, int Ny, int Nz, uint8_t
  PBC) {
14
15     int ix = blockIdx.x * blockDim.x + threadIdx.x;
16     int iy = blockIdx.y * blockDim.y + threadIdx.y;
17     int iz = blockIdx.z * blockDim.z + threadIdx.z;
18
19     if (ix >= Nx || iy >= Ny || iz >= Nz) {
20         return;
21     }
22
23     // central cell
24     int I = idx(ix, iy, iz);
25     float3 m0 = make_float3(mx[I], my[I], mz[I]);
26
27     if (is0(m0)) {
28         return;
29     }
30
31     uint8_t r0 = regions[I];
32     float3 B = make_float3(0.0,0.0,0.0);
33
34     int i_; // neighbor index
35     float3 m_; // neighbor mag
36     float a__; // inter-cell exchange stiffness
37
38     // left neighbor
39     i_ = idx(lclampx(ix-1), iy, iz); // clamps or wraps index
  according to PBC
40     m_ = make_float3(mx[i_], my[i_], mz[i_]); // load m
41     m_ = ( is0(m_)? m0: m_ ); // replace missing non-
  boundary neighbor
42     a__ = aLUT2d[symidx(r0, regions[i_])];
43     B += wx * a__ *(m_ - m0);
44
45     // right neighbor
46     i_ = idx(hclampx(ix+1), iy, iz);
47     m_ = make_float3(mx[i_], my[i_], mz[i_]);
48     m_ = ( is0(m_)? m0: m_ );
49     a__ = aLUT2d[symidx(r0, regions[i_])];
50     B += wx * a__ *(m_ - m0);
51
52     // back neighbor
53     i_ = idx(ix, lclampy(iy-1), iz);
54     m_ = make_float3(mx[i_], my[i_], mz[i_]);
55     m_ = ( is0(m_)? m0: m_ );
56     a__ = aLUT2d[symidx(r0, regions[i_])];
57     B += wy * a__ *(m_ - m0);
58
59     // front neighbor
60     i_ = idx(ix, hclampy(iy+1), iz);
61     m_ = make_float3(mx[i_], my[i_], mz[i_]);

```

```

62     m_ = ( is0(m_)? m0: m_ );
63     a__ = aLUT2d[symidx(r0, regions[i_])];
64     B += wy * a__ *(m_ - m0);
65
66     // only take vertical derivative for 3D sim
67     if (Nz != 1) {
68         // bottom neighbor
69         i_ = idx(ix, iy, lclampz(iz-1));
70         m_ = make_float3(mx[i_], my[i_], mz[i_]);
71         m_ = ( is0(m_)? m0: m_ );
72         a__ = aLUT2d[symidx(r0, regions[i_])];
73         B += wz * a__ *(m_ - m0);
74
75         // top neighbor
76         i_ = idx(ix, iy, hclampz(iz+1));
77         m_ = make_float3(mx[i_], my[i_], mz[i_]);
78         m_ = ( is0(m_)? m0: m_ );
79         a__ = aLUT2d[symidx(r0, regions[i_])];
80         B += wz * a__ *(m_ - m0);
81     }
82
83     float invMs = inv_Msat(Ms_, Ms_mul, I);
84     Bx[I] += B.x*invMs;
85     By[I] += B.y*invMs;
86     Bz[I] += B.z*invMs;
87 }

```

Listing C.4: CUDA kernel from `cuda/exchange.cu` to calculate the contribution to the effective field from symmetric exchange interactions.

Note that, instead of dividing by the cell discretisation sizes, their reciprocal is passed to the CUDA kernel. This means that the computationally expensive division operation is performed on the CPU, which is more efficient than calculating it on the GPU.

In summary, the steps to be followed to add a custom effective field to MuMax3 are:

1. Add the CUDA kernel to calculate the effective field to the `cuda` directory.
2. Add the corresponding Go file to the `cuda` directory, which calls the function defined in the CUDA wrapper file generated when the CUDA kernels are compiled.
3. Add a file in the `engine` directory to call the code from the `cuda` directory. If an energy contribution that already exists is being modified, instead of adding a new file, modify the existing file in the `engine` directory accordingly.
4. Add the new field to `SetEffectiveField()` from `engine/effectivefield.go` if a new energy term was added (as opposed to an existing term modified).
5. Compile the CUDA kernels by running `make` from the `cuda` directory.
6. Run `go install` from the `cmd/mumax3` directory, which puts the compiled MuMax3 binary in `$GOPATH/bin`.

C.2. Implementation of Higher-Order Exchange

To numerically calculate the effective field corresponding to the frustrated exchange functional (4.3), we perform a discretisation analogous to in (C.2). The effective field

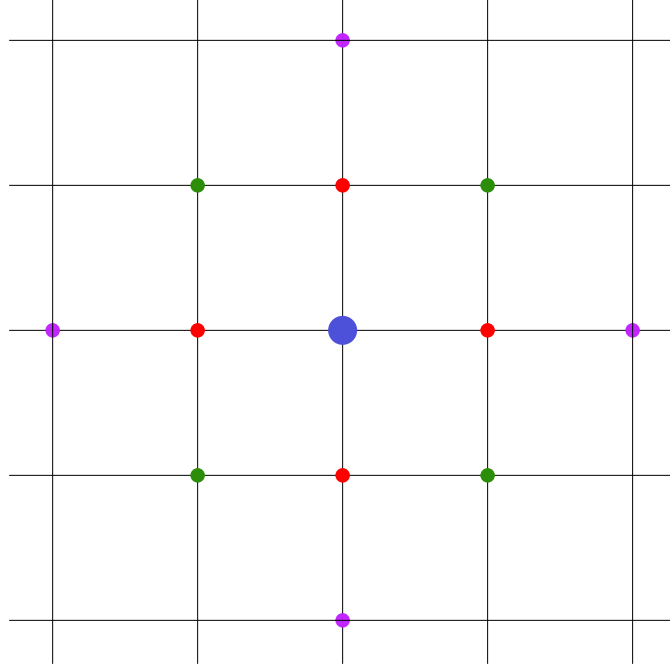


Figure C.2.: The stencil used to numerically evaluate the effective field for a magnet with competing exchange interactions.

reads

$$\mathbf{B}_{\text{eff}} = -\frac{I_1}{M_s} \sum_i \partial_i^2 \mathbf{m} - \frac{I_2}{M_s} \left[\sum_i \partial_i^4 \mathbf{m} + 2 \sum_{i>j} \partial_i^2 \partial_j^2 \mathbf{m} \right]. \quad (\text{C.3})$$

The discretised form of this expression is long, and we break it up into contributions from the various n th-nearest-neighbours. The colour coding for the contribution from each neighbour matches Fig. C.2.

$$\begin{aligned} \mathbf{B}_{\text{eff}} = & \frac{2I_1}{M_s} \left(\frac{1}{\Delta_x^2} + \frac{1}{\Delta_y^2} + \frac{1}{\Delta_z^2} \right) \mathbf{m} - \frac{6I_2}{M_s} \left(\frac{1}{\Delta_x^4} + \frac{1}{\Delta_y^4} + \frac{1}{\Delta_z^4} \right) \mathbf{m} \\ & - \frac{8I_2}{M_s} \left(\frac{1}{\Delta_x^2 \Delta_y^2} + \frac{1}{\Delta_x^2 \Delta_z^2} + \frac{1}{\Delta_y^2 \Delta_z^2} \right) \mathbf{m} \\ & + \sum_{\text{neighbours}} \left[-\frac{I_1}{M_s \Delta_i^2} + 4I_2 \left(\frac{1}{\Delta_i^4} + \frac{1}{\Delta_i^2 \Delta_j^2} + \frac{1}{\Delta_i^2 \Delta_k^2} \right) \right] \mathbf{m} \\ & - \sum_{\text{neighbours}} \frac{2I_2}{M_s \Delta_j^2 \Delta_k^2} \mathbf{m} - \sum_{\text{neighbours}} \frac{I_2}{M_s \Delta_i^4} \mathbf{m}. \quad (\text{C.4}) \end{aligned}$$

The corresponding CUDA kernel is shown below.

```

1 #include <stdint.h>
2 #include "exchange.h"
3 #include "float3.h"
4 #include "stencil.h"
5 #include "amul.h"
6
7 // See exchange_fourth_order.go for more details.
    
```


C.2. Implementation of Higher-Order Exchange

```

8
9 extern "C" __global__ void
10 addexchangefourthorder(float* __restrict__ Bx, float* __restrict__ By,
11     float* __restrict__ Bz,
12     float* __restrict__ mx, float* __restrict__ my, float*
13     __restrict__ mz,
14     float* __restrict__ Ms_, float Ms_mul,
15     float* __restrict__ I1, float* __restrict__ I2,
16     uint8_t* __restrict__ regions,
17     float wx, float wy, float wz, int Nx, int Ny, int Nz, uint8_t
18     PBC) {
19
20     int ix = blockIdx.x * blockDim.x + threadIdx.x;
21     int iy = blockIdx.y * blockDim.y + threadIdx.y;
22     int iz = blockIdx.z * blockDim.z + threadIdx.z;
23
24     if (ix >= Nx || iy >= Ny || iz >= Nz) {
25         return;
26     }
27
28     // central cell
29     int I = idx(ix, iy, iz);
30     float3 m0 = make_float3(mx[I], my[I], mz[I]);
31
32     if (is0(m0)) {
33         return;
34     }
35
36     uint8_t r0 = regions[I];
37     float3 B = make_float3(0.0,0.0,0.0);
38
39     int i_; // neighbor index
40     float3 m_; // neighbor mag
41     float I1__; // second-order exchange stiffness
42     float I2__; // fourth-order exchange stiffness
43
44     ////////////////
45     // Central Spin //
46     ////////////////
47     i_ = idx(ix, iy, iz);
48     m_ = make_float3(mx[i_], my[i_], mz[i_]);
49     // load m
50     m_ = ( is0(m_)? m0: m_ );
51     // replace missing non-boundary neighbor
52     I1__ = I1[symidx(r0, regions[i_])];
53     I2__ = I2[symidx(r0, regions[i_])];
54     B += 2 * I1__ * (wx*wx + wy*wy + wz*wz) * m_;
55     B -= 6 * I2__ * (wx*wx*cw*cw + wy*wy*wy*wy + wz*wz*wz*wz) * m_;
56     B -= 8 * I2__ * (wx*wx*wy*wy + wx*wx*wz*wz + wy*wy*wz*wz) * m_;
57
58     ////////////////
59     // Direct Nearest Neighbours //
60     ////////////////
61
62     // Left neighbour
63     i_ = idx(lclampx(ix-1), iy, iz);
64     // clamps or wraps index according to PBC

```

Appendix C. Numerical Implementation of Effective Fields in MuMax3

```

61     m_   = make_float3(mx[i_], my[i_], mz[i_]);
        // load m
62     m_   = ( is0(m_)? m0: m_ );
        // replace missing non-boundary neighbor
63     I1__ = I1[symidx(r0, regions[i_])];
64     I2__ = I2[symidx(r0, regions[i_])];
65     B    -= (I1__ * wx*wx) * m_;
66     B    += 4 * I2__ * (wx*wx*wx*wx + wx*wx*wy*wy + wx*wx*wz*wz) * m_;
67
68     // Right neighbour
69     i_   = idx(hclampx(ix+1), iy, iz);
        // clamps or wraps index according to PBC
70     m_   = make_float3(mx[i_], my[i_], mz[i_]);
        // load m
71     m_   = ( is0(m_)? m0: m_ );
        // replace missing non-boundary neighbor
72     I1__ = I1[symidx(r0, regions[i_])];
73     I2__ = I2[symidx(r0, regions[i_])];
74     B    -= (I1__ * wx*wx) * m_;
75     B    += 4 * I2__ * (wx*wx*wx*wx + wx*wx*wy*wy + wx*wx*wz*wz) * m_;
76
77     // Below neighbour
78     i_   = idx(ix, lclampy(iy-1), iz);
        // clamps or wraps index according to PBC
79     m_   = make_float3(mx[i_], my[i_], mz[i_]);
        // load m
80     m_   = ( is0(m_)? m0: m_ );
        // replace missing non-boundary neighbor
81     I1__ = I1[symidx(r0, regions[i_])];
82     I2__ = I2[symidx(r0, regions[i_])];
83     B    -= (I1__ * wy*wy) * m_;
84     B    += 4 * I2__ * (wy*wy*wy*wy + wy*wy*wx*wx + wy*wy*wz*wz) * m_;
85
86     // Above neighbour
87     i_   = idx(ix, hclampy(iy+1), iz);
        // clamps or wraps index according to PBC
88     m_   = make_float3(mx[i_], my[i_], mz[i_]);
        // load m
89     m_   = ( is0(m_)? m0: m_ );
        // replace missing non-boundary neighbor
90     I1__ = I1[symidx(r0, regions[i_])];
91     I2__ = I2[symidx(r0, regions[i_])];
92     B    -= (I1__ * wy*wy) * m_;
93     B    += 4 * I2__ * (wy*wy*wy*wy + wy*wy*wx*wx + wy*wy*wz*wz) * m_;
94
95     // Bottom neighbour
96     i_   = idx(ix, iy, lclampz(iz-1));
        // clamps or wraps index according to PBC
97     m_   = make_float3(mx[i_], my[i_], mz[i_]);
        // load m
98     m_   = ( is0(m_)? m0: m_ );
        // replace missing non-boundary neighbor
99     I1__ = I1[symidx(r0, regions[i_])];
100    I2__ = I2[symidx(r0, regions[i_])];
101    B    -= (I1__ * wz*wz) * m_;
102    B    += 4 * I2__ * (wz*wz*wz*wz + wz*wz*wx*wx + wz*wz*wy*wy) * m_;
103
104    // Top neighbour
105    i_   = idx(ix, iy, hclampz(iz+1));
        // clamps or wraps index according to PBC

```

C.2. Implementation of Higher-Order Exchange

```

106     m_   = make_float3(mx[i_], my[i_], mz[i_]);
           // load m
107     m_   = ( is0(m_)? m0: m_ );
           // replace missing non-boundary neighbor
108     I1__ = I1[symidx(r0, regions[i_])];
109     I2__ = I2[symidx(r0, regions[i_])];
110     B    -= (I1__ * wz*wz) * m_;
111     B    += 4 * I2__ * (wz*wz*wz*wz + wz*wz*wx*wx + wz*wz*wy*wy) * m_;
112
113
114     //////////////////////////////////////
115     // Diagonal Nearest Neighbours in z=0 Plane //
116     //////////////////////////////////////
117
118     // Bottom-left neighbour
119     i_   = idx(lclampx(ix-1), lclampy(iy-1), iz); // clamps or wraps
           index according to PBC
120     m_   = make_float3(mx[i_], my[i_], mz[i_]); // load m
121     m_   = ( is0(m_)? m0: m_ ); // replace missing
           non-boundary neighbor
122     I2__ = I2[symidx(r0, regions[i_])];
123     B    -= (2 * I2__ * wx*wx*wy*wy) * m_;
124
125     // Top-left neighbour
126     i_   = idx(lclampx(ix-1), hclampy(iy+1), iz); // clamps or wraps
           index according to PBC
127     m_   = make_float3(mx[i_], my[i_], mz[i_]); // load m
128     m_   = ( is0(m_)? m0: m_ ); // replace missing
           non-boundary neighbor
129     I2__ = I2[symidx(r0, regions[i_])];
130     B    -= (2 * I2__ * wx*wx*wy*wy) * m_;
131
132     // Bottom-right neighbour
133     i_   = idx(hclampx(ix+1), lclampy(iy-1), iz); // clamps or wraps
           index according to PBC
134     m_   = make_float3(mx[i_], my[i_], mz[i_]); // load m
135     m_   = ( is0(m_)? m0: m_ ); // replace missing
           non-boundary neighbor
136     I2__ = I2[symidx(r0, regions[i_])];
137     B    -= (2 * I2__ * wx*wx*wy*wy) * m_;
138
139     // Top-right neighbour
140     i_   = idx(hclampx(ix+1), hclampy(iy+1), iz); // clamps or wraps
           index according to PBC
141     m_   = make_float3(mx[i_], my[i_], mz[i_]); // load m
142     m_   = ( is0(m_)? m0: m_ ); // replace missing
           non-boundary neighbor
143     I2__ = I2[symidx(r0, regions[i_])];
144     B    -= (2 * I2__ * wx*wx*wy*wy) * m_;
145
146
147     //////////////////////////////////////
148     // Diagonal Nearest Neighbours in x=0 Plane //
149     //////////////////////////////////////
150
151     // Bottom-left neighbour
152     i_   = idx(ix, lclampy(iy-1), hclampz(iz+1)); // clamps or wraps
           index according to PBC
153     m_   = make_float3(mx[i_], my[i_], mz[i_]); // load m

```

Appendix C. Numerical Implementation of Effective Fields in MuMax3

```

154     m_      = ( is0(m_)? m0: m_ );           // replace missing
non-boundary neighbor
155     I2__   = I2[symidx(r0, regions[i_])];
156     B      -= (2 * I2__ * wy*wy*wz*wz) * m_;
157
158     // Top-left neighbour
159     i_     = idx(ix, hclampy(iy+1), hclampz(iz+1)); // clamps or wraps
index according to PBC
160     m_     = make_float3(mx[i_], my[i_], mz[i_]); // load m
161     m_     = ( is0(m_)? m0: m_ );           // replace missing
non-boundary neighbor
162     I2__   = I2[symidx(r0, regions[i_])];
163     B      -= (2 * I2__ * wy*wy*wz*wz) * m_;
164
165     // Bottom-right neighbour
166     i_     = idx(ix, lclampy(iy-1), lclampz(iz-1)); // clamps or wraps
index according to PBC
167     m_     = make_float3(mx[i_], my[i_], mz[i_]); // load m
168     m_     = ( is0(m_)? m0: m_ );           // replace missing
non-boundary neighbor
169     I2__   = I2[symidx(r0, regions[i_])];
170     B      -= (2 * I2__ * wy*wy*wz*wz) * m_;
171
172     // Top-right neighbour
173     i_     = idx(ix, hclampy(iy+1), lclampz(iz-1)); // clamps or wraps
index according to PBC
174     m_     = make_float3(mx[i_], my[i_], mz[i_]); // load m
175     m_     = ( is0(m_)? m0: m_ );           // replace missing
non-boundary neighbor
176     I2__   = I2[symidx(r0, regions[i_])];
177     B      -= (2 * I2__ * wy*wy*wz*wz) * m_;
178
179
180     ////////////////////////////////////////
181     // Diagonal Nearest Neighbours in y=0 Plane //
182     ////////////////////////////////////////
183
184     // Bottom-left neighbour
185     i_     = idx(lclampx(ix-1), iy, hclampz(iz+1)); // clamps or wraps
index according to PBC
186     m_     = make_float3(mx[i_], my[i_], mz[i_]); // load m
187     m_     = ( is0(m_)? m0: m_ );           // replace missing
non-boundary neighbor
188     I2__   = I2[symidx(r0, regions[i_])];
189     B      -= (2 * I2__ * wx*wx*wz*wz) * m_;
190
191     // Top-left neighbour
192     i_     = idx(lclampx(ix-1), iy, lclampz(iz-1)); // clamps or wraps
index according to PBC
193     m_     = make_float3(mx[i_], my[i_], mz[i_]); // load m
194     m_     = ( is0(m_)? m0: m_ );           // replace missing
non-boundary neighbor
195     I2__   = I2[symidx(r0, regions[i_])];
196     B      -= (2 * I2__ * wx*wx*wz*wz) * m_;
197
198     // Bottom-right neighbour
199     i_     = idx(hclampx(ix+1), iy, hclampz(iz+1)); // clamps or wraps
index according to PBC
200     m_     = make_float3(mx[i_], my[i_], mz[i_]); // load m

```

C.2. Implementation of Higher-Order Exchange

```

201   m_   = ( is0(m_)? m0: m_ );           // replace missing
non-boundary neighbor
202   I2__ = I2[symidx(r0, regions[i_])];
203   B    -= (2 * I2__ * wx*wx*wz*wz) * m_;
204
205   // Top-right neighbour
206   i_   = idx(hclampx(ix+1), iy, lclampz(iz-1)); // clamps or wraps
index according to PBC
207   m_   = make_float3(mx[i_], my[i_], mz[i_]); // load m
208   m_   = ( is0(m_)? m0: m_ );           // replace missing
non-boundary neighbor
209   I2__ = I2[symidx(r0, regions[i_])];
210   B    -= (2 * I2__ * wx*wx*wz*wz) * m_;
211
212
213   ////////////////////////////////////////////////////
214   // Next-Next-Next Nearest Neighbours //
215   ////////////////////////////////////////////////////
216
217   // Two over to left
218   i_   = idx(lclampx(ix-2), iy, iz);     // clamps or wraps
index according to PBC
219   m_   = make_float3(mx[i_], my[i_], mz[i_]); // load m
220   m_   = ( is0(m_)? m0: m_ );           // replace missing non-
boundary neighbor
221   I2__ = I2[symidx(r0, regions[i_])];
222   B    -= (I2__ * wx*wx*wx*wx) * m_;
223
224   // Two over to right
225   i_   = idx(hclampx(ix+2), iy, iz);     // clamps or wraps
index according to PBC
226   m_   = make_float3(mx[i_], my[i_], mz[i_]); // load m
227   m_   = ( is0(m_)? m0: m_ );           // replace missing non-
boundary neighbor
228   I2__ = I2[symidx(r0, regions[i_])];
229   B    -= (I2__ * wx*wx*wx*wx) * m_;
230
231   // Two below
232   i_   = idx(ix, lclampy(iy-2), iz);     // clamps or wraps
index according to PBC
233   m_   = make_float3(mx[i_], my[i_], mz[i_]); // load m
234   m_   = ( is0(m_)? m0: m_ );           // replace missing non-
boundary neighbor
235   I2__ = I2[symidx(r0, regions[i_])];
236   B    -= (I2__ * wy*wy*wy*wy) * m_;
237
238   // Two above
239   i_   = idx(ix, hclampy(iy+2), iz);     // clamps or wraps
index according to PBC
240   m_   = make_float3(mx[i_], my[i_], mz[i_]); // load m
241   m_   = ( is0(m_)? m0: m_ );           // replace missing non-
boundary neighbor
242   I2__ = I2[symidx(r0, regions[i_])];
243   B    -= (I2__ * wy*wy*wy*wy) * m_;
244
245   // Two bottom
246   i_   = idx(ix, iy, lclampz(iz-2));     // clamps or wraps
index according to PBC
247   m_   = make_float3(mx[i_], my[i_], mz[i_]); // load m

```

```

248     m_      = ( is0(m_)? m0: m_ );           // replace missing non-
boundary neighbor
249     I2__    = I2[symidx(r0, regions[i_])];
250     B       -= (I2__ * wz*wz*wz*wz) * m_;
251
252     // Two top
253     i_      = idx(ix, iy, hclampz(iz+2));   // clamps or wraps
index according to PBC
254     m_      = make_float3(mx[i_], my[i_], mz[i_]); // load m
255     m_      = ( is0(m_)? m0: m_ );           // replace missing non-
boundary neighbor
256     I2__    = I2[symidx(r0, regions[i_])];
257     B       -= (I2__ * wz*wz*wz*wz) * m_;
258
259
260     float invMs = inv_Msat(Ms_, Ms_mul, I);
261
262     Bx[I] += B.x*invMs;
263     By[I] += B.y*invMs;
264     Bz[I] += B.z*invMs;
265
266 }
    
```

Listing C.5: CUDA kernel for the calculation of the effective field of the frustrated exchange in the energy functional (11.1).

C.3. Implementation of an Applied Electric Field

The effective field resulting in the interaction between an externally applied electric field $\mathbf{E}_{\text{ext}} = E\hat{z}$ and the induced polarisation given by (4.18) is given by

$$\mathbf{B}_{\text{eff}} = \frac{2EP_{Ea}}{M_s} [(\nabla \cdot \mathbf{m})\hat{z} - \nabla m_z], \quad (\text{C.5})$$

where the quantities are as discussed in Section 4.1. The CUDA kernel is given below, where we have combined EP_{Ea} into a single variable E_{red} , as we work in rescaled units in Chapter 11. The effective field is discretised as

$$\mathbf{B}_{\text{eff}} = \frac{E_{\text{red}}}{M_s} \left[\left(\frac{m_x(i+1, j) - m_x(i-1, j)}{\Delta_x} + \frac{m_y(i, j+1) - m_y(i, j-1)}{\Delta_y} \right) \hat{z} - \frac{m_z(i+1, j) - m_z(i-1, j)}{\Delta_x} \hat{x} - \frac{m_z(i, j+1) - m_z(i, j-1)}{\Delta_y} \hat{y} \right], \quad (\text{C.6})$$

where i and j are the indices of the cells along the x - and y -axes respectively. This discretised form of the effective field due to the applied electric field is implemented in the CUDA kernel below.

```

1 #include <stdint.h>
2 #include "exchange.h"
3 #include "stencil.h"
4 #include "amul.h"
5
6 // Electric field term according to
    
```

C.3. Implementation of an Applied Electric Field

```

7 // Katsura, Nagaosa, Balatsky, Phys. Rev. Lett. 95, 057205 (2005).
8
9 extern "C" __global__ void
10 addelectric(float* __restrict__ Bx, float* __restrict__ By, float*
11 __restrict__ Bz,
12 float* __restrict__ mx, float* __restrict__ my, float*
13 __restrict__ mz,
14 float* __restrict__ Ms_, float Ms_mul,
15 float* __restrict__ eLUT2d, uint8_t* __restrict__ regions,
16 float wx, float wy, float wz, int Nx, int Ny, int Nz, uint8_t
17 PBC) {
18
19     int ix = blockIdx.x * blockDim.x + threadIdx.x;
20     int iy = blockIdx.y * blockDim.y + threadIdx.y;
21     int iz = blockIdx.z * blockDim.z + threadIdx.z;
22
23     if (ix >= Nx || iy >= Ny || iz >= Nz) {
24         return;
25     }
26
27     // central cell
28     int I = idx(ix, iy, iz);
29     float3 m0 = make_float3(mx[I], my[I], mz[I]);
30
31     if (is0(m0)) {
32         return;
33     }
34
35     uint8_t r0 = regions[I];
36     float3 B = make_float3(0.0,0.0,0.0);
37
38     int i_; // neighbor index
39     float3 m_; // neighbor mag
40     float ered_; // reduced electric field
41
42     // x derivatives
43
44     // right neighbor
45     i_ = idx(hclampx(ix+1), iy, iz); // clamps or wraps index
46     according to PBC
47     m_ = make_float3(mx[i_], my[i_], mz[i_]); // load m
48     m_ = ( is0(m_)? m0: m_ ); // replace missing non-
49     boundary neighbor
50     ered_ = eLUT2d[symidx(r0, regions[i_])];
51     B.x -= (ered_ * wx) * m_.z;
52     B.z += (ered_ * wx) * m_.x;
53
54     // left neighbor
55     i_ = idx(lclampx(ix-1), iy, iz); // clamps or wraps index
56     according to PBC
57     m_ = make_float3(mx[i_], my[i_], mz[i_]); // load m
58     m_ = ( is0(m_)? m0: m_ ); // replace missing non-
59     boundary neighbor
60     ered_ = eLUT2d[symidx(r0, regions[i_])];
61     B.x += (ered_ * wx) * m_.z;
62     B.z -= (ered_ * wx) * m_.x;

```

```

60  ////////////////////////////////////////////////////
61  // y derivatives //
62  ////////////////////////////////////////////////////
63
64  // above neighbor
65  i_ = idx(ix, hclampy(iy+1), iz);
66  m_ = make_float3(mx[i_], my[i_], mz[i_]);
67  m_ = ( is0(m_)? m0: m_ );
68  ered__ = eLUT2d[symidx(r0, regions[i_])];
69  B.y -= (ered__ * wy) * m_.z;
70  B.z += (ered__ * wy) * m_.y;
71
72  // below neighbor
73  i_ = idx(ix, lclampy(iy-1), iz);
74  m_ = make_float3(mx[i_], my[i_], mz[i_]);
75  m_ = ( is0(m_)? m0: m_ );
76  ered__ = eLUT2d[symidx(r0, regions[i_])];
77  B.y += (ered__ * wy) * m_.z;
78  B.z -= (ered__ * wy) * m_.y;
79
80
81  float invMs = inv_Msat(Ms_, Ms_mul, I);
82  Bx[I] += B.x*invMs;
83  By[I] += B.y*invMs;
84  Bz[I] += B.z*invMs;
85 }
    
```

Listing C.6: CUDA kernel to numerically calculate the effective magnetic field due to the interaction between an externally applied electric field and the induced polarisation from the magnetisation texture.

We must additionally write a function `engine.AddElectricEffectiveField`, and modify the function `engine.SetEffectiveField()` from Listing C.1 to call this function, in order to add the effective field from the applied electric field to the total effective field. We write a new file `engine/electric.go`, with the contents below.

```

1  package engine
2
3  import (
4      "github.com/mumax/3/cuda"
5      "github.com/mumax/3/data"
6  )
7
8  var (
9      Ered = NewScalarParam("Ered", "J/m2", "Electric field (V/m) *
10     Polarization (C/m2) * Lattice constant (m)", &ered)
11     ered exchParam
12
13     B_elec = NewVectorField("B_elec", "T", "Effective magnetic field
14     due to electric field", AddElectricEffectiveField)
15     E_elec = NewScalarValue("E_elec", "J", "Electric field energy
16     density", GetElectricFieldEnergy)
17     Edens_elec = NewScalarField("Edens_elec", "J/m3", "Total electric
18     field energy density", AddElectricFieldEnergyDensity)
19 )
20
21 func init() {
22     registerEnergy(GetElectricFieldEnergy, AddElectricFieldEnergyDensity)
23     ered.init(Ered)
24 }
    
```


C.3. Implementation of an Applied Electric Field

```
20 }
21
22 var AddElectricFieldEnergyDensity = makeEdensAdder(B_elec, -0.5)
23
24 func AddElectricEffectiveField(dst *data.Slice) {
25
26     // Force an update if time-varying
27     Ered.lut.source.update()
28
29     ms := Msat.MSlice()
30     defer ms.Recycle()
31     cuda.AddElectric(dst, M.Buffer(), ered.Gpu(), ms, regions.Gpu(), M.
32     Mesh())
33 }
34 func GetElectricFieldEnergy() float64 {
35     return -0.5 * cellVolume() * dot(&M_full, &B_elec)
36 }
```

Listing C.7: Go code to call the functions that calculate the effective field from the interaction between the applied electric field and the induced polarisation.

Appendix



Frustrated Magnet Ground State

It was stated in Section 5.4 that the ground state of a system described by the energy functional (5.14) is a conical state for an applied magnetic field of magnitude $B_{\text{ext}} < 1/4$ and a ferromagnetic state for $B_{\text{ext}} \geq 1/4$. The proof of this is provided in this Appendix by considering the magnetisation in Fourier space and writing the energy functional in completed square form. We write the magnetisation as a Fourier transform

$$\mathbf{m}(\mathbf{r}) = \sum_{\mathbf{q}} \mathbf{m}_{\mathbf{q}} e^{i\mathbf{q}\cdot\mathbf{r}}, \quad (\text{D.1})$$

where \mathbf{q} are the wavevectors of the Fourier modes. For second-order exchange term $(\nabla\mathbf{m})^2 = (\partial_a m^b)(\partial_a m^b)$, we see that

$$\partial_a m^b = i \sum_{\mathbf{q}} m_{\mathbf{q}}^b q^a e^{i\mathbf{q}\cdot\mathbf{r}}, \quad (\text{D.2})$$

and hence

$$(\nabla\mathbf{m})^2 = - \sum_{\mathbf{q}} \sum_{\mathbf{q}'} q^a q'^a m_{\mathbf{q}}^b m_{\mathbf{q}'}^b e^{i(\mathbf{q}+\mathbf{q}')\cdot\mathbf{r}}, \quad (\text{D.3})$$

the volume integral over which is

$$\begin{aligned} \int d^3r (\nabla\mathbf{m})^2 &= - \sum_{\mathbf{q}} \sum_{\mathbf{q}'} q^a q'^a m_{\mathbf{q}}^b m_{\mathbf{q}'}^b \int d^3r e^{i(\mathbf{q}+\mathbf{q}')\cdot\mathbf{r}} \\ &= -V \sum_{\mathbf{q}} \sum_{\mathbf{q}'} q^a q'^a m_{\mathbf{q}}^b m_{\mathbf{q}'}^b \delta_{\mathbf{q}-\mathbf{q}'} \\ &= V \sum_{\mathbf{q}} q^2 m_{\mathbf{q}}^a m_{-\mathbf{q}}^b \delta^{ab}, \end{aligned} \quad (\text{D.4})$$

where V is the total volume of the system. Similarly, the fourth order exchange term can be written as

$$\int d^3r (\nabla^2\mathbf{m})^2 = V \sum_{\mathbf{q}} q^4 m_{\mathbf{q}}^a m_{-\mathbf{q}}^b \delta^{ab}. \quad (\text{D.5})$$

Appendix D. Frustrated Magnet Ground State

Turning to the Zeeman term, we note that, upon integration, it vanishes for all \mathbf{m}_q where $q \neq 0$, and we therefore write it as

$$-\int d^3r \mathbf{B}_{\text{ext}} \cdot \mathbf{m} = -\int d^3r \mathbf{B}_{\text{ext}} \cdot \mathbf{m}_0 = V \left(\mathbf{m}_0 - \frac{\mathbf{B}_{\text{ext}}}{2} \right)^2 - V \mathbf{m}_0^2 - V \frac{\mathbf{B}_{\text{ext}}^2}{4}. \quad (\text{D.6})$$

Thus, (5.14) becomes

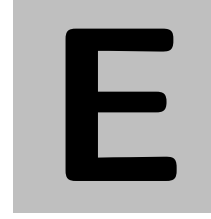
$$U = \frac{V}{2} \sum_{\mathbf{q}} m_{\mathbf{q}}^a \left(q^2 - \frac{1}{2} \right)^2 \delta^{ab} m_{-\mathbf{q}}^b - \frac{V}{8} \overbrace{\sum_{\mathbf{q}} m_{\mathbf{q}}^a \delta^{ab} m_{-\mathbf{q}}^b}^1 + \frac{V}{8} (\mathbf{m}_0 - 4\mathbf{B}_{\text{ext}})^2 - \frac{V}{8} \mathbf{m}_0^2 - 2V \mathbf{B}_{\text{ext}}^2, \quad (\text{D.7})$$

where, in the second term, we have used that $\mathbf{m}^2 = 1$, hence that $V \sum_{\mathbf{q}} m_{\mathbf{q}}^a \delta^{ab} m_{-\mathbf{q}}^b = \int d^3r \mathbf{m}^2 = V$. Splitting the first sum into $q = 0$ and $q \neq 0$ terms,

$$\begin{aligned} U &= \frac{V}{8} \sum_{\mathbf{q} \neq 0} m_{\mathbf{q}}^a \left(q^2 - \frac{1}{2} \right)^2 \delta^{ab} m_{-\mathbf{q}}^b + \frac{V}{8} \mathbf{m}_0^2 - \frac{V}{8} + \frac{V}{8} (\mathbf{m}_0 - 4\mathbf{B}_{\text{ext}})^2 \\ &\quad - \frac{V}{8} \mathbf{m}_0^2 - 2V \mathbf{B}_{\text{ext}}^2 \\ &= \frac{V}{2} \sum_{\mathbf{q} \neq 0} m_{\mathbf{q}}^a \left(q^2 - \frac{1}{2} \right)^2 \delta^{ab} m_{-\mathbf{q}}^b + \frac{V}{8} (\mathbf{m}_0 - 4\mathbf{B}_{\text{ext}})^2 - 2V \mathbf{B}_{\text{ext}}^2 - \frac{V}{8}. \end{aligned} \quad (\text{D.8})$$

The first term is positive semi-definite, the second term is non-negative, and the last two terms are a constant which bounds the energy from below. Therefore, a state satisfying $q = 1/\sqrt{2}$ and $\mathbf{m}_0 = 4\mathbf{B}_{\text{ext}}$ is a ground state. For $B_{\text{ext}} < 1/4$, this is fulfilled by a magnetisation vector field corresponding to the conical state (5.15). For $B_{\text{ext}} \geq 1/4$, the ferromagnetic state is a ground state.

Appendix



Derivation of the Cycloidal State Critical Current

In Chapter 7, we give an approximate value for the applied current/effective spin velocity required to create skyrmion/antiskyrmion pairs in the cycloidal state, which is given in (7.6). Here, we provide a derivation of this critical current.

We consider solutions to the equations of motion of the fluctuations in a domain wall (7.5) of the form of plane waves $\xi = \xi_0 e^{i(qx - \omega t)}$. For convenience, we define the variables

$$A = v_x + \frac{\pi}{2}, \quad (\text{E.1a})$$

$$B = \sqrt{2\kappa}, \quad (\text{E.1b})$$

$$C = \frac{2}{\lambda_c^2}, \quad (\text{E.1c})$$

$$D = \frac{\pi}{2} + \sqrt{2\kappa}. \quad (\text{E.1d})$$

Multiplying the equations of motion (7.5a) and (7.5b) together gives the solution for ω

$$\omega = \frac{\alpha i(2q^2 + C/B + BD) - 2Aq}{2(1 + \alpha^2)} \pm \frac{\sqrt{[2Aq - \alpha i(2q^2 + \frac{C}{B} + BD)]^2 + 4(1 + \alpha^2)[q^4 + q^2(BD + \frac{C}{B}) + CD - A^2q^2]}}{2(1 + \alpha^2)}. \quad (\text{E.2})$$

We write the discriminant, a complex number, in terms of its modulus r and phase ϕ , *i.e.*

$$\omega = \frac{\alpha i(2q^2 + C/B + BD) - 2Aq}{2(1 + \alpha^2)} \pm \frac{\sqrt{r} e^{i\phi}}{2(1 + \alpha)^2}. \quad (\text{E.3})$$

In order for the system to be stable, we require that $\text{Im}(\omega) < 0$, so the critical case is obtained by setting $\text{Im}(\omega) = 0$, *i.e.*

$$\alpha(2q^2 + C/B + BD) \pm \sqrt{r} \sin \frac{\phi}{2} = 0, \quad (\text{E.4})$$

Appendix E. Derivation of the Cycloidal State Critical Current

having used $\text{Im}(\sqrt{re^{i\phi}}) = \sqrt{r} \sin(\phi/2)$. Noting that $\sin(\phi/2) = \pm\sqrt{(1 - \cos \phi)/2}$, where $r \cos \phi$ is the real part of the discriminant, we can solve the above equation in the limit of small damping by Taylor expanding $\sqrt{r} \sin(\phi/2)$ to first order in α . This gives

$$\alpha(2q^2 + C/B + BD) \pm \frac{(B^2D + 2Bq^2 + C)A\alpha q}{\sqrt{B(Bq^4 + BCD + (B^2D + C)q^2)}} = 0. \quad (\text{E.5})$$

Minimising A (which is equal to $v_x + \pi/2$) with respect to q gives $q = \sqrt[4]{CD}$. Noting that, for $\kappa \rightarrow \kappa_c$, *i.e.* the anisotropy at which the cycloidal wavelength diverges, $\lambda_c \rightarrow \infty$. Then, $C \rightarrow 0$, and (E.5) reduces to $A = \sqrt{BD}$. Substituting back in the values from (E.1) yields

$$v_x = \sqrt{2\kappa_c + \frac{\pi}{2}\sqrt{2\kappa_c} - \frac{\pi}{2}} \approx 0.65, \quad (\text{E.6})$$

corresponding to (7.6). The **SageMath** notebook used in this calculation is provided below.

```

[1]: %display latex

A = var('A')
B = var('B')
C = var('C')
D = var('D')
q = var('q')
alpha = var('alpha')

# Restrict physical quantities to be real
assume(A, 'real')
assume(B, 'real')
assume(C, 'real')
assume(D, 'real')
assume(q, 'real')
assume(alpha, 'real')

# Discriminant of the quadratic equation
dis = (2*A*q - alpha*i*(2*q^2 + C/B + B*D))^2 + 4*(1+alpha^2) * (q^4 +
↪q^2*(B*D + C/B) + C*D - A^2 * q^2)

# Modulus of discriminant
r = sqrt(dis.real()^2 + dis.imag()^2)

# Discriminant is written as r*(cos(phi) + i*sin(phi))
cos_phi = dis.real() / r
sin_phi_2 = sqrt((1/2) * (1 - cos_phi))

```

Solve $\text{Im}(\omega) = 0$ for A , which is equal to critical current plus a constant of $\pi/2$.

```

[2]: LHS = (sqrt(r) * sin_phi_2).taylor(alpha, 0, 2)
RHS = alpha * (2*q^2 + C/B + B*D)

```

```

[3]: solve(LHS==RHS, A)[0].simplify_full().factor()

```

```

[3]: 
$$A = \frac{\sqrt{Bq^4 + BCD + (B^2D + C)q^2}}{\sqrt{B}q}$$


```

Minimise A with respect to q .

```

[4]: the_soln = sqrt(B*q^4 + (B^2*D + C)*q^2 + B*C*D) / (q * sqrt(B))
solve(the_soln.diff(q)==0, q)

```

```

[4]: 
$$\left[ q = i (CD)^{\frac{1}{4}}, q = - (CD)^{\frac{1}{4}}, q = -i (CD)^{\frac{1}{4}}, q = (CD)^{\frac{1}{4}} \right]$$


```

Plug this minimum value of q into the expression for A

```

[5]: the_soln(q=(C*D)^(1/4))

```

```

[5]:

```

Appendix E. Derivation of the Cycloidal State Critical Current

$$\frac{\sqrt{2BCD + (B^2D + C)\sqrt{CD}}}{(CD)^{\frac{1}{4}}\sqrt{B}}$$

Taking the limit $C \rightarrow 0$ gives the result.

Appendix

F

Integration of Frustrated Magnet Skymion Thiele Equations

In Chapter 11, we numerically integrate the equations of motion of the collective coordinates skyrmion radius R and helicity η over time for many values of the applied electric field amplitude E_0 and frequency ω . In this Appendix, we provide the code for this. We use SageMath [317], a free and open-source computer algebra system with Python-like syntax, with which Python modules can be used. Listing F.1 performs the integrations for $0 \leq E_0 \leq 2$ with a step size of 0.05 and $0 \leq \omega \leq 4$ with a step size of 0.02.

Obtaining the phase diagram Fig. 11.4(a) from the integration of the equations of motion of the collective coordinates is computationally intensive, as there are 8241 points, each of which represents an integration of (11.4) over dimensionless time $t \leq 0 \leq 1000$. As such, we take measures to make the computation more efficient. After the variables are defined, the various integrals over the radial coordinate ρ contained in (11.4) are computed just once, and fitted to various functions using the `optimize.curve_fit` from SciPy. The functions to which the integrals are fitted were chosen empirically, rather than using physical considerations. The collective coordinate integrations for various values of E_0 are parallelised using the Pool object of Python's multiprocessing library, allowing the calculation to be distributed over many CPU cores. To further accelerate the collective coordinate integration, we used a C function to calculate \dot{R} and $\dot{\eta}$, provided in Listing F.2. This C code is called from the SageMath script using the ctypes library. Compared to the code in Listing F.2 being written as a Python function, we found that this approximately halved the time required for each time integration of the collective coordinates.

```
1 import numpy as np
2 from scipy.optimize import curve_fit
3 from scipy.integrate import solve_ivp
4 from ctypes import c_double, cdll
5 from numpy.ctypeslib import ndpointer
6 import multiprocessing
7 from multiprocessing import Pool
8 import os
9
10
11 def linear_fit(R, m, c):
```

Appendix F. Integration of Frustrated Magnet Skyrmion Thiele Equations

```

12     return m*R + c
13
14 def inverse_linear_fit(R, a, b, c, d):
15     return a/(R-c) + b*(R-c) + d
16
17 def inverse_quadratic_linear_fit(R, a, b, c, d):
18     return a/R**2 + b/R + c + d*R
19
20 def quadratic_fit(R, a, b, c):
21     return a*R**2 + b*R + c
22
23 def inverse_fourth_order_fit(R, a, b, c, d, e, f):
24     return a/R**4 + b/R**3 + c/R**2 + d/R + e*R + f
25
26
27 # We use a C implementation of the time_derivatives function (called by
    ODE solver) to speed up the integration
28 # Compile using gcc -fPIC -shared -o c_fit.o Fit.c
29 lib = cdll.LoadLibrary("./c_fit.o")
30 CTimeDerivatives = lib.time_derivatives
31 CTimeDerivatives.restype = ndpointer(dtype=c_double, shape=(2,))
32
33
34 def get_thiele(Bz, E0, alpha, omega):
35
36     #####
37     # Use Total Skyrmion Energy to Calculate Optimal Radius #
38     #####
39
40     # Finer mesh of value of skyrmion radii to more accurately obtain
    that which minimises energy
41     R_finer = np.linspace(np.min(R_values), np.max(R_values), 1000)
42
43     # Arrays of various contributions to energies (obtained from the
    fitting run at the start)
44     E_exchange_values = inverse_quadratic_linear_fit(R_finer,
    E_exchangeFitParams[0], E_exchangeFitParams[1], E_exchangeFitParams
    [2], E_exchangeFitParams[3])
45     E_magnetic_values = -Bz * quadratic_fit(R_finer,
    E_magnetic_integralFitParams[0], E_magnetic_integralFitParams[1],
    E_magnetic_integralFitParams[2])
46     E_electric_values = -E0 * linear_fit(R_finer,
    E_electric_integralFitParams[0], E_electric_integralFitParams[1])
47     E_values = E_exchange_values + E_magnetic_values - E_electric_values
48
49
50     def time_derivatives(t, y):
51
52         """
53         Wrapper for C function call; calculates dR_dt and d\eta_dt.
54         """
55
56         R, eta = y
57
58         Bz = Bz_array[np.argmin(np.abs(t - times))]
59         Ez = Ez_array[np.argmin(np.abs(t - times))]
60
61         return CTimeDerivatives(c_double(t), c_double(R), c_double(eta),
    c_double(alpha), c_double(Ez), c_double(Bz), c_double(Gamma11FitParams
    [0]), c_double(Gamma11FitParams[1]), c_double(Gamma11FitParams[2]),

```

```

c_double(Gamma11FitParams[3]), c_double(Gamma22FitParams[0]), c_double(
(Gamma22FitParams[1]), c_double(G12FitParams[0]), c_double(
G12FitParams[1]), c_double(F_RexFitParams[0]), c_double(F_RexFitParams
[1]), c_double(F_RexFitParams[2]), c_double(F_RexFitParams[3]),
c_double(F_RexFitParams[4]), c_double(F_RexFitParams[5]), c_double(
Xi1FitParams[0]), c_double(Xi1FitParams[1]), c_double(Xi1FitParams[2])
, c_double(Xi1FitParams[3]), c_double(Xi1FitParams[4]), c_double(
Xi1FitParams[5]), c_double(Xi2FitParams[0]), c_double(Xi2FitParams[1])
, c_double(Xi2FitParams[2]), c_double(Xi2FitParams[3]), c_double(
Xi2FitParams[4]), c_double(Xi2FitParams[5]), c_double(Xi3FitParams[0])
, c_double(Xi3FitParams[1]), c_double(Xi3FitParams[2]), c_double(
Xi3FitParams[3]), c_double(Xi3FitParams[4]), c_double(Xi3FitParams[5])
, c_double(Xi4FitParams[0]), c_double(Xi4FitParams[1]))

62
63     optimal_R = R_finer[np.argmax(E_values)] # Radius that minimises
energy
64     init = [optimal_R, np.pi] # Initial R and eta
65
66     # Magnetic field array (constant Bz in this case)
67     Bz_array = np.zeros_like(times, dtype=float)
68     Bz_array[:] = Bz
69
70     # Electric field array
71     Ez_array = np.zeros_like(times, dtype=float)
72     Ez_array[:] = E0 * cos(omega*times)
73
74     # Perform the time integration
75     sol = solve_ivp(time_derivatives, [np.min(times), np.max(times)],
init, t_eval=times, method="Radau")
76
77     return sol
78
79
80 def initialiser(over_directory_in, times_in, omega_values_in, Bz_in,
E0_values_in, alpha_in, R_values_in, E_exchangeFitParams_in,
E_magnetic_integralFitParams_in, E_electric_integralFitParams_in,
Gamma11FitParams_in, Gamma22FitParams_in, G12FitParams_in,
F_RexFitParams_in, Xi1FitParams_in, Xi2FitParams_in, Xi3FitParams_in,
Xi4FitParams_in):
81
82     """
83     Called by each multiprocessing.Pool worker when it starts (to
initialise times, fields, fit parameters etc. for each thread).
84     See comment under section "Fit Quantities" for explanation of the
various values.
85     """
86
87     global over_directory
88     global times
89     global omega_values
90     global Bz
91     global E0_values
92     global alpha
93     global R_values
94     global E_exchangeFitParams
95     global E_magnetic_integralFitParams
96     global E_electric_integralFitParams
97     global Gamma11FitParams
98     global Gamma22FitParams
99     global G12FitParams

```

Appendix F. Integration of Frustrated Magnet Skyrmion Thiele Equations

```

100     global F_RexFitParams
101     global Xi1FitParams
102     global Xi2FitParams
103     global Xi3FitParams
104     global Xi4FitParams
105
106     over_directory = over_directory_in
107     times = times_in
108     omega_values = omega_values_in
109     Bz = Bz_in
110     E0_values = E0_values_in
111     alpha = alpha_in
112     R_values = R_values_in
113     E_exchangeFitParams = E_exchangeFitParams_in
114     E_magnetic_integralFitParams = E_magnetic_integralFitParams_in
115     E_electric_integralFitParams = E_electric_integralFitParams_in
116     Gamma11FitParams = Gamma11FitParams_in
117     Gamma22FitParams = Gamma22FitParams_in
118     G12FitParams = G12FitParams_in
119     F_RexFitParams = F_RexFitParams_in
120     Xi1FitParams = Xi1FitParams_in
121     Xi2FitParams = Xi2FitParams_in
122     Xi3FitParams = Xi3FitParams_in
123     Xi4FitParams = Xi4FitParams_in
124
125
126     def evolve(Eidx):
127
128         """
129         For the electric field input, loop through all omega values and
130         perform the integration.
131         This is the function called by each multiprocessing Pool process.
132         """
133
134         for omegaidx in range(len(omega_values)):
135
136             filename = "E0{:.2f}".format(E0_values[Eidx]) + "omega{:.2f}".
137             format(omega_values[omegaidx])
138
139             sol = get_thiele(Bz, E0_values[Eidx], alpha, omega_values[
140             omegaidx])
141             np.save(over_directory + "/R/E0{:.2f}".format(E0_values[Eidx]) +
142             "omega{:.2f}".format(omega_values[omegaidx]), sol.y[0, :])
143             np.save(over_directory + "/eta/E0{:.2f}".format(E0_values[Eidx])
144             + "omega{:.2f}".format(omega_values[omegaidx]), sol.y[1, :])
145
146
147     if __name__ == "__main__":
148
149         over_directory = "CollectiveCoordinateData"
150
151         if not os.path.exists(over_directory):
152
153             os.mkdir(over_directory)
154             os.mkdir(over_directory + "/R")
155             os.mkdir(over_directory + "/eta")
156             os.mkdir(over_directory + "/General")
157
158     #####

```

```

155 # Define Variables for Symbolic Algebra Required for Integration #
156 #####
157
158 # Here, the variables are defined, such as polar coordinate variables
159 # , helicity etc.
160
161 rho = var("rho") # Polar coordinate radius
162 psi = var("psi") # Polar coordinate angle
163
164 m = var("m") # Skyrmion vorticity
165 eta = var("eta") # Skyrmion helicity
166 R = var("R") # Skyrmion radius
167 w = var("w") # Skyrmion domain wall width
168
169 # Theta and phi as in main text
170 theta = 2 * arctan(sinh(R/w) / sinh(rho/w))
171 phi = m*psi + eta
172
173 # Components of magnetization
174 mx = cos(phi) * sin(theta)
175 my = sin(phi) * sin(theta)
176 mz = cos(theta)
177
178 # Components of Laplacian in polar coordinates
179 mxLaplacian = diff(mx, rho, 2) + (1/rho) * diff(mx, rho) + (1/rho^2)
180 * diff(mx, psi, 2)
181 myLaplacian = diff(my, rho, 2) + (1/rho) * diff(my, rho) + (1/rho^2)
182 * diff(my, psi, 2)
183 mzLaplacian = diff(mz, rho, 2) + (1/rho) * diff(mz, rho) + (1/rho^2)
184 * diff(mz, psi, 2)
185
186 # (\nabla m)^2 term
187 quadratic_term = -mx*mxLaplacian - my*myLaplacian - mz*mzLaplacian
188 quadratic_term = quadratic_term.simplify_full()
189
190 # (\nabla^2 m)^2 term
191 mLaplacian = vector([mxLaplacian, myLaplacian, mzLaplacian])
192 quartic_term = mLaplacian.dot_product(mLaplacian)
193 quartic_term = quartic_term.simplify_full()
194
195 R_values = np.arange(0.5, 10, 0.1) # Array of
196 radii used for fitting
197 dtheta_dR = diff(theta, R) # d\theta/dR
198 dtheta_drho = diff(theta, rho) # d\theta/d\rho
199 d2theta_dRdrho = diff(dtheta_drho, R) # d^2\theta/d\
200 rho^2
201 dE_2Integrand_dR = 0.5 * diff(rho*quadratic_term, R) # Derivative of
202 (\nabla m)^2 term with respect to R
203 dE_4Integrand_dR = 0.5 * diff(rho*quartic_term, R) # Derivative of
204 (\nabla^2 m)^2 term with respect to R
205
206 dw_width = 1.4 # Domain wall width
207 rho_cutoff = 50 # Cutoff in integration over radius rho for
208 fitting
209
210 times = np.linspace(0, 1000, 10000)
211
212 #####
213 # Fit Quantities #

```

Appendix F. Integration of Frustrated Magnet Skyrmion Thiele Equations

```

206 #####
207
208 # G12 is the  $G_{\{R\eta\}}$  from the manuscript
209 # Gamma11 and Gamma22 are as in the manuscript where 1 is R and 2 is
\eta
210 # F_rex is  $-dU_{ex} / dR$ 
211
212 # What I call Xi are parameters that show up in the analytical
expressions for the helicity-dependent
213 # parts of the generalised forces for the skyrmion profile ansatz we
use
214
215 # Xi1 is the integral of  $\cos(2\theta) d\theta / dR$  over  $\rho$ 
216 # Xi2 is the integral of  $\rho * d^2\theta / dR d\rho$  over  $\rho$ 
217 # Xi3 is the integral of  $\cos(\theta)\sin(\theta)$  over  $\rho$ 
218 # Xi4 is the integral of  $\rho * d\theta / d\rho$  over  $\rho$ 
219
220 G12 = np.zeros_like(R_values, dtype=float)
221 Gamma11 = np.zeros_like(R_values, dtype=float)
222 Gamma22 = np.zeros_like(R_values, dtype=float)
223 F_Rex = np.zeros_like(R_values, dtype=float)
224 Xi1 = np.zeros_like(R_values, dtype=float)
225 Xi2 = np.zeros_like(R_values, dtype=float)
226 Xi3 = np.zeros_like(R_values, dtype=float)
227 Xi4 = np.zeros_like(R_values, dtype=float)
228
229 for i in range(len(R_values)):
230     G12[i] = numerical_integral(rho * np.sin(theta(R=R_values[i], w=
dw_width, m=1)) * dtheta_dR(R=R_values[i], w=dw_width, m=1), 0,
rho_cutoff)[0]
231     Gamma11[i] = numerical_integral(rho * dtheta_dR(R=R_values[i], w=
dw_width, m=1)^2, 0, rho_cutoff)[0]
232     Gamma22[i] = numerical_integral(rho * sin(theta(R=R_values[i], w=
dw_width, m=1))^2, 0, rho_cutoff)[0]
233     F_Rex[i] = numerical_integral(-dE_4Integrand_dR(R=R_values[i], w=
dw_width, m=1) + dE_2Integrand_dR(R=R_values[i], w=dw_width, m=1), 0,
rho_cutoff)[0]
234     Xi1[i] = numerical_integral(cos(2*theta(R=R_values[i], w=dw_width
, m=1)) * dtheta_dR(R=R_values[i], w=dw_width, m=1), 0, rho_cutoff)[0]
235     Xi2[i] = numerical_integral(rho * d2theta_dRdrho(R=R_values[i], w
=dw_width, m=1), 0, rho_cutoff)[0]
236     Xi3[i] = numerical_integral(cos(theta(R=R_values[i], w=dw_width,
m=1)) * sin(theta(R=R_values[i], w=dw_width, m=1)), 0, rho_cutoff)[0]
237     Xi4[i] = numerical_integral(rho * dtheta_drho(R=R_values[i], w=
dw_width, m=1), 0, rho_cutoff)[0]
238
239
240 # The initial guesses p0 are chosen so that the solution converges, but
they are somewhat arbitrary
241 G12FitParams = curve_fit(linear_fit, R_values, G12, p0=[2., 1.])[0]
242 Gamma11FitParams = curve_fit(inverse_linear_fit, R_values, Gamma11,
p0=[1.17, 1.5, 0, 0])[0]
243 Gamma22FitParams = curve_fit(linear_fit, R_values, Gamma22, p0=[3.,
-0.5])[0]
244 F_RexFitParams = curve_fit(inverse_fourth_order_fit, R_values, F_Rex,
p0=[1.17, 1.5, 1, 1, 1, 1])[0]
245 Xi1FitParams = curve_fit(inverse_fourth_order_fit, R_values, Xi1, p0
=[1.17, 1.5, 1, 1, 1, 1])[0]
246 Xi2FitParams = curve_fit(inverse_fourth_order_fit, R_values, Xi2, p0
=[1.17, 1.5, 1, 1, 1, 1])[0]

```

```

247 Xi3FitParams = curve_fit(inverse_fourth_order_fit, R_values, Xi3, p0
=[1.17, 1.5, 1, 1, 1, 1])[0]
248 Xi4FitParams = curve_fit(linear_fit, R_values, Xi4, p0=[1.17, 1.5])
[0]
249
250
251 #####
252 # Fit Energy Integrals #
253 #####
254
255 # Fit integrals of energy density over space to obtain fitting
parameters to use during time integration of collective coordinates
256
257 E_exchange = np.zeros_like(R_values, dtype=float)
258 E_magnetic_integral = np.zeros_like(R_values, dtype=float)
259 E_electric_integral = Xi3 + Xi4
260
261 for i in range(len(R_values)):
262     E_exchange[i] = numerical_integral(-0.5*rho*
quadratic_term(R=R_values[i], w=dw_width, m=1) + 0.5*rho*quartic_term(
R=R_values[i], w=dw_width, m=1), 0, rho_cutoff)[0]
263     E_magnetic_integral[i] = numerical_integral(rho*(mz(R=R_values[i
], w=dw_width, m=1)-1), 0, rho_cutoff)[0]
264
265 E_exchangeFitParams = curve_fit(inverse_quadratic_linear_fit
, R_values, E_exchange, p0=[1.17, 1.5, 0, 1])[0]
266 E_magnetic_integralFitParams = curve_fit(quadratic_fit, R_values,
E_magnetic_integral, p0=[1.17, 1.5, 0])[0]
267 E_electric_integralFitParams = curve_fit(linear_fit, R_values,
E_electric_integral, p0=[1.17, 1.5])[0]
268
269 # Array of electric field amplitude and angular frequency, each pair
of which the collective coordinates are integrated
270 E0_values = np.arange(0., 2.05, 0.05)
271 omega_values = np.arange(0., 4.02, 0.02)
272
273 Bz = 1. # Magnetic field along z-axis
274 alpha = 0.01 # Gilbert damping constant
275
276 # Perform the collective coordinate integrations in parallel
277 with Pool(multiprocessing.cpu_count(), initialiser, initargs=(
over_directory, times, omega_values, Bz, E0_values, alpha, R_values,
E_exchangeFitParams, E_magnetic_integralFitParams,
E_electric_integralFitParams, Gamma11FitParams, Gamma22FitParams,
G12FitParams, F_RexFitParams, Xi1FitParams, Xi2FitParams, Xi3FitParams
, Xi4FitParams)) as p:
278
279     p.map(evolve, [Eidx for Eidx in range(len(E0_values))])

```

Listing F.1: SageMath code to integrate the Thiele equation for radius and helicity of a skyrmion in a frustrated magnet for many values of electric field amplitude and frequency.

```

1 /*
2 C functions to calculate d/dt(R) and d/dt(eta), as this is faster than
using Python functions (approximately halved
3 the time required to obtain the phase diagram in my testing)
4
5 Called by CCIntegration.sage

```

Appendix F. Integration of Frustrated Magnet Skyrmion Thiele Equations

```

6
7 Must be compiled prior to running CIntegration.sage with
8 gcc -fPIC -shared -o c_fit.o Fit.c
9 */
10
11 #include <stdlib.h>
12 #include <math.h>
13
14
15 ////////////////////////////////////////////////////
16 // Define Fits to Be Used //
17 ////////////////////////////////////////////////////
18
19 double * inverse_fourth_order_fit_array(const double * arr, int N, double
    a, double b, double c, double d, double e, double f)
20 {
21     double * result = (double *)malloc(sizeof(double) * N);
22     for (int i=0; i<N; i++)
23     {
24         double R = arr[i];
25         result[i] = a/(R*R*R*R) + b/(R*R*R) + c/(R*R) + d/R + f + e*R;
26     }
27     return result;
28 }
29
30 double inverse_fourth_order_fit(const double R, double a, double b,
    double c, double d, double e, double f)
31 {
32     return (1/(R*R)) * (a/(R*R) + b/R + c) + d/R + f + e*R;
33 }
34
35 double linear_fit(const double R, double m, double c)
36 {
37     return m*R + c;
38 }
39
40 double inverse_linear_fit(const double R, double a, double b, double c,
    double d)
41 {
42     return a/(R-c) + b*(R-c) + d;
43 }
44
45 double inverse_quadratic_linear_fit(const double R, double a, double b,
    double c, double d)
46 {
47     return a/(R*R) + b/R + c + d*R;
48 }
49
50 double quadratic_fit(const double R, double a, double b, double c)
51 {
52     return a*R*R + b*R + c;
53 }
54
55
56 ////////////////////////////////////////////////////
57 // Function Returning dR/dt and d\eta/dt //
58 ////////////////////////////////////////////////////
59
60 double * time_derivatives(double t, double R, double eta, double alpha,
    double Ez, double Bz, double Gamma11ParamA, double Gamma11ParamB,

```



```

double Gamma11ParamC, double Gamma11ParamD, double Gamma22ParamA,
double Gamma22ParamB, double G12FitParamA, double G12FitParamB, double
F_RexFitParamA, double F_RexFitParamB, double F_RexFitParamC, double
F_RexFitParamD, double F_RexFitParamE, double F_RexFitParamF, double
Xi1FitParamA, double Xi1FitParamB, double Xi1FitParamC, double
Xi1FitParamD, double Xi1FitParamE, double Xi1FitParamF, double
Xi2FitParamA, double Xi2FitParamB, double Xi2FitParamC, double
Xi2FitParamD, double Xi2FitParamE, double Xi2FitParamF, double
Xi3FitParamA, double Xi3FitParamB, double Xi3FitParamC, double
Xi3FitParamD, double Xi3FitParamE, double Xi3FitParamF, double
Xi4FitParamA, double Xi4FitParamB)
61 {
62
63 // t is time
64 // R is skyrmion radius
65 // \eta is skyrmion helicity
66 // alpha is Gilbert damping constant
67 // Ez is electric field
68 // Bz is magnetic field
69 // Gamma11<A,B,C,D> are the fit parameters for the dissipative tensor
\Gamma_{RR}
70 // Gamma22<A,B> are the fit parameters for the dissipative tensor \
Gamma_{\eta\eta}
71 // F_RexFitParam<A,B,C,D,E,F> are the fit parameters for -dU_ex/DR
72 // Xi1FitParams<A,B,C,D,E,F> are the fit parameters for the integral
of cos(2\theta) d\theta / dR over \rho
73 // Xi2FitParams<A,B,C,D,E,F> are the fit parameters for the integral
of \rho * d^2\theta / dRd\rho over \rho
74 // Xi3FitParams<A,B,C,D,E,F> are the fit parameters for the integral
of cos(\theta)sin(\theta) over \rho
75 // Xi4FitParams<A,B> are the fit parameters for the integral of \rho
* d\theta / d\rho over \rho
76
77 // Obtain the quantities described above from their fits
78 double Gamma11 = alpha * inverse_linear_fit(R, Gamma11ParamA,
Gamma11ParamB, Gamma11ParamC, Gamma11ParamD);
79 double Gamma22 = alpha * linear_fit(R, Gamma22ParamA, Gamma22ParamB);
80 double G12 = linear_fit(R, G12FitParamA, G12FitParamB);
81 double F_Rex = inverse_fourth_order_fit(R, F_RexFitParamA,
F_RexFitParamB, F_RexFitParamC, F_RexFitParamD, F_RexFitParamE,
F_RexFitParamF);
82 double Xi1 = inverse_fourth_order_fit(R, Xi1FitParamA, Xi1FitParamB,
Xi1FitParamC, Xi1FitParamD, Xi1FitParamE, Xi1FitParamF);
83 double Xi2 = inverse_fourth_order_fit(R, Xi2FitParamA, Xi2FitParamB,
Xi2FitParamC, Xi2FitParamD, Xi2FitParamE, Xi2FitParamF);
84 double Xi3 = inverse_fourth_order_fit(R, Xi3FitParamA, Xi3FitParamB,
Xi3FitParamC, Xi3FitParamD, Xi3FitParamE, Xi3FitParamF);
85 double Xi4 = linear_fit(R, Xi4FitParamA, Xi4FitParamB);
86
87 double F_R = F_Rex - Bz*G12 + Ez*cos(eta)*(Xi1 + Xi2);
88 double F_eta = -Ez*sin(eta)*(Xi3 + Xi4);
89
90 // The prefactor for both \dot{R} and \dot{\eta}
91 double prefactor = 1 / (G12*G12 + Gamma11*Gamma22);
92
93 double * return_array = (double *)malloc(sizeof(double) * 2);
94
95 return_array[0] = prefactor * (Gamma22*F_R + G12*F_eta);
96 return_array[1] = prefactor * (Gamma11*F_eta - G12*F_R);
97

```

Appendix F. Integration of Frustrated Magnet Skyrmion Thiele Equations

```
98     return return_array;  
99  
100 }
```

Listing F.2: C code used to calculate the time derivatives of the collective coordinates given the fit parameters.

Bibliography

- ¹H. Helmholtz, ‘Über Integrale der hydrodynamischen Gleichungen, welche den Wirbelbewegungen entsprechen.’, *J. Reine Angew. Math.* **55**, 25–55 (1858).
- ²W. Thomson, ‘4. On Vortex Atoms’, *Proc. Roy. Soc. Edinburgh* **6**, 94–105 (1869).
- ³H.-B. Braun, ‘Solitons in Real Space: Domain Walls, Vortices, Hedgehogs, and Skyrmions’, in *Topology in Magnetism*, edited by J. Zang, V. Cros and A. Hoffmann, Springer Series in Solid-State Sciences (Springer International Publishing, Cham, 2018), pp. 1–40.
- ⁴G. Derrick, ‘Comments on Nonlinear Wave Equations as Models for Elementary Particles’, *J. Math. Phys.* **5**, 1252–1254 (1964).
- ⁵R. H. Hobart, ‘On the Instability of a Class of Unitary Field Models’, *Proc. Phys. Soc.* **82**, 201 (1963).
- ⁶T. H. R. Skyrme and B. F. J. Schonland, ‘A Non-Linear Theory of Strong Interactions’, *Proc. R. Soc. Lond. A* **247**, 260–278 (1958).
- ⁷T. H. R. Skyrme and B. F. J. Schonland, ‘A Non-Linear Field Theory’, *Proc. R. Soc. Lond. A* **260**, 127–138 (1961).
- ⁸T. H. R. Skyrme and W. G. Penney, ‘Particle States of a Quantized Meson Field’, *Proc. R. Soc. Lond. A* **262**, 237–245 (1961).
- ⁹J. K. Perring and T. H. R. Skyrme, ‘A Model Unified Field Equation’, *Nucl. Phys.* **31**, 550–555 (1962).
- ¹⁰T. H. R. Skyrme, ‘A Unified Field Theory of Mesons and Baryons’, *Nucl. Phys.* **31**, 556–569 (1962).
- ¹¹T.-L. Ho, ‘Spinor Bose Condensates in Optical Traps’, *Phys. Rev. Lett.* **81**, 742–745 (1998).
- ¹²U. Al Khawaja and H. Stoof, ‘Skyrmions in a Ferromagnetic Bose–Einstein Condensate’, *Nature* **411**, 918–920 (2001).
- ¹³A. Knigavko and B. Rosenstein, ‘Magnetic Skyrmion Lattices in Heavy Fermion Superconductor UPt_3 ’, *Phys. Rev. Lett.* **82**, 1261–1264 (1999).
- ¹⁴D. C. Wright and N. D. Mermin, ‘Crystalline Liquids: The Blue Phases’, *Rev. Mod. Phys.* **61**, 385–432 (1989).
- ¹⁵A. N. Bogdanov, U. K. Röbner and A. A. Shestakov, ‘Skyrmions in Nematic Liquid Crystals’, *Phys. Rev. E* **67**, 016602 (2003).
- ¹⁶A. N. Bogdanov and D. Yablonskii, ‘Thermodynamically Stable “Vortices” in Magnetically Ordered Crystals. The Mixed State of Magnets’, *J. Exp. Theor. Phys.* **95**, 178 (1989).
- ¹⁷A. Bogdanov and A. Hubert, ‘Thermodynamically Stable Magnetic Vortex States in Magnetic Crystals’, *J. Magn. Magn. Mater.* **138**, 255–269 (1994).

Bibliography

- ¹⁸A. Bogdanov, ‘New Localized Solutions of the Nonlinear Field Equations’, *J. Exp. Theor. Phys.* **62**, 231 (1995).
- ¹⁹A. Bogdanov and A. Hubert, ‘The Stability of Vortex-Like Structures in Uniaxial Ferromagnets’, *J. Magn. Magn. Mater.* **195**, 182–192 (1999).
- ²⁰A. N. Bogdanov and U. K. Röbber, ‘Chiral Symmetry Breaking in Magnetic Thin Films and Multilayers’, *Phys. Rev. Lett.* **87**, 037203 (2001).
- ²¹U. K. Röbber, A. N. Bogdanov and C. Pfeleiderer, ‘Spontaneous Skyrmion Ground States in Magnetic Metals’, *Nature* **442**, 797–801 (2006).
- ²²K. Kadowaki, K. Okuda and M. Date, ‘Magnetization and Magnetoresistance of MnSi. I’, *J. Phys. Soc. Jpn.* **51**, 2433–2438 (1982).
- ²³Y. Ishikawa and M. Arai, ‘Magnetic Phase Diagram of MnSi near Critical Temperature Studied by Neutron Small Angle Scattering’, *J. Phys. Soc. Jpn.* **53**, 2726–2733 (1984).
- ²⁴S. Mühlbauer et al., ‘Skyrmion Lattice in a Chiral Magnet’, *Science* **323**, 915–919 (2009).
- ²⁵*Skyrmion Lattice in a Chiral Magnet*, (Feb. 2009) <https://www.tum.de/en/news-and-events/all-news/press-releases/details/31094> (visited on 11/10/2023).
- ²⁶X. Z. Yu et al., ‘Real-Space Observation of a Two-Dimensional Skyrmion Crystal’, *Nature* **465**, 901–904 (2010).
- ²⁷A. N. Bogdanov and C. Panagopoulos, ‘Physical Foundations and Basic Properties of Magnetic Skyrmions’, *Nat. Rev. Phys.* **2**, 492–498 (2020).
- ²⁸S. Li, X. Wang and T. Rasing, ‘Magnetic Skyrmions: Basic Properties and Potential Applications’, *Interdiscip Mater.* **2**, 260–289 (2023).
- ²⁹S. S. P. Parkin, M. Hayashi and L. Thomas, ‘Magnetic Domain-Wall Racetrack Memory’, *Science* **320**, 190–194 (2008).
- ³⁰A. Fert, V. Cros and J. Sampaio, ‘Skyrmions on the Track’, *Nat. Nanotechnol.* **8**, 152–156 (2013).
- ³¹R. Tomasello et al., ‘A Strategy for the Design of Skyrmion Racetrack Memories’, *Sci. Rep.* **4**, 6784 (2014).
- ³²X. Zhang et al., ‘Skyrmion-Skyrmion and Skyrmion-Edge Repulsions in Skyrmion-Based Racetrack Memory’, *Sci. Rep.* **5**, 7643 (2015).
- ³³F. Jonietz et al., ‘Spin Transfer Torques in MnSi at Ultralow Current Densities’, *Science* **330**, 1648–1651 (2010).
- ³⁴M. Yamanouchi et al., ‘Current-Induced Domain-Wall Switching in a Ferromagnetic Semiconductor Structure’, *Nature* **428**, 539–542 (2004).
- ³⁵J. Iwasaki, M. Mochizuki and N. Nagaosa, ‘Universal Current-Velocity Relation of Skyrmion Motion in Chiral Magnets’, *Nat. Commun.* **4**, 1463 (2013).
- ³⁶J. Müller and A. Rosch, ‘Capturing of a Magnetic Skyrmion with a Hole’, *Phys. Rev. B* **91**, 054410 (2015).
- ³⁷K. Everschor-Sitte et al., ‘Perspective: Magnetic Skyrmions—Overview of Recent Progress in an Active Research Field’, *J. Appl. Phys.* **124**, 240901 (2018).
- ³⁸X. Zhang, M. Ezawa and Y. Zhou, ‘Magnetic Skyrmion Logic Gates: Conversion, Duplication and Merging of Skyrmions’, *Sci. Rep.* **5**, 9400 (2015).

- ³⁹S. Luo et al., ‘Reconfigurable Skyrmion Logic Gates’, *Nano Lett.* **18**, 1180–1184 (2018).
- ⁴⁰X. Zhang et al., ‘Magnetic Skyrmion Transistor: Skyrmion Motion in a Voltage-Gated Nanotrack’, *Sci. Rep.* **5**, 11369 (2015).
- ⁴¹P. Upadhyaya et al., ‘Electric-Field Guiding of Magnetic Skyrmions’, *Phys. Rev. B* **92**, 134411 (2015).
- ⁴²S. Li et al., ‘Magnetic Skyrmions for Unconventional Computing’, *Mater. Horiz.* **8**, 854–868 (2021).
- ⁴³M. Alawad and M. Lin, ‘Survey of Stochastic-Based Computation Paradigms’, *IEEE Trans. Emerg. Topics Comput.* **7**, 98–114 (2019).
- ⁴⁴D. Pinna et al., ‘Skyrmion Gas Manipulation for Probabilistic Computing’, *Phys. Rev. Applied* **9**, 064018 (2018).
- ⁴⁵J. Zázvorka et al., ‘Thermal Skyrmion Diffusion Used in a Reshuffler Device’, *Nat. Nanotechnol.* **14**, 658–661 (2019).
- ⁴⁶Y. Huang et al., ‘Magnetic Skyrmion-Based Synaptic Devices’, *Proc. Spie.* **28**, 08LT02 (2017).
- ⁴⁷S. Li et al., ‘Magnetic Skyrmion-Based Artificial Neuron Device’, *Proc. Spie.* **28**, 31LT01 (2017).
- ⁴⁸K. M. Song et al., ‘Skyrmion-Based Artificial Synapses for Neuromorphic Computing’, *Nat. Electron.* **3**, 148–155 (2020).
- ⁴⁹G. Tanaka et al., ‘Recent Advances in Physical Reservoir Computing: A Review’, *Neural Networks* **115**, 100–123 (2019).
- ⁵⁰D. Prychynenko et al., ‘Magnetic Skyrmion as a Nonlinear Resistive Element: A Potential Building Block for Reservoir Computing’, *Phys. Rev. Applied* **9**, 014034 (2018).
- ⁵¹G. Bourianoff et al., ‘Potential Implementation of Reservoir Computing Models Based on Magnetic Skyrmions’, *AIP Adv.* **8**, 055602 (2018).
- ⁵²D. Pinna, G. Bourianoff and K. Everschor-Sitte, ‘Reservoir Computing with Random Skyrmion Textures’, *Phys. Rev. Applied* **14**, 054020 (2020).
- ⁵³R. Msiska et al., ‘Audio Classification with Skyrmion Reservoirs’, *Adv. Intell. Syst.* **5**, 2200388 (2023).
- ⁵⁴J. Love et al., ‘Spatial Analysis of Physical Reservoir Computers’, *Phys. Rev. Appl.* **20**, 044057 (2023).
- ⁵⁵S. Zhang et al., ‘Current-Induced Magnetic Skyrmions Oscillator’, *New J. Phys.* **17**, 023061 (2015).
- ⁵⁶M. Carpentieri et al., ‘Topological, Non-Topological and Instanton Droplets Driven by Spin-Transfer Torque in Materials with Perpendicular Magnetic Anisotropy and Dzyaloshinskii–Moriya Interaction’, *Sci. Rep.* **5**, 16184 (2015).
- ⁵⁷G. Finocchio et al., ‘Skyrmion Based Microwave Detectors and Harvesting’, *Appl. Phys. Lett.* **107**, 262401 (2015).
- ⁵⁸F. Garcia-Sanchez et al., ‘A Skyrmion-Based Spin-Torque Nano-Oscillator’, *New J. Phys.* **18**, 075011 (2016).

Bibliography

- ⁵⁹B. Göbel, I. Mertig and O. A. Tretiakov, ‘Beyond Skyrmions: Review and Perspectives of Alternative Magnetic Quasiparticles’, *Phys. Rep.*, Beyond Skyrmions: Review and Perspectives of Alternative Magnetic Quasiparticles **895**, 1–28 (2021).
- ⁶⁰Y. Liu, R. K. Lake and J. Zang, ‘Binding a Hopfion in a Chiral Magnet Nanodisk’, *Phys. Rev. B* **98**, 174437 (2018).
- ⁶¹G. P. Müller et al., ‘Coupled Quasimonopoles in Chiral Magnets’, *Phys. Rev. B* **101**, 184405 (2020).
- ⁶²S. Li et al., ‘Mutual Conversion Between a Magnetic Néel Hopfion and a Néel Toron’, *Phys. Rev. B* **105**, 174407 (2022).
- ⁶³M. Sallermann, H. Jónsson and S. Blügel, ‘Stability of Hopfions in Bulk Magnets with Competing Exchange Interactions’, *Phys. Rev. B* **107**, 104404 (2023).
- ⁶⁴H. Hopf, ‘Über die Abbildungen der dreidimensionalen Sphäre auf die Kugelfläche’, *Math. Ann.* **104**, 637–665 (1931).
- ⁶⁵M. Nakahara, *Geometry, Topology and Physics*, Graduate Student Series in Physics (Institute of Physics Publishing).
- ⁶⁶G. L. Naber, *Topology, Geometry and Gauge Fields: Foundations*, Vol. 25, Texts in Applied Mathematics (Springer, New York, NY, 2011).
- ⁶⁷Y. Liu et al., ‘Three-Dimensional Dynamics of a Magnetic Hopfion Driven by Spin Transfer Torque’, *Phys. Rev. Lett.* **124**, 127204 (2020).
- ⁶⁸V. I. Arnold and B. A. Khesin, *Topological Methods in Hydrodynamics*, Vol. 125, Applied Mathematical Sciences (Springer International Publishing, Cham, 2021).
- ⁶⁹D. Foster, ‘Massive Hopfions’, *Phys. Rev. D* **83**, 085026 (2011).
- ⁷⁰A. Thompson et al., ‘Constructing a Class of Topological Solitons in Magnetohydrodynamics’, *Phys. Rev. E* **89**, 043104 (2014).
- ⁷¹P. Sutcliffe, ‘Skyrmion Knots in Frustrated Magnets’, *Phys. Rev. Lett.* **118**, 247203 (2017).
- ⁷²J. H. C. Whitehead, ‘An Expression of Hopf’s Invariant as an Integral’, *Proc. Natl. Acad. Sci.* **33**, 117–123 (1947).
- ⁷³M. A. Berger, ‘Introduction to Magnetic Helicity’, *Plasma Phys. Contr. F.* **41**, B167 (1999).
- ⁷⁴J. J. Moreau, ‘Constantes d’un îlot tourbillonnaire en fluide parfait barotrope’, *C. R. Acad. Sci.* **252**, 2810–2812 (1961).
- ⁷⁵B. G.-g. Chen et al., ‘Generating the Hopf Fibration Experimentally in Nematic Liquid Crystals’, *Phys. Rev. Lett.* **110**, 237801 (2013).
- ⁷⁶P. J. Ackerman, J. van de Lagemaat and I. I. Smalyukh, ‘Self-Assembly and Electrostriction of Arrays and Chains of Hopfion Particles in Chiral Liquid Crystals’, *Nat. Commun.* **6**, 6012 (2015).
- ⁷⁷J.-S. B. Tai, J.-S. Wu and I. I. Smalyukh, ‘Geometric Transformation and Three-Dimensional Hopping of Hopf Solitons’, *Nat. Commun.* **13**, 2986 (2022).
- ⁷⁸P. J. Ackerman and I. I. Smalyukh, ‘Static Three-Dimensional Topological Solitons in Fluid Chiral Ferromagnets and Colloids’, *Nat. Mater.* **16**, 426–432 (2017).

- ⁷⁹I. Luk'yanchuk et al., 'Hopfions Emerge in Ferroelectrics', *Nat. Commun.* **11**, 2433 (2020).
- ⁸⁰L. Faddeev, 'Quantization of Solitons, Princeton Preprint IAS-75-QS70', Institute for Advanced Study, Princeton (1975).
- ⁸¹L. Faddeev and A. J. Niemi, 'Stable Knot-Like Structures in Classical Field Theory', *Nature* **387**, 58–61 (1997).
- ⁸²P. Sutcliffe, 'Knots in the Skyrme–Faddeev Model', *Proc. Roy. Soc. Lond. A* **463**, 3001–3020 (2007).
- ⁸³A. F. Vakulenko and L. V. Kapitanskii, 'Stability of Solitons in S^2 of a Nonlinear σ -Model', *Proc. USSR Acad. Sci.* **246**, 840–842 (1979).
- ⁸⁴F. N. Rybakov et al., 'Magnetic Hopfions in Solids', *APL Mater.* **10**, 111113 (2022).
- ⁸⁵I. L. Bogolubsky, 'Three-Dimensional Topological Solitons in the Lattice Model of a Magnet with Competing Interactions', *Phys. Lett. A* **126**, 511–514 (1988).
- ⁸⁶R. Dittrich et al., 'A Path Method for Finding Energy Barriers and Minimum Energy Paths in Complex Micromagnetic Systems', *J. Magn. Magn. Mater.* **250**, 12–19 (2002).
- ⁸⁷G. Henkelman and H. Jónsson, 'A Dimer Method for Finding Saddle Points on High Dimensional Potential Surfaces Using Only First Derivatives', *J. Chem. Phys.* **111**, 7010–7022 (1999).
- ⁸⁸P. Sutcliffe, 'Hopfions in Chiral Magnets', *J. Phys. A: Math. Theor.* **51**, 375401 (2018).
- ⁸⁹J.-S. B. Tai and I. I. Smalyukh, 'Static Hopf Solitons and Knotted Emergent Fields in Solid-State Noncentrosymmetric Magnetic Nanostructures', *Phys. Rev. Lett.* **121**, 187201 (2018).
- ⁹⁰C. Donnelly et al., 'Three-Dimensional Magnetization Structures Revealed with X-Ray Vector Nanotomography', *Nature* **547**, 328–331 (2017).
- ⁹¹C. Donnelly et al., 'Experimental Observation of Vortex Rings in a Bulk Magnet', *Nat. Phys.* **17**, 316–321 (2021).
- ⁹²N. Kent et al., 'Creation and Observation of Hopfions in Magnetic Multilayer Systems', *Nat. Commun.* **12**, 1562 (2021).
- ⁹³F. Zheng et al., 'Hopfion Rings in a Cubic Chiral Magnet', *Nature* **623**, 718–723 (2023).
- ⁹⁴B. Göbel et al., 'Topological Hall Signatures of Magnetic Hopfions', *Phys. Rev. Research* **2**, 013315 (2020).
- ⁹⁵S. S. Pershoguba, D. Andreoli and J. Zang, 'Electronic Scattering off a Magnetic Hopfion', *Phys. Rev. B* **104**, 075102 (2021).
- ⁹⁶Z. Zhang et al., 'Magnon Scattering Modulated by Omnidirectional Hopfion Motion in Antiferromagnets for Meta-Learning', *Sci. Adv.* **9**, eade7439 (2023).
- ⁹⁷C. Saji et al., 'Hopfion-Driven Magnonic Hall Effect and Magnonic Focusing', *Phys. Rev. Lett.* **131**, 166702 (2023).
- ⁹⁸L. Bo et al., 'Spin Excitation Spectrum of a Magnetic Hopfion', *Appl. Phys. Lett.* **119**, 212408 (2021).
- ⁹⁹D. Raftrey and P. Fischer, 'Field-Driven Dynamics of Magnetic Hopfions', *Phys. Rev. Lett.* **127**, 257201 (2021).

Bibliography

- ¹⁰⁰K. Sobucki et al., ‘Magnon Spectrum of Bloch Hopfion Beyond Ferromagnetic Resonance’, *APL Mater.* **10**, 091103 (2022).
- ¹⁰¹Z. Khodzhaev and E. Turgut, ‘Hopfion Dynamics in Chiral Magnets’, *J. Phys. Condens. Matter* **34**, 225805 (2022).
- ¹⁰²X. S. Wang, A. Qaiumzadeh and A. Brataas, ‘Current-Driven Dynamics of Magnetic Hopfions’, *Phys. Rev. Lett.* **123**, 147203 (2019).
- ¹⁰³P. Weiss, ‘L’hypothèse du champ moléculaire et la propriété ferromagnétique’, *J. Phys. Theor. Appl.* **6**, 661–690 (1907).
- ¹⁰⁴W. Heisenberg, ‘Zur Theorie des Ferromagnetismus’, *Z. Phys.* **49**, 619–636 (1928).
- ¹⁰⁵F. Bloch, ‘Zur Theorie des Austauschproblems und der Remanenzerscheinung der Ferromagnetika’, in *Zur Theorie des Austauschproblems und der Remanenzerscheinung der Ferromagnetika: Probleme des Atomkernbaues*, edited by F. Bloch (Springer, Berlin, Heidelberg, 1932), pp. 295–335.
- ¹⁰⁶L. D. Landau and E. M. Lifshitz, ‘On the Theory of the Dispersion of Magnetic Permeability in Ferromagnetic Bodies’, *Phys. Z. Sowjetunion* **8**, 101–114 (1935).
- ¹⁰⁷J. Brown William Fuller, ‘Micromagnetics, Domains, and Resonance’, *J. Appl. Phys.* **30**, S62–S69 (1959).
- ¹⁰⁸W. F. Brown, ‘Micromagnetics: Successor to Domain Theory?’, *J. Phys. Radium* **20**, 101 (1959).
- ¹⁰⁹W. F. Brown, *Micromagnetics*, Vol. 18, Interscience Tracts on Physics and Astronomy (Interscience Publishers).
- ¹¹⁰L. Lopez-Diaz et al., ‘Micromagnetic Simulations Using Graphics Processing Units’, *J. Phys. D: Appl. Phys.* **45**, 323001 (2012).
- ¹¹¹J. Leliaert et al., ‘Fast Micromagnetic Simulations on GPU—Recent Advances Made with MuMax3’, *J. Phys. D: Appl. Phys.* **51**, 123002 (2018).
- ¹¹²F. Bloch, ‘Zur Theorie des Ferromagnetismus’, *Z. Phys.* **61**, 206–219 (1930).
- ¹¹³L. D. Landau and E. M. Lifshitz, *Electrodynamics of Continuous Media*, 2nd ed., Vol. 8, Course of Theoretical Physics (Pergamon Press, 1984).
- ¹¹⁴P. Bak and M. H. Jensen, ‘Theory of Helical Magnetic Structures and Phase Transitions in MnSi and FeGe’, *J. Phys. C: Solid State Phys.* **13**, L881 (1980).
- ¹¹⁵J. Masell and K. Everschor-Sitte, ‘Current-Induced Dynamics of Chiral Magnetic Structures: Creation, Motion, and Applications’, in *Chirality, Magnetism and Magnetolectricity: Separate Phenomena and Joint Effects in Metamaterial Structures*, edited by E. Kamenetskii (Springer International Publishing, Cham, 2021), pp. 147–181.
- ¹¹⁶S. Blundell, *Magnetism in Condensed Matter*, Vol. 4, Oxford Master Series in Condensed Matter Physics (Oxford University Press, 2001).
- ¹¹⁷R. Skomski, ‘Magnetic Exchange Interactions’, in *Handbook of Magnetism and Magnetic Materials*, edited by M. Coey and S. Parkin (Springer International Publishing, Cham, 2020), pp. 1–50.
- ¹¹⁸C. Kittel, ‘Physical Theory of Ferromagnetic Domains’, *Rev. Mod. Phys.* **21**, 541–583 (1949).

- ¹¹⁹S.-Z. Lin and S. Hayami, ‘Ginzburg-Landau Theory for Skyrmions in Inversion-Symmetric Magnets with Competing Interactions’, *Phys. Rev. B* **93**, 064430 (2016).
- ¹²⁰I. Dzyaloshinsky, ‘A Thermodynamic Theory of “Weak” Ferromagnetism of Antiferromagnetics’, *J. Phys. Chem. Solids* **4**, 241–255 (1958).
- ¹²¹T. Moriya, ‘Anisotropic Superexchange Interaction and Weak Ferromagnetism’, *Phys. Rev.* **120**, 91–98 (1960).
- ¹²²K. M. D. Hals and K. Everschor-Sitte, ‘Twists in Ferromagnetic Monolayers with Trigonal Prismatic Symmetry’, *Phys. Rev. B* **99**, 104422 (2019).
- ¹²³Y. Tokura and N. Kanazawa, ‘Magnetic Skyrmion Materials’, *Chem. Rev.* **121**, 2857–2897 (2021).
- ¹²⁴K. M. D. Hals and K. Everschor-Sitte, ‘New Boundary-Driven Twist States in Systems with Broken Spatial Inversion Symmetry’, *Phys. Rev. Lett.* **119**, 127203 (2017).
- ¹²⁵S. Heinze et al., ‘Spontaneous Atomic-Scale Magnetic Skyrmion Lattice in Two Dimensions’, *Nat. Phys.* **7**, 713–718 (2011).
- ¹²⁶E. Ruff et al., ‘Multiferroicity and Skyrmions Carrying Electric Polarization in GaV_4S_8 ’, *Sci. Adv.* **1**, e1500916 (2015).
- ¹²⁷A. K. Nayak et al., ‘Magnetic Antiskyrmions Above Room Temperature in Tetragonal Heusler Materials’, *Nature* **548**, 561–566 (2017).
- ¹²⁸G. H. O. Daalderop, P. J. Kelly and M. F. H. Schuurmans, ‘First-Principles Calculation of the Magnetocrystalline Anisotropy Energy of Iron, Cobalt, and Nickel’, *Phys. Rev. B* **41**, 11919–11937 (1990).
- ¹²⁹J. Trygg et al., ‘Total Energy Calculation of the Magnetocrystalline Anisotropy Energy in the Ferromagnetic $3d$ Metals’, *Phys. Rev. Lett.* **75**, 2871–2874 (1995).
- ¹³⁰W. F. Brown, ‘Virtues and Weaknesses of the Domain Concept’, *Rev. Mod. Phys.* **17**, 15–19 (1945).
- ¹³¹H. Kronmüller, ‘Theory of Nucleation Fields in Inhomogeneous Ferromagnets’, *Phys. Status Solidi B* **144**, 385–396 (1987).
- ¹³²J. M. D. Coey, ‘History of Magnetism and Basic Concepts’, in *Handbook of Magnetism and Magnetic Materials*, edited by J. M. D. Coey and S. S. Parkin (Springer International Publishing, Cham, 2021), pp. 3–51.
- ¹³³N. H. N. Hayashi, K. S. K. Saito and Y. N. Y. Nakatani, ‘Calculation of Demagnetizing Field Distribution Based on Fast Fourier Transform of Convolution’, *Jpn. J. Appl. Phys.* **35**, 6065 (1996).
- ¹³⁴A. Hubert and R. Schäfer, *Magnetic Domains* (Springer Berlin, Heidelberg, 1998).
- ¹³⁵I. Dzyaloshinskii, ‘On the Magneto-Electrical Effect in Antiferromagnets’, *Soviet Physics JETP-USSR* **10**, 628–629 (1960).
- ¹³⁶D. Astrov, ‘The Magnetoelectric Effect in Antiferromagnets’, *J. Exp. Theor. Phys.* **38**, 984–985 (1960).
- ¹³⁷T. Kimura, ‘Spiral Magnets as Magnetoelectrics’, *Annu. Rev. Mater. Res.* **37**, 387–413 (2007).
- ¹³⁸Y. Tokura, S. Seki and N. Nagaosa, ‘Multiferroics of Spin Origin’, *Rep. Prog. Phys.* **77**, 076501 (2014).

Bibliography

- ¹³⁹H. Katsura, N. Nagaosa and A. V. Balatsky, ‘Spin Current and Magnetoelectric Effect in Noncollinear Magnets’, *Phys. Rev. Lett.* **95**, 057205 (2005).
- ¹⁴⁰S.-W. Cheong and M. Mostovoy, ‘Multiferroics: A Magnetic Twist for Ferroelectricity’, *Nat. Mater.* **6**, 13–20 (2007).
- ¹⁴¹V. G. Bar’yakhtar, V. A. L’Vov and D. A. Yablonskiĭ, ‘Inhomogeneous Magnetoelectric Effect’, *J. Exp. Theor. Phys.* **37**, 565 (1983).
- ¹⁴²M. Mostovoy, ‘Ferroelectricity in Spiral Magnets’, *Phys. Rev. Lett.* **96**, 067601 (2006).
- ¹⁴³C. Psaroudaki and C. Panagopoulos, ‘Skyrmion Qubits: A New Class of Quantum Logic Elements Based on Nanoscale Magnetization’, *Phys. Rev. Lett.* **127**, 067201 (2021).
- ¹⁴⁴T. L. Gilbert, ‘Formulation, Foundations and Applications of the Phenomenological Theory of Ferromagnetism.’, PhD thesis (Jan. 1956).
- ¹⁴⁵T. Gilbert, ‘A Phenomenological Theory of Damping in Ferromagnetic Materials’, *IEEE Trans. Magn.* **40**, 3443–3449 (2004).
- ¹⁴⁶C. Liu et al., ‘Origin of Low Gilbert Damping in Half Metals’, *Appl. Phys. Lett.* **95**, 022509 (2009).
- ¹⁴⁷T. Kubota et al., ‘Half-Metallicity and Gilbert Damping Constant in $\text{Co}_2\text{Fe}_x\text{Mn}_{1-x}\text{Si}$ Heusler Alloys Depending on the Film Composition’, *Appl. Phys. Lett.* **94**, 122504 (2009).
- ¹⁴⁸J. Zang et al., ‘Dynamics of Skyrmion Crystals in Metallic Thin Films’, *Phys. Rev. Lett.* **107**, 136804 (2011).
- ¹⁴⁹M. E. Lucassen et al., ‘Current-Driven and Field-Driven Domain Walls at Nonzero Temperature’, *Phys. Rev. B* **79**, 224411 (2009).
- ¹⁵⁰K. Everschor, ‘Current-Induced Dynamics of Chiral Magnetic Structures: Skyrmions, Emergent Electrodynamics and Spin-Transfer Torques’, PhD thesis (Universität zu Köln, 2012).
- ¹⁵¹J. H. Han, *Skyrmions in Condensed Matter*, Vol. 278, Springer Tracts in Modern Physics (Springer International Publishing, Cham, 2017).
- ¹⁵²N. Nagaosa and Y. Tokura, ‘Topological Properties and Dynamics of Magnetic Skyrmions’, *Nat. Nanotechnol.* **8**, 899–911 (2013).
- ¹⁵³T. Lancaster, ‘Skyrmions in Magnetic Materials’, *Contemp. Phys.* **60**, 246–261 (2019).
- ¹⁵⁴T. Schulz et al., ‘Emergent Electrodynamics of Skyrmions in a Chiral Magnet’, *Nat. Phys.* **8**, 301–304 (2012).
- ¹⁵⁵K. Everschor-Sitte and M. Sitte, ‘Real-Space Berry Phases: Skyrmion Soccer (Invited)’, *J. Appl. Phys.* **115**, 172602 (2014).
- ¹⁵⁶Z. Li and S. Zhang, ‘Domain-Wall Dynamics and Spin-Wave Excitations with Spin-Transfer Torques’, *Phys. Rev. Lett.* **92**, 207203 (2004).
- ¹⁵⁷J. C. Slonczewski, ‘Current-Driven Excitation of Magnetic Multilayers’, *J. Magn. Magn. Mater.* **159**, L1–L7 (1996).
- ¹⁵⁸X. Han et al., ‘Spin-Orbit Torques: Materials, Physics, and Devices’, *Appl. Phys. Lett.* **118**, 120502 (2021).

- ¹⁵⁹W. F. Brown, ‘Thermal Fluctuations of a Single-Domain Particle’, *Phys. Rev.* **130**, 1677–1686 (1963).
- ¹⁶⁰A. Lyberatos, D. V. Berkov and R. W. Chantrell, ‘A Method for the Numerical Simulation of the Thermal Magnetization Fluctuations in Micromagnetics’, *J. Phys. Condens. Matter* **5**, 8911 (1993).
- ¹⁶¹J. Leliaert et al., ‘Adaptively Time Stepping the Stochastic Landau-Lifshitz-Gilbert Equation at Nonzero Temperature: Implementation and Validation in MuMax3’, *AIP Adv.* **7**, 125010 (2017).
- ¹⁶²R. F. L. Evans et al., ‘Stochastic Form of the Landau-Lifshitz-Bloch Equation’, *Phys. Rev. B* **85**, 014433 (2012).
- ¹⁶³P. Nieves et al., ‘The Classical Two-Sublattice Landau-Lifshitz-Bloch Equation for All Temperatures’, *Low Temp. Phys.* **41**, 739–744 (2015).
- ¹⁶⁴U. Atxitia, D. Hinzke and U. Nowak, ‘Fundamentals and Applications of the Landau-Lifshitz-Bloch Equation’, *J. Phys. D: Appl. Phys.* **50**, 033003 (2016).
- ¹⁶⁵D. A. Garanin, ‘Fokker-Planck and Landau-Lifshitz-Bloch Equations for Classical Ferromagnets’, *Phys. Rev. B* **55**, 3050–3057 (1997).
- ¹⁶⁶C. Abert, ‘Micromagnetics and Spintronics: Models and Numerical Methods’, *Eur. Phys. J. B* **92**, 120 (2019).
- ¹⁶⁷A. Vansteenkiste et al., ‘The Design and Verification of MuMax3’, *AIP Adv.* **4**, 107133 (2014).
- ¹⁶⁸J. R. Dormand and P. J. Prince, ‘A Family of Embedded Runge-Kutta Formulae’, *J. Comput. Appl. Math.* **6**, 19–26 (1980).
- ¹⁶⁹A. A. Thiele, ‘Steady-State Motion of Magnetic Domains’, *Phys. Rev. Lett.* **30**, 230–233 (1973).
- ¹⁷⁰O. A. Tretiakov et al., ‘Dynamics of Domain Walls in Magnetic Nanostrips’, *Phys. Rev. Lett.* **100**, 127204 (2008).
- ¹⁷¹D. J. Clarke et al., ‘Dynamics of a Vortex Domain Wall in a Magnetic Nanostrip: Application of the Collective-Coordinate Approach’, *Phys. Rev. B* **78**, 134412 (2008).
- ¹⁷²M. Ezawa, ‘Giant Skyrmions Stabilized by Dipole-Dipole Interactions in Thin Ferromagnetic Films’, *Phys. Rev. Lett.* **105**, 197202 (2010).
- ¹⁷³T. Adams et al., ‘Long-Wavelength Helimagnetic Order and Skyrmion Lattice Phase in Cu_2OSeO_3 ’, *Phys. Rev. Lett.* **108**, 237204 (2012).
- ¹⁷⁴A. Tonomura et al., ‘Real-Space Observation of Skyrmion Lattice in Helimagnet MnSi Thin Samples’, *Nano Lett.* **12**, 1673–1677 (2012).
- ¹⁷⁵S. Seki, S. Ishiwata and Y. Tokura, ‘Magnetoelectric Nature of Skyrmions in a Chiral Magnetic Insulator Cu_2OSeO_3 ’, *Phys. Rev. B* **86**, 060403 (2012).
- ¹⁷⁶J. S. White et al., ‘Electric Field Control of the Skyrmion Lattice in Cu_2OSeO_3 ’, *J. Phys. Condens. Matter* **24**, 432201 (2012).
- ¹⁷⁷J. S. White et al., ‘Electric-Field-Induced Skyrmion Distortion and Giant Lattice Rotation in the Magnetoelectric Insulator Cu_2OSeO_3 ’, *Phys. Rev. Lett.* **113**, 107203 (2014).
- ¹⁷⁸I. Kézsmárki et al., ‘Néel-Type Skyrmion Lattice with Confined Orientation in the Polar Magnetic Semiconductor GaV_4S_8 ’, *Nat. Mater.* **14**, 1116–1122 (2015).

Bibliography

- ¹⁷⁹A. Soumyanarayanan et al., ‘Tunable Room-Temperature Magnetic Skyrmions in Ir/Fe/Co/Pt Multilayers’, *Nat. Mater.* **16**, 898–904 (2017).
- ¹⁸⁰S. Seki et al., ‘Observation of Skyrmions in a Multiferroic Material’, *Science* **336**, 198–201 (2012).
- ¹⁸¹S. Buhrandt and L. Fritz, ‘Skyrmion Lattice Phase in Three-Dimensional Chiral Magnets from Monte Carlo Simulations’, *Phys. Rev. B* **88**, 195137 (2013).
- ¹⁸²A. Bauer and C. Pfleiderer, ‘Generic Aspects of Skyrmion Lattices in Chiral Magnets’, in *Topological Structures in Ferromagnetic Materials: Domain Walls, Vortices and Skyrmions*, edited by J. Seidel (Springer International Publishing, Cham, 2016), pp. 1–28.
- ¹⁸³S. Rohart, J. Miltat and A. Thiaville, ‘Path to Collapse for an Isolated Néel Skyrmion’, *Phys. Rev. B* **93**, 214412 (2016).
- ¹⁸⁴S.-G. Je et al., ‘Direct Demonstration of Topological Stability of Magnetic Skyrmions via Topology Manipulation’, *ACS Nano* **14**, 3251–3258 (2020).
- ¹⁸⁵J. Hagemester et al., ‘Stability of Single Skyrmionic Bits’, *Nat. Commun.* **6**, 8455 (2015).
- ¹⁸⁶H. Oike et al., ‘Interplay Between Topological and Thermodynamic Stability in a Metastable Magnetic Skyrmion Lattice’, *Nat. Phys.* **12**, 62–66 (2016).
- ¹⁸⁷D. Cortés-Ortuño et al., ‘Thermal Stability and Topological Protection of Skyrmions in Nanotracks’, *Sci. Rep.* **7**, 4060 (2017).
- ¹⁸⁸A. Yoshimori, ‘A New Type of Antiferromagnetic Structure in the Rutile Type Crystal’, *J. Phys. Soc. Jpn.* **14**, 807–821 (1959).
- ¹⁸⁹M. Uchida et al., ‘Real-Space Observation of Helical Spin Order’, *Science* **311**, 359–361 (2006).
- ¹⁹⁰M. Ezawa, ‘Compact Merons and Skyrmions in Thin Chiral Magnetic Films’, *Phys. Rev. B* **83**, 100408 (2011).
- ¹⁹¹R. Knapman et al., ‘Current-Induced H-Shaped-Skyrmion Creation and Their Dynamics in the Helical Phase’, *J. Phys. D: Appl. Phys.* **54**, 404003 (2021).
- ¹⁹²J. Müller et al., ‘Magnetic Skyrmions and Skyrmion Clusters in the Helical Phase of Cu_2OSeO_3 ’, *Phys. Rev. Lett.* **119**, 137201 (2017).
- ¹⁹³A. O. Leonov et al., ‘Three-Dimensional Chiral Skyrmions with Attractive Interparticle Interactions’, *J. Phys. Condens. Matter* **28**, 35LT01 (2016).
- ¹⁹⁴J. C. Loudon et al., ‘Direct Observation of Attractive Skyrmions and Skyrmion Clusters in the Cubic Helimagnet Cu_2OSeO_3 ’, *Phys. Rev. B* **97**, 134403 (2018).
- ¹⁹⁵A. O. Leonov, C. Pappas and I. I. Smalyukh, ‘Field-Driven Metamorphoses of Isolated Skyrmions Within the Conical State of Cubic Helimagnets’, *Phys. Rev. B* **104**, 064432 (2021).
- ¹⁹⁶S. Rohart and A. Thiaville, ‘Skyrmion Confinement in Ultrathin Film Nanostructures in the Presence of Dzyaloshinskii-Moriya Interaction’, *Phys. Rev. B* **88**, 184422 (2013).
- ¹⁹⁷T. Okubo, S. Chung and H. Kawamura, ‘Multiple- q States and the Skyrmion Lattice of the Triangular-Lattice Heisenberg Antiferromagnet under Magnetic Fields’, *Phys. Rev. Lett.* **108**, 017206 (2012).
- ¹⁹⁸A. O. Leonov and M. Mostovoy, ‘Multiply Periodic States and Isolated Skyrmions in an Anisotropic Frustrated Magnet’, *Nat. Commun.* **6**, 8275 (2015).

- ¹⁹⁹J. T. Chalker, ‘Geometrically Frustrated Antiferromagnets: Statistical Mechanics and Dynamics’, in *Introduction to Frustrated Magnetism: Materials, Experiments, Theory*, edited by C. Lacroix, P. Mendels and F. Mila (Springer Berlin, Heidelberg, Berlin, Heidelberg, 2011), pp. 3–22.
- ²⁰⁰T. Kurumaji et al., ‘Skyrmion Lattice with a Giant Topological Hall Effect in a Frustrated Triangular-Lattice Magnet’, *Science* **365**, 914–918 (2019).
- ²⁰¹M. Hirschberger et al., ‘Skyrmion Phase and Competing Magnetic Orders on a Breathing Kagomé Lattice’, *Nat. Commun.* **10**, 5831 (2019).
- ²⁰²N. D. Khanh et al., ‘Nanometric Square Skyrmion Lattice in a Centrosymmetric Tetragonal Magnet’, *Nat. Nanotechnol.* **15**, 444–449 (2020).
- ²⁰³X. Zhang et al., ‘Skyrmion Dynamics in a Frustrated Ferromagnetic Film and Current-Induced Helicity Locking-Unlocking Transition’, *Nat. Commun.* **8**, 1717 (2017).
- ²⁰⁴J. A. M. Paddison et al., ‘Magnetic Interactions of the Centrosymmetric Skyrmion Material Gd_2PdSi_3 ’, *Phys. Rev. Lett.* **129**, 137202 (2022).
- ²⁰⁵M. Sitte et al., ‘Current-Driven Periodic Domain Wall Creation in Ferromagnetic Nanowires’, *Phys. Rev. B* **94**, 064422 (2016).
- ²⁰⁶S. X. Wang and A. M. Taratorin, *Magnetic Information Storage Technology*, Academic Press Series in Electromagnetism (Academic Press).
- ²⁰⁷K. Everschor-Sitte et al., ‘Skyrmion Production On Demand by Homogeneous DC Currents’, *New J. Phys.* **19**, 092001 (2017).
- ²⁰⁸D. R. Rodrigues, N. Sommer and K. Everschor-Sitte, ‘Facilitating Domain Wall Injection in Magnetic Nanowires by Electrical Means’, *Phys. Rev. B* **101**, 224410 (2020).
- ²⁰⁹N. Romming et al., ‘Writing and Deleting Single Magnetic Skyrmions’, *Science* **341**, 636–639 (2013).
- ²¹⁰J. Sampaio et al., ‘Nucleation, Stability and Current-Induced Motion of Isolated Magnetic Skyrmions in Nanostructures’, *Nat. Nanotechnol.* **8**, 839–844 (2013).
- ²¹¹S. Zhang, A. K. Petford-Long and C. Phatak, ‘Creation of Artificial Skyrmions and Antiskyrmions by Anisotropy Engineering’, *Sci. Rep.* **6**, 31248 (2016).
- ²¹²K. Fallon et al., ‘Controlled Individual Skyrmion Nucleation at Artificial Defects Formed by Ion Irradiation’, *Small* **16**, 1907450 (2020).
- ²¹³C. Deger, I. Yavuz and F. Yildiz, ‘Current-Driven Coherent Skyrmion Generation’, *Sci. Rep.* **9**, 3513 (2019).
- ²¹⁴W. Jiang et al., ‘Blowing Magnetic Skyrmion Bubbles’, *Science* **349**, 283–286 (2015).
- ²¹⁵F. Büttner et al., ‘Field-Free Deterministic Ultrafast Creation of Magnetic Skyrmions by Spin–Orbit Torques’, *Nat. Nanotechnol.* **12**, 1040–1044 (2017).
- ²¹⁶R. Zarzuela et al., ‘Stability and Dynamics of In-Plane Skyrmions in Collinear Ferromagnets’, *Phys. Rev. B* **101**, 054405 (2020).
- ²¹⁷T. Yokouchi et al., ‘Creation of Magnetic Skyrmions by Surface Acoustic Waves’, *Nat. Nanotechnol.* **15**, 361–366 (2020).
- ²¹⁸W. Koshibae and N. Nagaosa, ‘Creation of Skyrmions and Antiskyrmions by Local Heating’, *Nat. Commun.* **5**, 5148 (2014).

Bibliography

- ²¹⁹U. Ritzmann et al., ‘Asymmetric Skyrmion-Antiskyrmion Production in Ultrathin Ferromagnetic Films’, *Phys. Rev. B* **102**, 174409 (2020).
- ²²⁰M. Stier et al., ‘Skyrmion–Anti-Skyrmion Pair Creation by In-Plane Currents’, *Phys. Rev. Lett.* **118**, 267203 (2017).
- ²²¹J. A. Brock et al., ‘Current-Induced Generation of Skyrmions in Pt/Co/Os/Pt Thin Films’, *Phys. Rev. B* **102**, 024443 (2020).
- ²²²J. Masell et al., ‘Combing the Helical Phase of Chiral Magnets with Electric Currents’, *Phys. Rev. B* **102**, 180402 (2020).
- ²²³J. Müller, ‘Magnetic Skyrmions on a Two-Lane Racetrack’, *New J. Phys.* **19**, 025002 (2017).
- ²²⁴D. G. Akhmetov, *Vortex Rings* (Springer Berlin, Heidelberg, 2009).
- ²²⁵I. E. Dzyaloshinskii and B. A. Ivanov, ‘Localized Topological Solitons in a Ferromagnet’, *JETP Lett.* **29**, 540 (1979).
- ²²⁶A. B. Borisov and F. N. Rybakov, ‘Stationary Precession Topological Solitons with Nonzero Hopf Invariant in a Uniaxial Ferromagnet’, *JETP Lett.* **88**, 264–267 (2008).
- ²²⁷N. Papanicolaou, ‘Dynamics of Magnetic Vortex Rings’, in *Singularities in Fluids, Plasmas and Optics*, edited by R. E. Caffisch and G. C. Papanicolaou, NATO ASI Series (Springer Netherlands, Dordrecht, 1993), pp. 151–158.
- ²²⁸N. R. Cooper, ‘Propagating Magnetic Vortex Rings in Ferromagnets’, *Phys. Rev. Lett.* **82**, 1554–1557 (1999).
- ²²⁹P. Sutcliffe, ‘Vortex Rings in Ferromagnets: Numerical Simulations of the Time-Dependent Three-Dimensional Landau-Lifshitz Equation’, *Phys. Rev. B* **76**, 184439 (2007).
- ²³⁰G. Yu et al., ‘Room-Temperature Creation and Spin–Orbit Torque Manipulation of Skyrmions in Thin Films with Engineered Asymmetry’, *Nano Lett.* **16**, 1981–1988 (2016).
- ²³¹S. Woo et al., ‘Spin-Orbit Torque-Driven Skyrmion Dynamics Revealed by Time-Resolved X-Ray Microscopy’, *Nat. Commun.* **8**, 15573 (2017).
- ²³²R. Msiska et al., ‘Nonzero Skyrmion Hall Effect in Topologically Trivial Structures’, *Phys. Rev. Appl.* **17**, 064015 (2022).
- ²³³X. Z. Yu et al., ‘Skyrmion Flow Near Room Temperature in an Ultralow Current Density’, *Nat. Commun.* **3**, 988 (2012).
- ²³⁴X. Zhang, Y. Zhou and M. Ezawa, ‘Magnetic Bilayer-Skyrmions without Skyrmion Hall Effect’, *Nat. Commun.* **7**, 10293 (2016).
- ²³⁵H. T. Fook et al., ‘Mitigation of Magnus Force in Current-Induced Skyrmion Dynamics’, *IEEE Trans. Magn.* **51**, 1–4 (2015).
- ²³⁶I. Purnama et al., ‘Guided Current-Induced Skyrmion Motion in 1D Potential Well’, *Sci. Rep.* **5**, 10620 (2015).
- ²³⁷P. Lai et al., ‘An Improved Racetrack Structure for Transporting a Skyrmion’, *Sci. Rep.* **7**, 45330 (2017).
- ²³⁸R. Tomasello et al., ‘Chiral Skyrmions in an Anisotropy Gradient’, *Phys. Rev. B* **98**, 024421 (2018).

- ²³⁹S. Huang et al., ‘Stabilization and Current-Induced Motion of Antiskyrmion in the Presence of Anisotropic Dzyaloshinskii-Moriya Interaction’, *Phys. Rev. B* **96**, 144412 (2017).
- ²⁴⁰K.-W. Kim et al., ‘Asymmetric Skyrmion Hall Effect in Systems with a Hybrid Dzyaloshinskii-Moriya Interaction’, *Phys. Rev. B* **97**, 224427 (2018).
- ²⁴¹S. L. Zhang et al., ‘Manipulation of Skyrmion Motion by Magnetic Field Gradients’, *Nat. Commun.* **9**, 2115 (2018).
- ²⁴²B. Göbel and I. Mertig, ‘Skyrmion Ratchet Propagation: Utilizing the Skyrmion Hall Effect in AC Racetrack Storage Devices’, *Sci. Rep.* **11**, 3020 (2021).
- ²⁴³X. Zhao et al., ‘Current-Induced Magnetic Skyrmions with Controllable Polarities in the Helical Phase’, *Nano Lett.* **22**, 8793–8800 (2022).
- ²⁴⁴D. Song et al., ‘Experimental Observation of One-Dimensional Motion of Interstitial Skyrmion in FeGe’, *arXiv:2212.08991 [cond-mat]*, 10.48550/arXiv.2212.08991 (2022).
- ²⁴⁵M. Garst, ‘Topological Skyrmion Dynamics in Chiral Magnets’, in *Topological Structures in Ferroic Materials: Domain Walls, Vortices and Skyrmions*, edited by J. Seidel (Springer International Publishing, Cham, 2016), pp. 29–53.
- ²⁴⁶M. Garst, J. Waizner and D. Grundler, ‘Collective Spin Excitations of Helices and Magnetic Skyrmions: Review and Perspectives of Magnonics in Non-Centrosymmetric Magnets’, *J. Phys. D: Appl. Phys.* **50**, 293002 (2017).
- ²⁴⁷M. Lonsky and A. Hoffmann, ‘Dynamic Excitations of Chiral Magnetic Textures’, *APL Mater.* **8**, 100903 (2020).
- ²⁴⁸A. Barman et al., ‘The 2021 Magnonics Roadmap’, *J. Phys. Condens. Matter* **33**, 413001 (2021).
- ²⁴⁹A. A. Serga, A. V. Chumak and B. Hillebrands, ‘YIG Magnonics’, *J. Phys. D: Appl. Phys.* **43**, 264002 (2010).
- ²⁵⁰A. Khitun, M. Bao and K. L. Wang, ‘Magnonic Logic Circuits’, *J. Phys. D: Appl. Phys.* **43**, 264005 (2010).
- ²⁵¹T. Brächer and P. Pirro, ‘An Analog Magnon Adder for All-Magnonic Neurons’, *J. Appl. Phys.* **124**, 152119 (2018).
- ²⁵²A. V. Chumak et al., ‘Magnon Spintronics’, *Nat. Phys.* **11**, 453–461 (2015).
- ²⁵³B. Lenk et al., ‘The Building Blocks of Magnonics’, *Phys. Rep.* **507**, 107–136 (2011).
- ²⁵⁴V. V. Kruglyak, S. O. Demokritov and D. Grundler, ‘Magnonics’, *J. Phys. D: Appl. Phys.* **43**, 264001 (2010).
- ²⁵⁵E. M. Lifshitz and L. P. Pitaevskii, *Statistical Physics Part 2: Theory of the Condensed State*, Vol. 9, Course of Theoretical Physics (Butterworth-Heinemann Ltd, 1980).
- ²⁵⁶M. Mochizuki, ‘Spin-Wave Modes and Their Intense Excitation Effects in Skyrmion Crystals’, *Phys. Rev. Lett.* **108**, 017601 (2012).
- ²⁵⁷Y. Onose et al., ‘Observation of Magnetic Excitations of Skyrmion Crystal in a Helimagnetic Insulator Cu_2OSeO_3 ’, *Phys. Rev. Lett.* **109**, 037603 (2012).
- ²⁵⁸D. R. Rodrigues et al., ‘Nonlinear Dynamics of Topological Ferromagnetic Textures for Frequency Multiplication’, *Phys. Rev. Applied* **16**, 014020 (2021).

Bibliography

- ²⁵⁹J.-V. Kim, ‘Chapter Four - Spin-Torque Oscillators’, in *Solid State Physics*, Vol. 63, edited by R. E. Camley and R. L. Stamps, Solid State Physics (Academic Press, 2012), pp. 217–294.
- ²⁶⁰S. I. Kiselev et al., ‘Microwave Oscillations of a Nanomagnet Driven by a Spin-Polarized Current’, *Nature* **425**, 380–383 (2003).
- ²⁶¹V. S. Pribiag et al., ‘Magnetic Vortex Oscillator Driven by D.C. Spin-Polarized Current’, *Nat. Phys.* **3**, 498–503 (2007).
- ²⁶²Y. Okamura et al., ‘Microwave Magnetoelectric Effect via Skyrmion Resonance Modes in a Helimagnetic Multiferroic’, *Nat. Commun.* **4**, 2391 (2013).
- ²⁶³T. Schwarze et al., ‘Universal Helimagnon and Skyrmion Excitations in Metallic, Semiconducting and Insulating Chiral Magnets’, *Nat. Mater.* **14**, 478–483 (2015).
- ²⁶⁴M. d’Aquino et al., ‘A Novel Formulation for the Numerical Computation of Magnetization Modes in Complex Micromagnetic Systems’, *J. Comput. Phys.* **228**, 6130–6149 (2009).
- ²⁶⁵S.-Z. Lin, C. D. Batista and A. Saxena, ‘Internal Modes of a Skyrmion in the Ferromagnetic State of Chiral Magnets’, *Phys. Rev. B* **89**, 024415 (2014).
- ²⁶⁶C. Schütte and M. Garst, ‘Magnon-Skyrmion Scattering in Chiral Magnets’, *Phys. Rev. B* **90**, 094423 (2014).
- ²⁶⁷M. Beg et al., ‘Dynamics of Skyrmionic States in Confined Helimagnetic Nanostructures’, *Phys. Rev. B* **95**, 014433 (2017).
- ²⁶⁸V. P. Kravchuk et al., ‘Spin Eigenmodes of Magnetic Skyrmions and the Problem of the Effective Skyrmion Mass’, *Phys. Rev. B* **97**, 064403 (2018).
- ²⁶⁹M.-A. Bisotti et al., *FinMag: Finite-Element Micromagnetic Simulation Tool*, 2018.
- ²⁷⁰Z. V. Gareeva and K. Y. Guslienko, ‘Magnetic Skyrmion Dynamics in Thin Cylindrical Dots’, *Phys. Status Solidi RRL* **10**, 227–232 (2016).
- ²⁷¹D. R. Rodrigues et al., ‘Effective Description of Domain Wall Strings’, *Phys. Rev. B* **97**, 134414 (2018).
- ²⁷²B. F. McKeever et al., ‘Characterizing Breathing Dynamics of Magnetic Skyrmions and Antiskyrmions Within the Hamiltonian Formalism’, *Phys. Rev. B* **99**, 054430 (2019).
- ²⁷³J.-V. Kim et al., ‘Breathing Modes of Confined Skyrmions in Ultrathin Magnetic Dots’, *Phys. Rev. B* **90**, 064410 (2014).
- ²⁷⁴M. Mruczkiewicz, M. Krawczyk and K. Y. Guslienko, ‘Spin Excitation Spectrum in a Magnetic Nanodot with Continuous Transitions Between the Vortex, Bloch-Type Skyrmion, and Néel-Type Skyrmion States’, *Phys. Rev. B* **95**, 094414 (2017).
- ²⁷⁵R. D. McMichael and M. D. Stiles, ‘Magnetic Normal Modes of Nanoelements’, *J. Appl. Phys.* **97**, 10J901 (2005).
- ²⁷⁶G. New, *Introduction to Nonlinear Optics* (Cambridge University Press, 2011).
- ²⁷⁷G. Chien and P. Gray, ‘A 900-MHz Local Oscillator Using a DLL-based Frequency Multiplier Technique for PCS Applications’, *IEEE J. Solid-State Circuits* **35**, 1996–1999 (2000).
- ²⁷⁸H. Mulaosmanovic et al., ‘Reconfigurable Frequency Multiplication with a Ferroelectric Transistor’, *Nat. Electron.* **3**, 391–397 (2020).

- ²⁷⁹P. Campagnola, ‘Second Harmonic Generation Imaging Microscopy: Applications to Diseases Diagnostics’, *Anal. Chem.* **83**, 3224–3231 (2011).
- ²⁸⁰A. S. Borovik-Romanov and S. K. Sinha, *Spin Waves and Magnetic Excitations*, Vol. 22.1, Modern Problems in Condensed Matter Sciences (North-Holland, 1988).
- ²⁸¹T. Brächer, P. Pirro and B. Hillebrands, ‘Parallel Pumping for Magnon Spintronics: Amplification and Manipulation of Magnon Spin Currents on the Micron-Scale’, *Phys. Rep.* **699**, 1–34 (2017).
- ²⁸²J. Iwasaki, A. J. Beekman and N. Nagaosa, ‘Theory of Magnon-Skyrmion Scattering in Chiral Magnets’, *Phys. Rev. B* **89**, 064412 (2014).
- ²⁸³P. Virtanen et al., ‘SciPy 1.0: Fundamental Algorithms for Scientific Computing in Python’, *Nat. Methods* **17**, 261–272 (2020).
- ²⁸⁴S. van der Walt et al., ‘scikit-image: Image Processing in Python’, *PeerJ* **2**, e453 (2014).
- ²⁸⁵G. Csaba and W. Porod, ‘Coupled Oscillators for Computing: A Review and Perspective’, *Appl. Phys. Rev.* **7**, 011302 (2020).
- ²⁸⁶R. Knapman et al., ‘Spacetime Magnetic Hopfions: From Internal Excitations and Braiding of Skyrmions’, *arXiv:2305.07589 [cond-mat]*, 10.48550/arXiv.2305.07589 (2023).
- ²⁸⁷H.-B. Braun, ‘Fluctuations and Instabilities of Ferromagnetic Domain-Wall Pairs in an External Magnetic Field’, *Phys. Rev. B* **50**, 16485–16500 (1994).
- ²⁸⁸X. S. Wang, H. Y. Yuan and X. R. Wang, ‘A Theory on Skyrmion Size’, *Communications Physics* **1**, 1–7 (2018).
- ²⁸⁹A. Pikovsky, M. Rosenblum and J. Kurths, *Synchronization: A Universal Concept in Nonlinear Sciences*, Cambridge Nonlinear Science Series (Cambridge University Press, 2001).
- ²⁹⁰M. Kobayashi and M. Nitta, ‘Winding Hopfions on $R^2 \times S^1$ ’, *Nucl. Phys. B* **876**, 605–618 (2013).
- ²⁹¹D. Auckly and L. Kapitanski, ‘Analysis of S^2 -Valued Maps and Faddeev’s Model’, *Commun. Math. Phys.* **256**, 611–620 (2005).
- ²⁹²J. Jäykkä and J. Hietarinta, ‘Unwinding in Hopfion Vortex Bunches’, *Phys. Rev. D* **79**, 125027 (2009).
- ²⁹³M. Staley, ‘Understanding Quaternions and the Dirac Belt Trick’, *Eur. J. Phys.* **31**, 467 (2010).
- ²⁹⁴L. Yong-Kai and Y. Shi-Jie, ‘Three-Dimensional Solitons in Two-Component Bose-Einstein Condensates’, *Chinese Phys. B* **23**, 110308 (2014).
- ²⁹⁵V. Kravchuk, ‘Problems in Micromagnetism’, Manuscript in preparation, 2023.
- ²⁹⁶Y. Zhou et al., ‘Dynamically Stabilized Magnetic Skyrmions’, *Nat. Commun.* **6**, 8193 (2015).
- ²⁹⁷K. Shibata et al., ‘Towards Control of the Size and Helicity of Skyrmions in Helimagnetic Alloys by Spin–Orbit Coupling’, *Nat. Nanotechnol.* **8**, 723–728 (2013).
- ²⁹⁸S. L. Zhang et al., ‘Direct Observation of Twisted Surface Skyrmions in Bulk Crystals’, *Phys. Rev. Lett.* **120**, 227202 (2018).

Bibliography

- ²⁹⁹Z. Hou et al., ‘Current-Induced Helicity Reversal of a Single Skyrmionic Bubble Chain in a Nanostructured Frustrated Magnet’, *Adv. Mater.* **32**, 1904815 (2020).
- ³⁰⁰X. Zhang et al., ‘Dynamic Transformation Between a Skyrmion String and a Bimeron String in a Layered Frustrated System’, *Phys. Rev. B* **104**, L220406 (2021).
- ³⁰¹X. Yao, J. Chen and S. Dong, ‘Controlling the Helicity of Magnetic Skyrmions by Electrical Field in Frustrated Magnets’, *New J. Phys.* **22**, 083032 (2020).
- ³⁰²M. Mostovoy, ‘Electrically-Excited Motion of Topological Defects in Multiferroic Materials’, *J. Phys. Soc. Jpn.* **92**, 081005 (2023).
- ³⁰³K.-W. Moon et al., ‘Magnetic Bubblecade Memory Based on Chiral Domain Walls’, *Sci. Rep.* **5**, 9166 (2015).
- ³⁰⁴E. Raimondo et al., ‘Temperature-Gradient-Driven Magnetic Skyrmion Motion’, *Phys. Rev. Appl.* **18**, 024062 (2022).
- ³⁰⁵P. Tengdin et al., ‘Imaging the Ultrafast Coherent Control of a Skyrmion Crystal’, *Phys. Rev. X* **12**, 041030 (2022).
- ³⁰⁶J. Nothhelfer et al., ‘Method and Device for Providing Anyons, Use of the Device’, European Patent Application EP3751472A1/International Patent Application WO2020EP66120 (2019).
- ³⁰⁷X. Z. Yu et al., ‘Motion Tracking of 80-nm-Size Skyrmions Upon Directional Current Injections’, *Sci. Adv.* **6**, eaaz9744 (2020).
- ³⁰⁸S. Seki et al., ‘Formation and Rotation of Skyrmion Crystal in the Chiral-Lattice Insulator Cu_2OSeO_3 ’, *Phys. Rev. B* **85**, 220406 (2012).
- ³⁰⁹B. Ding et al., ‘Observation of Magnetic Skyrmion Bubbles in a van Der Waals Ferromagnet Fe_3GeTe_2 ’, *Nano Lett.* **20**, 868–873 (2020).
- ³¹⁰W. Jiang et al., ‘Mobile Néel Skyrmions at Room Temperature: Status and Future’, *AIP Adv.* **6**, 055602 (2016).
- ³¹¹S. Woo et al., ‘Observation of Room-Temperature Magnetic Skyrmions and Their Current-Driven Dynamics in Ultrathin Metallic Ferromagnets’, *Nat. Mater.* **15**, 501–506 (2016).
- ³¹²K. Litzius et al., ‘Skyrmion Hall Effect Revealed by Direct Time-Resolved X-Ray Microscopy’, *Nat. Phys.* **13**, 170–175 (2017).
- ³¹³W. Jiang et al., ‘Direct Observation of the Skyrmion Hall Effect’, *Nat. Phys.* **13**, 162–169 (2017).
- ³¹⁴A. Casiraghi et al., ‘Individual Skyrmion Manipulation by Local Magnetic Field Gradients’, *Commun. Phys.* **2**, 1–9 (2019).
- ³¹⁵K.-Y. Meng et al., ‘Observation of Nanoscale Skyrmions in $\text{SrIrO}_3/\text{SrRuO}_3$ Bilayers’, *Nano Lett.* **19**, 3169–3175 (2019).
- ³¹⁶M. Baer, *findiff Software Package*, 2018.
- ³¹⁷The Sage Developers, *SageMath, The Sage Mathematics Software System*, 2022.

Acknowledgements

First and foremost, I would like to thank my supervisor, Karin Everschor-Sitte, for allowing me to be a part of her research group. She has been an excellent role model and has been instrumental in both my academic and personal development.

I would also like to thank my second supervisor, Jairo Sinova, for his support, especially during the initial stages of my PhD.

I thank Studienstiftung des deutschen Volkes for providing financial support for the majority of my PhD.

I thank all the people with whom I have collaborated on scientific projects during the past few years. In particular, I would like to explicitly thank Davi Rodrigues and Sebastián Díaz, who were excellent mentors from whom I learned a lot.

I am very grateful to Ran Cheng for the research stay in his group at the University of California, Riverside.

I want to express my profound appreciation for my teammates over the years who have both helped me academically and created an enjoyable office atmosphere. In particular, I would like to thank Benjamin McKeever, who was always happy to answer my questions and give useful advice during the early months of my PhD. I would also like to acknowledge Alessandro Pignedoli for his expertise in analytical calculations, and Jonas Nothhelfer for going out of his way to help with IT-related problems. I thank Petra Schmidt for her extensive help with administrative matters. I am grateful to the other people with whom I have interacted on a day-to-day basis including Robin Msiska, Jake Love, Sandra Shaju, Omer Fetai, Atreya Majumdar, Maria Azhar, Anna Birk Hellenes, Uday Chopra, Timo Pulch, and V.K. Bharadwaj for creating a positive group atmosphere.

I wish to thank Maria Azhar and Alessandro Pignedoli for their useful comments on this Thesis, as well as my mum for her attention to detail in proofreading it.

I would like to express my heartfelt thanks to all of my friends outside of my academic life. In particular, I would like to thank Rahul Prathepan for his friendship throughout the years. I would also like to thank Nicola Bogo and Elio Casalini for the amusing times we had outside of work.

Finally, I am extremely grateful to my family, especially my mum and dad, Mandy and Mark Knapman, and my brother, Thomas Knapman, for their unwavering love and support throughout my life.

Part V.

Anhänge gemäß Prüfungsordnung

List of Publications

Preprints

- R. Knapman, T. Tausendpfund, S. A. Díaz, and K. Everschor-Sitte, ‘Space-time Magnetic Hopfions: From Internal Excitations and Braiding of Skyrmions’, arXiv:2305.07589 (2023).
For this project, I performed both the collective coordinate and micromagnetic modelling and performed the analysis of the resulting data, with input from the other authors. Furthermore, I created all of the figures in the preprint. The results of this investigation are presented in Chapter 11 of this Thesis.

Peer-Reviewed Publications

- R. Knapman, D. R. Rodrigues, J. Masell, and K. Everschor-Sitte, ‘Current-Induced H-Shaped-Skyrmion Creation and Their Dynamics in the Helical Phase’, Journal of Physics D: Applied Physics **54**, 404003 (2021).
Here, I performed the numerical modelling and the analysis of the results, and was responsible for investigating methods through which skyrmions could be created in the cycloidal background, including proposing the protocol discussed in the publication. I created all of the figures contained within it. The results are discussed in Chapters 5, 7, and 9 of this Thesis.
- D. R. Rodrigues, J. Nothhelfer, M. Mohseni, R. Knapman, P. Pirro, and K. Everschor-Sitte, ‘Nonlinear Dynamics of Topological Ferromagnetic Textures for Frequency Multiplication’, Physical Review Applied **16**, 014020 (2021).
For this publication, I wrote the code used to obtain the power spectra of the skyrmion resonance modes. I contributed to Fig. 1, and created Fig. 2 from data supplied by co-authors. The results of this work are discussed in Chapter 10 of this Thesis.

Curriculum Vitae

Personal Details

Name	Ross John Knapman
Date of Birth	15th July 1997
Place of Birth	Northallerton, United Kingdom
Nationality	British

Education

2019 – Present	PhD, Johannes Gutenberg University Mainz, Mainz, Germany
2015 – 2019	Master of Physics, Durham University, Durham, United Kingdom
2013 – 2015	A Levels, Paston Sixth Form College, North Walsham, United Kingdom
2011 – 2013	GCSEs, Broadland High School, Hoveton, United Kingdom

Employment

08.2022 – Present	Research Associate, University of Duisburg-Essen, Duisburg, Germany
08.2019 – 07.2022	Research Associate, Johannes Gutenberg University Mainz, Mainz, Germany
06.2017 – 09.2017	DAAD RISE Intern, German Aerospace Center (DLR) Oberpfaffenhofen, Weßling, Germany

Teaching Experience

WS 2023 – 2024	Tutor, Elektrodynamik, University of Duisburg-Essen
WS 2020 – 2021	Tutor, Experimentalphysik 5c (Physik der kondensierten Materie), Johannes Gutenberg University Mainz
SS 2020	Senior Assistant, Mathematische Rechenmethoden, Johannes Gutenberg University Mainz
WS 2019 – 2020	Tutor, Experimentalphysik 5a (Atom- und Quantenphysik), Johannes Gutenberg University Mainz